

70 42029

CR 114253

SPACE RESEARCH COORDINATION CENTER



THE ROOM TEMPERATURE DEFORMATION AND FRACTURE OF SEVERAL POLYCRYSTALLINE GRAPHITES

BY

CLARENCE A. ANDERSSON

DEPARTMENT OF
METALLURGICAL/MATERIALS ENGINEERING

SRCC REPORT NO. 138

✓ NGL-39-011-002

UNIVERSITY OF PITTSBURGH

PITTSBURGH, PENNSYLVANIA

19 AUGUST 1970

CASE FILE
COPY

The Space Research Coordination Center, established in May, 1963, has the following functions: (1) it administers predoctoral and postdoctoral fellowships in space-related science and engineering programs; (2) it makes available, on application and after review, allocations to assist new faculty members in the Division of the Natural Sciences and the School of Engineering to initiate research programs or to permit established faculty members to do preliminary; work on research ideas of a novel character; (3) in the Division of the Natural Sciences it makes an annual allocation of funds to the interdisciplinary Laboratory for Atmospheric and Space Sciences; (4) in the School of Engineering it makes a similar allocation of funds to the Department of Metallurgical and Materials Engineering and to the program in Engineering Systems Management of the Department of Industrial Engineering; and (5) in concert with the University's Knowledge Availability Systems Center, it seeks to assist in the orderly transfer of new space-generated knowledge in industrial application. The Center also issues periodic reports of space-oriented research and a comprehensive annual report.

The Center is supported by an Institutional Grant (~~NSG-416~~) from the National Aeronautics and Space Administration, strongly supplemented by grants from the A. W. Mellon Educational and Charitable Trust, the Maurice Falk Medical Fund, the Richard King Mellon Foundation and the Sarah Mellon Scaife Foundation. Much of the work described in SRCC reports is financed by other grants, made to individual faculty members.

THE ROOM TEMPERATURE DEFORMATION AND FRACTURE OF SEVERAL
POLYCRYSTALLINE GRAPHITES

by

Clarence Allan Andersson

B. Met. E., New York University, 1959

Submitted to the Graduate Faculty

of the School of Engineering

in partial fulfillment of

the requirements for the degree of

Doctor


of

Philosophy

University of Pittsburgh

1970

The author grants permission
to reproduce single copies.

A handwritten signature in dark ink, appearing to read "Clarence A. Andersson", written over a horizontal line.

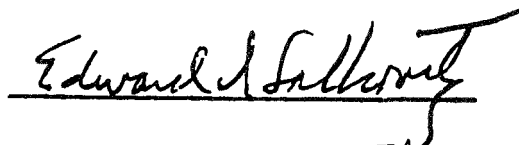
Signed

ACKNOWLEDGEMENTS

I am indebted to many people, both directly and indirectly, for making this dissertation possible. I especially wish to express my gratitude for the guidance, encouragement and help of my advisor Professor Edward I. Salkovitz, and for the comments and criticisms of the examining committee: Professors Joel I. Abrahms, Jean R. Blachere, Harold D. Brody and T. C. Woo. I would also like to acknowledge the encouragement of Mr. Morton B. Blinn, Dr. Gerald R. Kilp and Mr. David C. Goldberg of the Westinghouse Electric Corporation and the assistance in mechanical testing received from Mr. Edwin Vandergrift and Mr. George Yatsko. Finally, great credit is also due to my wife Amy for her managerial skills.

ABSTRACT

Signature



THE ROOM TEMPERATURE DEFORMATION AND FRACTURE OF SEVERAL
POLYCRYSTALLINE GRAPHITES

Clarence Allan Andersson, Ph.D.

University of Pittsburgh, 1970

The room temperature mechanical properties of four commercial polycrystalline graphites were investigated. The tensile deformation and fracture were correlated to the particle sizes, the particle preferred orientations, the bulk densities and the stress axis directions.

With regard to the deformation, the total strain at a given stress was found to be comprised of three strain components: (a) a linear elastic strain; (b) an elastically constrained nonlinear plastic strain; and (c) a residual strain arising from the relief of internal stresses by crack formation. The dependence of the elastic strain on the preferred orientation, the stress axis direction, the fraction porosity and the extent of deformation was determined. The plastic deformation was found to be limited by the magnitude of the elastic

deformation, i.e., the plastic strain was proportional to the n^{th} power ($n \approx 3$) of the product of the elastic compliance for the fully dense material and the applied stress. The residual strain was found to be linearly proportional to the maximum elastic strain that the material had been subjected to. These results were combined into a single deformation equation.

The fracture mechanism for polycrystalline graphite was determined. The materials were shown to develop large cracks during deformation. By quantitatively assessing the effects of the particle sizes, pore fractions, degrees of preferred orientation and the stress axis directions on each of the parameters of the equation for the brittle fracture of a body containing such a crack, a fracture criterion was derived. Particle sizes affect the number of single particle fractures required to create the critical crack. Increasing porosity is shown to significantly decrease both the elastic moduli and the fracture surface energies and to slightly increase the critical crack size. Elastic moduli decrease and the probabilities of particle fracture increase with preferential orientation of basal planes normal to the stress axis.

Several improvements in testing and analytic techniques were achieved. Established X-ray diffraction procedures to determine relative basal plane densities as functions of orientation were modified to enable intensity determinations at all angles. Fracture toughness values were obtained from center-notched tensile specimens containing natural cracks rather than saw cuts. By considering transverse strain

interactions between neighboring crystallites as well as longitudinal interactions, an improved method was developed to calculate the elastic moduli of polycrystalline materials from both the single crystal elastic constants and the X-ray diffraction preferred orientations. The exponential dependencies of the elastic moduli on both fraction porosity and the fraction of cracked particles were theoretically derived.

DESCRIPTORS

Deformation	Density (mass/volume)
Fracture properties	Grain size
Graphite	Preferred orientation
X ray analysis	

TABLE OF CONTENTS

ACKNOWLEDGEMENTS	ii
ABSTRACT	iii
LIST OF FIGURES	x
LIST OF TABLES	xx
1.0 INTRODUCTION	1
1.1 A General Description of Polycrystalline Graphites . .	2
1.11 Structure of Polycrystalline Graphites	2
1.12 General Characteristics of the Deformation of Polycrystalline Graphites	5
1.13 General Characteristics of the Strengths of Polycrystalline Graphites	6
1.2 Review of the Literature	7
1.21 Deformation of Single Crystal Graphite	7
1.22 Deformation of Polycrystalline Graphites	11
1.23 Fracture Criteria for Polycrystalline Graphites .	20
1.3 Statement of the Problem	29
1.31 Deformation of Polycrystalline Graphites	29
1.32 Fracture Criterion	30
1.4 The Approach of the Thesis	32
2.0 EXPERIMENTAL PROCEDURES	33
2.1 Materials	33
2.2 Sampling	33
2.3 Specimen Designs for Mechanical Testing	35
2.31 Fracture Toughness Specimens	35

2.32	Tensile Specimens	36
2.33	Ring-shaped Specimens	36
2.4	Mechanical Test Procedures	37
2.41	Tensile Tests	37
2.42	Fracture Toughness Tests	38
2.43	Ring-shaped Specimen Tests	38
2.5	Densities	39
2.6	Crystallite Preferred Orientations	39
3.0	RESULTS AND ANALYSES	41
3.1	Tensile Deformation of Polycrystalline Graphites	41
3.11	The Longitudinal Stress-Strain Curves	41
3.12	The Transverse Stress-Strain Curves	42
3.13	The Relationships between the Measured Strains	43
3.14	The Stress Dependence of the Nonlinear Strain Component	44
3.15	The Stress and Strain Dependence of the Linear Strain Component	47
3.16	The Relationships Between the Elastic Compliance and the Nonelastic Strain Component	49
3.2	The Effect of Density on the Elastic Modulus	51
3.21	Experimental Densities of the Tested Graphites	51
3.22	Calculation of the Elastic Moduli of Fully Dense Materials	51
3.3	The Effect of the Preferred Orientation on the Elastic Modulus	54

3.31	The Relative Planar Densities of Basal Plane Normals	54
3.32	The Relative Densities of Basal Plane Normals per Unit Solid Conical Angle	54
3.33	The Calculated Elastic Moduli of the Polycrys- talline Materials	56
3.4	Microscopic Observations During Deformation	60
3.5	Fracture Toughness	61
4.0	DISCUSSION	64
4.1	Deformation of Polycrystalline Graphites	64
4.11	The Residual Strain Component	65
4.12	The Elastic Strain Component	67
4.13	The Plastic Strain Component	69
4.14	The Deformation Equation	70
4.15	Further Justification of the Deformation Model	74
4.2	Fracture of Polycrystalline Graphites	77
4.21	The Fracture Process	77
4.22	The Fracture Criterion	79
5.0	CONCLUSIONS	87
5.1	A Summary of the Results	87
5.2	Suggestions for Future Work	94
APPENDIX A DERIVATION OF THE EFFECTS OF PENNY-SHAPED CRACKS ON THE ELASTIC COMPLIANCE OF AN ISOTROPIC BODY		183
APPENDIX B DERIVATION OF THE EFFECTS OF SPHERICAL VOIDS ON THE ELASTIC COMPLIANCE OF AN ISOTROPIC BODY		189

APPENDIX C	THE DETERMINATION OF THE RELATIVE DENSITY OF BASAL	
	PLANE NORMALS PER UNIT SOLID CONICAL ANGLE	194
APPENDIX D	A DETERMINATION OF THE ELASTIC MODULI OF POLYCRYSTAL-	
	TALLINE GRAPHITES FROM THE ELASTIC CONSTANTS OF SINGLE	
	CRYSTALS USING A PARTICLE PAIR CONSTANT STRAIN MODEL . . .	198
BIBLIOGRAPHY		216

LIST OF FIGURES

Figure 1.	A schematic representation of the deformation curves of polycrystalline graphites.	100
Figure 2.	The center-notched fracture toughness specimen used to test ATJ and ZTA graphites.	101
Figure 3.	The center-notched fracture toughness specimen used for AXZ and AXF-5Q graphites.	102
Figure 4.	The tensile specimen used for testing ATJ and ZTA graphites	103
Figure 5.	The tensile specimen used to test AXZ and AXF-5Q graphites	104
Figure 6.	The longitudinal stress- strain curve of a ZTA graphite specimen with the tensile stress cyclically applied parallel to the pressing direction.	105
Figure 7.	The longitudinal stress-strain curve of a ZTA graphite specimen with the tensile stress cyclically applied 30° to the pressing direction	106
Figure 8.	The longitudinal stress-strain curve of a ZTA graphite specimen with the tensile stress cyclically applied 60° to the pressing direction.	107
Figure 9.	The longitudinal stress-strain curve of a ZTA graphite specimen with the tensile stress cyclically applied perpendicular to the pressing direction . . .	108
Figure 10.	The longitudinal stress-strain curve of an ATJ graphite specimen with the tensile stress cyclically	

	applied parallel to the pressing direction.	109
Figure 11.	The longitudinal stress-strain curve of an ATJ graphite specimen with the tensile stress cyclically applied perpendicular to the pressing direction . .	110
Figure 12.	The longitudinal stress-strain curve of an AXF-5Q graphite specimen with the tensile stress cyclically applied	111
Figure 13.	The longitudinal stress-strain curve of an AXZ graphite specimen with the tensile stress cyclically applied	112
Figure 14.	The average stress-strain curve for seven ZTA graphite specimens with the tensile stress applied parallel to the pressing direction	113
Figure 15.	The average stress-strain curve for eight ZTA graphite specimens with the tensile stress applied 30° to the pressing direction	114
Figure 16.	The average stress-strain curve for four ZTA graphite specimens with the tensile stress applied 60° to the pressing direction	115
Figure 17.	The average stress-strain curve for five ZTA graphite specimens with the tensile stress applied perpendicular to the pressing direction	116
Figure 18.	The average stress-strain curve for seven ATJ graphite specimens with the tensile stress applied parallel to the pressing direction.	117

Figure 19.	The average stress-strain curve for six ATJ graphite specimens with the tensile stress applied perpendicular to the pressing direction	118
Figure 20.	The average stress-strain curve for five AXF-5Q graphite specimens	119
Figure 21.	The average stress-strain curve for six AXZ graphite specimens	120
Figure 22.	The average stress-strain curves of four commercial graphite grades	121
Figure 23.	The longitudinal and transverse stress-strain curves of a ZTA graphite specimen with the tensile stress cyclically applied parallel to the pressing direction.	122
Figure 24.	The longitudinal and transverse stress-strain curves of ZTA graphite specimens with the tensile stress cyclically applied perpendicular to the pressing direction	123
Figure 25.	The longitudinal and transverse stress-strain curves of an ATJ graphite specimen with the tensile stress cyclically applied parallel to the pressing direction.	124
Figure 26.	The longitudinal and transverse stress-strain curves of an ATJ graphite specimen with the tensile stress cyclically applied perpendicular to the pressing direction	125
Figure 27.	The longitudinal and transverse stress-strain curves of an AXF-5Q graphite specimen with the tensile stress	

	cyclically applied	126
Figure 28.	The longitudinal and transverse stress-strain curves of an AXZ graphite specimen with the tensile stress cyclically applied.	127
Figure 29.	The relationships between the residual strain, ϵ_o , and: (a) the strain at the maximum stress per cycle, ϵ_m ; (b) the strain at half the maximum stress per cycle, $\epsilon_{\frac{1}{2}}$. ZTA graphite with the applied tensile stress parallel to the pressing direction.	128
Figure 30.	The relationships between the residual strain, ϵ_o , and: (a) the strain at the maximum stress per cycle, ϵ_m ; (b) the strain at half the maximum stress per cycle, $\epsilon_{\frac{1}{2}}$. ZTA graphite with the applied tensile stress 30° to the pressing direction.	129
Figure 31.	The relationships between the residual strain, ϵ_o , and: (a) the strain at the maximum stress per cycle, ϵ_m ; (b) the strain at half the maximum stress per cycle, $\epsilon_{\frac{1}{2}}$. ZTA graphite with the applied tensile stress 60° to the pressing direction.	130
Figure 32.	The relationships between the residual strain, ϵ_o , and: (a) the strain at the maximum stress per cycle, ϵ_m ; (b) the strain at half the maximum stress per cycle, $\epsilon_{\frac{1}{2}}$. ZTA graphite with the applied tensile stress perpendicular to the pressing direction. . . .	131

- Figure 33. The relationships between the residual strain, ϵ_o , and: (a) the strain at the maximum stress per cycle, ϵ_m ; (b) the strain at half the maximum stress per cycle, $\epsilon_{\frac{1}{2}}$. ATJ graphite with the applied tensile stress parallel to the pressing direction. 132
- Figure 34. The relationships between the residual strain, ϵ_o , and: (a) the strain at the maximum stress per cycle, ϵ_m ; (b) the strain at half the maximum stress per cycle, $\epsilon_{\frac{1}{2}}$. ATJ graphite with the applied tensile stress perpendicular to the pressing direction. 133
- Figure 35. The relationships between the residual strain, ϵ_o , and: (a) the strain at the maximum stress per cycle, ϵ_m ; (b) the strain at half the maximum stress per cycle, $\epsilon_{\frac{1}{2}}$. AXF-5Q graphite. 134
- Figure 36. The relationships between the residual strain, ϵ_o , and: (a) the strain at the maximum stress per cycle, ϵ_m ; (b) the strain at half the maximum stress per cycle, $\epsilon_{\frac{1}{2}}$. AXZ graphite. 135
- Figure 37. The relationships between the residual strains, ϵ_o , and the strains at the maximum stresses per cycle, ϵ_m , for several graphite grades and orientations 136
- Figure 38. The stress dependence of the nonlinear strain component, ϵ_{pm} , for ZTA graphite stressed parallel to the pressing direction 137
- Figure 39. The stress dependence of the nonlinear strain

	component, ϵ_{pm} , for ZTA graphite stressed 30° to the pressing direction.	138
Figure 40.	The stress dependence of the nonlinear strain component, ϵ_{pm} , for ZTA graphite stressed 60° to the pressing direction.	139
Figure 41.	The stress dependence of the nonlinear strain component, ϵ_{pm} , for ZTA graphite stressed perpendicular to the pressing direction.	140
Figure 42.	The stress dependence of the nonlinear strain component, ϵ_{pm} , for ATJ graphite stressed parallel to the pressing direction	141
Figure 43.	The stress dependence of the nonlinear strain component, ϵ_{pm} , for ATJ graphite stressed perpendicular to the pressing direction.	142
Figure 44.	The stress dependence of the nonlinear strain component, ϵ_{pm} , for AXF-5Q graphite	143
Figure 45.	The stress dependence of the nonlinear strain component, ϵ_{pm} , for AXZ graphite.	144
Figure 46.	The relationships between the residual strains, ϵ_o , and the elastic strains at the maximum stresses per cycle, ϵ_{em} , for several graphite grades and orientations.	145
Figure 47.	The elastic strain dependence of the elastic compliance for ZTA graphite stressed parallel to the pressing direction.	146

Figure 48.	The elastic strain dependence of the elastic compliance for ZTA graphite stressed 30° to the pressing direction.	147
Figure 49.	The elastic strain dependence of the elastic compliance for ZTA graphite stressed 60° to the pressing direction.	148
Figure 50.	The elastic strain dependence of the elastic compliance for ZTA graphite stressed perpendicular to the pressing direction	149
Figure 51.	The elastic strain dependence of the elastic compliance for ATJ graphite stressed both parallel to and perpendicular to the pressing direction. . .	150
Figure 52.	The elastic strain dependence of the elastic compliance for AXZ graphite.	151
Figure 53.	The elastic strain dependence of the elastic compliance for AXF-5Q graphite.	152
Figure 54.	The effect of the volume fraction porosity on the elastic moduli of several graphite grades and orientations.	153
Figure 55.	The relative intensity of 0002 plane normals as a function of the angle ϕ from the pressing direction. ZTA graphite.	154
Figure 56.	The relative intensity of 0002 plane normals as a function of the angle ϕ from the pressing direction. ATJ graphite.	155

- Figure 57. (a) X ray diffraction intensity of 0002 planes measured in the x_1 - x_3 plane; and (b) the equivalent intensity in three dimensions. (c) A volume element of the bulk material showing the relationship between the densities of 0002 planes and the solid angles 156
- Figure 58. The vector transformation to determine the intensity $I(K, \beta, \alpha)$ from $I(\phi, \xi)$, where α is the angle from the pressing direction, x_3 , of the new axis under consideration, y_3 ; K is the orientation angle from y_3 ; and β is the rotational angle from y_1 about y_3 . 157
- Figure 59. The relative density of 0002 plane normals per unit solid conical angle, K , from an axis that has been rotated by an angle α from the pressing direction. ZTA graphite. 158
- Figure 60. The relative density of 0002 plane normals per unit solid conical angle, K , from an axis that has been rotated by an angle α from the pressing direction. ATJ graphite. 159
- Figure 61. The relative density of 0002 plane normals per unit solid conical angle, K . Isotropic graphite. 160
- Figure 62. Models used to calculate polycrystalline properties from single crystal properties. 161
- Figure 63. Calculated elastic moduli as a function of the angle, , from the pressing direction and the basal plane

shear compliance, s_{44} . ZTA graphite.	162
Figure 64. Calculated elastic moduli as a function of the angle, θ , from the pressing direction and the basal plane shear compliance, s_{44} . ATJ graphite. . . .	163
Figure 65. Calculated elastic moduli as a function of the basal plane shear compliance, s_{44} . Isotropic graphite. . . .	164
Figure 66. An area of a ZTA graphite ring-shaped specimen prior to loading	165
Figure 67. The area of a ZTA graphite ring-shaped specimen (shown in Figure 66) under stress.	166
Figure 68. The area of the ZTA graphite ring-shaped specimen (shown in Figures 66 and 67) after failure.	167
Figure 69. The critical crack extention force (critical energy release rate or fracture surface energy), G_{Ic} , as a function of the fraction porosity, f_p , for several graphite grades.	168
Figure 70. The calculated stress-strain curves of four grades of polycrystalline graphite.	169
Figure 71. Schematic representations of crack nuclei.	170
Figure 72. The Knibb's (Knudsen) criteria for failure of polycrystalline graphite: failure stress, σ_f , as a function of the particle size, d , and the volume fraction porosity, f_p	171
Figure 73. The probability, P_n , that n graphite flour particles in adjacent positions are cracked.	172

Figure 74. The fracture stresses, σ_f , of several polycrystal-
line graphites as a function of certain material
parameters. 173

Figure 75. Schematic diagrams used in the calculation of the
effect of penny-shaped cracks on the elastic
compliance. 174

Figure 76. Schematic diagrams used in the calculation of the
effect of spherical pores on the elastic compliance . 175

Figure 77. Axes rotations used in the averaging model of
Appendix D. 176

LIST OF TABLES

Table 1.	The elastic constants of single crystal graphite determined on compression-annealed pyrolytic graphite.
Table 2.	Poisson's ratios for several graphite grades
Table 3.	The linear relationships between the various strain components
Table 4.	Fracture toughness parameters for several graphite grades
Table 5.	The parameters of the deformation equation for several graphite grades
Table 6.	Fracture toughness data and failure criterion parameters

1.0 INTRODUCTION

The purpose of this work was to perform analyses of both the tensile deformation and fracture of polycrystalline graphites, and to develop an improved model which would relate this behavior to certain measurable physical properties. To achieve these ends, several high strength commercial grades were selected in such a manner that the variables of particle size, porosity and degree of preferred orientation could be investigated. The materials were subjected to tensile and fracture tests, and in addition, to microscopic, density and X-ray diffraction analyses. Deformation and fracture models were developed to explain the results obtained. Finally, based on these models and the test results, analytic equations which agree with the physical occurrences have been introduced.

In the present section, synthetic polycrystalline graphites will be briefly described with emphasis on their general structure and mechanical behavior. Some previous work on the mechanical properties will be summarized in order to define some of the accomplishments and deficiencies in the prevailing theories of deformation and in the criteria for fracture. Also, the approach used in the work is outlined.

The materials and specimen configurations will be detailed in the second major section. The procedures used to determine the mechanical and physical properties will then be outlined. The test results are given in the third section. In addition, the deformation model is introduced. Based on it, the strains are separated into components and these in turn are related to the physical properties and occurrences.

In the fourth major section, the deformation analysis is discussed in detail, and a synthesis of the conclusions in the form of an equation is presented. Finally in this latter section, a model for fracture and a improved fracture criterion will be presented.

1.1 A General Description of Polycrystalline Graphites

1.11 Structure of Polycrystalline Graphites

Commercial polycrystalline graphites are porous composite structures consisting of flour particles (or grist) "cemented" together with a binder, analogous to bricks and mortar. The flour particles serve as the main structural element. These are generally artificially produced graphitic materials based on petroleum-derived coke, although they can be natural flakes, lampblack or other carbon products derived from a variety of hydrocarbons. The maximum flour particle dimensions used in synthetic graphites can vary from less than 0.001 to 0.5 inches. These particles are not single crystals, but consist of a mass of subcrystals or crystallites which correspond somewhat to grains in metals. The crystallites have the well known hexagonal structure of graphite to various degrees of perfection, the perfection being dependent on the starting materials, graphitizing temperatures, etc. Except for certain graphite flours, the crystallites are not randomly oriented. Instead, there is a high degree of preferred orientation of the crystallites resulting in highly anisotropic flour particles. Microscopic examination of flours usually reveals an oblong shape having a layered or striated

structure with basal planes preferentially oriented parallel to the striations. The anisotropy and the shape, in conjunction with the deformation applied during production, are the major causes for the anisotropy of the synthetic bulk materials. To obtain isotropic graphites, the flours should be spherical in shape and should have a random orientation of the crystallites.

The purpose of the binder is to hold the initially formed bulk together as well as to form an integral part of the final structure. The desired characteristics of the binders are high viscosities at room temperature (to facilitate handling), low volatile expulsion (a major source of porosity), high coking value (a high percentage of carbon should remain after hydrocarbon breakdown) and structural integrity in the final product. The most widely used binder is pitch; however a wide variety of proprietary binders are used. Binders fall into two main categories: those that graphitize (form hexagonal layered structures) and those that do not (remain "glassy"). Graphitizing types are the most widely used, pitch falling into this category.

Production of polycrystalline, commercial graphites is both varied and proprietary, so only general remarks will be made. ^{(1)*} Preliminary steps include milling of the flour to desired size distributions, heating to remove volatiles and mixing with binder (usually heated pitch). The cooled mixture is ground to a particular particle size and molded. Compacting and shaping is carried out by an extrusion or pressing operation. It is this operation that orients the

*Parenthetical references placed superior to the line of text refer to the bibliography.

the flour particles, resulting in the anisotropy of the bulk material. Molded graphites have their c-axes preferentially oriented in the pressing direction while extruded grades have the c-axes oriented radially. Isotropic graphites are obtained by isostatically pressing to avoid this physical alignment. Baking (heating to 1200°C) is carried out to carbonize the binder. Most volatiles are released before 600°C is reached and heating rates are kept below 4°C per hour. To obtain high densities an impregnation of an organic (e.g., pitch) is made prior to the graphitization step. Graphitization is carried out at temperatures between 2500 and 3000°C to crystallize the carbon in order to achieve the graphite structure. Some materials (such as ZTA) are hot pressed and thus achieve high densities and high degrees of preferred orientation.

Graphites can be engineered to have a wide variety of properties depending on both the starting materials and the production methods. In fact, quality control is a difficult problem for any single grade. Properties of the flours vary depending on the source of the petroleum coke, the treatments given the coke, even when they were produced. For a given flour, different graphites can be produced by changing binders. Variations in production result from particle size distributions, binder percentages, deformation pressures, deformation rates, rates of volatile production, graphitizing temperatures and a multitude of other small variations. Due to the inherent complexities, complete characterization of any grade would be an enormous and difficult task. There are however, certain properties of the final product which produce first order contributions to the mechanical properties of interest in the present work. These are: (a) degree of anisotropy in the bulk material;

(b) density of the material; (c) flour particle sizes; (d) flour particle properties; and (e) graphitizability of the binder. Of these five items, the first three are measurable. Flour particle properties are difficult to assess since they are dependent on the starting materials, graphitization temperatures, crystallite perfection, crystallite preferred orientations, etc. The study will show however, that in the graphites studied the flour particle properties are not as significant as the first three items. Binder graphitizability has been eliminated from the study by choosing grades in which the binders are reasonably graphitic. A good estimate of the mechanical properties can therefore be made from the knowledge of anisotropy, density and particle sizes.

1.12 General Characteristics of the Deformation of Polycrystalline Graphites

The deformation of graphite has best been characterized by a stress-strain curve obtained by cyclically stressing the material to increasingly higher values. A schematic representation is shown in Figure 1. The notation on this figure will be retained throughout this work. Loading a specimen to failure would result in the nonlinear curve O A E J. On the other hand, loading to some stress, σ_m , at point A, and then unloading along A B C gives rise to a permanent set (or residual strain), ϵ_o . Reloading to ϵ_m occurs along curve C D A resulting in the hysteresis loop A B C D A. Continued loading follows the original O A E J curve. If the specimen is unloaded at point E and then reloaded, the hysteresis loop E F G H E is obtained. The

modulus of elasticity, E , is generally defined to be the slope of the reloading curves (e.g. C D A or G H E) at stresses approaching zero. Any loading cycle can then be arbitrarily divided into a linear and non-linear component, i.e., the strain, $\epsilon - \epsilon_0$, at any stress, σ , between 0 and σ_m , is equal to an elastic strain, ϵ_e , and a non-elastic strain, ϵ_p .

Other general observations have been made with regard to cyclically loaded stress-strain curves. Hysteresis loops are wider at higher deformations. Initial increments in permanent sets are small compared to those obtained at higher deformations for equivalent changes in σ_m or ϵ_m . The modulus of elasticity decreases with deformation. Also the strain, ϵ_m , achieved on reloading to σ_m , from zero stress is sometimes larger than the value prior to unloading, especially at higher deformations. The deformation curves in tension or compression are different though both follow the schema of Figure 1.

1.13 General Characteristics of the Strengths of Polycrystalline Graphites

Although they display nonlinear stress-strain relationships, graphites fail like brittle materials at room temperature. The fractures resemble cleavage failures with no reduction in area in tension. In fact, it has been shown that an increase in area generally results (and therefore in volume) which is indicative of the occurrence of internal cracking. In tension the total strain to failure is always less than one percent. In common with other brittle materials the

compressive strengths (less than 20,000 psi) are considerably greater than the tensile strengths (less than 10,000 psi), and, at room temperature, compression failures occur due to transverse tensile stresses.

Three physical properties have been shown to have large effects on the mechanical properties. First, due to the anisotropy of most flour particles and manufacturing techniques, most synthetic graphites display some degree of bulk anisotropy. The against-grain (c-axes preferentially orientated in the tensile direction) strengths are less than the with-grain (a-axes preferentially oriented in the tensile direction) strengths. Second fine flour particle graphites deform more and have greater strengths than do coarse particle graphites. Finally, strengths of graphites decrease with decreasing densities.

An interesting mechanical property of graphite distinguishes it from most other materials. The strength of graphite increases (approximately doubles) from room temperature to a temperature between 2000 and 2500°C. The increase occurs with no great change in the permanent deformation. Above the peak temperature, the strengths decrease at a rapid rate and are accompanied by increasing elongations. To a large degree, high temperature deformation is due to a specific volume increase.

1.2 Review of the Literature

1.21 Deformation of Single Crystal Graphite

The crystal structure of graphite is a highly anisotropic

hexagonal layered structure, consisting of covalently bonded carbon atoms within the layers (C-C bond=10.5 e.v., $a_o=1.42 \text{ \AA}$). The interlayer bonding is of the van der Waals type (interlayer separation = 3.37 \AA). The weak interlayer bonding combined with the low mobility of the covalently bonded carbon atoms makes the attainment of perfect crystals difficult, even when temperatures as high as 3000°C are used. The resulting defects fall into two categories: ⁽¹⁾ (a) layer stacking defects (turbostratic defects) in which layers are either displaced linearly, displaced angularly or contain stacking faults, and (b) carbon bond defects consisting of vacancies, dislocations, twins, crystallite boundaries, etc. Since melting is not a workable process and most graphitic products are derived from organic materials, the resulting materials are greatly influenced by their histories. These problems influence the deformation studies of graphites, even those concerned with "nearly perfect" single crystals.

A reasonably complete study of the deformation of a single crystal-like material was made by Blakslee, et. al. ⁽²⁾ Pyrolytic graphite was annealed under compression perpendicular to the substrate. This procedure both promoted crystallite growth and aligned the c-axes, although the a-axes remained randomly oriented. The latter factor should have had little effect since hexagonal crystals are elastically isotropic in the basal plane. The material was otherwise structurally good. The advantage of the material was that it could be produced in sizes large enough to permit the use of several standard testing methods (ultrasonic velocities, sonic resonances, and static tests)

and values could be cross-correlated. The elastic constants, c_{ij} , and compliances, s_{ij} , were determined for this material, Table 1, and were compared favorably with those obtained by other workers. The one exception was the shear modulus, $c_{44} = 1/s_{44}$, for which the range of values tabulated for all investigators was: $0.010 \times 10^{11} < c_{44} < 0.452 \times 10^{11}$ dynes/cm² ($2.2 \times 10^{-11} < s_{44} < 100 \times 10^{-11}$ cm²/dyne). This variation was attributable to highly mobile basal plane dislocations and the higher value of c_{44} was thought to approach the intrinsic value.

There were several other observations of interest in this paper. The stress-strain curves both parallel and perpendicular to the basal planes were linear. However, the torsional test used to obtain the shear modulus gave a curve with an initial linear slope but became non-linear at higher stresses. These shear curves also showed permanent deformation on removal of stress, as well as hysteresis loops on reapplication of the stress. Shear strengths for these materials were found to be in the range of 130 to 360 psi.

(3)

Soule and Nezbeda determined the effect of dislocations on basal plane shear and the shear modulus. Shear testing both natural single crystal graphite and compression annealed pyrolytic graphite, they determined average values for s_{44} of 15×10^{-11} and 36×10^{-11} cm²/dyne respectively for the two types. Natural crystals with the least microscopically observed imperfections had s_{44} values in the range of 7×10^{-11} cm²/dyne. Lower values were achieved by pinning the dislocations with boron atoms. Boron was diffused into natural crystals and the shear modulus was measured ultrasonically as a function of boron concentration (ranging from 7 to 1500 ppm). Initially

there was a rapid rise in c_{44} which saturated at higher concentrations to $.45 \times 10^{11}$ dynes/cm² ($s_{44}=2.2 \times 10^{-11}$ cm²/dyne). These values were taken to be the intrinsic elastic shear constants for graphite. Additional observations were made in this paper with regard to basal plane slip. Natural graphite stress-strain curves were characterized by easy glide with an average yield stress of 4.2 psi and a strain hardening rate approaching zero. Compression annealed samples did not slip as easily (average yield stress was 83 psi) probably due to the presence of a greater number of dislocation pinning points. Stress cycling of the latter increased both the yield stress and the strain hardening rates but the shear modulus was constant. The authors presented an expression for the total shear strain, γ :

$$\gamma = G^{-1}\tau + H\tau^n \quad (1)$$

where G is the shear modulus, τ is the shear stress, and H and n are constants governing the plastic strain. The constant n was evaluated to be 4.2 for the natural graphite and 3.6 to 3.8 for the compression annealed graphite. It is interesting to note that after several strain cycles n approached the value 3 for the natural graphite, a value that is pertinent to the present work.

Additional evidence for dislocation pinning is given by
(4)
Seldin and Nezbeda. Measuring the elastic constants of graphite natural single crystals and compression annealed pyrolytic graphite before and after neutron irradiation, they found little change in the elastic constants other than c_{44} . Irradiation at 50°C caused an

increase and saturation in the value of c_{44} similar to the effect of boron doping. It was contended that as the dislocations became pinned during irradiation, the modulus approached the "real" value for the material.

To summarize, perfection in a single crystal of graphite is difficult to achieve. The deformation is characterized by linear stress-strain curves except for shear in the basal plane. The yield strength is low and extensive plastic deformation is observed. A wide range of c_{44} values occur, the other elastic constants being fairly invariant.

1.22 Deformation of Polycrystalline Graphites

The first and most widely accepted analysis of the deformation of polycrystalline graphites was reported by Jenkins.⁽⁵⁾ He tested samples of a British reactor grade in compression by cyclically stressing to successively higher values and recording both stresses and strains. He noted that on the initial loading to a given value of stress, σ_m , that the total strain, ϵ_m , could be ascribed to a combination of a linear (Hookean) strain, ϵ_e , and a nonlinear strain, ϵ_p , such that:

$$\epsilon_m = \epsilon_e + \epsilon_p \quad (2)$$

Jenkins' analysis of the non-linear strain concluded that it was produced by plastic deformation in isolated parts of the structure which was limited by the restraining elastic matrix, a mechanical analogy

being a friction block backed by a spring. This friction block moved when the applied force exceeded the friction force, but was retarded by the elastic reaction of the spring. From this model, three equations were developed. For the initial stress imposition:

$$\epsilon_m = A\sigma_m + B\sigma_m^2 \quad (3)$$

where A is the elastic compliance (the reciprocal of Young's Modulus at infinitesimally small stresses) and B is a constant governing the non-linear strain. On removal of the stress:

$$\epsilon_m - \epsilon = A(\sigma_m - \sigma) + \frac{1}{2} B(\sigma_m - \sigma)^2 \quad (4)$$

where σ and ϵ are values of stress and strain less than σ_m . Further stress imposition up to the previous maximum was governed by:

$$\epsilon - \epsilon_o = A\sigma + \frac{1}{2} B\sigma^2 \quad (5)$$

where ϵ_o is the permanent set (or residual strain). The term B was given as a parameter proportional to the reciprocal of the shear modulus which depends on the volume fraction of plastic material. Compressive tests to 1200 psi (a value significantly below the fracture stress) agreed well with the parabolic equations and the A and B parameters were obtained for the material. Jenkins notes that deviations occurred when higher stress levels were attempted. Although the equations were derived without regard to microstructural mechanisms, he does make an interpretation that the nonlinear strain and the associated hysteresis loops are caused by a slip mechanism associated with basal plane dis-

location movement in the striations within the flour particles. This plastic deformation is said to be opposed by the binder, which is more randomly oriented.

Another significant paper was produced by Jenkins⁽⁶⁾ at about the same time as the one cited above. In this, the deformation and fracture of a polycrystalline graphite was observed under a microscope. A thin strip of polished graphite was cemented to a brass strip and the surface observed as the brass was bent. Stress concentrations were induced by nicking the brass. The observations were summarized as follows: (a) fracture in graphite proceeded easily along striations in the grist (flour) particles, especially under shear at angles to the direction of maximum strain; (b) it was extremely difficult to fracture the particles perpendicular to the striations; (c) the boundary between the grist and binder was sometimes weak; (d) cracks traveled preferentially through the grist; (e) cracks traveled rapidly between pores where they were stabilized by relief of the stress concentrations; and (f) isolated stabilized cracks appear well before fracture. Jenkins concluded that the grist was the weak link due to easy slip and fracture, and the binder was therefore the strong link. He also concluded that crack nucleation is easy, but propagation is difficult. Once again in this paper there is emphasis on shear as a prime mode of deformation, largely by slip and by shear fracture.

Slagle⁽⁷⁾ takes issue with some of Jenkins' results and interpretations. He notes that Jenkins does not account for the extensive cracking observed, especially in tensile tests of polycrystalline graphites (Jenkins later corrected this deficiency).⁽⁸⁾ Smith's paper⁽⁹⁾

is cited to support his contention that due to the lack of sufficient slip systems to deform plastically, interlayer cracking is necessary if graphite is to deform inelastically. Issue is also taken with Jenkins' test method used to study deformation microscopically. The thin specimen is stated to be uncharacteristic of bulk material and that, by imposing a uniform strain field, it artificially increases stresses in the high modulus regions above that which would occur in the bulk. To overcome these objections, Slagle made microscopic observations of the deformation of a thick ring-shaped specimen. This specimen is stressed by an external compressive load, and depending on the region examined the effects of tension, compression and shear can be determined. Stress concentrations can be introduced by notching the specimen. The observations in the tensile region were summarized as follows: (a) on loading, cracks occur in flour particles in the layer planes (striations) perpendicular to the stress; (b) further loading does not cause crack extension but widens the cracks and forms others in the region parallel to the layer planes; (c) cracks form preferentially near pores; (d) after failure, some cracks not involved in the fracture path close but the larger ones remain open. Observations on notched compression samples indicated that the tensile and compression mechanisms are the same, i.e., cracks formed in striations parallel to the compression stress direction. In compression higher stresses were required to generate the same number of cracks.

Tensile stress-strain relationships were also obtained by Slagle for the graphite parallel and perpendicular to the extrusion direction. The Jenkins analysis did not adequately describe the results, especially at higher stresses. One interesting result was that the permanent set, ϵ_o , was linearly proportional to the maximum strain, ϵ_m , above some minimum value ($\epsilon_m \approx .5 \times 10^{-3}$). No difference in the proportionality constant was found as a function of orientation. Slagle concludes that the plastic deformation model is not supported by his investigation but that the inelastic behavior must be related to interlayer crack formation. An alternate model was proposed. It was argued that cooling a bulk graphite (even an isotropic one) from its graphitization temperature stresses individual flake particles, and fractures some, and that the system is internally strained. This results from anisotropy in both the elastic constants and the thermal expansion coefficients. The resulting strains will be both tensile and compressive depending on orientation and location. Permanent set occurring after loading and then unloading is explained by a shift in the distribution of the strains caused by elimination by fracture of some of the particles from the supporting structure. An attempt is made to explain the hysteresis loops by this model. If it is assumed that the specimen consists of columnar arrays of particles arranged randomly in parallel and in series forming a complicated network, the unloading curve of the loop would differ from the loading curve by compressively loading those arrays which had large permanent sets on loading. Differences noted between tensile and compressive deformation curves are said to be caused by the asymmetric strain distribution curve in agreement with

(10)
Seldin; and because cracked particles in compression retain their load bearing quality.

In answer to the criticism that his simple equations for deformation of polycrystalline graphites did not fit the curves at high stresses and did not account for observed flour particle fractures, Jenkins⁽⁸⁾ reported a more sophisticated modification based on the analysis of Bilby et. al.⁽¹¹⁾ and Cottrell.⁽¹²⁾ It is noted that at higher stresses the microcracks play an important role. When a shear stress is applied to these, plastic fronts move from the crack tips. This causes additional elastic and plastic displacements in the direction of the stress which are additive:

$$\epsilon_m = \epsilon_a + \epsilon_p + \sigma_m / E \quad (6)$$

where σ_m/E is the elastic strain of the material free of cracks (σ_m is the stress and E is Youngs Modulus), ϵ_a is an additional elastic strain due to the cracks and ϵ_p is the plastic strain associated with the plastic fronts. The derivation leads to equations which modify his previous three equations (3, 4 and 5). On initial loading:

$$\epsilon_m = \frac{\sigma_m}{E} \left(1 + \frac{Q}{\pi} \right) + \left[\frac{4}{E\pi^2} Q \bar{\sigma}_y \right] \ln \sec \left(\frac{\pi \sigma_m}{2 \bar{\sigma}_y} \right) \quad (7)$$

where Q is a function of geometry and proportional to the crack population, $\bar{\sigma}_y$ is the overall yield stress of the material to which the curve becomes asymptotic. On unloading there is a friction stress opposing the return of the dislocations equal to twice $\bar{\sigma}_y$ and:

$$\epsilon_m - \epsilon = \frac{(\sigma_m - \sigma)}{E} \left(1 + \frac{Q}{\pi}\right) + \left[\frac{8Q \bar{\sigma}_y}{E \pi^2} \right] \ln \sec \left[\frac{\pi(\sigma_m - \sigma)}{4 \bar{\sigma}_y} \right] \quad (8)$$

The permanent set, ϵ_o , is produced from this equation by setting σ equal to zero. Reapplication of the stress will be governed by:

$$\epsilon - \epsilon_o = \frac{\sigma}{E} \left(1 + \frac{Q}{\pi}\right) + \left[\frac{8Q \bar{\sigma}_y}{E \pi^2} \right] \ln \sec \left(\frac{\pi \sigma}{4 \bar{\sigma}_y} \right) \quad (9)$$

The logarithmic term can be expanded to give a polynomial, and equation 7 written as:

$$\begin{aligned} \epsilon_m = \frac{\sigma_m}{E} \left(1 + \frac{Q}{\pi}\right) + \left[\frac{4 Q \bar{\sigma}_y}{E \pi^2} \right] & \left[\frac{1}{2} \left(\frac{\pi \sigma_m}{2 \bar{\sigma}_y} \right)^2 \right. \\ & \left. + \frac{1}{12} \left(\frac{\pi \sigma_m}{2 \bar{\sigma}_y} \right)^4 + \dots \right] \end{aligned} \quad (10)$$

On initial loading for stresses up to half of the yield stress, $\bar{\sigma}_y$, the simple equation was found to be adequate:

$$\epsilon_m = A \sigma_m + B \sigma_m^2 \quad (11)$$

where

$$A = (1 + Q/\pi) / E \quad (12)$$

and

$$B = Q/2 E \bar{\sigma}_y \quad (13)$$

At higher stresses equation 10 was used to properly describe the deformation curve. The modified equations predict that: (a) the apparent elastic modulus will be lowered by large numbers of cracks; (b) the curve will bend over asymptotically to $\bar{\sigma}_y$; and (c) cycling will produce permanent sets and static hystereses.

Seldin⁽¹⁰⁾ reported a rather comprehensive study on eight grades of molded graphites, concentrating on ATJ and ZTA, two of the types studied in the present investigation. Some pertinent results are cited here. Stress-strain curves in both tension and compression were determined parallel to and perpendicular to the applied stress direction. The longitudinal curves were similar to those previously reported.^(5,13)

Transverse curves were found to be different between the tension and compression tests. In compression, the ratio of the transverse strain, ϵ_t , to the longitudinal strain, ϵ_l , was constant (Poisson's ratio was not a function of stress). On unloading, the positive transverse strain resulted in a positive permanent set. In tension, on the other hand, the nonlinear transverse curve had a curvature opposite to the longitudinal curve, i.e., the slope $d\epsilon_t/d\sigma_l$ tended toward zero. Poisson's ratio was therefore a function of stress. Stress cycling produced no hysteresis loops. On unloading in this case, the initially negative transverse strain resulted in a positive permanent set. Tensile loading of graphite therefore, causes an increase in volume.

Annealing experiments were also reported in the above paper. Pre-annealed specimens were stressed in tension and/or compression several times with intermediate high temperature anneals. Longitudinal dimensional measurements were taken at each stage. In all cases, the

original dimensions were recoverable. In addition, the stress-strain curves after annealing were repeatable.

Although the present study concerns itself with room temperature mechanical properties, a study of the elevated temperature creep properties by Zukas and Green⁽¹⁴⁾ provides pertinent information with regard to deformation. The creep tests in compression and tension were performed on ZTA graphite in the temperature region of 2500°C. In addition to standard creep results as a function of eight different orientations relative to the pressing direction, microscopic examinations are reported. In tension, the creep rates were highest when samples were oriented in the pressing direction and lowest when oriented perpendicular to the pressing direction (the difference being five orders of magnitude). Intermediate orientations gave intermediate rates. If basal plane slip were a controlling mechanism, the intermediate orientations would be expected to have higher creep rates due to more favorable basal plane orientation. The compression tests showed a slight tendency to produce higher intermediate orientation creep rates. The stress dependence on creep rate was found to be the same in tension or compression and was not influenced by orientation, nor was the activation energy for creep. Microscopic observations prior to and after creep testing showed cracks similar to those previously noted for room temperature deformation. Strain measurements made on the photomicrographs produced overall results that agreed with the mechanical measurements. However, strains measured parallel to the tensile axes across regions which were free of cracks showed significantly lower strains (in many cases undetectable) than those which contained cracks. Transverse strains were measured to

be zero. From the activation energies and the stress dependences of creep rates, it was concluded that the same deformation process was rate controlling in both tension and compression. Also an overwhelming amount of the strain resulted from crack growth. Finally creep strengths at 2500°C were a function of the crystallographic orientation of the basal planes, the resolved normal stress being the controlling factor rather than the resolved shear stresses.

1.23 Fracture Criteria for Polycrystalline Graphites

A vast amount of engineering data has been produced with respect to the mechanical strengths of the wide variety of graphite and carbon products available. Due to differences in starting materials, production methods and testing techniques, these properties vary widely. After determining the mechanical properties of interest to them, many investigators have attempted to correlate them to physical properties and have reported these observations. As previously stated, the physical properties which have the greatest effect are preferred orientations of flour particles, ^(10,13,15) bulk densities, ^(13,15,16,17,18) and flour particle sizes. ⁽¹⁸⁾ In addition, strengths of graphites have been related to mechanical properties such as the modulus of elasticity ^(13,16,19) (high moduli result in high strengths) and strains to failure ^(13,16,19) (some graphites appear to fail at a relatively constant maximum strain, the failure stress being the value necessary to achieve that strain).

A number of papers have attempted analytic correlations. In these, various fracture criteria have been developed utilizing the

physical significances of properties. Most of these are based on the observation that graphite fractures in a brittle manner and that the energy required to create the fracture must be supplied by the applied strain energy. The physical properties are noted to effect one or the other of the energies, and based on established theories for brittle fracture the analytic expressions are derived. This essentially is the approach of the present work and therefore some of the previously published correlations will be cited.

Mostly and Orchard⁽¹³⁾ in reviewing the results of extensive testing of British reactor graphite grades noted that the correspondence between Young's moduli and strengths implied that failure was related to the applied strain energy. Strain energies, S.E., were calculated for two grades by the relationship:

$$S.E. = \sigma_f^2 / 2Y_s \quad (14)$$

where σ_f is the fracture stress, and Y_s is a modulus defined by:

$$Y_s = \sigma_m / (\epsilon_m - \epsilon_o) \quad (15)$$

in the symbolism of Figure 1. For a single grade, the strain energies were found to be the same for specimens tested both parallel and perpendicular to the extension direction. The "moduli" were different in the two directions. The strain energies were however different between the grades, the difference having been attributed to degrees of structural perfection achieved by graphitization. The effect of density on the mechanical properties was investigated by a series of

impregnations of graphite specimens with a sugar solution, baking to 1050°C, and flexure testing. The procedure increased the densities, the moduli, the flexural strengths, and the strain energies, while the strains to failure remained constant. A linear relationship was found between strength and modulus, indicating that the impregnant was acting parallel to the original structure.

The effect of graphitization was determined by heat treating initially ungraphitized specimens to temperatures varying between 1000° and 2600°C and then flexure testing at room temperature. With increasing heat treatment temperature, the density remained constant, but the modulus decreased. However, the strain to failure increased such that the strain energies remained constant, i.e., the squares of the strengths were proportional to the moduli. Combined heat treatments and impregnations showed that the sequence did not effect the results. Neutron irradiation of graphite specimens resulted in increases in both strength and moduli, such that the constant strain energy criterion was maintained. From the investigations, it was concluded that failure of graphite will result when sufficient strain energy is available to perform the work to propagate a crack across misoriented boundaries between grains.

Mason⁽¹⁶⁾ added insight to the strain energy criterion by noting it was based on the Griffith criterion for failure:

$$\sigma_o \geq (2E_o W_s / \pi c)^{\frac{1}{2}} \quad (16)$$

where σ_o is the strength of the crystallite, E_o is its modulus of elasticity, and W_s is the surface energy of a crack of length c . The strain

energy relationship was modified to account for density by:

$$\sigma_f^2/E^2 = (\sigma_o^2/E)(d/d_o) \quad (17)$$

where d is the density and the zero subscript relates to crystal properties. From equation 17 and a comparison of properties parallel and perpendicular to the extrusion direction, Mason contended that the orientation strength differences can be attributed to differences in crack lengths. He concludes from his analysis of the previously cited work, (13) that the relationship between strength and modulus depends on variations of the crack size as well as the density.

A most successful attempt at formulating a fracture criterion, (20) based on the ceramic work of Knudsen, was applied to commercial graphites by Knibbs. (18) Knibbs microscopically studied the fracture of three graphites of widely varying flour particle sizes. He concluded that fracture was associated with cleavage of the larger particles and that fracture proceeded similarly in the three grades. Stating that the grains contain incipient cracks whose lengths are equal to the flour particle sizes, the Griffith equation could be written as:

$$\sigma_o = (4E\sigma_s/\pi)^{\frac{1}{2}} d_{\max}^{-\frac{1}{2}} \quad (18)$$

where σ_o is the failure strength of a fully dense isotropic graphite whose maximum particle size is d_{\max} . To account for the anisotropy effect, a weighted average strength, $\bar{\sigma}_f$, was defined to be:

$$\bar{\sigma}_f = 1/3 \sigma_{||} + 2/3 \sigma_{\perp} \quad (19)$$

where $\sigma_{||}$ is the strength parallel to the deformation axis and σ_{\perp} is the strength perpendicular. Finally, the density effect on strength is determined by an empirical equation used in ceramics:

$$\bar{\sigma}_f = \sigma_o \exp (-m f_p) \quad (20)$$

where f_p is the volume fraction of pores, and m is a constant. Knudsen made an attempt to derive this equation from the change in load bearing areas with changing pore fraction, but this is unsatisfactory since it does not account for stress concentrations associated with the voids. Combining the equations, the average strength should be determined by:

$$\bar{S} \propto d_{\max}^n \exp (-m f_p) \quad (21)$$

where n is substituted for the value $1/2$ to check its validity. Literature values for twelve nearly isotropic grades were analyzed, the constants were determined, and to within ± 14 percent:

$$\bar{S} = 1.2 \times 10^8 d_{\max}^{-.5} \exp (-6.8 f_p) \text{ cm}^{.5} \quad (22)$$

This equation correlates well for the nearly isotropic graphites over wide ranges of particle sizes and densities. Highly anisotropic grades however, show significant deviations. Also, pore fraction is heavily weighted and it is pointed out that an increase in pore fraction of one percent results in a strength reduction of 6.8 percent. Similar values of m ($4 < m < 9$) were found for various ceramics by Knudsen.

Two other approaches to failure criteria based on the energy required to produce fracture will be cited. In these works, instead of analyzing the energy balances required to produce failure in standard tensile specimens, the specimens tested were specifically designed to measure the energies. First, Tattersall and Tappin⁽²¹⁾ noted that the Griffith energy balance criterion is:

$$W_s = -dU/dA \quad (23)$$

where W_s is the surface energy, U is the elastic stored energy and A is the area of the fracture. As fracture proceeds, the term $-dU/dA$ changes as the crack size increases. Whether the crack proceeds is dependent on the second differential of strain energy with respect to the crack area. If $-d^2U/dA^2$ is positive the crack will accelerate because the released strain energy is greater than the energy to create the new surface area. If $-d^2U/dA^2$ is negative, external work must be done to keep the crack moving. The approach used was to measure the applied energy required to make the crack grow, by using a "hard" test machine and by shaping the specimen so that crack initiation requires only small loads. The three-point load flexure specimen used was a square bar containing two thin cuts which reduced the cross-section at the center of the specimen to an isosceles triangle. In the test fixture the top point of the triangle was oriented to be loaded in tension and a load-deflection curve to failure was recorded. The work done was the area under the curve divided by the area of the triangular fractured faces. Results for a British Reactor grade were determined to be: $W_s = 10^5$ ergs/cm² (.6 in-lb/in²).

A more sophisticated approach than the one cited above has been developed to predict fracture loads of structures containing sharp flaws: linear elastic fracture mechanics. The theory as developed by (22,23) Irwin and numerous subsequent investigators can be based on either an energy approach (similar to that previously described) or on a stress intensity (at the flaw tip) approach, both leading to the same results. An excellent review by Wessel et. al. (24) will be briefly outlined. A more detailed review is attainable in an ASTM publication. (25)

In an energy approach, the criterion for crack propagation is that the energy supplied to the crack tip during incremental crack extension is greater than or equal to the energy absorbed by the crack tip during that extension. Five energy components must be accounted for: (a) strain energy; (b) external work; (c) kinetic energy; (d) energy to form the new surfaces; and (e) energy to perform plastic work at the crack tip. Since the kinetic energy is generally small, it can be neglected and the criterion for crack extension can be written as:

$$\frac{d W_e}{d A} \delta A \geq \frac{d U}{d A} \delta A + \frac{d W_p}{d A} \delta A + \frac{d W_s}{d A} \delta A \quad (24)$$

where W_e is the work of the external forces, U is the strain energy, W_p is the plastic work, W_s is the surface energy, and A is the crack area. Crack extension begins when:

$$\frac{d W_e}{d A} - \frac{d U}{d A} = \frac{d W_p}{d A} + \frac{d W_s}{d A} \quad (25)$$

The left hand side of this equation is defined as G_c , the critical energy release rate (alternatively called the critical crack extension force, or the fracture surface energy), and is equivalent to twice the surface energy in the Griffith treatment. It has been shown that G_c is a function of the material, temperature, strain rate and the state of stress at the crack tip. Its magnitude must be empirically determined on a cracked body for which the energy release rate is known.

The alternative approach to fracture mechanics is via an analysis of the stress intensity at the crack tip. This stress intensity is mathematically derived from the elastic stress field at the tip of an existing crack which has a radius of curvature approaching zero. The stresses derived are proportional to a stress intensity factor, K , which is a function of the geometry, the applied loads, the size, location and orientation of the crack. Crack propagation in this approach occurs when the stress intensity at the crack tip reaches a critical level, K_c . As with G_c , K_c must be experimentally determined from a body of known geometry containing a known crack. Irwin has shown that the energy release rate and the stress intensity approaches are equivalent and the constants from each are related by:

$$K = (G E)^{\frac{1}{2}} \quad (26)$$

for plane stress conditions, and:

$$K = G E / (1 - \nu^2)^{\frac{1}{2}} \quad (27)$$

for plane strain conditions, where G is the energy release rate (or the crack extension force), E is the elastic modulus, and ν is Poisson's ratio. As an example, for an infinite plate of unit thickness containing a crack of finite length, $2c$, perpendicular to a uniaxial stress field, under plane stress conditions the failure stress, σ_f , is given by:

$$\sigma_f = K_c (\pi c)^{-\frac{1}{2}} = (EG/\pi c)^{\frac{1}{2}} \quad (28)$$

(26)
 Corum used the fracture toughness method to determine the energy release rates for a single reactor graphite grade. Both the energy and the stress intensity approaches were used on specimens cut parallel and perpendicular to the extrusion direction. The specimens, rectangular prisms having centrally located lateral saw cuts, were tested in four-point flexure with the notch on the tensile surface. The crack depth to beam depth ratio (c/d) was varied. For the specimens cut parallel to the extrusion direction (the crack running perpendicular to the extrusion direction), G_{Ic} was determined to be .39 in-lb/in² (± 10 percent). For the transverse specimens G_{Ic} was .29 in - lb/in² (± 12 percent). The term G_{Ic} is the critical crack extension force for the opening mode for which the crack surfaces move opposite and perpendicular to each other.

Corum also noted in this paper the effect of particle orientation on the propagation of the cracks. When the particles were oriented with striations parallel to the fracture path, the mode was transgranular and easy. Conversely, misoriented particles caused intergranular fractures. Examinations of fractured surfaces indicated that fracture proceeded

uniformly from the entire length of the notch whereas it tended to radiate from a small localized area in the unnotched specimens.

Except for the effect of orientation in Corum's paper, no attempts were made in the last two citations to correlate the fracture criteria with physical properties of the materials investigated. Only a single material was studied in each case. It appears that the fracture mechanics approach to a failure criterion would be useful if the effects of porosity, orientation and grain size could be evaluated.

1.3 Statement of the Problem

1.3.1 Deformation of Polycrystalline Graphites

The analysis developed by Jenkins is widely accepted to aptly describe the deformation of graphite. A major deficiency in the simplified theory, that observed cracks were not accounted for and the fit was poor at higher deformations, appears to have been solved in the later paper. The important achievements of Jenkins' analysis is his model of limited basal plane slip restricted by elastic constraints, and the observation that the total strain can be divided into linear and non-linear strain components. Jenkins proposes the non-linear strain is due to basal plane slip, which is the only non-linear deformation mode observed in graphite single crystal slip. Objections to plastic deformation models raised by Slagle are that there are insufficient slip systems available to polycrystalline graphites and that shear failures

are not observed microscopically (microcracks form by cleavage). Also, basal plane slip does not control creep, but tensile creep rates are direct functions of the number of basal planes normal to the stress.

An alternate deformation mechanism has been proposed by Slagle, but with no equations. Cooling anisotropic bodies from elevated temperatures introduces an internal strain distribution which is changed by deformation. Permanent sets are attributed to the elimination of supporting elements by microcracks, and hysteresis loops to the unloading curve differing from the loading curve by compressively loading those regions which had large permanent sets on loading. Slagle's hysteresis loop explanation is unsatisfactory because it ignores the observation of loops in basal plane shear. Also, it would predict the elimination of the loops on successive cycles to a constant stress, since the majority of microcracks are formed on the initial loading. This is contrary to observation.

It appears that both of the extant theories of deformation adequately describe certain observations, but have deficiencies in other areas. A reevaluation of the deformation is required to clarify the points of contention.

1.32 Fracture Criterion

Since polycrystalline graphites are observed to fracture in a brittle manner, attempts to develop failure criteria have been based on the Griffith theory. Physical properties have been noted to have effect on the energy balance criteria. The Knudsen approach has been the most

successful attempt at correlating physical properties to measured strengths. It, however, has certain shortcomings. First, the anisotropy effects are not truly accounted for. Instead, weighted average strengths are used. The pore fraction effect on strength is based on an empirical relationship used in ceramics and appears to be heavily "weighted" in the equation. Also, there is the implication that the constants in the Griffith equation (E and W_s) are universal for graphite. The grades which deviate greatly from the derived relationship probably do so because of a deviation of the product EW_s .

The fracture mechanics approach to failure criteria has gained wide acceptance. The major objection to its use is that preexisting flaws are expected to be present in the material in order for the theory to predict failure stresses. Fracture mechanics does not provide an answer to the mechanism whereby materials, initially relatively free of flaws, fail. In a material such as graphite, where microcracks are observed during deformation, there should be a bridge between fracture mechanics and tensile failure. The effects of physical properties on fracture toughness requires attention also, to give a clue to the effects previously cited.

Although the Knudsen treatment has been fairly successful, it is not entirely satisfactory. The fracture toughness approach to failure criteria, as used by Corum, also has limitations. It appears however, that an expansion of the latter to include physical properties effects would be fruitful.

1.4 The Approach of the Thesis

The deformation of polycrystalline graphites will be determined by analyzing the tensile deformation curves of several commercial grades of graphite. The contributions of certain of the physical properties to the components of the stress-strain curve will be assessed, and an equation based on the determined model will be presented. It will be shown that the strain, ϵ_m , at any level of stress is the sum of three component strains which are not entirely independent: (a) the elastic (Hookean) strain; (b) the elastically constrained plastic strain; and (c) the permanent set due to internal stress relief by cracks.

The fracture criteria will be attained by determining the effect of preferred orientation, porosity and particle size on the fracture toughness relationships. From the equation of the failure stress of material containing a penny shaped crack:

$$\sigma_f = \left[\frac{\pi E G_{Ic}}{4(1-\nu^2) c} \right]^{\frac{1}{2}} \quad (29)$$

it will be shown that the preferred orientation and porosity effect both the elastic modulus, E , and the energy release rate G_{Ic} ; and that the critical crack length, c , is a function of the maximum particle size, as well as the preferred orientation.

2.0 EXPERIMENTAL PROCEDURES

2.1 Materials

Four grades of commercial graphite, two from each of two producers, were chosen for investigation. Grades ATJ and ZTA were produced by the Carbon Products Division, Union Carbide Corporation. Grades AXZ and AXF-5Q were produced by Poco Graphite, Incorporated. The grades were selected primarily for their good mechanical properties and to enable the investigation of the variables of the flour particle size, density, and degree of preferred orientation. Grades ATJ and ZTA have larger particle sizes (.005 inch maximum size) than the AXZ and AXF-5Q (.0005 inch maximum size) grades but are still considered fine grained. The densities of the materials as given by the manufacturers in grams per square centimeter were: 1.94 (ZTA), 1.84 (AXF-5Q), 1.72 (ATJ) and 1.55 (AXZ); the theoretical density is 2.26. Finally, both AXZ and AXF-5Q are isotropic grades whereas ATJ has a slight preferred orientation and ZTA is highly orientated.

Half of a 24 by 20 by 9 inch billet provided the material to study the ATJ. The ZTA specimens were obtained from a 14 inch diameter, 9 inch long billet and a 14 by 9 by 3 inch slab cut diametrically from a second billet. Two 5 by 5 by 3 inch AXZ billets and one 4 1/2 inch diameter by 6 inch long AXF-5Q billet provided these specimens.

2.2 Sampling

Specimen blanks were cut from billets to meet several criteria. The specimens were to be as large as possible in order to approach good

fracture toughness practice. Where possible, only the interior of the billet was to be used to eliminate processing surface effects (higher densities, higher preferred orientations, etc.). Where applicable, the blanks were cut at various orientations (four for ZTA and two for ATJ). Finally, the blanks for both the ZTA and ATJ were cut to eliminate possible effects of variation across the billet, i.e., all the specimens of a particular orientation were not cut from a single region.

The isotropic grades were cut in only one direction. The ATJ block was sectioned in order to obtain the two basic orthogonal orientations: with the long dimension parallel to the production pressing direction and with the long direction perpendicular to the pressing direction. Parallel and perpendicular specimens were similarly cut from the ZTA billet. In addition, specimens that were oriented 30° and 60° to the pressing direction were cut from the slab obtained from the second billet.

Specimen blanks were machined from the sectioned billets. Both the ZTA and ATJ blanks measured 8.00 by 2.000 by .750 inches, whereas the AXF-5Q and AXZ measured 5.00 by 1.250 by .625 inches. All of the blanks obtained from the billets of the two latter grades were machined into either fracture toughness or tensile specimens. The ZTA blanks cut at 30° and 60° to the pressing direction were all made into tensile specimens. Eight blanks randomly selected, were chosen for each of the conditions of orthogonal orientation and specimen type from the remaining ZTA and ATJ.

2.3 Specimen Designs for Mechanical Testing

2.3.1 Fracture Toughness Specimens

The sizes of the fracture toughness specimens were designed to be as large as possible consistent with the bulk material geometries. The particular specimen geometry used was a modification of standard center-notch specimen.⁽²⁴⁾ A center-notch fracture toughness specimen was selected so that the results could be correlated with the tensile test results. This presumes that tensile failures originate at internal flaws. Preliminary testing using the standard design revealed that a significant number of specimens broke through the loading pin-holes even though a sharp notch existed at the midpoint. The pinhole region was therefore increased in thickness. The specimen shown in Figure 2 was used to test both ATJ and ZTA and that in Figure 3 to test AXZ and AXF-5Q. ATJ samples with gauge thicknesses ranging between 0.30 to 0.50 inches were initially tested. No differences in the K_{Ic} values as a function of thickness were discernable, indicating that the test conditions were plain-strain for specimen thicknesses in excess of 0.30 inches.

The center crack was created by end milling a 2 inch long by 1/8 inch deep groove of width equal to the desired crack length in the specimen blank. A thick webbed I-beam cross-section was achieved. A 1/8 inch diameter hole was drilled through the minimum thickness at the center of the specimen and notched perpendicular to the blank length with a shallow saw cut. The width of the specimen was compressed tightly in a vise to give a slight tensile stress along the length axis.

A polyethylene rod ($1/8$ inch diameter and slightly longer than web thickness) was inserted and then compressed in a table model Instron testing machine using fixtures designed for the task. The compression generated a hydrostatic force which caused the specimen interior to fracture perpendicular to the specimen length. The induced crack proceeded across the web, but was stopped by the thickness increase at the exteriors of the specimen width. The blanks were subsequently machined to their final dimensions. In this manner, a natural center-cracked specimen was obtained. Crack lengths were varied between 0.69 and 0.90 inches for the larger specimens and between 0.45 and 0.61 inches for the smaller specimens.

2.32 Tensile Specimens

The tensile specimens were designed to be similar to the fracture toughness specimens so that the results of the two tests would correlate. The initial design used was identical to the fracture toughness specimen without the center-crack. However, specimen failures in the pin-holes necessitated a further reduction in the cross-sectional area. This was achieved by reducing the specimen width resulting in the specimens shown in Figure 4 and 5.

2.33 Ring-shaped Specimens

In order to microscopically study the behavior of graphite under stress, ring-shaped specimens were prepared as suggested by Slagle.⁽⁷⁾

These measured 1.25 inches outside diameter, by .625 inside diameter by .25 inches thick. The flat surfaces were metallographically polished.

2.4 Mechanical Test Procedures

2.41 Tensile Tests

Prior to testing, SR-4 resistance strain gages were cemented to the specimens in one of several configurations. Two types of gauges were used: single grids, and overlapping double grids (oriented 90° to one another). The single grid gauges were attached at the center of the gauge lengths in pairs, on opposite sides of the specimen. The double grids were also attached in pairs, but on adjacent specimen sides.

Testing was accomplished in a 10,000 pound Instron testing machine. Load was transferred to the specimens by steel pin grips manufactured specifically for these tests. Alignment was accomplished through the use of universal joints in the loading train. The specimens were cyclically loaded and unloaded to successively higher maximum values until specimen failure occurred. Referring to Figure 1 the procedure used for each cycle was to increase the load (at a cross-head speed of .02 inches per minute) to one half the cycle's maximum stress value. The test machine was stopped and both the load (from the Instron's chart recorder) and strains (as measured on a Baldwin-Lima-Hamilton SR-4 Strain Indicator) were read. The calibrated loads were recorded to the nearest pound and the strains to the nearest microstrain unit. Loading was continued to the cycle's maximum value, then unloaded to half

the maximum, and finally to zero; in each case load and strain values were recorded under static conditions. Load and longitudinal strain at failure were also determined. A number of tests were autographically recorded on an x-y recorder. Most of the single grid gauges were wired to average the resistance changes of the individual gages, although on a few specimens the strains were recorded individually to check the alignment. The double gauges were all recorded individually, two longitudinal and two transverse readings per specimen.

2.42 Fracture Toughness Tests

Two single grid strain gauges were cemented on each of the fracture toughness specimens. On the larger specimens these were placed longitudinally one inch above the crack (to remove them from any region of stress intensification) on opposite edges (the minimum dimension surface). On the smaller specimens, one was placed on each of the opposite faces (the maximum dimension surface), $3/4$ inch above and below the crack. The test procedure used was the same as used for the tensile tests.

2.43 Ring-shaped Specimen Tests

A load application device was constructed which consisted of two 3 inch long parallel bars with $1/4$ inch holes drilled near either end of each. Two $1/4$ inch bolts were inserted into the holes. The ring specimen, properly oriented, was centered in the assembly and load was applied by alternately tightening nuts threaded on the bolts. No attempt was made to measure the load.

The procedure consisted of visually observing or photographing the region near the inside diameter between the load application points with a Leitz Wetzlar metallograph. This was done prior to loading and after successively increasing loads.

2.5 Densities

Samples for density measurements were cut from the broken tensile specimens from the regions where the fractures occurred. These measured approximately 1/2 inch square by the thickness of the specimen. The densities were assessed from the specimen buoyancy in water. The procedure consisted of: weighing the sample and a thin wire separately in air using an analytic balance, paraffin coating the sample with the wire attached, and re-weighing in air. A final weighing of the coated sample was made while it was submerged in a water bath to a specific depth. The total volume (graphite plus paraffin) was determined from the weight difference in air and water, and a knowledge of the density of water. From a similar density determination of the paraffin alone, the volumes of paraffin on each sample were determined from the paraffin volume subtracted from the total volume. The graphite density was then the graphite sample weight in air divided by its volume.

2.6 Crystallite Preferred Orientations

Crystallite preferred orientations of the graphites studied were determined by a transmission X-ray diffraction technique which is a modification of one used by Bacon.⁽²⁶⁾ Samples were cut from the

fractured regions of the tensile specimens and ground to a uniform thickness of approximately 1 millimeter. These were placed in a fixture which had the capacity to rotate the specimen 360° about an axis at the Bragg angle from the beam. The fixture was set on a General Electric Model XRD-5 X-ray Diffraction Unit, the plane of the specimen having been rotated 13° (the Bragg angle for the 0002 plane) from the copper tube X-ray beam. A scintillation counter was set at 26° from the beam. The specimen was oriented initially with the pressing direction in the plane of the initial and diffracted beams. X-ray tube voltage was 48kv at 26 ma current. Counts per 10 seconds were recorded. The specimen was rotated about an axis normal to the pressing direction in 5° increments for a total of 180° . Scintillation counts were recorded at each step. To ensure that the measurements were not affected by drift in the X-ray equipment, the procedure was duplicated for each specimen measured, giving a total of four data points per angular setting per specimen. The procedure proved to be very repeatable.

3.0 RESULTS AND ANALYSES

3.1 Tensile Deformation of Polycrystalline Graphites

3.1.1 The Longitudinal Stress-Strain Curves

Typical measured stress-strain curves for the graphites and orientations investigated are presented in Figures 6 through 13. These were obtained by cyclically loading the tensile specimens between zero and sequentially higher stresses until failure occurred. For clarity, not all the cycles measured are shown in some of the figures. The general shape of these curves conform to those obtained by other investigators. The features have been previously outlined in section 1.1.2, and generally fit the description of Jenkins on the loading and reloading curve sections. However, since half the hysteresis loops are decidedly asymmetrical, this analysis is less than satisfactory in its description of the unloading curve.

The average total stress, $\bar{\sigma}_m$, versus total strain, $\bar{\epsilon}_m$, curves (thick lines) are shown in Figures 14 through 21. Included on these figures are the mean failure stresses, $\bar{\sigma}_f$, the mean failure strains, $\bar{\epsilon}_f$, and the ranges of stress-strain values measured (narrow lines). The qualitative effects of the physical properties on the mechanical properties can be observed in the summary plot, Figure 22. For pressed graphites, the stresses required to achieve a given strain increase with the angle of the tensile axis to the pressing direction. Also strengths increase and strains to failure decrease with this orientation angle. However for constant particle size (ATJ and ZTA), the deformation curves averaged over the various orientations are comparable. The grades with

finer particle sizes (AXF-5Q and AXZ) have greater elongations prior to failure and also have greater strengths than coarser particle grades (ZTA and ATJ) when averaged over all orientations. Between the two isotropic grades, increase in density (AXF-5Q with respect to AXZ) increases the stress required to attain a given strain, the strength, and the failure strain. Finally, the Young's moduli increase with both density and angle from the pressing direction.

3.12 The Transverse Stress-Strain Curves

The results of this series of tests were erratic. Several lots of strain gauges were used in the tests, some of which proved to be faulty on examination of the data after testing. Typical stress-strain curves from the valid tests are presented in Figures 23 through 28. For clarity, only two stress-strain cycles are shown for each of the longitudinal and transverse curves. The shapes of the transverse curves are in general agreement with those determined by Seldin.⁽¹⁰⁾ However, in contradiction to Selden's results, hysteresis loops are apparent in most of the figures. These transverse curves also show positive permanent sets at zero stress after unloading. Combined with the positive longitudinal permanent sets, a volume increase occurs. For the graphites tested the $\Delta V/V$ ranged between .0005 and .0016 at fracture.

The slopes of the maximum stress, σ_m , versus total transverse strain are shown to increase with increasing deformation. Just as the curvature of the longitudinal stress-strain curve (σ_m versus ϵ_m) can be largely attributed to the positive residual strain component, ϵ_o ,

the opposite curvature of the transverse curves is also due to the positive permanent set. Negative transverse residual strains (as those observed in compression testing by Seldin) cause the longitudinal and transverse curves to have similar shapes, i.e., a decrease in slope with increasing deformation. It is difficult to justify the above observations with a slip mechanism. The major contribution to the permanent set is probably the relief of internal stresses by the creation of internal cracks during deformation.

Values for Poisson's ratio, ν , were obtained from the data, and are given in Table 2 along with the values for ATJ and ZTA reported by Seldin. The latter were based on the ratio of the total (non-linear) strains. In the present case, only the linear strain components were used by taking Poisson's ratio to be the negative of the ratio of the slopes near zero stress of the transverse to the longitudinal stress-strain curves. These values were determined on the loading curves of the last cycle prior to failure.

3.13 The Relationships between the Measured Strains

During the cyclically stressed tensile tests, three strain measurements were made for each load application cycle: (a) the initial value at zero stress, ϵ_o (the residual strain); (b) the total strain at half the stress of the previous maximum stress that had been applied to the specimen, $\epsilon_{\frac{1}{2}}$; and (c) the total strain at the reapplied maximum stress, ϵ_m . The latter value generally agreed reasonably well with the ϵ_m value determined on the initial loading to the particular maximum

stress, with slight disparities at higher levels of deformation. Plotting those strains versus one another reveals interesting relationships. In Figures 29 through 36, ϵ_o is plotted as a function of both ϵ_m and $\epsilon_{\frac{1}{2}}$ for the various graphites and orientations tested. Ignoring the initial transition region at low strain values, the relationships are seen to be linear. In most of these figures, the deviations of the data points from the mean value line (heavy solid line) is relatively small. However, even for the plots with larger deviations from the mean, the linearity of the points from a single sample is excellent. The equations of the mean lines were determined by regression analyses of the data points where ϵ_o exceeded 2×10^{-4} . The dashed lines represent the deviations (three standard deviations) of the data points from the mean lines. The symbols containing X's are extrapolations to the failure strains.

From these curves, it is apparent that a "steady state" relationship between the strains is not achieved until ϵ_o exceeds 2×10^{-4} (or ϵ_m exceeds 5×10^{-4} to 10×10^{-4} , depending on the grade and orientation). The low deformation values of the stress-strain curves are shown to be transitory. On the composite plot, Figure 37, the mean value lines for ϵ_o as a function of ϵ_m have been extrapolated back to zero values of ϵ_o , showing that a minimum value of ϵ_m is required to produce the steady state increase in the residual strain.

3.14 The Stress Dependence of the Nonlinear Strain Component

Jenkins has made a strong argument that the nonlinearity of the deformation of polycrystalline graphite is due to elastically constrained

plastic deformation. Therefore, the total strain can be separated into an elastic component and a plastic component. Slagle, on the other hand, attributes the nonlinearity to microcrack formation. The author believes that the problem can be resolved by combining the two approaches. This involves separating the total strain into three component strains rather than two. In other words, when stress is applied, the material will strain elastically, plastically and form microcracks simultaneously. This is essentially the implication of Jenkins' equation 5 (the expression that describes the reloading curve) if the residual strain is attributed to the strain relief caused by the cracking. Therefore, the strain, ϵ , at any stress, σ , can be expressed as:

$$\epsilon = \epsilon_o + \epsilon + \epsilon_p \quad (30)$$

Generalizing equation 5:

$$\epsilon = \epsilon_o + A\sigma + B\sigma^n \quad (31)$$

where A is the elastic compliance, B and n are constants governing the magnitude of the plastic deformation. The implication of the linear relationships between the measured strains presented in the prior section is that the strain components given here are not totally independent.

By substituting the strains at two levels of stress, (e.g., σ_m and $1/2\sigma_m$) a pair of simultaneous equations may be written:

$$\epsilon_m - \epsilon_o = A \sigma_m + B \sigma_m^n \quad (32)$$

and

$$\epsilon_{\frac{1}{2}} - \epsilon_o = \frac{1}{2} A \sigma_m + B \left(\frac{1}{2} \sigma_m \right)^n \quad (33)$$

If the pair of stresses and strains refer to a single reloading cycle, ϵ_o and A are equal in the two equations, and the elastic component can be eliminated:

$$\epsilon_m + \epsilon_o - 2\epsilon_{\frac{1}{2}} = (1 - 2^{\frac{1-n}{2}}) B \sigma_m^n \quad (34)$$

The logarithm of this equation can be written:

$$\ln(\epsilon_m + \epsilon_o - 2\epsilon_{\frac{1}{2}}) = \ln(1 - 2^{\frac{1-n}{2}}) + \ln B + n \ln \sigma_m \quad (35)$$

If B and n are constants over a range of stress levels, their magnitudes can be determined from measurements of σ_m , ϵ_m , ϵ_o and $\epsilon_{\frac{1}{2}}$.

The results for the steady state region of the deformation curves ($\epsilon_o > 2 \times 10^{-4}$) are plotted on Figures 38 through 45 for the various grades and orientations. The average values for n as determined by regression analyses are also included. These range between 2.3 and 3.2 with a weighted average (based on the number of data points on each plot) of 3.0. This differs from the derived value of 2 given by Jenkins, but is in close agreement with the values experimentally determined on compression annealed pyrolytic graphite.⁽³⁾ Soule and Nezbeda determined the stress dependence of this material and found that after strain hardening, n approached a value of 3. It was decided to use this

experimentally determined value for all grades and orientations in the subsequent data treatment.

The weighted average values for B, calculated by setting n to equal 3, are also given in Figures 38 through 45. The range of B among the materials examined is two orders of magnitude. In fact, the high and the low values occur for two orientations of the same graphite: B for ZTA tested perpendicular to the extrusion direction is $16 \times 10^{-16} \text{ psi}^{-3}$ and tested parallel to the extrusion direction is $1310 \times 10^{-16} \text{ psi}^{-3}$. This variation is to be expected if the plastic deformation is constrained by the elastic strain. The value of B would then be a function of the elastic modulus to the n^{th} power. If the ratio of the moduli in the two orientations were about 4.6, then the ratio of the B terms would be expected to be 100 for n equal to 3.

3.15 The Stress and Strain Dependence of the Linear Strain Component

The elastic strain component (ϵ_{em}) can be determined by solving equations 32 and 33. At a given maximum stress per cycle,

$$\epsilon_{em} = A \sigma_m = [2^n \epsilon_{\frac{1}{2}} - \epsilon_m + (1-2^n) \epsilon_o] / (2^{n-1} - 1) \quad (36)$$

Substituting the value of 3 for n, this equation becomes:

$$\epsilon_{em} = A \sigma_m = [8 \epsilon_{\frac{1}{2}} - \epsilon_m - 7 \epsilon_o] / 3 \quad (37)$$

The elastic compliance (the reciprocal of the elastic modulus) is:

$$A = 1/E = \epsilon_{em} / \sigma_m \quad (38)$$

Examination of the cyclically stressed deformation curves indicates that the slopes of the loading curves near zero stress decrease with deformation. When values are substituted into equations 37 and 38 the compliance is shown to increase nonlinearly with increasing strain, in agreement with the previous observation. This phenomena is expected for systems which experience crack formation during deformation. To determine the expected relationship between elastic compliance and deformation, a stress analysis was made on the effect of a single micro-crack on the compliance. In addition, the effect of introducing a multitude of independent cracks was determined. The results, detailed in Appendix A, show that the compliance is expected to increase exponentially with the volume fraction of cracks added, f_c :

$$A = A_i \exp(k f_c) \quad (39)$$

where A_i is the initial compliance and k is a constant dependent only on Poisson's ratio. The relationship is independent of the size of the cracks, assuming that they are spaced several crack diameters apart.

In the previous sections, the measured strains ϵ_o , $\epsilon_{\frac{1}{2}}$ and ϵ_m were found to be linearly related. By simple algebraic manipulation of the equations, the calculated elastic strain, ϵ_{em} , can also be shown to be linearly related to the other strains. The values for the various strain relationships are given in Table 3. A plot of ϵ_o versus ϵ_{em}

appears in Figure 46. The lines have been extrapolated into the transition region (the region of nonlinear strain dependencies) to zero values of ϵ_o . If the permanent set is interpreted to be caused by internal stress relief due to strain induced cracking, and each crack is assumed to yield a small constant increment of permanent set, then the number of microcracks created will be a linear function of the maximum elastic strain applied. There is a value of ϵ_{em} (ranging between 4×10^{-4} and 10×10^{-4}) below which relatively few cracks are formed. The transition region, to be consistent with this analysis is caused by microfractures in regions that are relatively weaker.

If the fraction of cracks formed, f_c , is then proportional to the maximum elastic strain above some minimum threshold strain, ϵ_{th} , then equation 39 may be rewritten as:

$$A = A_i \exp \left[k_c (\epsilon_{em} - \epsilon_{th}) \right] \quad (40)$$

A plot of $\ln A$ versus ϵ_{em} should yield a straight line of slope k_c . The value of A_i can be determined at ϵ_{em} equal to ϵ_{th} . These relationships are shown in Figures 47 through 53. The average values for k_c were determined by regression analyses. The exponential relationships appear to be good for those materials that experienced large deformations. The uncertainties are greater for the lower deformations.

3.16 The Relationships Between the Elastic Compliance and the Nonelastic Strain Components

In section 3.22, a method is described for determining the compliances of fully dense material, A_o , from the experimental values.

As indicated in section 3.14, n has been assigned the value 3. If the experimental values of B , the coefficient in equation 31, are divided by the cube of A_0 , the nonlinear strain can be rewritten as:

$$\epsilon_p = C_0 (A_0 \sigma)^3 \quad (41)$$

where C_0 is a new proportionality constant of the stress dependence of the nonlinear component. Whereas the B term ranged two orders of magnitude, the variation of C_0 is relatively small. With the exception of the value of AXZ graphite (57×10^2), C_0 ranged between 22×10^2 to 40×10^2 . The mean value was 32×10^2 , with a standard deviation of 12×10^2 . The errors result not only from experimental deviations, but also from the approximation of setting the value of the stress dependence n equal to 3. The large deviation of C_0 for AXZ results from its larger deviation of experimental n from the mean value.

From the results of this treatment it is apparent that the nonlinear strains are related to the linear elastic constants and the model of elastically constrained plastic deformation becomes credible. Those crystallites which are favorably oriented for shear, do so plastically because of the extremely low critical yield stress. The extent of the shear deformation resolved to the stress direction is limited however by neighboring regions which are not similarly oriented and therefore strain elastically. Consequently the extent of elastic strain controls the deformation.

It can be argued that this mechanism occurs on the crystallite scale rather than on the flour particle-binder scale because of the

success of the calculations. The term $A_0\sigma_m$ is the contribution to the elastic strain of the crystallites and is only dependent on their preferred orientations. Attempts to make similar calculations using the macroelastic strain, $\epsilon_{em} = A\sigma_m$, were less successful and led to variable values of n .

3.2 The Effect of Density on the Elastic Modulus

3.21 Experimental Densities of the Tested Graphites

The average densities in grams per cubic centimeter of the four graphite grades tested were: (a) ZTA: 1.90 ($s=0.03$); (b) ATJ: 1.65 ($s=0.03$); (c) AXF 5Q: 1.73 ($s=0.01$); and (d) AXZ: 1.51 ($s=0.03$); where s is the standard deviation. The volume fraction of porosity, f_p , was calculated from the relationship:

$$f_p = (d_{th} - d_{ex}) / d_{th} \quad (42)$$

where d_{th} is the theoretical density for graphite ($d_{th} = 2.26$ grams per cubic centimeter) and d_{ex} is the experimental value. The average volume fractions of porosity of the four grades were: (a) ZTA: 0.158 ($s=0.014$); (b) ATJ: 0.270 ($s=0.012$); (c) AXF-5Q: 0.235 ($s=0.006$); and (d) AXZ: 0.332 ($s=0.012$).

3.22 Calculation of the Elastic Moduli of Fully Dense Materials

A variety of relationships to determine the elastic moduli of graphite as a function of densities (or pore fractions) have been

proposed. Some investigators have shown linear fits between the moduli and the pore fractions. (13,16,17,28) Others find the moduli to be exponentially related to the pore fractions. (29) Power functions and polynomial fits are also commonly used for ceramics. In the present investigation, the spread in the density values for a particular grade were not sufficiently large to experimentally determine which of the proposed treatments should be used to determine the moduli of the fully dense materials. The relationship was therefore theoretically derived from continuum elasticity theory in Appendix B.

It is shown that the exponential dependence for the modulus of a sample, empirically developed by Spriggs, (30) is valid and:

$$E = E_0 \exp(-k_p f_p) \quad (43)$$

where E_0 is the modulus of the fully dense material, f_p is the volume fraction of pores, and k_p is a constant for a given material, analytically found to be (for spherical pores):

$$k_p = \frac{72(1+\nu)}{14-10\nu} + \frac{4(1-\nu^2)}{\pi} \quad (44)$$

where ν is Poisson's ratio. Equation 43 is independent of pore size, but k_p and therefore E would be affected by the pore shape.

By changing ν by an order of magnitude (from 0.03 to 0.3), the magnitude of k_p is only changed by 50 percent (from 6.6 to 9.7). Since k_p is in the exponent of equation 43, E is thus not drastically affected by Poisson's ratio. Experimentally, Cost et. al. (29) found k_p to be 3.5 for a series of isotropic graphites. This value agrees with the

average value determined for alumina ($k_p=3.4$) by Spriggs.⁽³⁰⁾ The discrepancy between the theoretical and experimental values is attributed to the assumptions involved in the calculations, i.e., spherical pores in a homogeneous isotropic solid. That the theoretical magnitude is higher than the experimental one is consistent with the results of Bazaj and Cox.⁽³¹⁾ These investigators evaluated the stress concentration factors for a fine particle size graphite by testing round-notched tensile specimens. The ratio of the theoretical (K_{th}) to the experimental (K_e) stress concentration factors were 1.3 for 1/4 inch radii notches, and 1.5 for 1/16 inch radii. Solving the equations for a pore size radius of 0.0005 inches, K_{th}/K_e is 4.0. Although this extrapolation is not exactly valid, (the equations are shown to deviate from experiment when the radii approach the size of the particles), the relative differences between elastic continuum calculations and real materials are clear.

As a result of the above, the elastic moduli and compliances for fully dense materials were calculated from equation 43, using a value of 3.5 for k_p . The experimental densities and the compliances (A_i in equation 40) provided the other input values. The data and the moduli versus pore fraction functions are plotted in Figure 54.

3.3 The Effect of the Preferred Orientation on the Elastic Modulus

3.31 The Relative Planar Densities of Basal Plane Normals

The X-ray intensities of (0002) plane defractions were measured incrementally as a function of the angle from the pressing direction in a plane which contained the pressing direction. The results were subjected to Fourier analyses and the intensities, $I(\phi)$, as functions of orientations from the pressing direction, ϕ , were found to be adequately described by a four parameter equation:

$$I(\phi)' = a_0' + a_1' \cos 2\phi + a_2' \cos 4\phi + a_3' \cos 6\phi \quad (45)$$

The data were normallized to eliminate experimental variations between tests by dividing by the mean intensity, a_0' , and multiplying by 1000 to eliminate fractional quantities. Equation 45 then becomes:

$$I(\phi) = 1000 + a_1 \cos 2\phi + a_2 \cos 4\phi + a_3 \cos 6\phi \quad (46)$$

The average results and ranges are plotted in Figures 55 and 56 for the ZTA and ATJ respectively. Equation 46 is also given with the average values of the parameters.

3.32 The Relative Densities of Basal Plane Normals per Unit Solid

It is of interest for some of the following sections to determine the relative density of basal plane normals per unit solid angle

in order to relate preferred orientations to bulk polycrystalline properties. This density distribution differs from the experimentally determined planar distributions. The latter is schematically shown in Figure 57 (a) and (b). With reference to Figure 56 (c) which represents a spherical volume of material, the size of an element of volume between the angles of ϕ and $\phi+d\phi$, and ξ and $\xi+d\xi$ is given by:

$$dV = \sin \phi \, d\phi \, d\xi \quad (47)$$

The relative number of basal plane normals (i.e., the density per unit solid angle) which are oriented at this angle is then:

$$I(\phi) \, dV = I(\phi) \sin \phi \, d\phi \, d\xi \quad (48)$$

The differences between the planar and volume distributions become apparent at orientations close to the pressing direction. As ϕ approaches 0° , the relative intensity approaches its maximum in the former case yet goes to zero in the latter as the volume element becomes smaller.

It is of further interest to generalize equation 48 to consider cases in which the axis, e.g. the stress axis, differs from the pressing direction. Another distribution function must be generated if the axis under consideration is rotated from the axis of symmetry as in Figure 58. By vector transformation the planar relative intensity, $I(\phi)$ becomes $I(K, \beta, \alpha)$, where α is the angle between the new axis and axis of symmetry, K is an orientation angle from the new axis, β is the rotational angle about the new axis. The transformation has been derived in Appendix C. The density of basal plane normals per unit

solid angle in the new coordinates is then:

$$I(\kappa, \beta, \alpha) dV = I(\kappa, \beta, \alpha) \sin \kappa d\kappa d\beta \quad (49)$$

The treatment can be carried one step further by performing the integral with respect to β . This has also been done in Appendix C. The result is the density of (0002) plane normals per unit solid conical angle:

$$L(\kappa, \alpha) dV = L(\kappa, \alpha) \sin \kappa d\kappa \quad (50)$$

The average intensity values determined by X-ray diffraction have been processed by the above treatment. The results for ZTA, for axis orientations, α , of 0° , 30° , 60° , and 90° are shown in Figure 59. Densities for orientations of 0° and 90° for ATJ are given in Figure 60. Figure 61 contains an equivalent curve for the isotropic case.

3.33 The Calculated Elastic Moduli of the Polycrystalline Materials

There have been several papers written on the subject of the calculation of the polycrystalline elastic moduli of graphite from a knowledge of the crystal elastic constants and of the preferred orientations. (32,33) The various methods used take the same fundamental approach. The relative (0002) density distribution functions of ϕ are multiplied by the crystal elastic modulus function of ϕ . This is then integrated over all the orientations and divided by the density integral to give the average modulus.

The uniaxial stress models used are of generally two types:

(a) constant applied stress, as shown in Figure 62 (a); and (b) constant applied strain as shown in Figure 62 (b). Price⁽³²⁾ has given the relationships for these. For constant stress:

$$\bar{E}_\sigma = \frac{\int_0^{\pi/2} I(\phi) \sin \phi \, d\phi}{\int_0^{\pi/2} I(\phi) \left[1/E(\phi) \right] \sin \phi \, d\phi} \quad (51)$$

For constant strain:

$$\bar{E}_\epsilon = \frac{\int_0^{\pi/2} I(\phi) E(\phi) \sin \phi \, d\phi}{\int_0^{\pi/2} I(\phi) \sin \phi \, d\phi} \quad (52)$$

where $I(\phi) \sin \phi \, d\phi$ is the relative density of $\langle 0002 \rangle$ directions per solid angle as a function of the angle ϕ from the axis of symmetry, and where:

$$1/E(\phi) = s'_{33}(\phi) = s_{11} \sin^4 \phi + s_{33} \cos^4 \phi + (s_{44} + 2s_{13}) \sin^2 \phi \cos^2 \phi \quad (53)$$

for the stress axis parallel to the axis of symmetry, and:

$$1/E(\phi) = s'_{11}(\phi) = s_{11} \cos^4 \phi + s_{33} \sin^4 \phi + (s_{44} + 2s_{13}) \sin^2 \phi \cos^2 \phi \quad (54)$$

for the perpendicular stress axis. The s_{ij} are the elastic compliances of the hexagonal crystal.

The models of constant stress and constant strain give the extreme values of the possible average polycrystalline moduli, since the actual state of each crystallite must be intermediate to be in the lowest strain energy configuration.

Price shows that the constant stress model produces the better approximation. Since s_{11} is very much smaller than s_{33} , the contribution of the reciprocal of s_{11} overwhelms s_{33} reciprocal. In the constant strain model, most of the stress is supported by the particles oriented to have high moduli, and the resulting calculated average moduli are very much too large. The converse is true in the constant stress model. It should be noted that both models are unidirectional and do not consider lateral interactions between crystallites.

Slagle⁽³³⁾ has proposed that the above models can be modified to give intermediate states. By considering pairs of particles which are in a state of constant stress with respect to one another, a modified constant strain model can be developed by placing the pairs in turn in a state of constant strain, as in Figure 61 (c). Similarly, a modified constant stress model can be generated, as in Figure 61 (d). An obvious extension of this would be to consider three and four particle combinations. As developed by Slagle, the two particle models are also unidirectional; i.e., the particles are considered to be sufficiently long so that the strain interactions between particles at the interfaces can be neglected and the transverse stresses set to zero. Since the particles are nearly equiaxial, the models are somewhat deficient, yet the results are considerably better than the single particle models.

In an attempt to account for the transverse strain interactions, the modified constant strain model was extended in the present work to consider short particles. Complete transverse strain interactions between individual particles in each pair are accounted for. These give rise to transverse stresses which in turn modify the axial stresses.

The derivation of this model along with the long particle model is found in Appendix D. Calculations of the average elastic moduli were made utilizing one, two and three particle models. These were evaluated by determining how closely the experimental values were approximated and by how closely the ratio of the modulus normal to and parallel to the pressing directions were approximated. Since the shear compliance, s_{44} , is known to be variable within the limits of 0.2×10^{-10} to $10 \times 10^{-10} \text{ cm}^2/\text{dyne}$, several models could be adjusted to give magnitudes close to the experimental ones. However, the criterion of the ratio of the moduli was best met by the models of Appendix D. This ratio is slightly high for one of these and slightly low for the other.

Since each of these cases represent the extremes of the same model (very long or very short particles in the stress direction), it was decided to average the values to approximate the intermediate actuality. The curves in Figures 63, 64 and 65 are the average of the calculations as a function of s_{44} for ZTA, ATJ and the isotropic grades respectively. Included in the figures are the experimental moduli, the band representing one standard deviation.

For ATJ and ZTA, a magnitude of a s_{44} between $1.1 \times 10^{-10} \text{ cm}^2/\text{dyne}$ used in the calculations would give reasonable results. For the two isotropic grades, agreement between experiment and calculation occurs for an s_{44} range between 0.8×10^{-10} and $1.0 \times 10^{-10} \text{ cm}^2/\text{dyne}$. The sensitivity of the calculations to the basal plane shear compliance is apparent in the figures. The degree of crystallite perfection is therefore very important to the overall elastic modulus of the polycrystalline material.

3.4 Microscopic Observations During Deformation

In an attempt to determine the mechanics which lead to fracture in the graphites investigated, ring-shaped specimens were observed under a microscope as deformations were progressively increased. Due to a resolution difficulty, the observations for the fine particle grades, AXZ and AXF -5Q were inconclusive. However, for both ATJ and ZTA in all orientations, the results were in agreement with those presented by Slagle⁽⁷⁾ and Knibbs.⁽¹⁸⁾ It would be expected that the processes for the fine particle materials should be similar.

Figures 66, 67 and 68, are a series of composite micrographs taken of a ZTA specimen oriented such that the pressing and tensile stress directions coincided. This orientation was selected because the preferential orientation of the flour particles intensifies the effects, and clearly shows the stages of failure. Figure 66 shows an area near the inside diameter of the ring prior to deformation. As the specimen was incrementally loaded, the same area was examined. The first cracks to form were those near the I.D. As deformation continued, the depth to which independent cracks formed progressively increased. Figure 67 is a composite of the area under high stress prior to fracture, and the fracture is shown in Figure 68.

Although the micrographs are of the surface and the effects in the interior (due to the triaxiality of the stress state) should be more influential in the fracture, certain observations can be made.

It is clear from these micrographs that the flour particles tend

to fail by a cleavage mechanism normal to the applied tensile stress. In Figure 67 the first cracks to form were those in the regions A, B and C. The long cracks between D and E and between B and G formed by a crack linkage mechanism, i.e., separated cracks were interconnected via a path through pores and around particles not suitably oriented. The pore structure may or may not cause the termination of a crack. Examples of cracks between pores are at I, J and K. Examples of cracks ending within the flour particles are at E and H.

A comparison of Figures 67 and 68 shows that the final fracture path is initiated at major crack linkages, e.g., between B and G. The crack continues through favorably oriented flour particles and around others. The pores as well as some of the previously formed cracks may be excluded from this path. For example, rather than including either the crack at J or the major pore to its left, the fracture proceeded between the two. A certain amount of branching from the major fracture is apparent. Whether this occurred prior to, during or subsequent to the fracture passing through the region is not certain.

3.5 Fracture Toughness

The results of fracture mechanics are commonly presented in the form of two parameters. From a knowledge of the specimen geometry, the size of the crack and the failure load, either the critical stress intensity factor, K_{Ic} , or the critical crack extension force, G_{Ic} , can be used to describe the fracture toughness. In general, these are material parameters which can be utilized to predict failure loads in

the given material for crack sizes and geometries other than those of the test specimen. The value of K_{Ic} is related to both G_{Ic} and the elastic modulus. Since in polycrystalline graphites the modulus is dependent on such variables as stress axis orientation and the density, K_{Ic} is a constant only if these variables are held constant. The G_{Ic} should be relatively independent, though not totally, of such conditions.

The test results from the standard notched specimens were analyzed using the equations given in the literature. ^(24,25) The critical stress intensity factor is obtained from:

$$K_{Ic} = \frac{P}{B} \frac{c^{\frac{1}{2}}}{W} \left[1.77 + 0.277 \left(\frac{2c}{W} \right) - .510 \left(\frac{2c}{W} \right)^2 + 2.7 \left(\frac{2c}{W} \right)^3 \right] \quad (55)$$

where P is the fracture load, W and B are specimen width and thickness, and c is one half the initial crack length. For plane strain conditions, the critical crack extension force is related to K_{Ic} by:

$$G_{Ic} = K_{Ic}^2 (1 - \nu^2) / E \quad (56)$$

where ν is Poisson's ratio and E is the elastic modulus. These relationships are determined for isotropic materials, but should be approximately valid for the anisotropic case for bulk polycrystalline materials. To simplify the treatment where ν was directionally dependent, an average value was used. This error should be small since ν^2 is small. The value of the modulus used was the experimental one determined on each fracture toughness specimen at a reasonable distance from the crack. To account for the variation of E with deformation, the values used were found by

extrapolation to the failure strains. The mean K_{Ic} and G_{Ic} magnitudes are given in Table 4, along with standard deviations.

On examining the results, the effects of orientation on K_{Ic} are obvious. For ATJ, which has the same G_{Ic} in the orthogonal directions, K_{Ic} is 20 per cent greater in the with-grain direction. For ZTA, a 25 per cent difference in G_{Ic} corresponds to a 120 per cent difference in K_{Ic} at the two orientations.

The mean G_{Ic} values for the various grades appear to be density dependent. It will be recalled that G_{Ic} can be considered as equivalent to twice the surface energy in the Griffith equation. Its value would be expected to vary linearly with the new surface area created by the crack and this area would decrease linearly with the pore fraction. Figure 69 is then a plot of G_{Ic} versus the average volume (or area) fraction porosity. The mean line (heavy solid line) as determined by regression analysis is plotted along with the standard deviation of the data points from the mean line (the broken line). The mean line equation is also presented.

The differences in G_{Ic} observed for ZTA graphite in the orthogonal directions can be accounted for by a similar argument. Examination of the fractured surfaces shows that the total surface areas of the specimens tested with stress axes perpendicular to the pressing direction is greater than those tested parallel. The cracks run perpendicular to the stress axes in both cases. However, because fewer flour particles are favorably oriented in the former case, the microscopic path is more devious. The G_{Ic} in this direction would be expected to be greater than that tested parallel by the ratio of the surface areas.

4.0 DISCUSSION

4.1 Deformation of Polycrystalline Graphites

The controversy with regard to the deformation mechanisms of polycrystalline graphites has prompted the present re-evaluation. From the treatment of the test results in the previous section, it is apparent that the stress-strain curves cannot be adequately described by the analysis of either Jenkins or Slagle, exclusive of the other. Rather, a combination of the two is required.

The nonlinearity of the total strain, ϵ_m , at any given stress, σ_m , according to Jenkins can be attributed to two component strains: a linear strain, and a non-linear strain. Slagle, although he does not give equations, effectively agrees with the two component analysis, but argues that the non-linear component is attributed to internal stress relief by deformation cracking rather than basal plane shear. It has been shown in the present work that the deformation is more adequately described if the strains are separated into three components: elastic, ϵ_e , plastic, ϵ_p , and internal strain relief, ϵ_o . The strain at any stress level is then the summation of the three.

In the following sections, these three components of the strain will be discussed in detail. Also, an analytic expression based on a synthesis of the results in section 3 will be given for the deformation of polycrystalline graphites.

4.11 The Residual Strain Component

The evidence obtained in this study indicates that the residual strain component is attributable to crack induced internal stress relief, rather than to plastic deformation. The internal stress arises in the polycrystalline material during cool-down from the graphitization temperature. There exists differences in both the thermal expansion coefficients and the elastic constants between neighboring crystallites as a function of orientation differences. The crystallites adjust their strains in all directions in such a way as to achieve the lowest strain energy. If a single crystallite fractures, the balance of stresses and strains in all directions in the proximity readjusts to a new configuration. In other words, if a crack occurs in a particle normal to the applied stress direction; lateral as well as axial strain adjustments would be expected. The positive permanent sets observed in both the axial and transverse deformation curves are the consequence of this three dimensional strain readjustment.

Clearly, the residual strain is an extremely complex phenomena dependent on the complex internal strain which in turn, varies with the preferred orientation of the crystallites, the temperature from which the material is cooled, the elastic constants (c_{111} especially), the crystallite size, etc. Therefore, a comparison of the curves in Figures 29 through 37 shows no discernible relationship between the grades. However, the pattern is the same for all the graphites and orientations tested. There is an initial transient period during which

little increase in ϵ_o with ϵ_{em} (or ϵ_m) occurs. Subsequent to surpassing a critical strain value, linear dependencies between these strains arise. If each crack contributes to a constant increment of ϵ_o , then the number of cracks formed is a linear function of the maximum applied elastic strain. Further, the rates of increase of ϵ_o with ϵ_{em} are then expected to be functions of the number of cracks formed per maximum elastic strain increment, the sizes of the cracks formed, the magnitude of the internal stresses, and the internal stress distribution

Jenkins, on the other hand, proposes that the residual strain is caused by plastic deformation in the basal plane. Examination of the ϵ_o versus ϵ_m curves for ZTA graphite shows that the slopes continually decrease with increasing stress axis angle from the pressing direction. If the residual strains were plastic, it would be expected that the intermediate orientations which are better resolved for shear would have higher slopes than the principal orthogonal directions. Except for perhaps, a small fraction the permanent set phenomena cannot be attributed to plastic deformation.

Finally, it should be noted that the residual strain is strain dependent for a given material and orientation. This is evidenced by the good fits of the data points to the average ϵ_o versus ϵ_m lines, especially in certain grades, and the small slope differences between orientations. The stress dependence of ϵ_o is then the magnitude that gives the correct ϵ_m or ϵ_{em} value.

4.12 The Elastic Strain Component

The analytic treatments detailed in the appendices give the relationships between the physical status of polycrystalline graphites and the elastic deformation. In appendices C and D, a method is described to determine the elastic compliance of fully dense material as a function of preferred orientation. The effect of porosity on increasing the compliance is derived in Appendix B. Finally, the further increase in the elastic compliance due to deformation cracking is established in Appendix A. Therefore, in principle, it is possible to determine the elastic strain of a polycrystalline graphite at any stage of deformation. However, due to the expected discrepancies between real materials and physical models, some of the parameters must be experimentally determined. The intent of section 3.1 was to measure these parameters.

From the results of section 3.3, it was shown that the elastic properties of fully dense materials are effected primarily by the s_{44} value. The basal plane shear coefficient is variable between graphites and is dependent on such things as crystallite perfection and dislocation pinning. But, these in turn are difficult to measure and consequently lead to inherent uncertainties in the calculations. In spite of the difficulties, the calculations give reasonable results.

The compliances of materials less than theoretically dense have been shown to be exponentially dependent on the volume fraction of pores. The rate constant calculated is two to three times higher than those experimentally determined by other investigators. Due to the ideality of the model, this difference may be considered to be small and the

model considered to be in good agreement with the data. That other investigators find linear relationships between elastic properties and pore fractions is explained by the near linearity of the exponential curve in the pore fraction range between 0.15 and 0.35. Since most graphites fall into this range, the choice between the linear or exponential dependencies is generally of small consequence. However, if extrapolation out of this range is important, the analytically verified relationship should be used.

It has been established from elasticity theory that for a polycrystalline material, the compliance is exponentially related to the number of cracks introduced, independent of crack size. Jenkins, on the other hand, from plasticity theory derives a linear dependence, thus:

$$A = A_i \left(1 + \frac{g g' n c}{\pi d g''} \right) \quad (57)$$

where A_i is the compliance of the crack free material, n is the number of cracks of size $2c$, d is the grain thickness normal to the basal plane, and g , g' and g'' are geometric factors. It is difficult to experimentally assess the crack densities as a function of deformation, and therefore selection of the correct dependency is not possible. However, a self consistent argument has been developed in this thesis to show that the exponential relationship is to be preferred: If the number of cracks, n , are linearly dependent on the elastic strain, ϵ_{em} (as is the strain due to internal stress relief by crack formation, ϵ_o), then the elastic compliances should have the same dependence on both n and ϵ_{em} . On this basis the derivation founded on the elasticity model rather than the Bilby-Cottrell model has been selected to describe polycrystalline

graphites.

4.13 The Plastic Strain Component

The plastic strain, ϵ_p , has been shown to be proportional to the n^{th} power of both the elastic compliance and the stress, where n is approximately 3. The compliance that gives the best relationship is the one obtained on extrapolation to full density: A_0 . This is the elastic constant associated with the preferred orientations of the crystallites. The model proposed by Jenkins, whereby the plastic deformation is limited by the amount of elastic strain occurring, appears to have validity. Jenkins uses the same model to explain the residual strain component as well and therefore strays from the physical realities. The equation given for the initial loading curve (equation 3) can be used to empirically describe the transition region of σ_m versus ϵ_m . Jenkins however suggests that at high deformations, this curve becomes asymptotic to some overall yield stress value due to the increased plastic deformation associated with the stress concentrating cracks. Evaluations in the present work indicate that the plastic component is relatively unaffected by the deformation cracks. Further, the author is convinced that the cause of the deviations from Jenkins' parabolic equation of stress dependence is actually twofold. First, the stress dependence of the plastic strain is more nearly cubic; and second, at higher deformations, the linear increase in ϵ_0 with maximum elastic strain must be added along with ϵ_{em} and ϵ_p to obtain the value of ϵ_m .

On the other hand, Slagle's denial of the existence of a plastic component is contrary to observation. The only deformation mode observed on single crystals which shows non-linear behavior and hysteresis loops is that of basal plane shear. Slagle recognizes the importance of the s_{44} elastic constant in determining the polycrystalline elastic modulus.⁽³²⁾ However, due to the extremely low critical yield stress observed for basal plane shear, the linear portion of the deformation is extremely small. Most of the shear deformation curve is nonlinear with a strain hardening coefficient between 3 and 4. Hence, the linear elastic portion of the polycrystalline stress-strain curve would also be expected to be nearly nonexistent. Another way of viewing this is that s_{44} in equations 53 and 54 is not a constant, but is deformation dependent.

4.14 The Deformation Equation

The stress and strain dependencies of the three strain components have been determined in Section 3.0. The analysis of this work indicates that a single equation can be written to describe the deformation for both the initial loading and reloading cycles:

$$\epsilon = A\sigma + B\sigma^n + \epsilon_o \quad (58)$$

or:

$$\epsilon = A_o\sigma \exp[k_p f_p + k_c(\epsilon_{em} - \epsilon_{th})] + C_o[A_o\sigma]^n + \epsilon_o \quad (59)$$

where:

- A_o = the elastic compliance of a fully dense polycrystalline graphite dependent on the degree of preferred orientation, in^2/lb ;
- k_p = the rate of compliance increase per unit fraction porosity;
- f_p = the volume fraction porosity;
- k_c = the rate of compliance increase per unit elastic strain increase;
- ϵ_{em} = the elastic strain component at the maximum stress, σ_m , that the material has been subjected to;
- ϵ_{th} = the threshold elastic strain;
- σ = the stress, lb/in^2 ;
- C_o = the proportionality constant of the stress dependence of the nonlinear strain;
- n = the power function of the stress dependence of the nonlinear strain;
- ϵ_o = the residual strain (permanent set) which is linearly dependent on either the maximum total strain that the specimen has been subjected to or equivalently, the maximum elastic strain.

An equation for the unloading curve equation has not been determined due to the inconsistency of $d^2\sigma/d\epsilon^2$ between the various grades tested.

Several problems arise in the use of equation 59 to describe the initial loading curve, ϵ_m versus σ_m . Since the elastic compliance

is dependent on ϵ_{em} , the elastic strain is dependent on itself. Also, ϵ_o is dependent on ϵ_{em} . This problem does not arise in Jenkins' simplified treatment. However, examination of equations 7 through 13 in which the equations are modified to account for cracks, shows that a similar problem occurs. All of these contain the factor Q which is a constant for a given crack population. If the number of cracks increase with deformation as observed, Q must also vary. Jenkins analysis consequently suffers from the same problem.

The other deficiency of equation 59 is that it only gives the relationships between stresses and strains at higher deformations, in the regions of steady state. This is of small consequence, since it has been shown that at low deformations, the state is transitory. Again the Jenkins modifications suffer from the same problem, and he empirically uses his simplified equations to describe the transition region.

The parameters for equation 59 are given in Table 5. The power function, n , has been universally set to 3, the average value. With the exception of AXZ graphite, whose experimental value is 2.4, this is not a poor approximation since the calculated values of C_o are reasonably close for the other grades and orientations.

Using the average values for C_o , 32×10^2 , and n , 3, the stress-strain curves have been calculated from these data and are plotted in Figure 70. These curves correspond reasonably well with those on Figure 22 since they are syntheses of the analyses performed in Section 3.0. The slight deviations between the two figures result from the use of average properties wherever possible. The calculations would still be more functional if the dependencies of k_c and ϵ_o on ϵ_{em} could

also be related to the physical properties. The complexity of those relationships has previously been explained, and other than qualitative explanations, no success at definition has been achieved. Since both k_c and the rate of increase of ϵ_o with ϵ_{em} should be functions of the numbers of cracks formed, they are themselves related. High k_c values correspond to high $d\epsilon_o/d\epsilon_{em}$ values. However, why the number of cracks formed is a strain related function rather than a stress and strain related function is elusive. In spite of the difficulties, our model has approached the physical realities better than the previous ones.

To summarize the implications of equation 59, when stress is applied to a polycrystalline graphite, several things occur simultaneously. The material strains elastically, the extent depending on the initial elastic constant. In addition a certain amount of basal plane plastic shear occurs with a strain hardening exponent of approximately 3. The extent of this plasticity is limited by the elastic deformation. When the elastic strain surpasses a critical value, cracks are introduced into the material at a rate proportional to the strain. Cracking causes two effects: (a) the relief of internal stresses adding an increment of strain to the above two components; and (b) an increase in the elastic compliance due to stress concentration, which in turn increases the elastic strain component. Unloading prior to failure causes the elastic and plastic components to reverse themselves. At zero stress, the residual strain is composed primarily of the internal stress relief component, although a small amount may be accounted for by unrecoverable

plasticity. On reloading, only the elastic and plastic components change, until the previous maximum stress is exceeded. Hence, the differences between the equation for the initial loading and the reloading curves are that in the latter case, the residual strain component is a constant, as is the compliance. In the former case, these are strain dependent.

4.15 Further Justification of the Deformation Model

The choice of the present elastic model over the Bilby-Cottrell plastic model to characterize crack induced deformation in graphite can be further justified. For the reasons previously cited, extensive basal plane shear is not an operable mechanism. The questions then arise: does a different plastic deformation mechanism exist and does the extensive non-basal plane elevated temperature plasticity have a room temperature complement? It is of some interest then, to examine the latter.

Smith⁽⁹⁾ has shown from photomicroscopy that the large deformations above 2000°C are associated with cracked flake particles. As the temperatures were increased above 2500°C, the crack densities decreased, but the individual cracks were longer and more widely opened. The plasticity is not accompanied by reductions in areas, and is due to the cracks opening normal to their surfaces. This is confirmed by Zukas and Green⁽¹⁴⁾ whose findings were previously outlined in section 1.22. In tension, creep resistance of ZTA increased continuously as the stress axis was varied from the pressing direction. The resolved stress normal to the basal planes was shown to have the greatest influence on extent of

deformation. Although the authors do not state it, the resolved normal stress, in the tangential direction also controls the compressive creep. Because the induced tensile hoop stress is lower in magnitude than the axial stress and because the stress dependence on creep is very high in polycrystalline graphite, the compressive creep rate is less than the tensile creep rate at all orientations. The differences are greatest when the stress axis coincides with the pressing direction, where the fewest numbers of basal plane normals are tangentially oriented. The creep rate differences in tension and compression become less for those stress directions in which the density of tangentially oriented 0002 directions is high. The opening crack mode of deformation is also microscopically confirmed in this work.

The Bilby-Cottrell model can be evoked to rationalize the elevated temperature deformation, but again basal plane slip cannot be. An alternative to this type of slip is called for. The answer is partially provided by the work of Fischbach⁽³⁴⁾ on high temperature (2500°-2900°C) creep of pyrolytic graphite. Tensile stresses were applied parallel to the layer planes of this highly oriented material and strains were measured in the three orthogonal directions. Up to 8 percent axial strain, the volume was observed to increase slightly. This was associated with the increase in the transverse strain parallel to the layer planes and is observed to be caused by dewrinkling of those planes (elimination of kinks, twins, etc.). Above 8 percent to 34 percent axial elongation, little volume change occurs. In fact, the rate of transverse dimensional decrease is the same parallel to and perpendicular to the straightened layer planes. This remarkable occurrence can

can neither be explained by basal plane nor non-basal plane (prism plane) glide. Some mass transport mechanism is required to cause equal deformations parallel and perpendicular to the c-axis. Fischbach suggests that this might be provided for by Nabarro-Herring diffusion. The measured stress dependencies and activation energies for pyrolytic graphite are consistent with this. He concludes that mass transport by diffusion is the rate controlling process above 2000°C in graphite for graphitization, annealing of irradiation damage and plastic deformation.

In the polycrystalline material ZTA, the activation energy for creep is the same as that for the pyrolytic material, but the stress dependence is very much higher. The existence of stress concentrating cracks normal to applied stress direction may partially explain the latter. Also, progressive elimination of twins, kinks, or other dewrinkling on a micro-scale, may require higher stress dependencies. Nevertheless, no slip systems other than the two associated with the basal plane have been observed at any temperature. Elevated temperature deformation is clearly by mechanisms which would be inoperative at room temperature.

From the above, and the reasoning in sections 4.12 and 4.13, it is concluded that the only plastic deformation at room temperature is that which is elastically constrained. Jenkins use of the Bilby-Cottrell plasticity model is not physically founded. Finally, cracks effect the strain elastically.

4.2 Fracture of Polycrystalline Graphite

4.21 The Fracture Process

It is clear from the microstructural studies of the fracturing process that there are three stages involved. The first stage, starting relatively early, and continuing throughout in the deformation process, is the formation of independent cleavage cracks through suitably oriented flour particles. These tend to form normal to or at small angles to the stress axis for all orientations. As the applied stress axis varies from the pressing direction, the density of fractured flour particles per unit strain decreases. Increasing the applied stress not only increases the number of fractured particles, but causes linkages to occur between previously cracked ones and also limited crack extension. This second stage is also dependent on stress axis orientation. The total crack lengths are functions of the probabilities that neighboring particles are suitably oriented. Thus, for anisotropic grades, the observed cracks are longer when the material is stressed parallel to the pressing direction than at other orientations. Less energy is required to fracture the smaller misoriented regions between cleaved flour particles. The final stage of complete fracture occurs when the "linked" or extended microcracks are sufficiently long to meet the critical crack length criteria.

The processes normally associated with crack formation are those of nucleation and growth. In graphite, a nucleation stage during deformation is not required as it is in metals and other materials. The latter require a certain amount of plastic deformation for cracks to nucleate

by dislocation mechanisms. In graphite, these sites preexist in the zero stress state. A summary of the crack "nuclei" on the crystallite scale has been given by Soule and Nezbeda⁽³⁾ and are shown schematically in Figure 70. Some of these are experimentally observed. The only process necessary is that of growth and this requires relatively low stresses. Therefore, the observed cleavage of flour particles is easy and occurs early in deformation.

The growth of cracks via the linkage mechanism or via crack extension in the later stages is the controlling step in fracture. Most of the work of the fracture process is required to circumvent or fracture the misoriented regions. From the fracture toughness tests, it has been shown that the G_{TC} values (effectively, energy per unit area to create the new surfaces in the misoriented regions) do not vary greatly between the orientations for a single grade (0 per cent for ATJ and 25 per cent for ZTA). If the critical crack lengths were the same irrespective of orientation, it would be expected from strain energy considerations that orientations with higher moduli would fail at lower stresses. That this is contrary to observation is attributed to the relative ease of slow crack growth and crack linkages for those low moduli orientations in which particle basal planes are preferentially oriented perpendicular to the stress axis. At final fracture, the critical crack lengths are then vastly different between the orientations, and the strength of the material is attributable to both the elastic modulus and the critical crack length. These are both in turn functions of the preferred orientations in such a manner that, as the modulus increases, the probability the existence of an extensive crack decreases. For example in ZTA

graphite, as the modulus increased from 1.6×10^6 to 4.5×10^6 psi the calculated critical crack length decreased from .29 to .12 inches.

The observed limited crack growth is analogous to the pop-in phenomena observed in fracture toughness testing of other materials. When a crack begins to propagate it is accompanied by a release of the strain energy. If the strain energy release rate per unit of area increase of the crack, $-dU/dA$, is greater than the work, G_I , required to create the surfaces, the crack will continue to grow. However, if $-dU/dA$ decreases with increasing area, it is possible for propagation to cease. This is the case for small cracks in polycrystalline graphites and has also been observed by Corum⁽²⁵⁾ in fracture toughness testing of graphite in flexure. Catastrophic failure occurs when $-dU/dA$ never falls below G_I as the area increases. The work to create surfaces under these conditions is defined as the critical value, G_{Ic} .

4.22 Fracture Criteria

Fracture toughness data have been determined for each of the grades. This information forms a criteria for failure if knowledge of pre-existing crack sizes is available. It is then only a matter of substitution of the size into the proper geometry dependent equation to determine the fracture strength. However, it has been shown that polycrystalline graphites are in a class of materials that generate their own cracks. Therefore, fracture toughness is useful only in those cases in which the pre-existing cracks are larger than the self-generated ones. The calculated magnitude of the latter for the

grades tested are listed in Table 6 along with the average fracture stresses, the elastic constants, the fracture toughness parameter and other parameters to be described. The size was calculated on the basis of a penny-shaped crack since this form represents the least area for a given dimension and therefore requires the fewest number of cracked particles to form it. From these values, therefore, unless the pre-existing crack size exceeded 0.12 inches in ATJ graphite, the fracture toughness failure criteria is not applicable. It does, on the other hand, account for the exceedingly low values intermittently encountered when testing numbers of specimens.

The criteria suggested by Knibbs⁽¹⁸⁾ was also tried. Figure 72 shows the results along with his regression analysis lines. Taking into account test procedure differences, the fit is reasonable except for ZTA. It is, however, unsatisfactory since it is based on the weighted average of the strength and does not account for stress axis orientation differences. An alternate procedure has therefore been developed. It is somewhat similar to the Knudsen⁽²⁰⁾ approach, but it is expanded to account for other parameters which have been measured in this work.

The fracture stress, σ_f , for a material containing a penny-shaped crack can be determined from:⁽³⁵⁾

$$\sigma_f = \left[\frac{\pi G_{Ic} E}{4 (1-\nu^2) c} \right]^{\frac{1}{2}} \quad (60)$$

where G_{Ic} is the critical crack extension force, E is the modulus of the material at failure, ν is Poisson's ratio and c is half the critical crack diameter. For a polycrystalline material consisting of

nearly spherical particles, the self-generated crack size can be related to the number of cracked particles contained in the critical crack area, n_c , the average particle diameter, d , and the areal fraction of porosity, f_p , by the relationship:

$$c = \frac{d}{2} \left[\frac{n_c}{(1-f_p)} \right]^{\frac{1}{2}} \quad (61)$$

It is as difficult to assess the magnitude of n_c as it is c , but relative values as a function of crystallite preferred orientation and stress axis orientation can be determined. In Appendix C a method is given to determine the relative density of c -axes per unit solid conical angle as a function of stress axis rotation: $L(K, \alpha) \sin K$. Since we are considering cleavage stresses, the resolved normal stress, σ_n , on these basal planes can be approximated by:

$$\sigma_n = \sigma_a \cos^2 K \quad (62)$$

where the transverse and shear stresses are considered to be small; σ_a is the applied axial stress, and K is the angle from the stress axis. The relative number of particles which will crack at any given stress level as a function of K will be proportional to:

$$\frac{L(K, \alpha) \sin K \cos^2 K}{\text{Total number of particles}} = \frac{L(K, \alpha) \sin K \cos^2 K}{\int_0^{\pi/2} L(K, \alpha) \sin K dK} \quad (63)$$

The total relative number of cracked particles, N , is found by integration of this equation, and:

$$N(\alpha, \sigma) = \frac{\int_0^{\pi/2} L(K, \alpha) \sin K \cos^2 K \, dK}{\int_0^{\pi/2} L(K, \alpha) \sin K \, dK} \quad (64)$$

For a given distribution of crystallites, a comparative value of the relative numbers of cracked particles for a given stress as a function of stress axis orientation can be determined. This is then the relative probability that a single particle will be cracked, P_1 , where:

$$P_1 = N(\alpha, \sigma) \quad (65)$$

Experimental values have been substituted into equation 72 and the resulting values of P_1 are listed in Table 6.

In a crack linkage mechanism, it is of interest to determine the probability P_n , that n adjacent particles have been cracked at the given stress level. Assuming that the events are initially independent of one another then:

$$P_n = P_1^n \quad (66)$$

This probability has been plotted versus n in Figure 73 for the various grades and orientations.

Finally, the orientation effect on fracture criteria can be assessed. Most proposed failure criteria show a strength dependence on the grain size to the minus one half power as would be found by substituting equation 61 into equation 60. This assumes the crack length is related to grain size. However, from the previous discussion, the average crack length would be somewhat larger than d , and would be proportional to the square root of the average number, \bar{n} , of adjacently

cracked particles, where:

$$\bar{n} = \frac{\sum_{n=1}^{\infty} n P_1^n}{\sum_{n=1}^{\infty} P_1^n} \quad (67)$$

This summation has been performed and the results are also in Table 6.

This shows that for ZTA, the average number of adjacent cracks against the grain is twice the with-grain value.

The failure criterion is finally arrived at by substituting the value of \bar{n} for n_c in equation 61 (assuming a proportionality between the two), and substituting this equation in turn into equation 60.

Therefore:

$$\sigma_f \propto \left\{ \frac{\pi G_{Ic} E}{2(1-\nu^2) d} \left[\frac{1-f_p}{\bar{n}} \right]^{\frac{1}{2}} \right\}^{\frac{1}{2}} \quad (68)$$

Values of σ_f have been plotted against the right hand side of the equation in Figure 74. The grain sizes were microscopically determined by lineal measurements on polished specimens. The average proportionality is 187 with a standard deviation on the slope of 35. Even with the simplifications involved in the deviation, the fit is reasonable. Since it compensates for the preferred particle orientations, it represents a considerable improvement over the Knudsen criteria.

The values of G_{Ic} used in equation 68 to determine the points on Figure 74 were the experimentally determined values. Similarly, the moduli used were the experimental values at failure. Both of these parameters have been shown to be dependent on the pore fraction. In addition, the moduli also change with deformation. To enable the

prediction of the strength of a graphite for which the physical properties of grain size, density and degree of preferred orientation are known, it will be necessary to expand equation 68 by substituting the equation of Figure 69 for G_{Ic} and equation 43 for E . The deformation dependence of the moduli can be neglected since it is not known prior to testing and the error of doing so will be within the scatter of the prediction. Also, the differences in Poisson's ratios between graphite grades and stress axis orientations have negligible effects. Therefore, by using equation 68 in conjunction with the methods of this paper, it is possible to predict strengths from physical property measurements.

The concepts of polycrystalline graphite fracture of the disorientation will now be summarized. On initial application of strain, only negligible amounts of particle cracking occur, but the strain energy is increased. Strain energy is controlled by the elastic modulus of the material, which in turn is a function of the degree of preferred orientation, the stress axis direction, the pore fraction and the number of cracked particles. Increasing the strain further increases the strain energy, and also causes individual flake particles to cleave. A certain fraction of these will be neighbors, and the number of adjacently fractured particles is governed not only by the magnitude of the applied strain, but also by the degree of preferred orientation and the stress direction. Knowledge of the latter two items enable the calculation of the average number of neighboring particles suitably oriented to enter into coincident fracture. This average can be considered to be the crack "unit", and its area is a function of the particle size and the

calculated number.

Further straining causes crack extension and/or linkages between crack "units" through regions not as suitably oriented for fracture. Although the strain energy is increasing, the various cracking processes reduce it below the value for an equivalent crack-free material. This effect is reflected in the reduction of measured modulus with increasing deformation. When the rate of strain energy reduction per unit area of crack extension becomes equivalent to the fracture energy required for that area increase, failure occurs, i.e., one of the linked or extended cracks has become critically large. This crack can be considered to be composed of multiples of the "unit" crack and the critical crack area is then a function of the "unit crack" area, the number of "unit cracks" in the extended crack and the fraction porosity. As previously stated, the "unit crack" area is particle size and orientation dependent. The number of "units" increases with applied strain. Finally, increasing pore fraction decreases the number of "units" required for a given critical crack dimension.

The physical property effects on the strength criterion (equation 68) can be recapitulated as follows: Decreasing the particle size necessitates greater numbers of single particle fractures to form a crack of given dimensions. Since the higher deformations required to fracture more particles raise the strain energy, the critical crack size for failure decreases. Although a smaller critical crack size must be produced for failure, reduced particle sizes increase strength. Preferential orientation of basal planes normal to the stress axis both

decreases the elastic modulus and increases the probability of single particle failure. Both consequences combine to tolerate greater strains and larger cracks; however the associated stress levels are decreased. Finally, porosity causes the elastic modulus to decrease exponentially with pore fraction, causes the surface energy to decrease linearly with pore fraction, and causes the critical crack length to increase slightly with pore fraction. Since the strength is related to the square root of the modulus, it would be expected that the rate of decrease in strength with pore fraction would be less than that for the modulus. However in the porosity range of most graphites, the combined porosity effects on all the parameters give an apparent rate of exponential decrease in strength that is approximately the same as the rate of decrease in the modulus.

5.0 CONCLUSIONS

The goals established for this study were to determine the mechanisms of deformation and fracture of polycrystalline graphite at room temperature. In order to accomplish this, previously established testing and analytic techniques were first attempted. In many areas these were either deficient or insufficiently proven or in dispute. It was therefore necessary to improve many previous techniques, or to develop new ones; and where treatments were in controversy, to theoretically establish the correct one. A summary of the results as well as the improvements in both testing techniques and analyses of this work follows. Suggestions for possible expansion of this work will be presented in the second subsection.

5.1 Summary of the Results

The major achievements of the work were the development of improved, self-consistent models for both the deformation and fracture of polycrystalline graphites. Analysis of the test data with respect to these led to the following:

- (A) A single analytic equation was determined, which describes both the initial loading and the reloading stress-strain curves. This was accomplished by considering the total strain at a given stress to be comprised of three strain components: (a) a linear elastic strain component; (b) an elastically constrained plastic strain component; and (c) a

residual strain component resulting from crack induced internal stress relief. On initial loading both the elastic compliance and the residual strain in the equation are dependent on the maximum applied elastic strain. The equation for reloading to the previously applied maximum stress differs from the above due to the constancy of the compliance and the residual strain. It has been established that the initial stages of deformation are transitory. The deformation equation given in this paper then only describes the steady state, higher deformation regions.

- (B) A fracture criterion for polycrystalline graphite was determined which accounts for the effects on the strength of the flour particle size, the flour particle preferred orientation and the bulk density. Decreasing the particle size increases the strength by increasing the number of particle fractures required to form the critical crack. Consequently higher stress levels are necessitated. Preferential orientation of basal planes normal to the stress axis both decreases the elastic modulus and increases the probability of particle fracture. Both consequences allow greater strains and the existence of larger cracks prior to failure, however the associated stress levels are decreased. Porosity significantly decreases both the elastic modulus and the fracture surface energy but increases

the crack dimensions only slightly for a given number of cracked particles.

The other important results of the dissertation are:

- (C) The residual strain cannot be explained by a plastic deformation mechanism. Instead it arises from crack induced internal stress relief. The residual strain is a complex phenomena and is dependent on such factors as degree of crystallite preferred orientation, the graphitization temperature, crystallite elastic constants and thermal expansion coefficients, crystallite sizes, etc.
- (D) Above some transient region, there exist linear relationships between the residual strains and: (a) the total strains at the maximum stress per cycle; (b) the strain at half the maximum stress; and (c) the elastic strain component at the maximum stress. The linearity can be explained if the number of deformation cracks is linearly proportional to the elastic strain at the maximum applied stress.
- (E) The elastic strain component can in principle be analytically derived from a knowledge of the preferred orientation, the fraction porosity and the state of deformation. Some of the parameters must be experimentally determined however.
- (F) An improved method to determine the elastic modulus of fully dense polycrystalline graphite from X-ray diffraction analysis has been developed. The uncertainty in this

method is a consequence of variable c_{44} elastic coefficients between graphites.

- (G) The elastic modulus has been analytically derived to be exponentially dependent on the volume fraction porosity. The calculated rate constant is two to three times greater than the experimentally determined values.
- (H) Analysis of the experimental data of this work, combined with an interpretation of the work of other investigators, indicates that the introduction of cracks into polycrystalline graphite affects the elastic strain component only. The plastic strain component should be relatively unaffected. The present analysis concludes that the excess elastic deformation at the crack tip causes the elastic modulus to be exponentially dependent on the number of cracked crystallites or particles. The observed exponential dependencies of the moduli on the maximum elastic strain can be explained if a linear relationship exists between the numbers of deformation cracks and the maximum applied elastic strain.
- (I) The extent of plastic deformation is limited by the elastic deformation in the direction of stress application. It has been shown in this work that the plastic strain component is proportional to the n^{th} power of both the average crystallite elastic compliance and the applied stress. The value of n is approximately 3 for the graphites investigated.

- (J) Crack nuclei exist prior to load application. The three stages of fracture are then: (a) the formation of independent cleavage cracks through suitably oriented flour particles; (b) linkage of these independent cracks and/or limited crack extension through regions not suitably oriented; and (c) catastrophic failure of one of those extended cracks.
- (K) The critical crack extension force does not vary greatly between orientations of a single grade. The variation that does exist results from fracture surface area differences as a function of preferred particle orientation. Between grades, the critical crack extension force decreases with increasing porosity.
- (L) Critical crack lengths are dependent on the degree of preferred orientation, the flour particle size and the pore fraction.
- (M) Since polycrystalline graphites generate their own cracks, the fracture toughness approach to failure criteria is valid only for those conditions in which preexisting cracks are larger than those formed during deformation.
- (N) The Knudsen fracture criterion applied to graphite does not account for orientation effects and thus is not totally satisfactory.

With respect to testing techniques, several improvements were made. For example, in the determination of the preferred orientation using X-ray diffraction, the Bacon technique was found lacking. Bacon

used a method in which the specimen was held fixed at the Bragg angle from the beam and the planar density for 0002 directions was determined from a flat photographic plate. In this method, the measured intensity is not only dependent on the density of basal planes as a function of orientation from the pressing direction, but also of angular position on the plate. In fact, at higher angles no diffraction occurs, necessitating extrapolation into these regions. This problem was surmounted in the present work by substituting a scintillation counter as the measuring device and fixing it at twice the Bragg angle from the incident beam. The intensity of 0002 diffractions as a function of orientation was determined by rotating the specimen plane positioned at the Bragg angle, about an axis perpendicular to the bisector of the incident and diffracted beam. In this manner, no correction to the measured intensity data was necessary and intensity values at any angle from the pressing direction could be determined. This simple modification of the Bacon technique represents a significant improvement.

Another testing technique improvement was made by the introduction of a natural crack into the fracture toughness specimen. Previous investigators of polycrystalline graphite had used thin saw cuts to provide the notch without establishing the effect of the radius of curvatures of the notch tip on their experimental results. Although for polycrystalline graphite this effect is probably insignificant, the problem was avoided in the present work. The use of a center-notch tensile specimen also eliminated inherent perplexities involved in the flexure tests of other investigations. For graphites, since the tensile

and compression stress-strain curves are not identical and both are nonlinear, the stress distribution in flexure is complex and the use of textbook strength of materials treatments is not valid. The introduction of a stress-raiser into the volume under tension further complicates the situation. Since graphite always fails in a tensile stress mode, the pure uniaxial tensile stress application specimen is to be preferred for mechanistic studies. Direct comparison with the results from standard tensile tests should also be facilitated.

With respect to analytic techniques, the extension of previous analyses of the relative densities of basal plane normals from X-ray diffraction data, as detailed in Appendix C, broadens the usefulness of this method. The modulus of elasticity as a function of the angle from the pressing direction had been previously determined by holding the density distribution of 0002 directions fixed and performing the orientation tensor transformations on the elastic constants. In the present work, this has been accomplished in Appendix D by the reverse process, i.e., fixing the elastic constant distribution as a function of angle from the stress axis and transforming the 0002 intensity vector distribution. Although these methods lead to equivalent results, treatment of the more complex stress distribution models is facilitated by the procedures developed in this paper. An additional advantage arose in the determination of the fracture criterion. From the relative density of basal plane normals per unit conical angle, the preferred orientation effect on the relative critical crack size could be accounted for. The flexibility of the present procedure thus gives it a distinct advantage over the previous ones.

The procedure developed in Appendix D to calculate the theoretical elastic modulus is an improvement of the uniaxial models presented by Slagle. Transverse strain interactions between crystallites which were neglected in previous calculations can now be accounted for. Although it was deemed unnecessary in the present work, the method can be extended to enable calculation of all the elastic constants of the polycrystalline material at any angle from the pressing direction. This can be achieved by solving the simultaneous equations for all six stress components for each particle pair, determining the six strain components, and then in turn incorporating these into an averaging procedure similar to the one given. Again, it will probably be necessary to average the values thus determined with those of the long particle models.

5.2 Suggested Future Work

Graphites with larger particle sizes, different flour particle properties and a variety of binders are commercially available. The universality of the analyses of this work should be checked by application of the methods to other grades. For instance, it is known that materials with glassy, nongraphitizable binders tend to preferentially fracture through the binder. Although the fracture criterion developed herein probably is still valid, the change in failure mechanism may alter some of the parameters.

It has also been suggested that the longitudinal elastic moduli calculation in Appendix D could be extended to calculate the other elastic constants. The quality of the calculation method could be

verified by this extension. Attempts have been made to calculate the coefficients of thermal expansion from the uniaxial stress models. It is felt by the author that these have been deficient due to the neglect of transverse strain interactions. Application of the methods of Appendices C and D in conjunction with the derived deformation equation should improve the calculations.

The analyses should be applied to elevated temperature mechanical properties. As an example, it is known that significant increases in the strength of graphite occur with increasing temperature. This can partially be attributed to measured elastic moduli increases with temperature. The author feels that the critical crack extension force probably also increases, and elevated temperature fracture toughness tests should be performed. Since deformation at temperatures above 2000°C is associated with mass transport phenomena, strain rate dependencies of deformation and fracture require assessment.

Since polycrystalline graphite can be classified as a brittle material, it is possible that some of the approaches and analyses of this paper may be directly applicable to some and partially applicable to other polycrystalline brittle materials. A brief review of the literature uncovered several areas of pertinence. The remainder of this section will examine these.

It is clear that the uncommon mechanical behavior of polycrystalline graphite results from its layered structure and the extreme directional dependence of all its crystalline properties. The weak interplanar bonding causes the basal plane elastic shear constant,

critical shear stress and cleavage strength to be unusually low. In the polycrystalline body, these phenomena cause the observed low elastic moduli, the nonlinear stress-strain curves, the large numbers and sizes of deformation cracks, etc. Few materials have structures and/or properties that are as anisotropic as graphite, however work on some of these has been reported. Magnesium dititanate⁽³⁸⁾ and Beta-Eucryptite⁽³⁹⁾ have been mechanically characterized and appear to deform and fracture similarly to graphite. It appears that the procedures of the present work could be fruitfully applied to better characterize these materials. Although no mechanical property work was uncovered for them, other possible candidates are the nitrides of boron, tungsten and niobium, and the selenides of indium and gallium. These have crystal structures in common with graphite and most have c/a ratios that are greater.

The more common polycrystalline anisotropic ceramics (e.g., Al_2O_3 , BeO and TiO_2) do not in general behave mechanically as does graphite. Their structures exhibit less directionality and lack a plane of extreme weakness. As a result the polycrystalline bodies have high elastic moduli and high yield stresses. Deformation is generally elastic except for very small grain size materials which evidence slight plasticity at high stress levels. Minimal numbers and sizes of deformation cracks ensue because the high moduli require the existence of only small cracks for failure. Therefore, for the larger grain size ceramics, both the deformation and fracture processes are simpler than those for graphite. For the finer grained materials, the fracture process in many ceramics is controlled by nucleation of the cracks by

plastic deformation and therefore also differs from graphite. Nevertheless, certain features of the present work should be generally applicable.

The models used to calculate the elastic modulus from the crystal elastic constants and the preferred orientation could be adapted to any anisotropic material. However, these more complicated methods are probably unnecessary for most since the lesser degree of crystalline anisotropy causes the single particle constant stress and constant strain calculations to agree reasonably.

The empirical relationship between porosity and modulus suggested by Spriggs⁽³⁰⁾ has been analytically proven. Its wide use in the field of ceramics is therefore justified. It would be beneficial to generalize the treatment of Appendix B to consider ellipsoidal shaped pores. The rate constant could then be determined as a function of shape and if necessary as a function of pore orientation relative to the stress axis.

Analogously, the relationship between the elastic modulus and the fraction of cracked particles has been determined. Where pertinent, this can be applied to other materials.

It is in the area of failure criteria that the approach used in this dissertation could be most applicable to other brittle materials. A number of papers dealing with the strengths of polycrystalline ceramic bodies^(40,41) utilize the Knudsen equation⁽²⁰⁾ to relate these to the physical properties of porosity and grain size. Others^(42,43) have modified this equation in order to obtain better data fits and still others have relied on statistical fits of strengths with physical

properties.⁽⁴⁴⁾ Although the Knudsen treatment is loosely based on the theoretical Griffith criteria, it is largely empirical. There is no a priori reason for the strength to be exponentially dependent on the fraction porosity, for instance.

Recent attempts at resolving physical property effects on strengths have returned to the theoretical criteria. Hasselman⁽⁴⁵⁾ believes that the pore size as well as the pore fraction influences the strength. He states that stress concentrations associated with the pores affect strength for a pore size of the order of or greater than the flaw size. The critical crack size in the Griffith equation was modified by increasing its length by the magnitude of the pore diameter. The pore size effect was experimentally confirmed in a previous paper⁽⁴⁶⁾ wherein the addition of a small fraction of pores into a glass caused a precipitous drop in strength. Strength continued to decrease with further pore additions, but at a lesser rate. The initial drop was attributed to the addition of stress raisers (i.e., pores) near the fracture producing flaws.

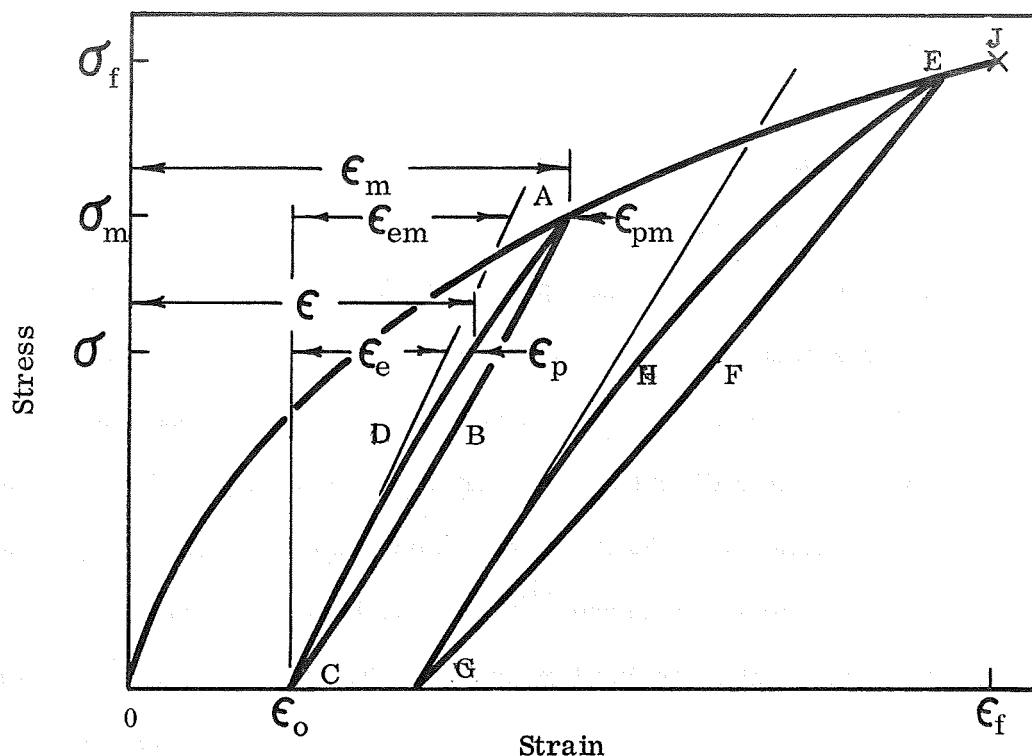
A linear relationship between the grain size and the measured maximum crack size in high density TiO_2 has been determined by Kirchner and Gruver.⁽⁴⁷⁾ Using literature values for both the fracture surface energy and the elastic modulus, these authors substituted the measured crack lengths into the Griffith equation and arrived at a strength - grain size - crack size correlation.

The procedure used in section 4.22 to determine the strength dependency of graphite on its physical properties was to determine the

effect of those properties on each of the parameters of the theoretical brittle fracture equation. With certain modifications, this could be adapted to other brittle materials. Elastic modulus - porosity relationships are commonly reported for ceramics. (30,41,42,44,48,49)

The nature of the relationship is disputed, but it is clear from the present work that the exponential one is to be preferred. Fracture toughness data have been determined on a number of ceramics, (21,50) but porosity, grain size and preferred orientation effects on these have not. Crack size as a function of orientation and grain size has been only qualitatively discussed, (47) although measurements in that paper show the crack sizes to be larger than the grain size. The increase in crack length with pore size has been noted. (45) The work on ceramic materials is therefore seen to be fragmented. To achieve rigorous failure criteria for the materials, all the physical properties effects on the parameters should be determined on each.

The failure criteria developed for graphite was based on the observed fracture mechanism which certainly is not universal for all brittle materials. Suitable modifications for the particular material is therefore required. As an example, in high modulus materials, the critical crack sizes are small. Therefore, the size of the pore as well as the pore fraction could prove to be significant. The criteria require alteration depending on whether failure occurs by simple brittle fracture or is associated with plastic deformation. For a given material these may be grain size (51) or temperature dependent (52) and more than one criteria would be required.



σ_m = the maximum applied stress prior to unloading

ϵ_m = the total strain at the maximum applied stress

ϵ_o = the residual strain after unloading from the maximum stress

σ = an arbitrary stress level between zero and the maximum stress

ϵ = the total strain at the arbitrary stress level

ϵ_e = the linear strain component of the total strain

ϵ_p = the nonlinear strain component of the total strain

ϵ_{em} = the linear strain component of the total strain at the maximum stress

ϵ_{pm} = the nonlinear strain component of the total strain at the maximum stress

σ_f = the failure stress

ϵ_f = the failure strain

Figure 1. A schematic representation of the deformation curves of polycrystalline graphites.

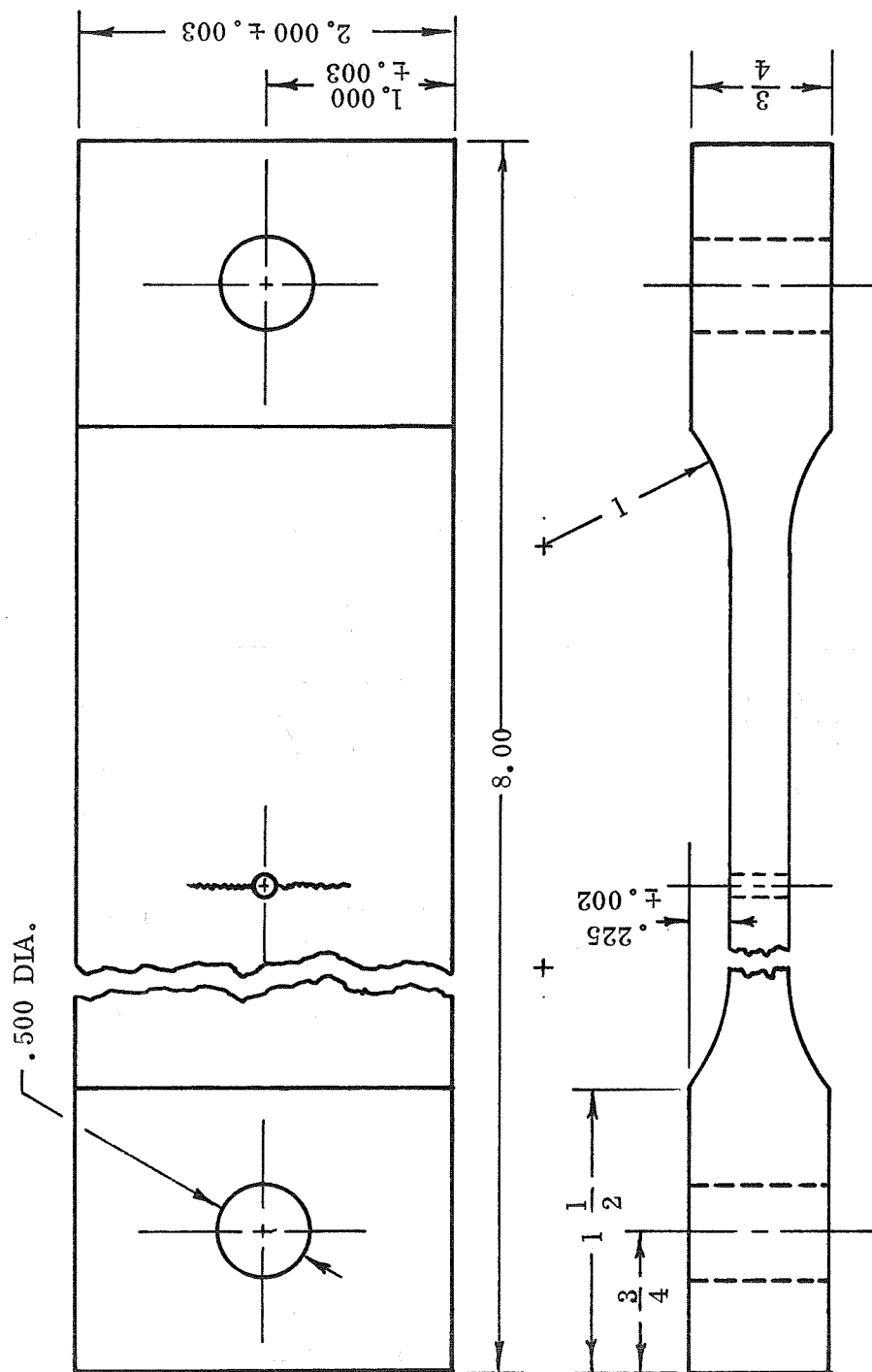


Figure 2. The center-notched fracture toughness specimen used to test ATJ and ZTA graphites.

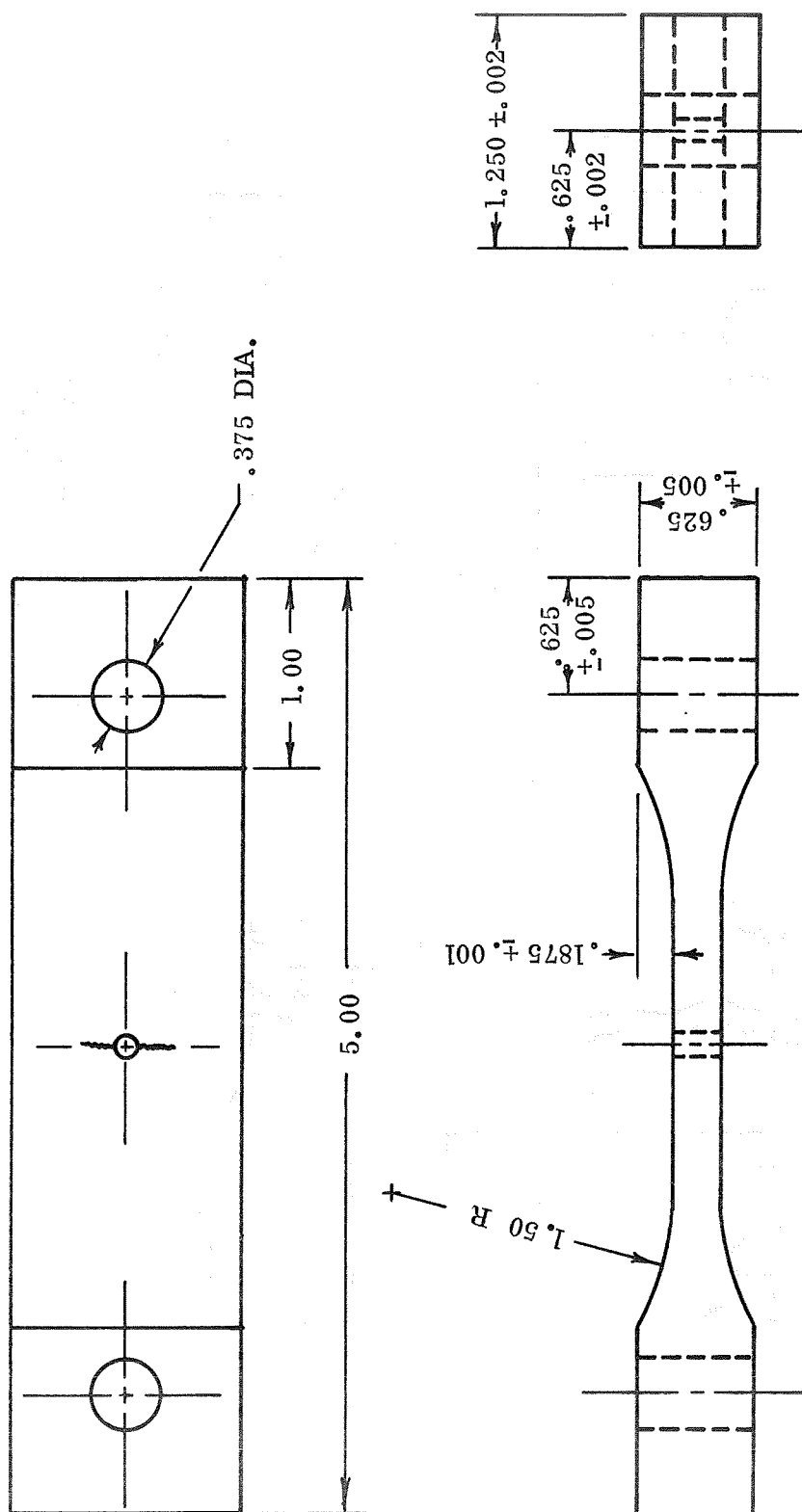


Figure 3. The center-notched fracture toughness specimen used for AX Z and AXF-5Q graphites.

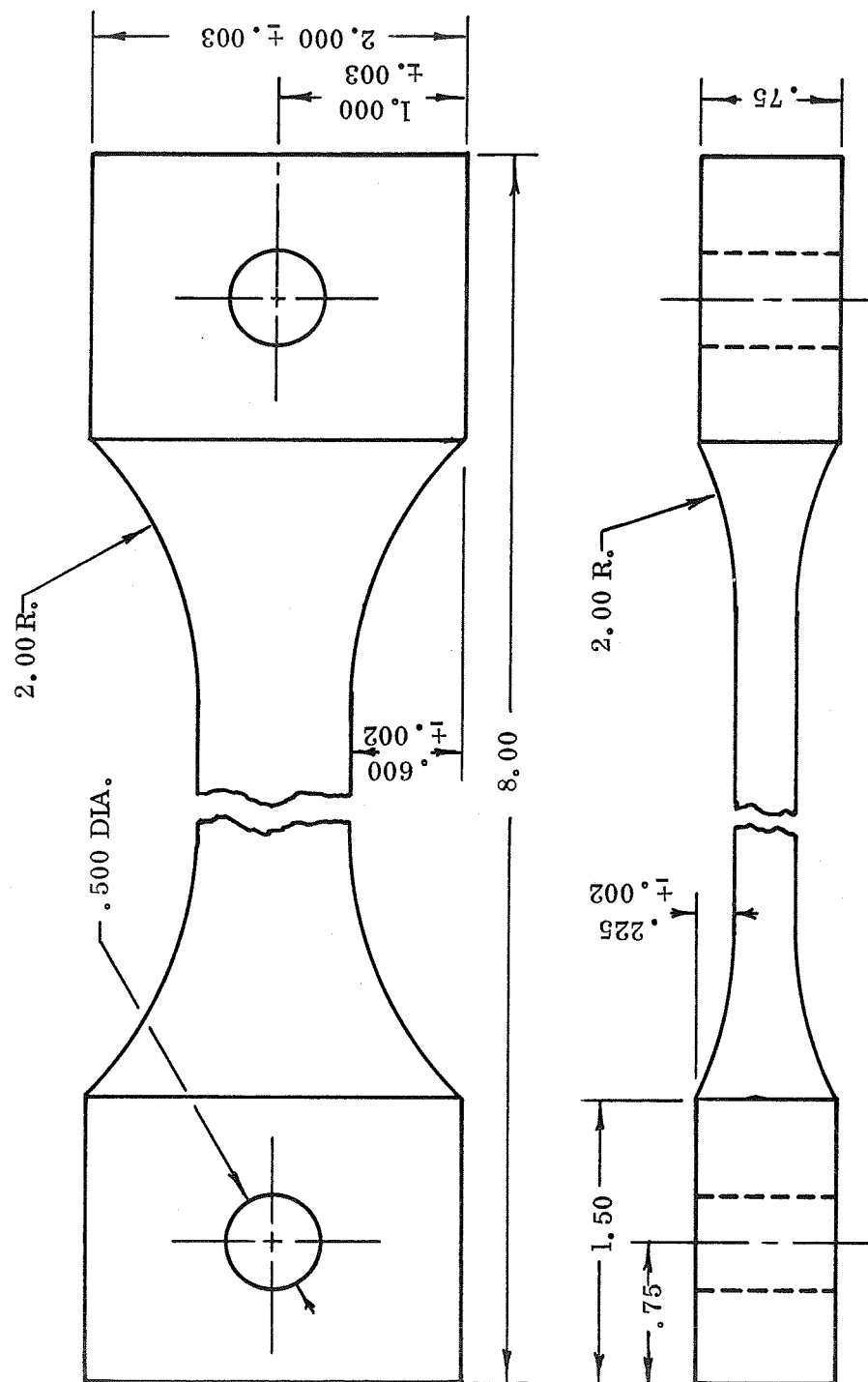


Figure 4. The tensile specimen used for testing ATJ and ZTA graphites.

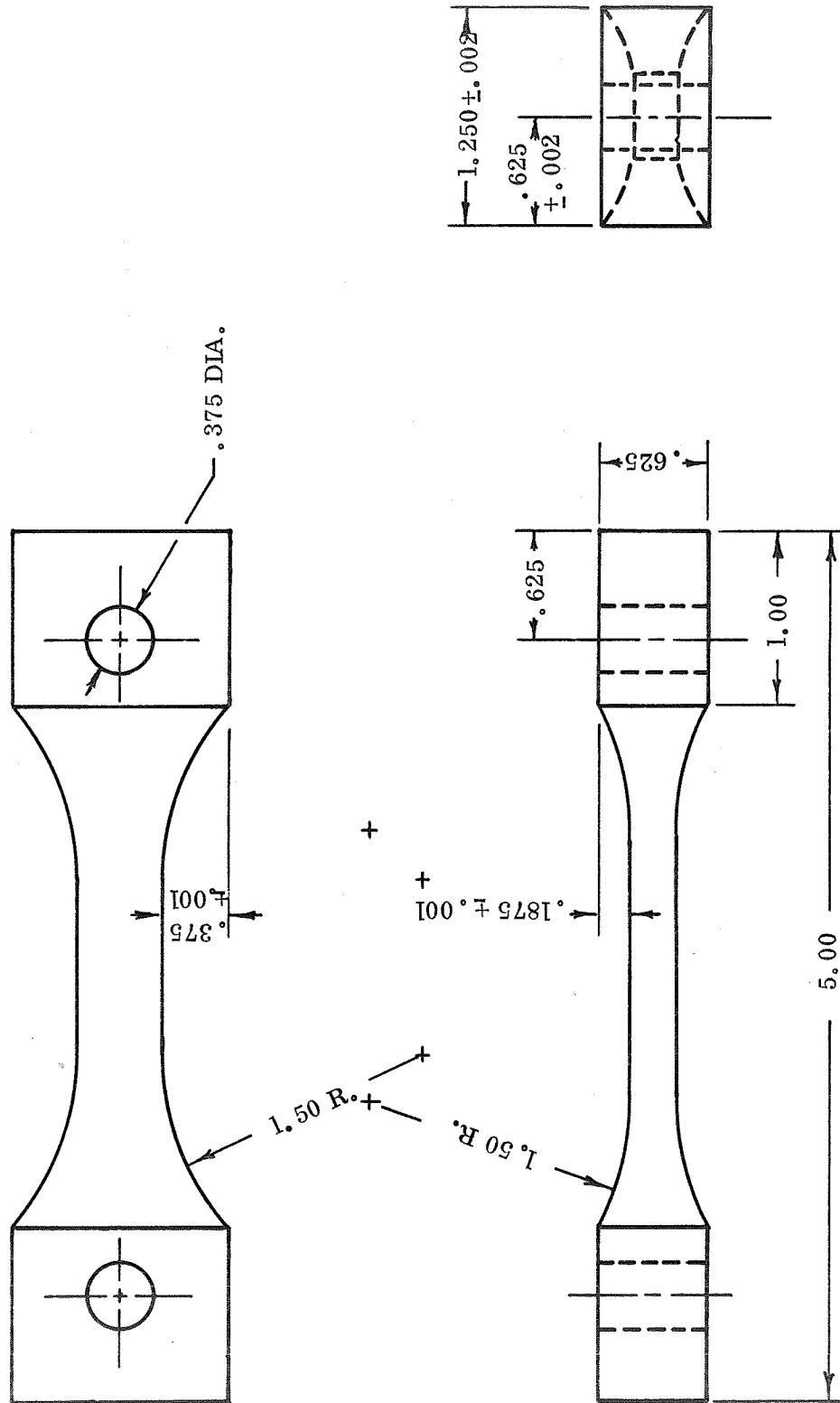


Figure 5. The tensile specimen used to test AXZ and AXF-5Q graphites.

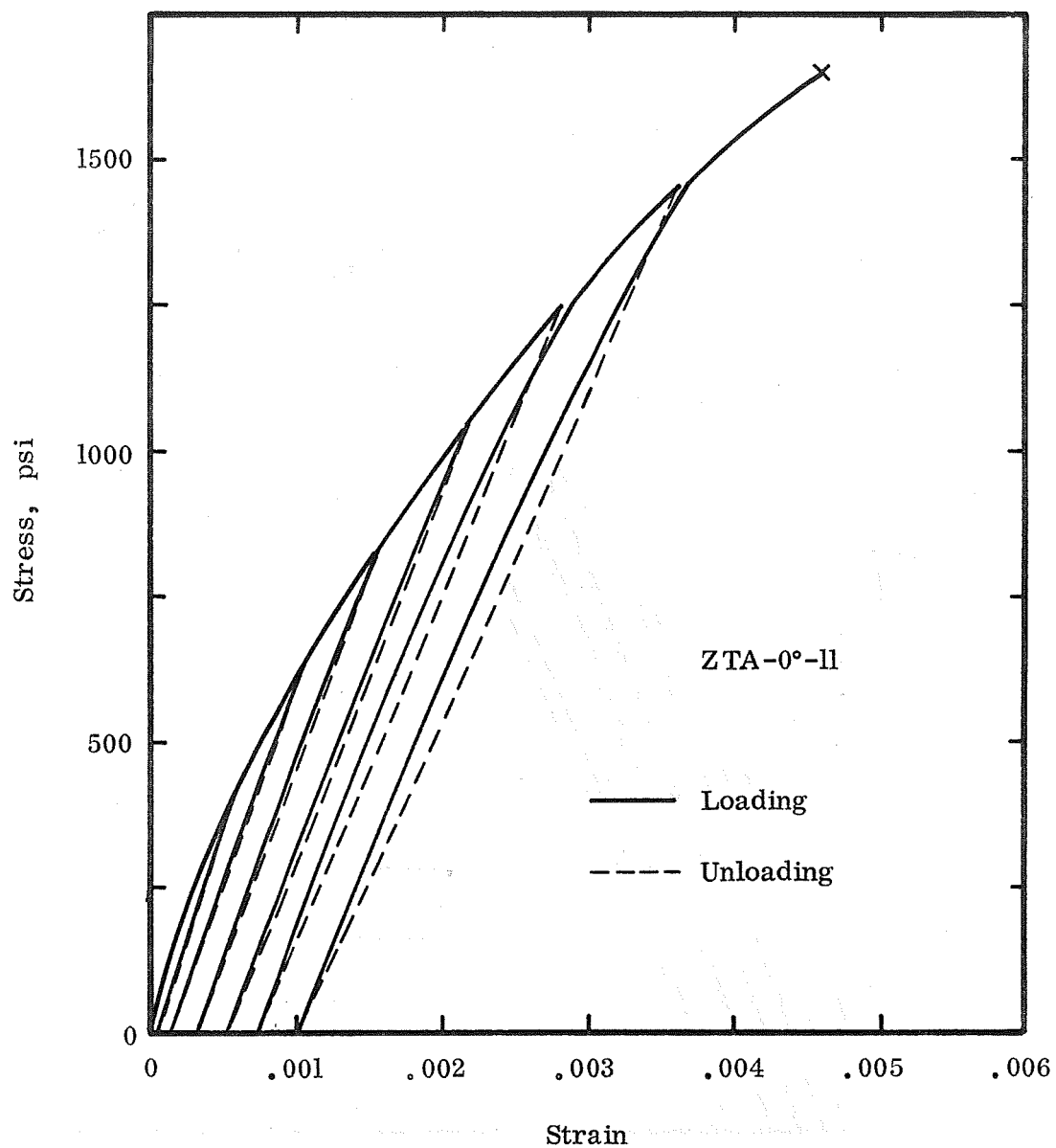


Figure 6. The longitudinal stress-strain curve of a ZTA graphite specimen with the tensile stress cyclically applied parallel to the pressing direction.

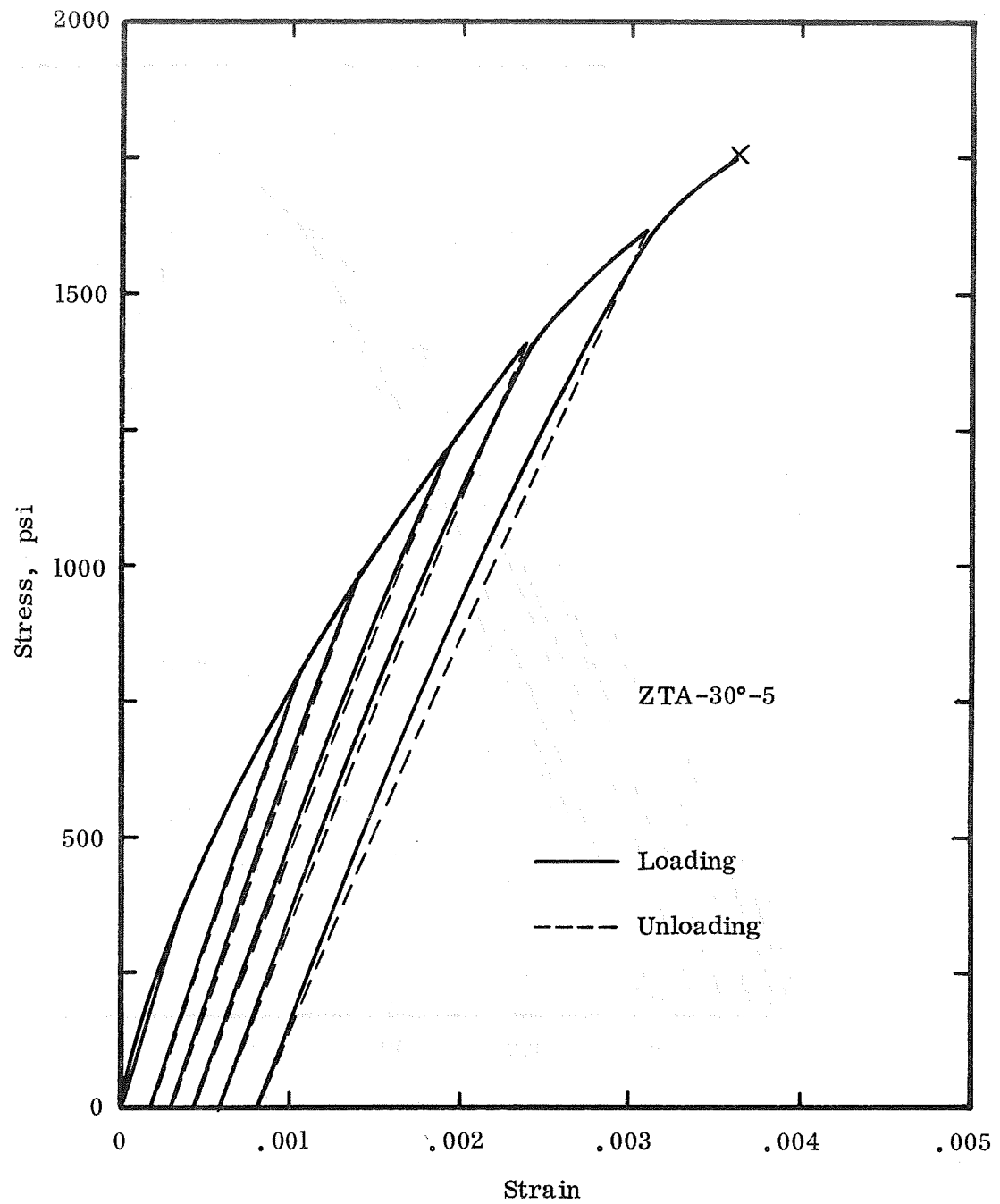


Figure 7. The longitudinal stress-strain curve of a ZTA graphite specimen with the tensile stress cyclically applied 30° to the pressing direction.

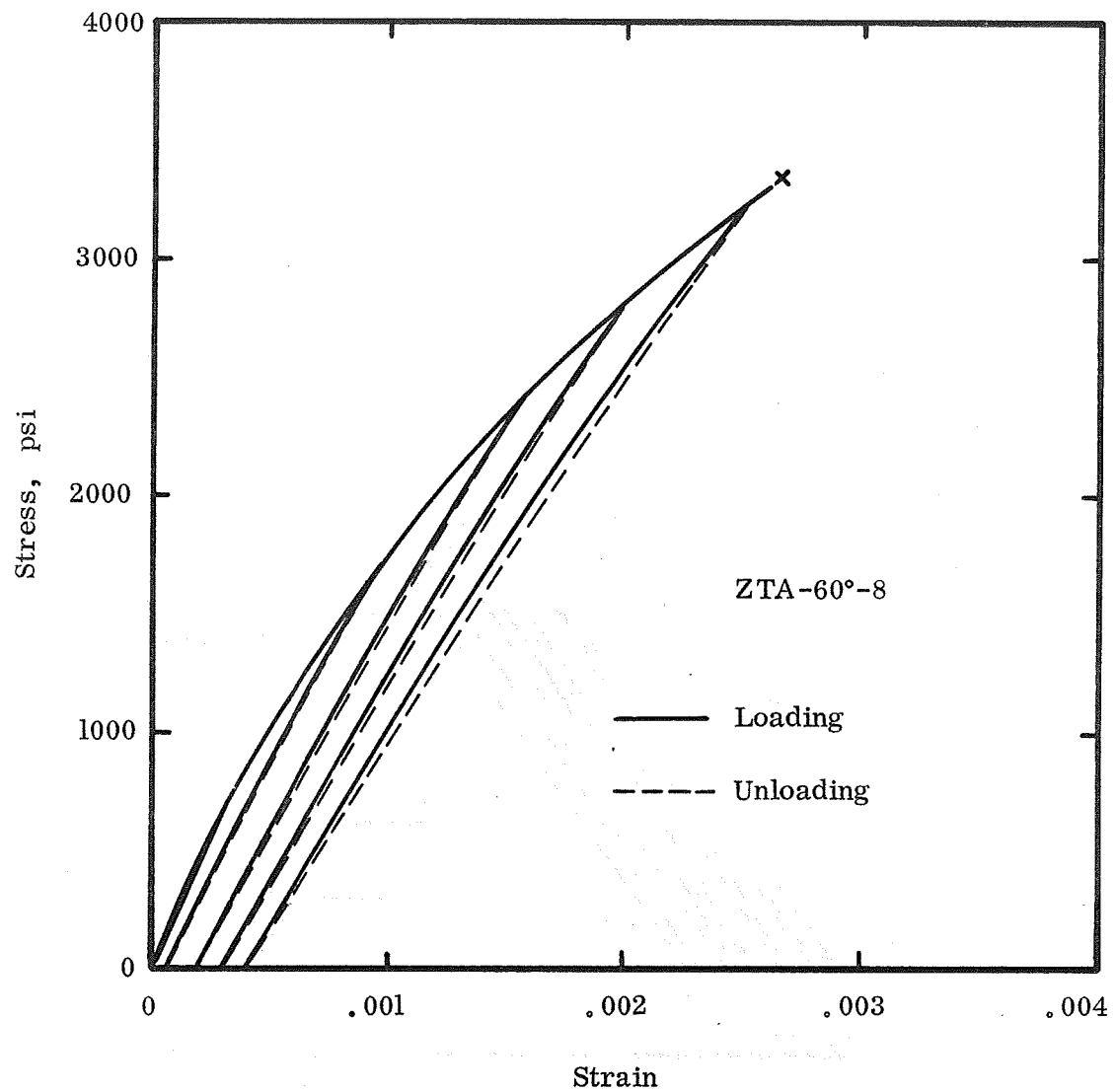


Figure 8. The longitudinal stress-strain curve of a ZTA graphite specimen with the tensile stress cyclically applied 60° to the pressing direction.

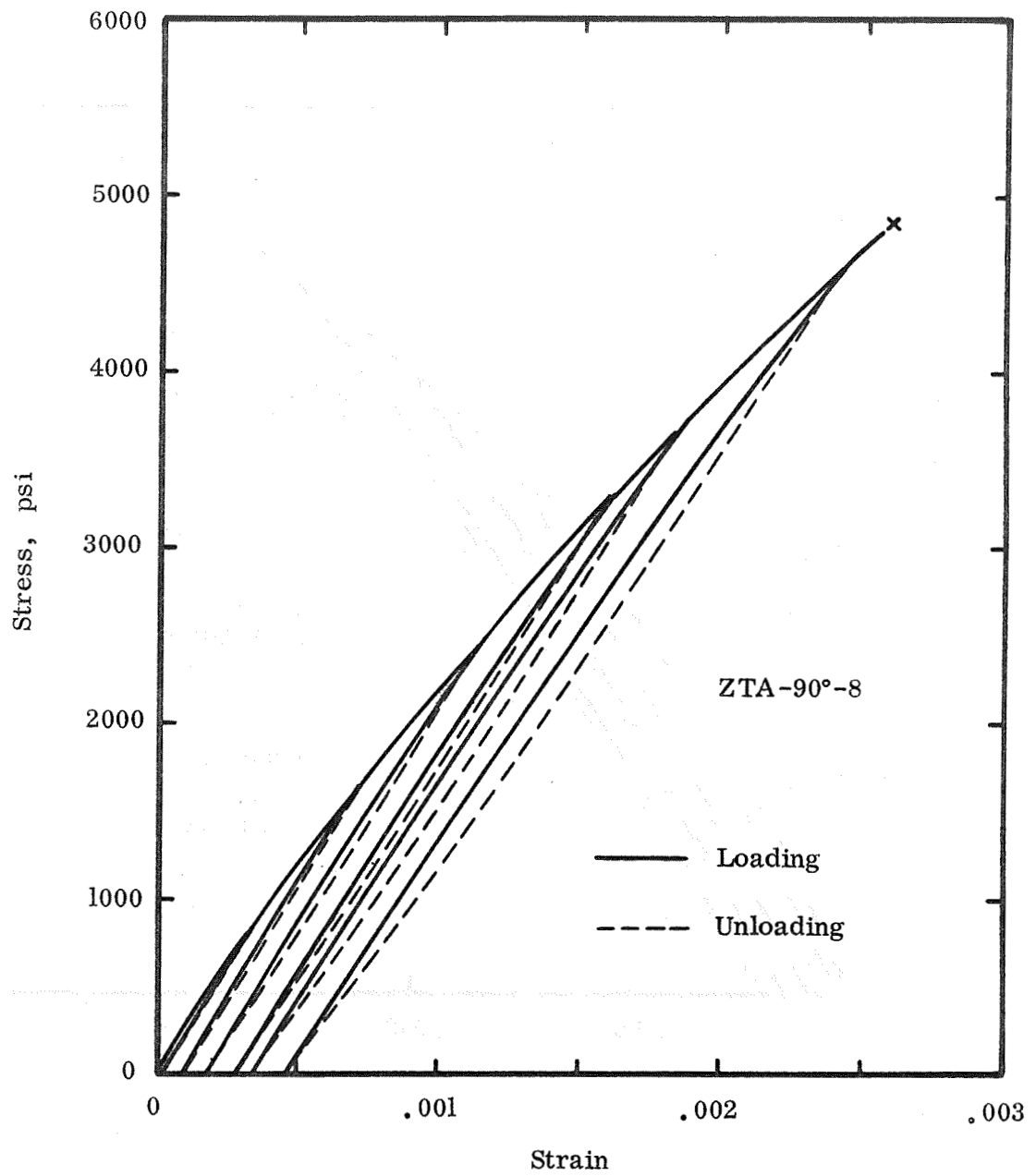


Figure 9. The longitudinal stress-strain curve of a ZTA graphite specimen with the tensile stress cyclically applied perpendicular to the pressing direction.

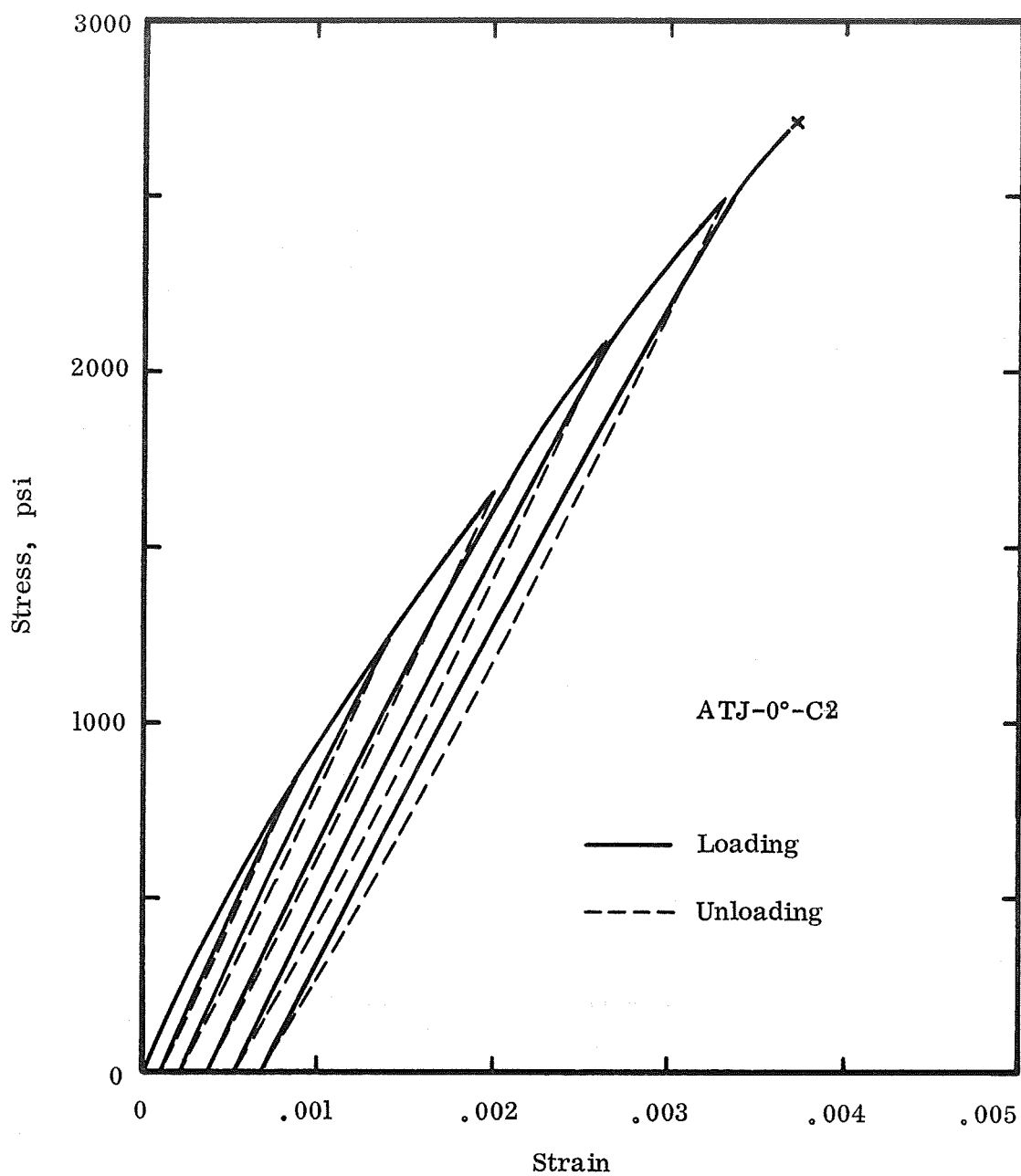


Figure 10. The longitudinal stress-strain curve of an ATJ graphite specimen with the tensile stress cyclically applied parallel to the pressing direction.

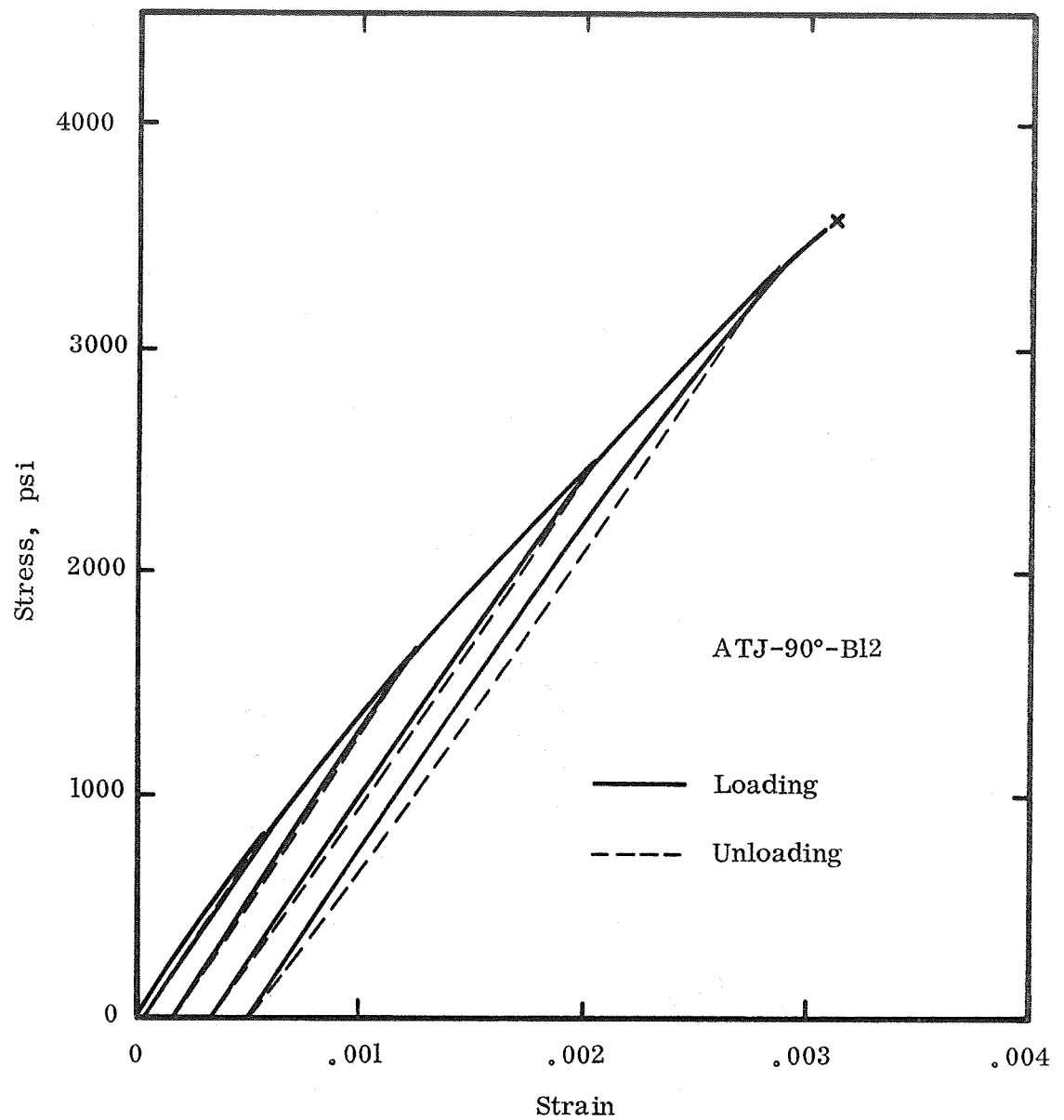


Figure 11. The longitudinal stress-strain curve of an ATJ graphite specimen with the tensile stress cyclically applied perpendicular to the pressing direction.

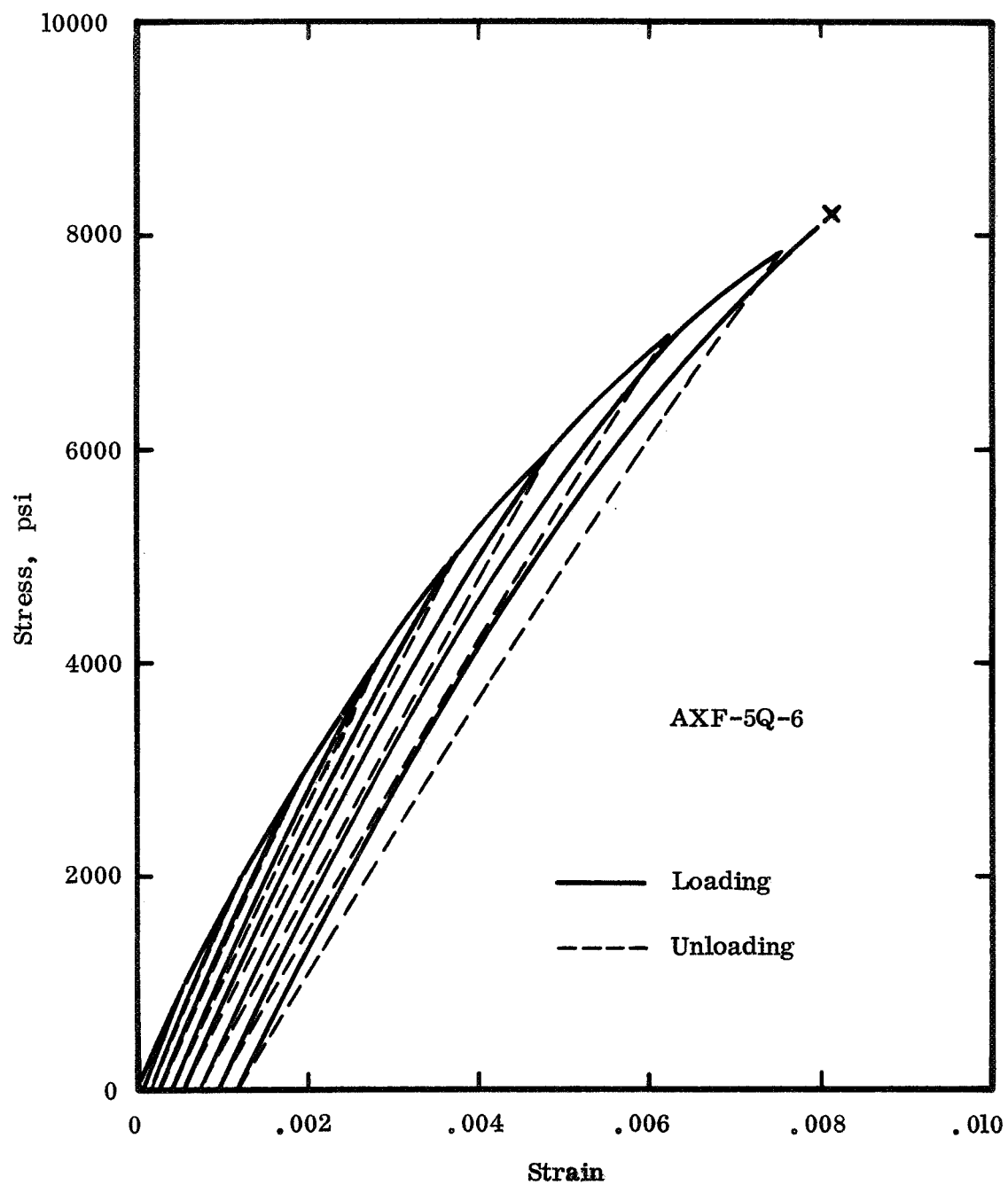


Figure 12. The longitudinal stress-strain curve of an AXF-5Q graphite specimen with the tensile stress cyclically applied.

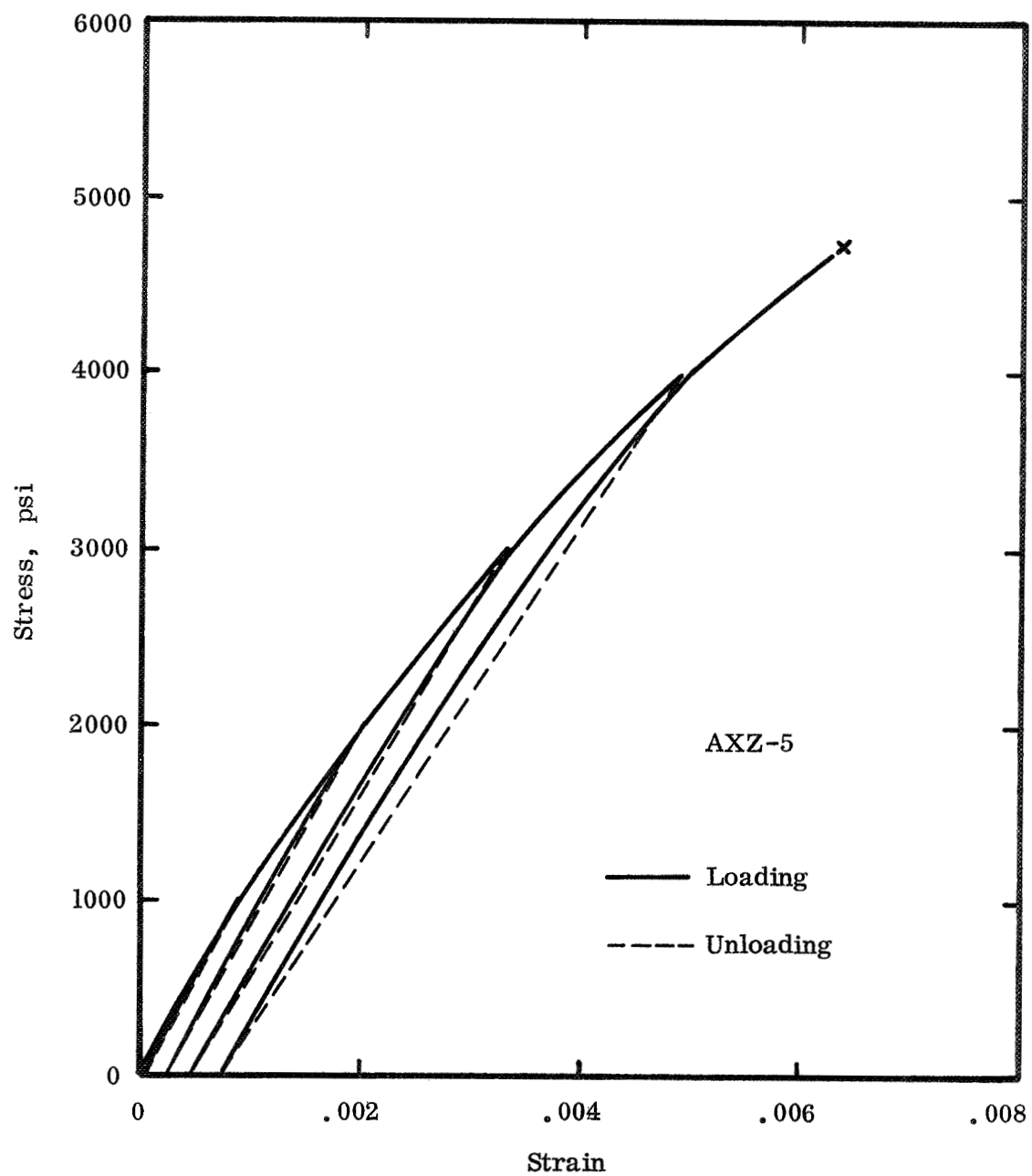


Figure 13. The longitudinal stress-strain curve of an AXZ graphite specimen with the tensile stress cyclically applied.

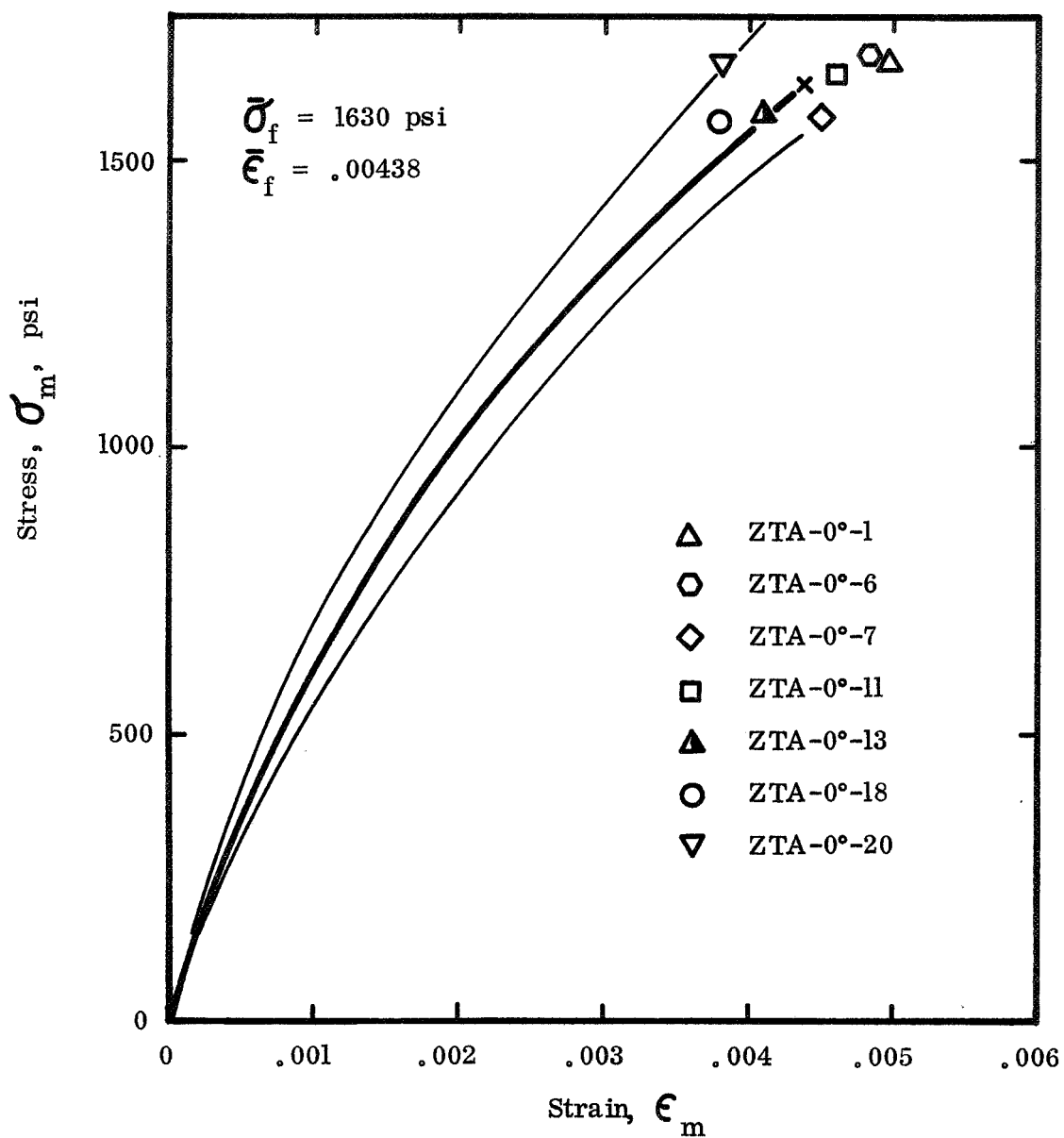


Figure 14. The average stress-strain curve for seven ZTA graphite specimens with the tensile stress applied parallel to the pressing direction.

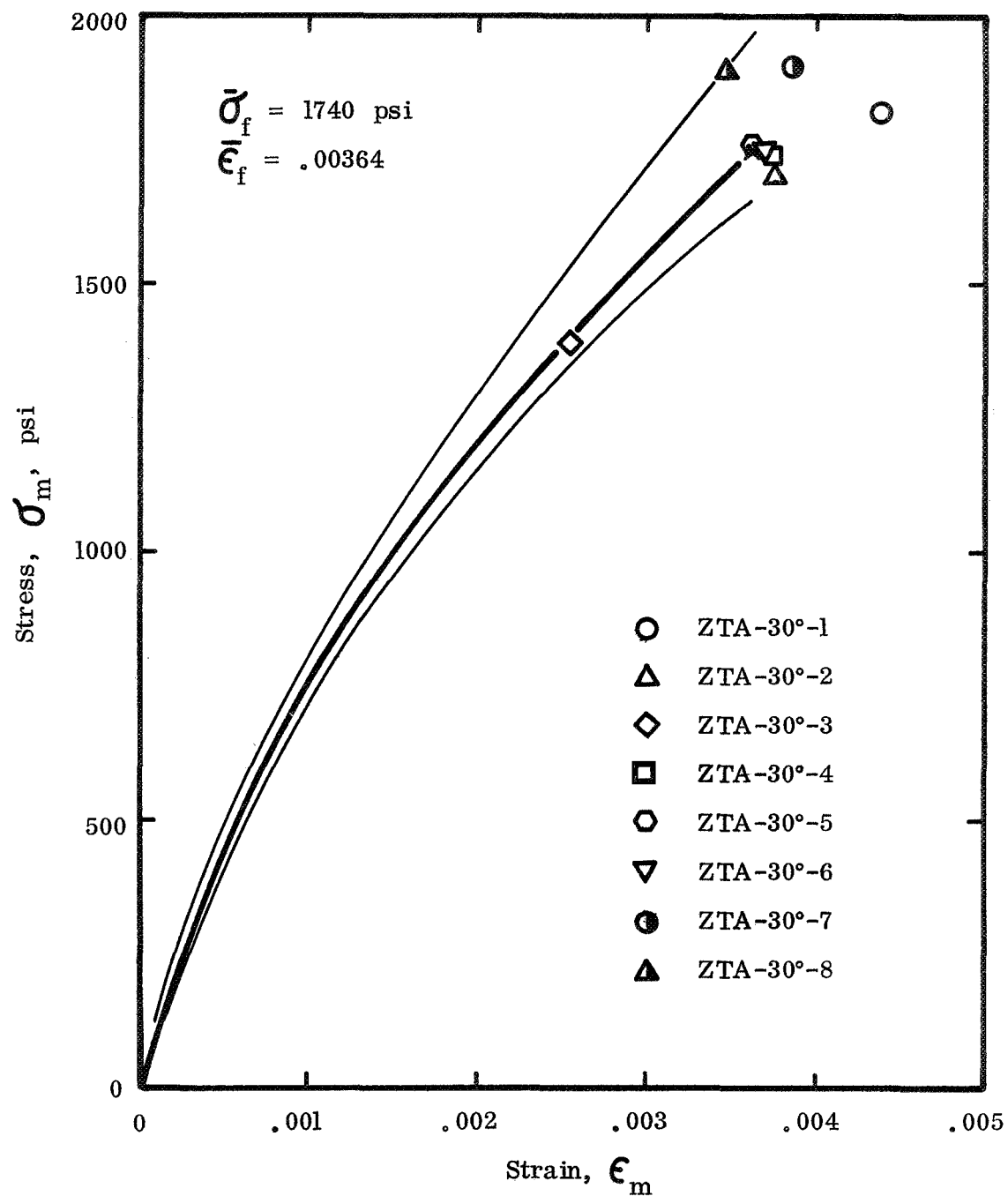


Figure 15. The average stress-strain curve for eight ZTA graphite specimens with the tensile stress applied 30° to the pressing direction.

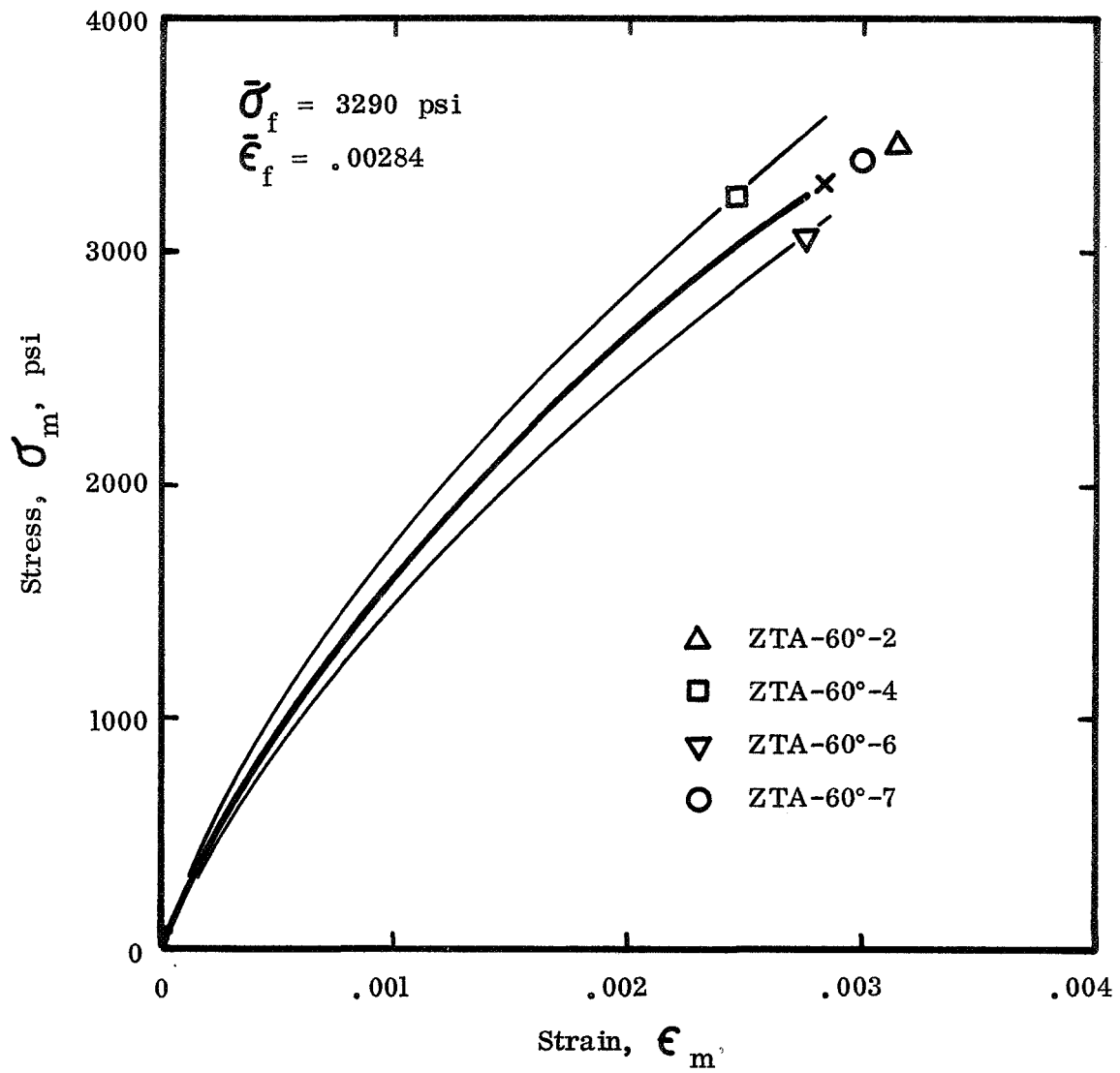


Figure 16. The average stress-strain curve for four ZTA graphite specimens with the tensile stress applied 60° to the pressing direction.

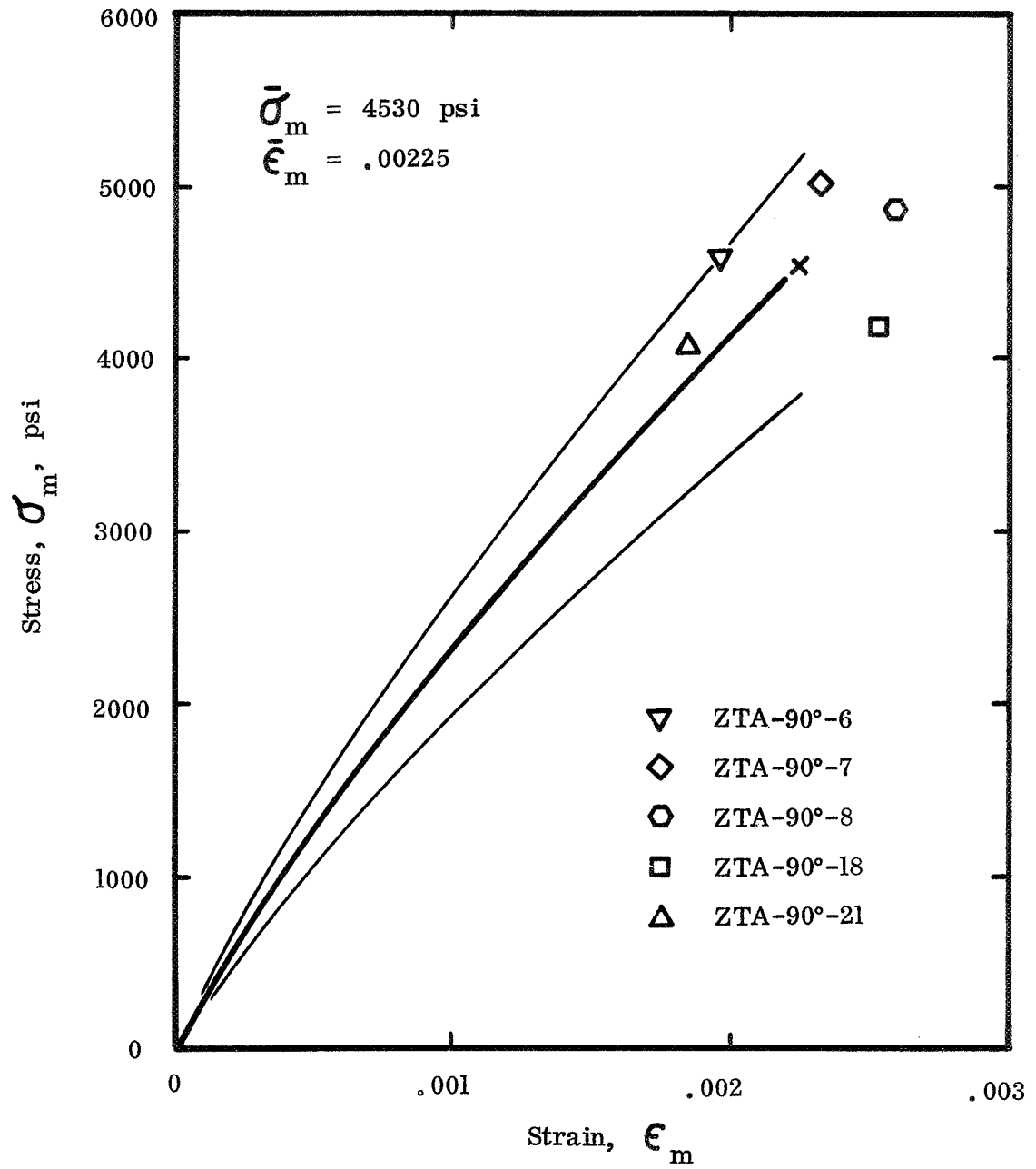


Figure 17. The average stress-strain curve for five ZTA graphite specimens with the tensile stress applied perpendicular to the pressing direction.

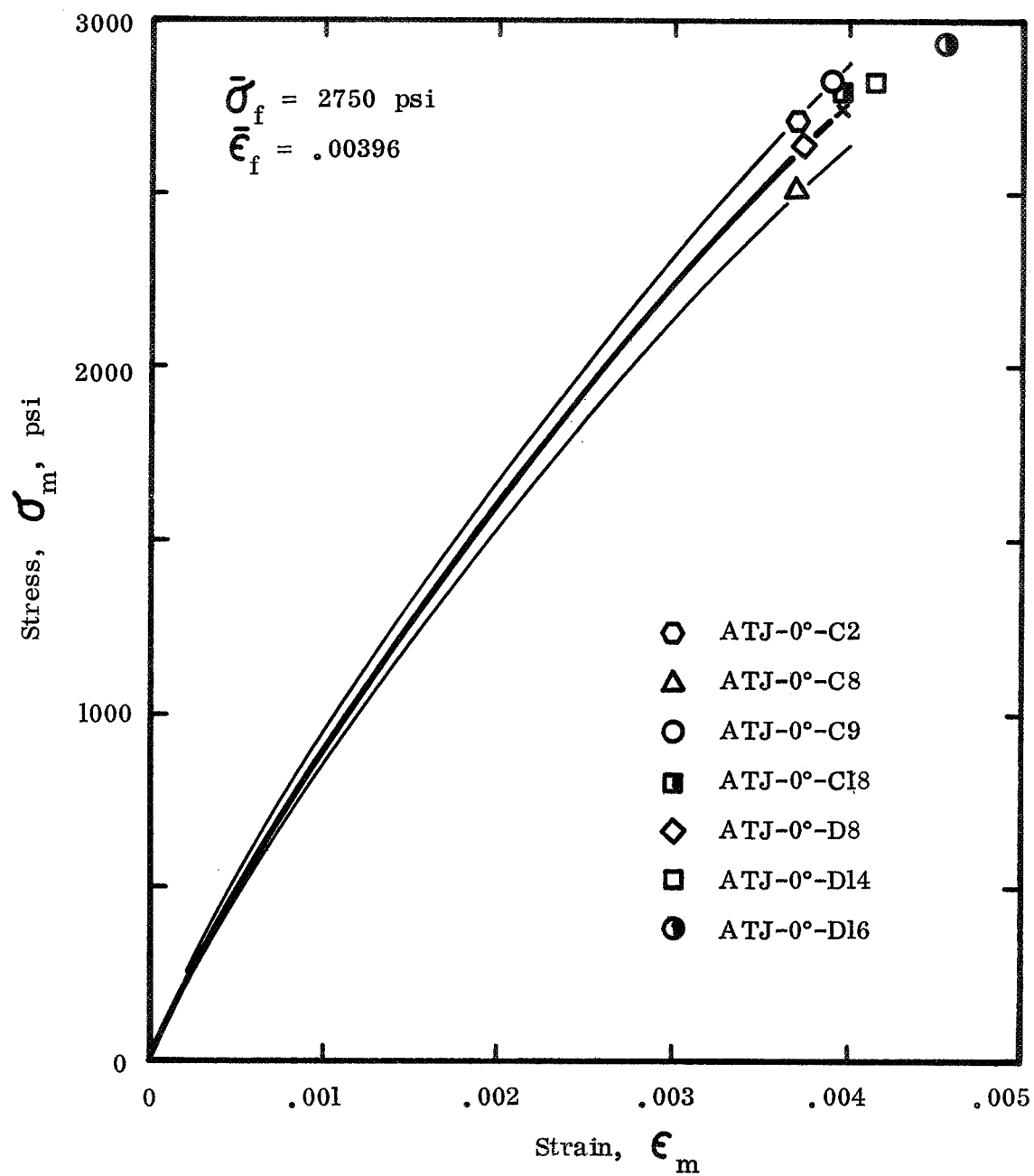


Figure 18. The average stress-strain curve for seven ATJ graphite specimens with the tensile stress applied parallel to the pressing direction.

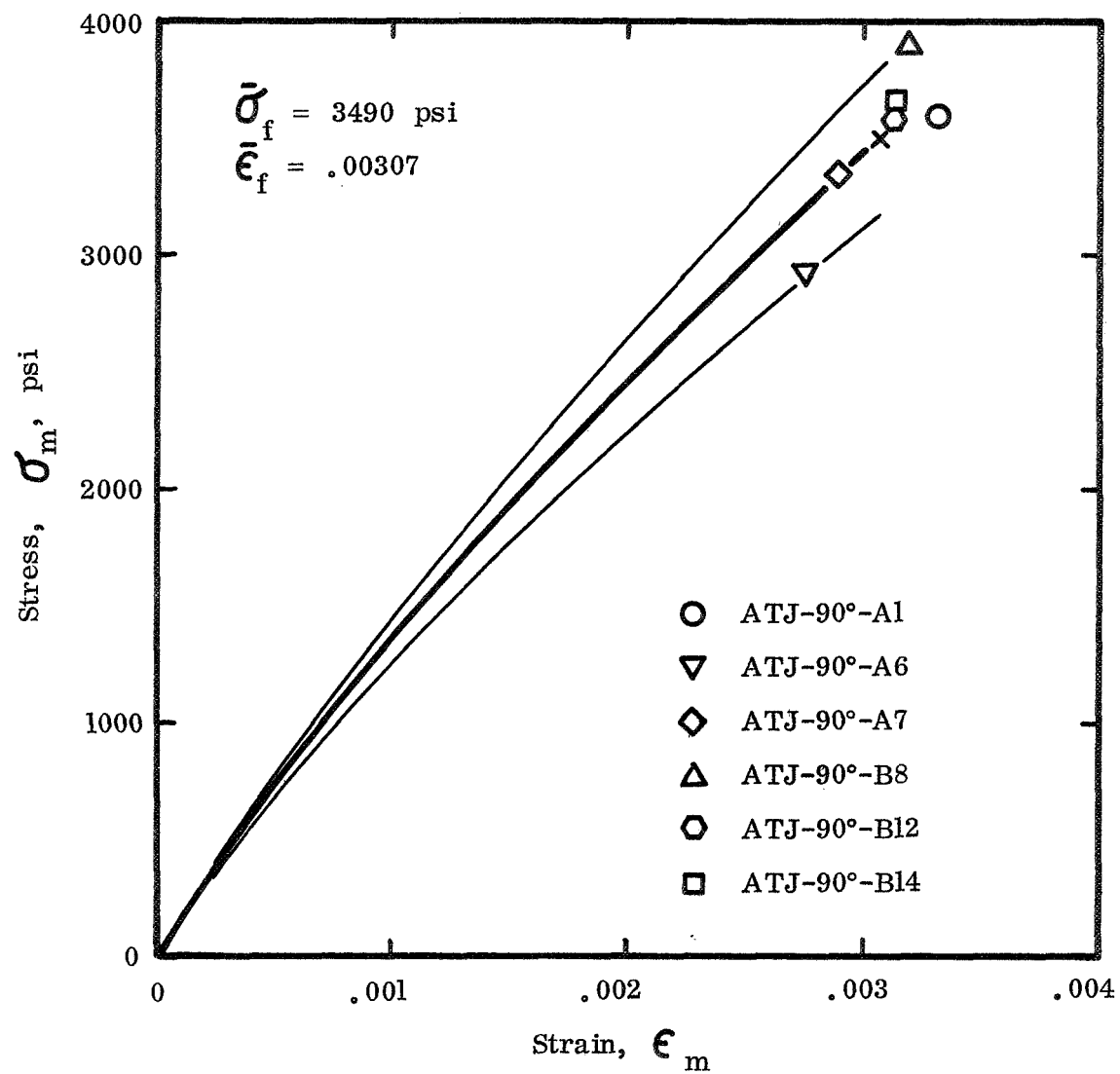


Figure 19. The average stress-strain curve for six ATJ graphite specimens with the tensile stress applied perpendicular to the pressing direction.

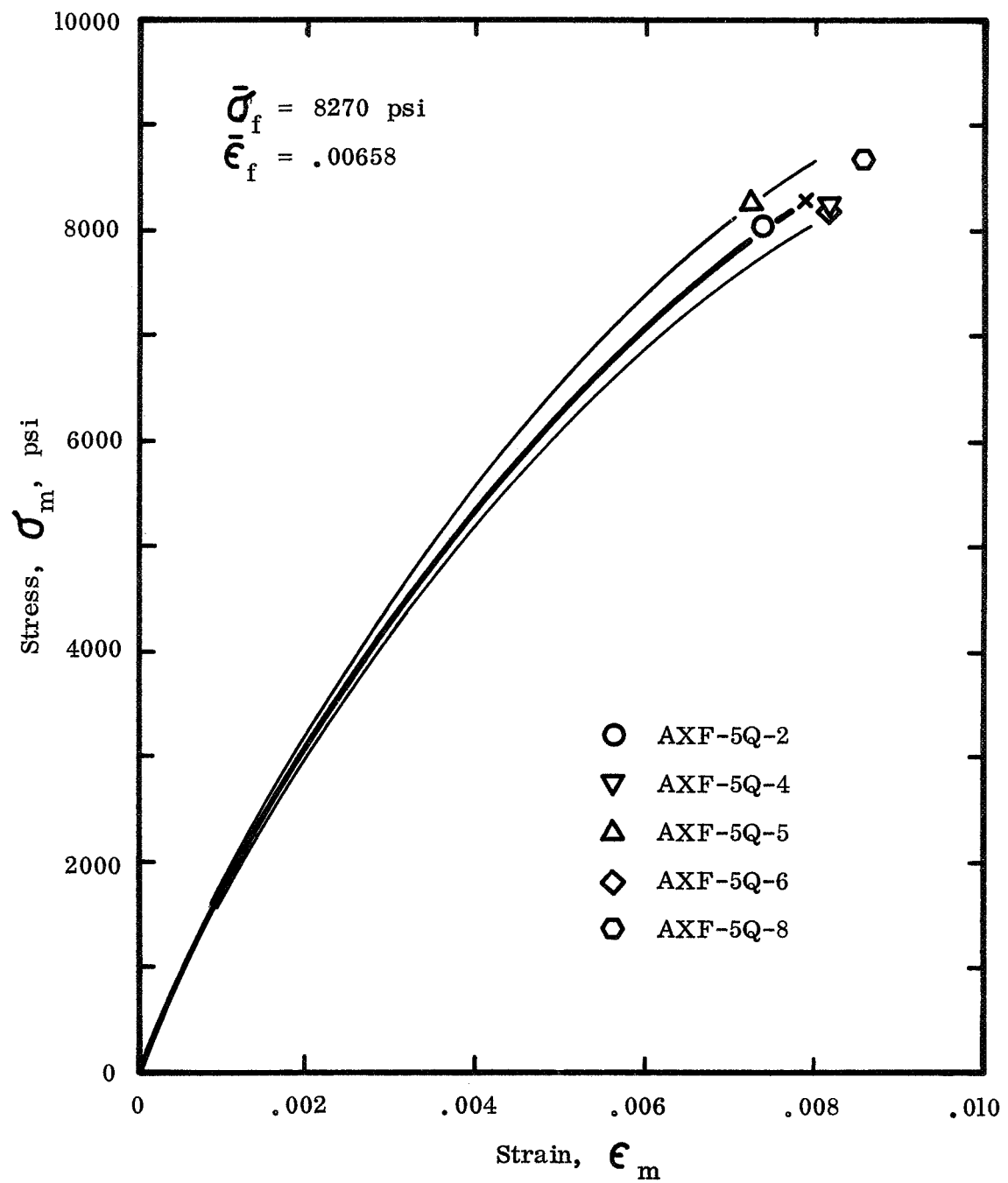


Figure 20. The average stress-strain curve for five AXF-5Q graphite specimens.

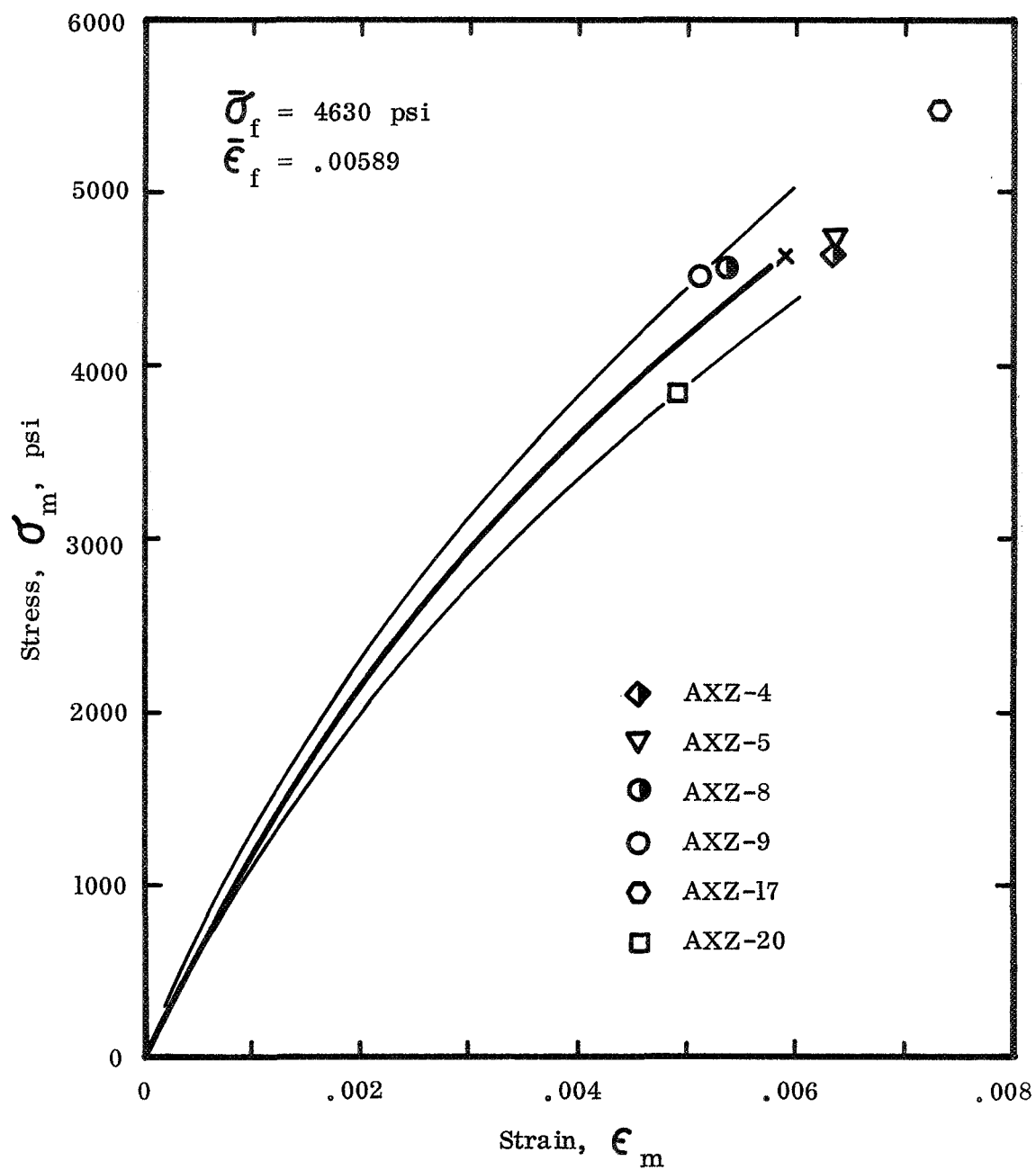


Figure 21. The average stress-strain curve for six AXZ graphite specimens.

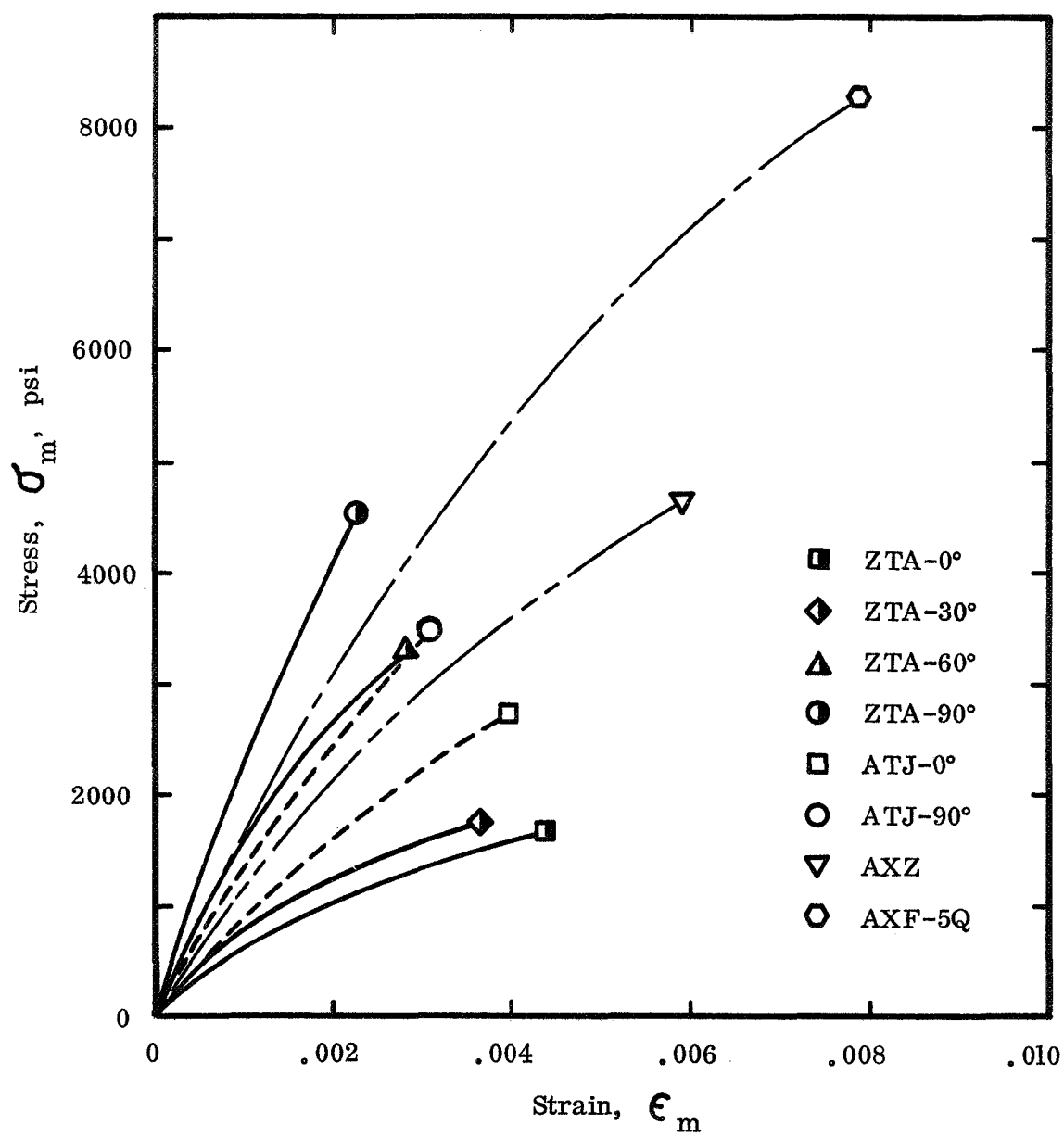


Figure 22. The average stress-strain curves of four commercial graphite grades.

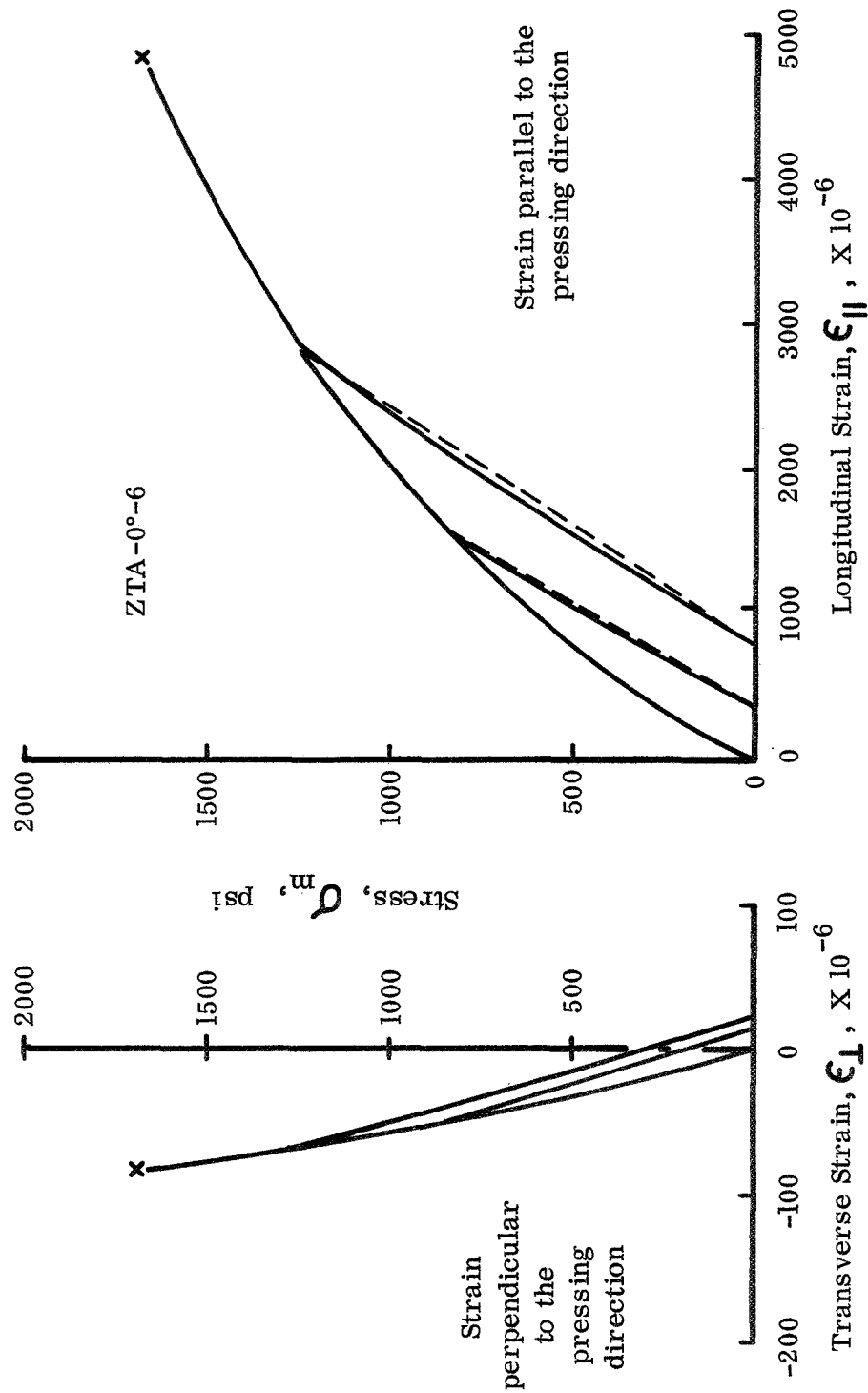


Figure 23. The longitudinal and transverse stress-strain curves of a ZTA graphite specimen with the tensile stress cyclically applied parallel to the pressing direction. The transverse strain was measured perpendicular to the pressing direction.

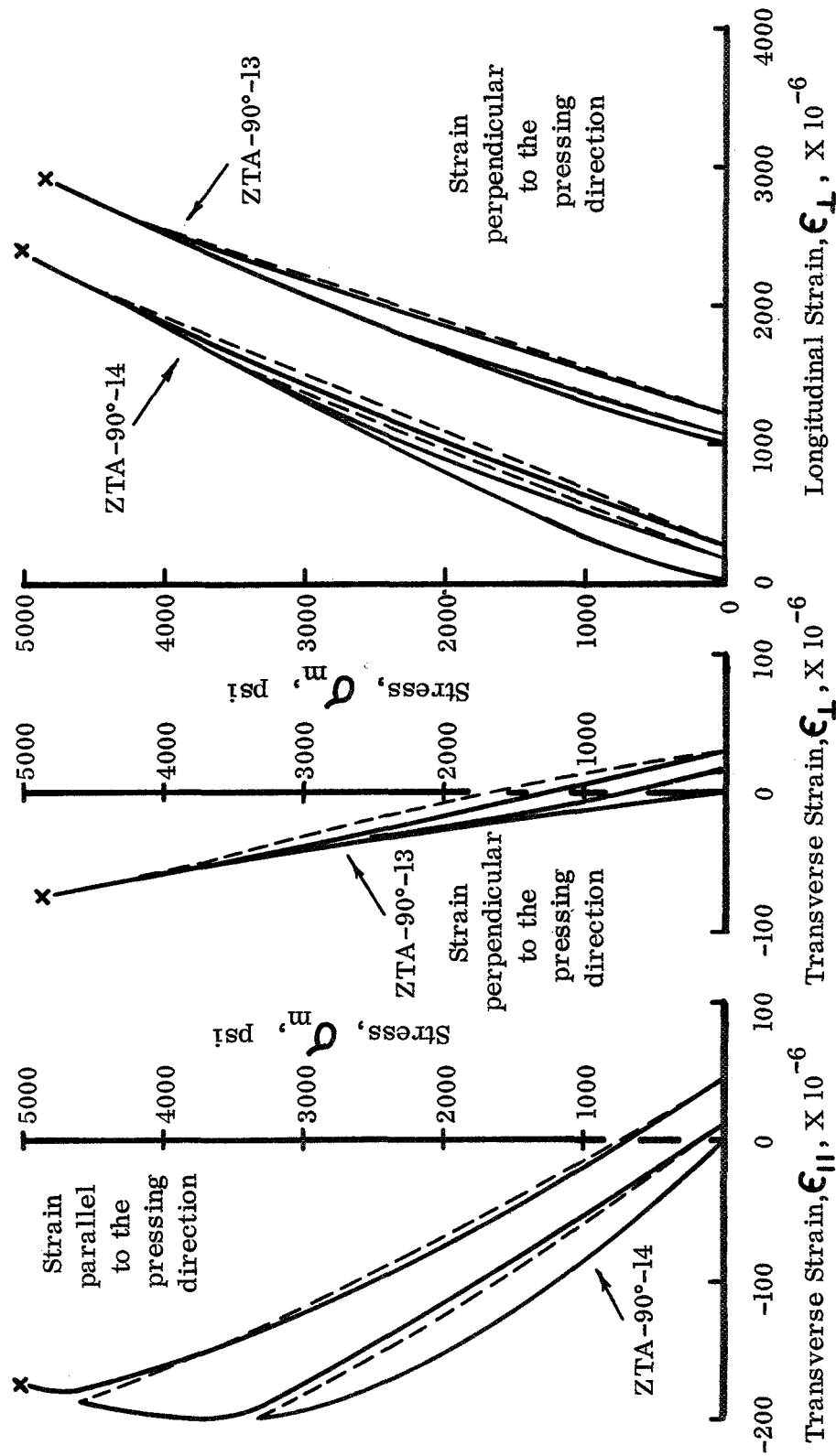


Figure 24. The longitudinal and transverse stress-strain curves of ZTA graphite specimens with the tensile stress cyclically applied perpendicular to the pressing direction. The transverse strain in the curve on the left was measured parallel to the pressing direction. The transverse strain in the curve in the middle was measured perpendicular to the pressing direction.

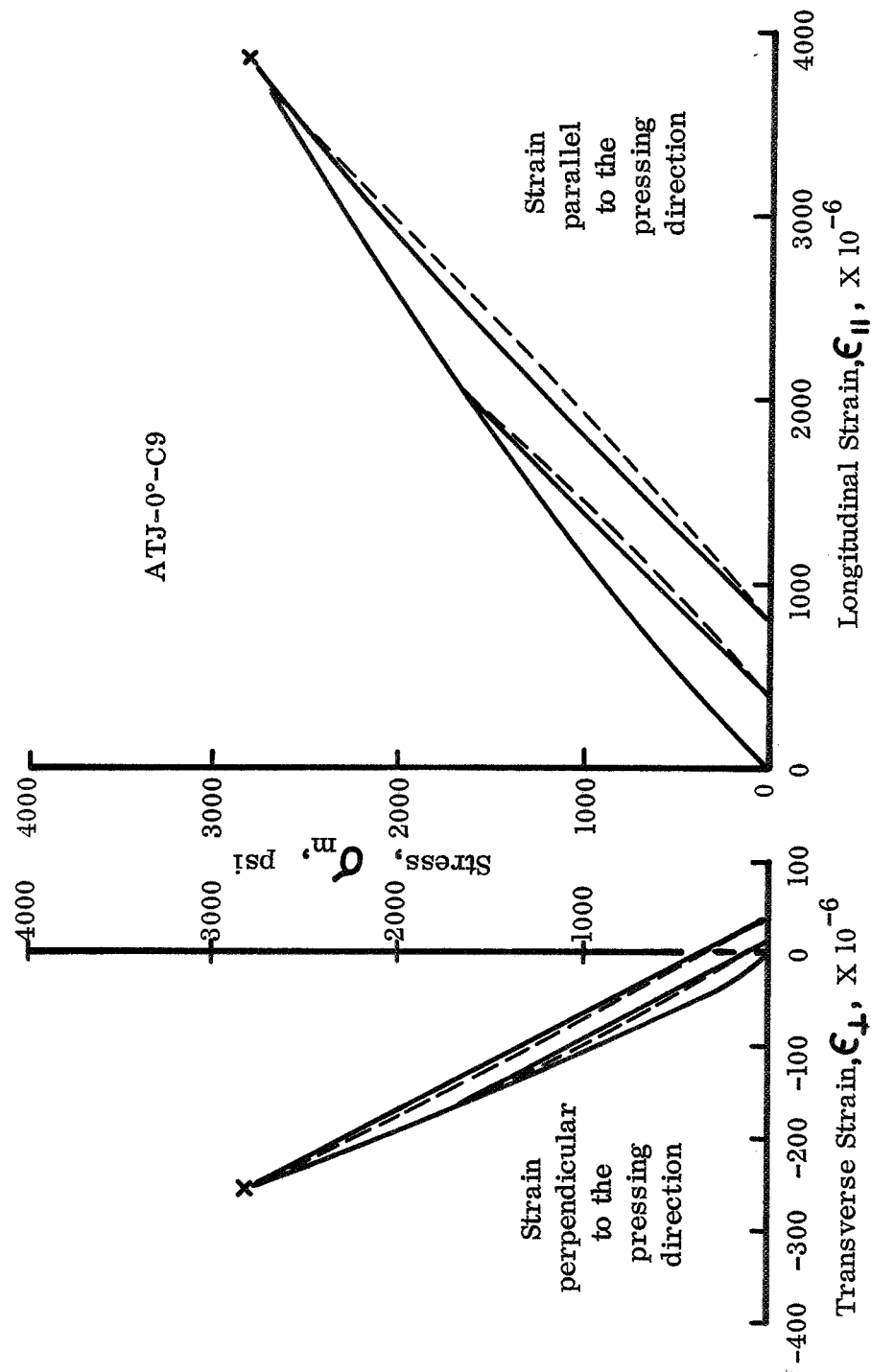


Figure 25. The longitudinal and transverse stress-strain curves of an ATJ graphite specimen with the tensile stress cyclically applied parallel to the pressing direction. The transverse strain was measured perpendicular to the pressing direction.

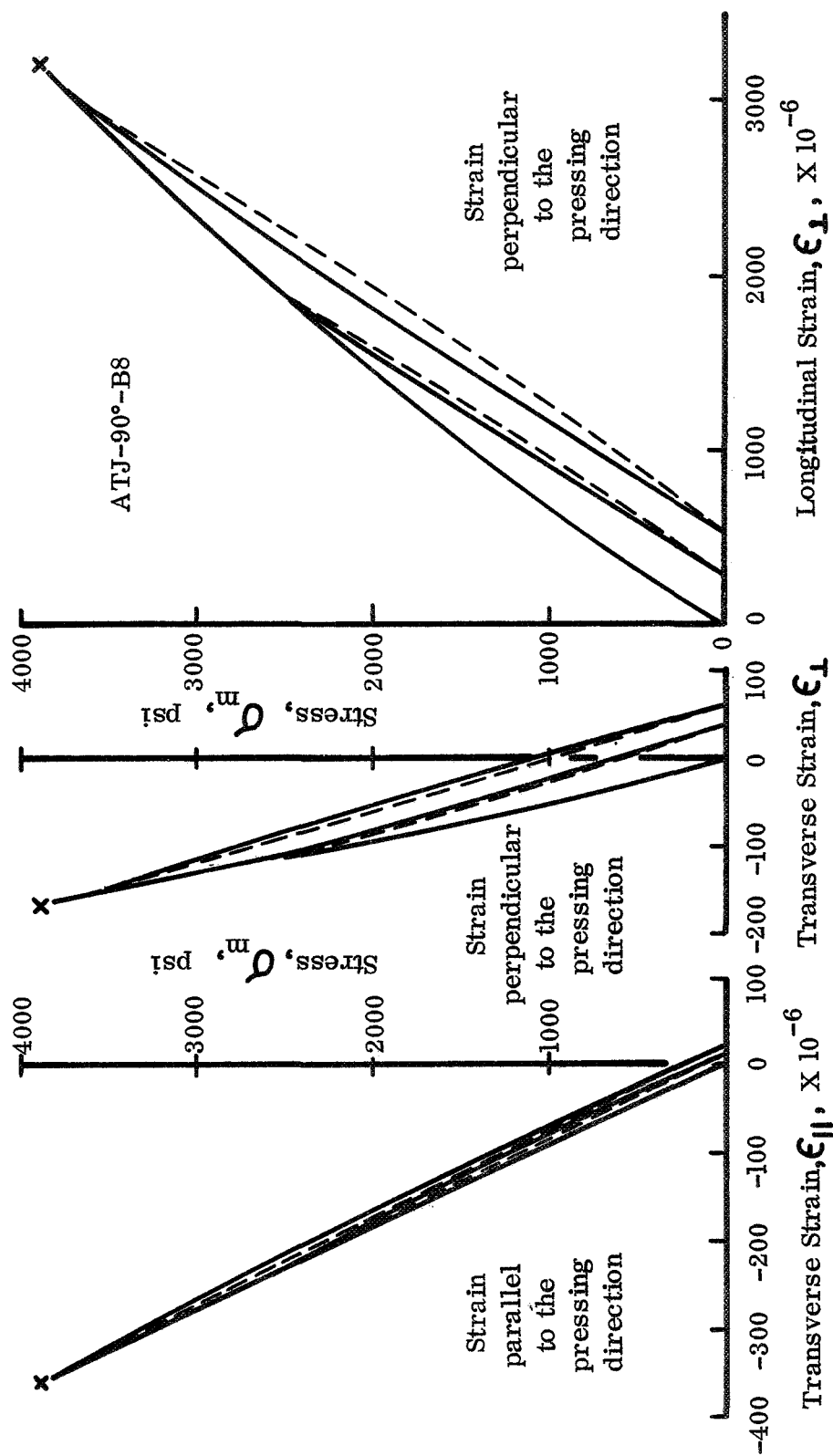


Figure 26. The longitudinal and transverse stress-strain curves of an ATJ graphite specimen with the tensile stress cyclically applied perpendicular to the pressing direction. The transverse strain in the curve on the left was measured parallel to the pressing direction. The transverse strain in the curve in the middle was measured perpendicular to the pressing direction.

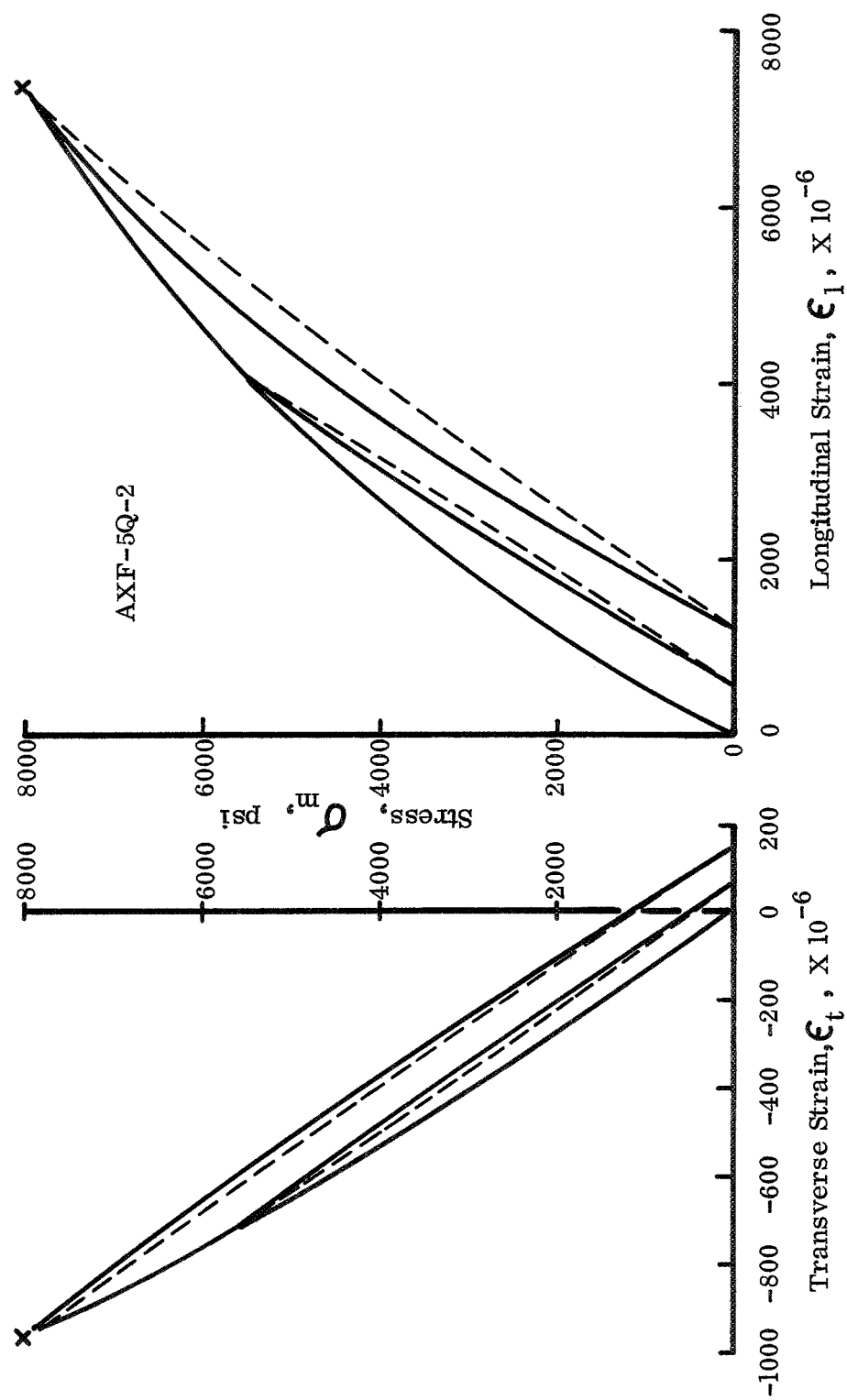


Figure 27. The longitudinal and transverse stress-strain curves of a AXF-5Q graphite specimen with the tensile stress cyclically applied.

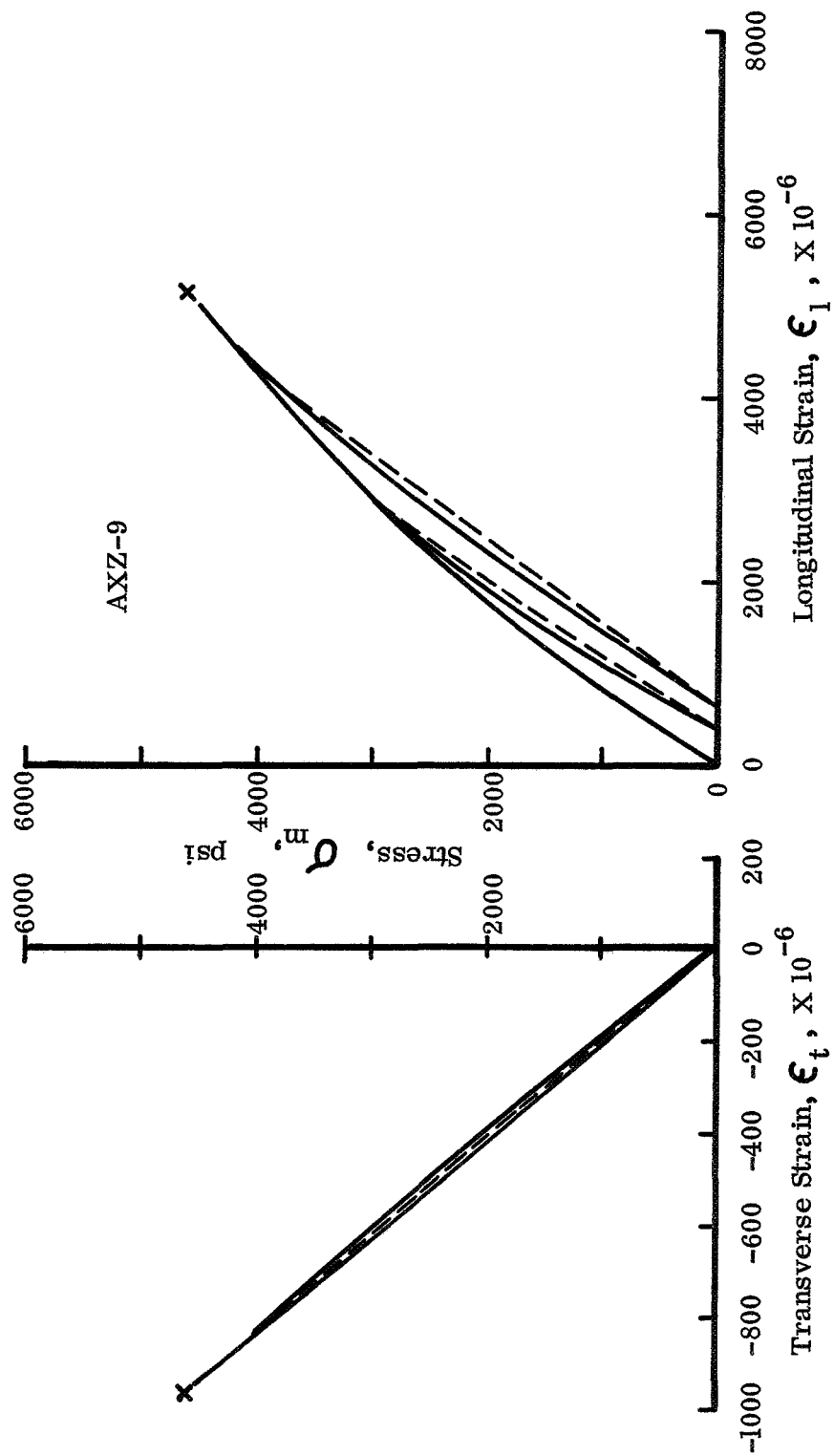


Figure 28. The longitudinal and transverse stress-strain curves of an AXZ graphite specimen with the tensile stress cyclically applied.

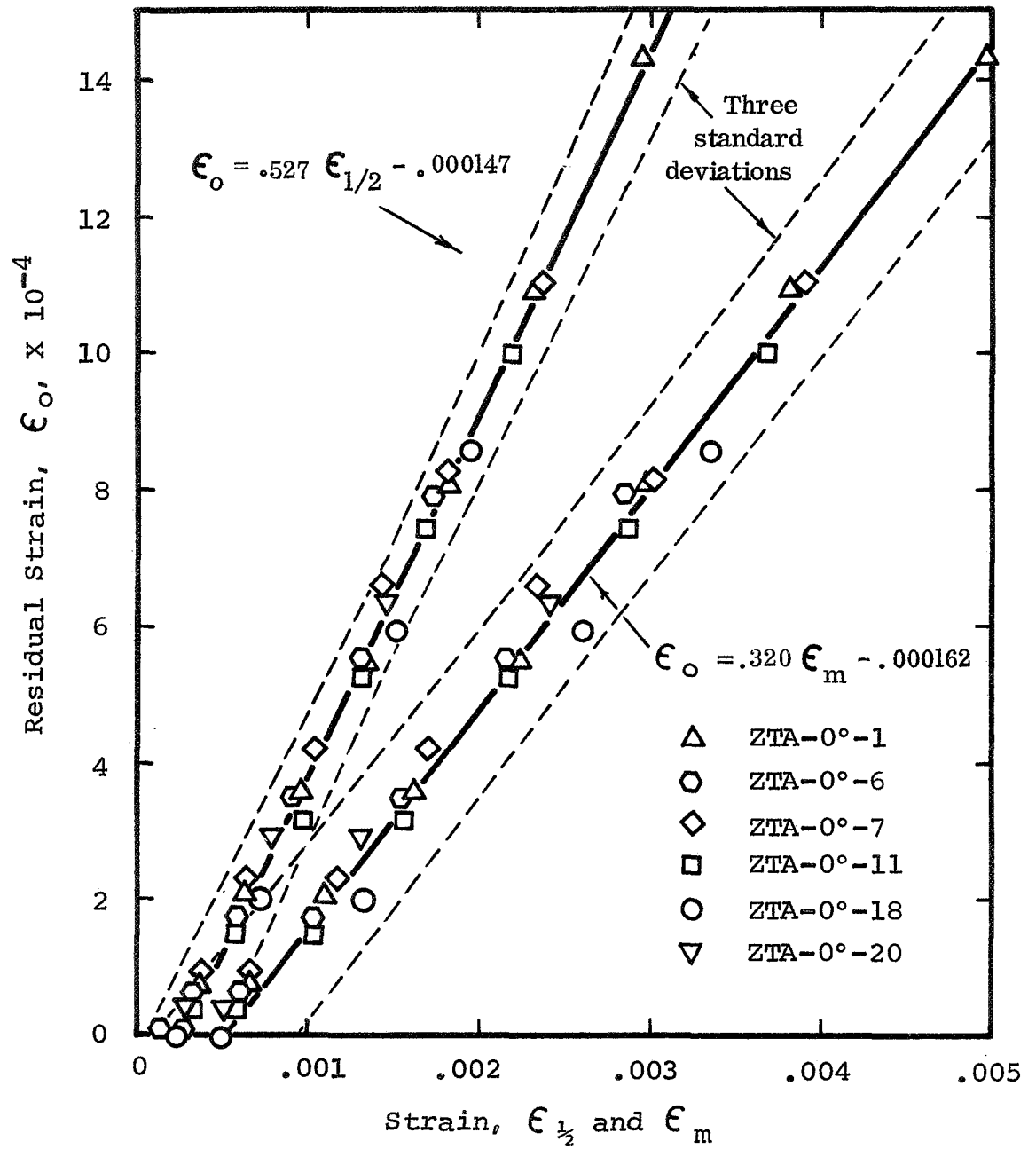


Figure 29. The relationships between the residual strain, ϵ_o , and: (a) the strain at the maximum stress per cycle, ϵ_m ; (b) the strain at half the maximum stress per cycle, $\epsilon_{1/2}$. ZTA graphite with the applied tensile stress parallel to the pressing direction.

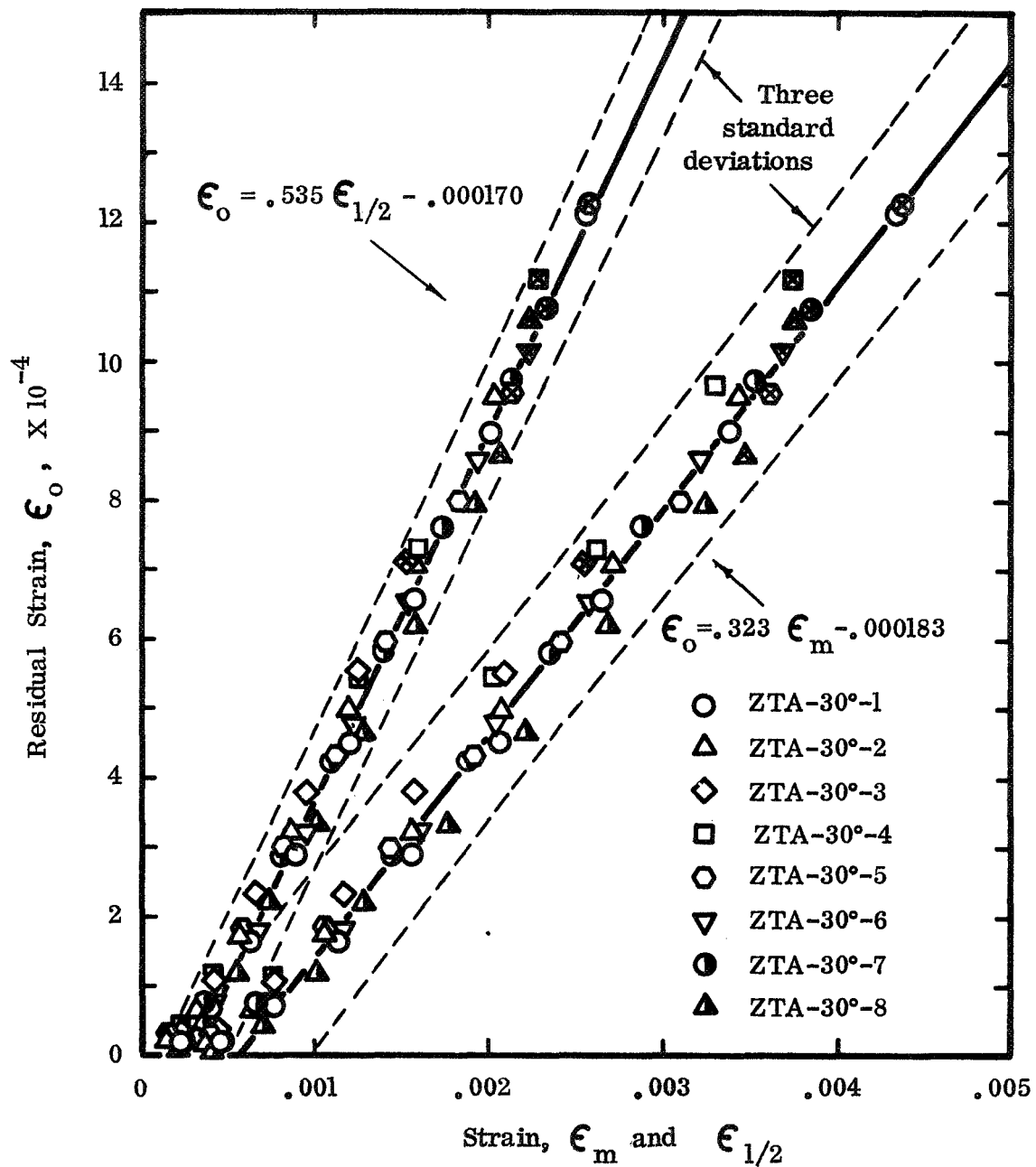


Figure 30. The relationships between the residual strain, ϵ_0 , and: (a) the strain at the maximum stress per cycle, ϵ_m ; (b) the strain at half the maximum stress per cycle, $\epsilon_{1/2}$. ZTA graphite with the applied tensile stress 30° to the pressing direction.

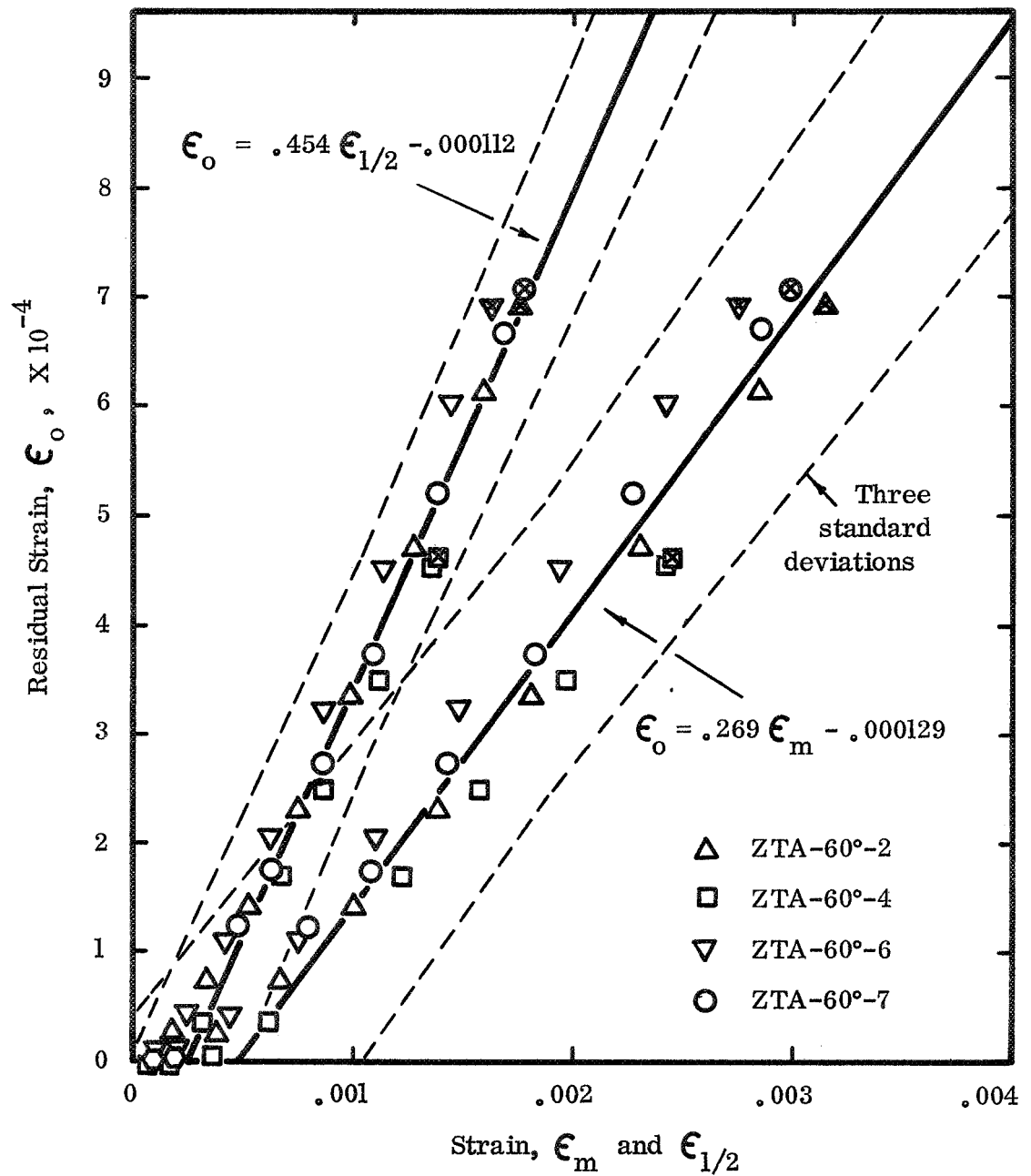


Figure 31. The relationships between the residual strain, ϵ_o , and: (a) the strain at the maximum stress per cycle, ϵ_m ; (b) the strain at half the maximum stress per cycle, $\epsilon_{1/2}$. ZTA graphite with the applied loading stress 60° to the pressing direction.

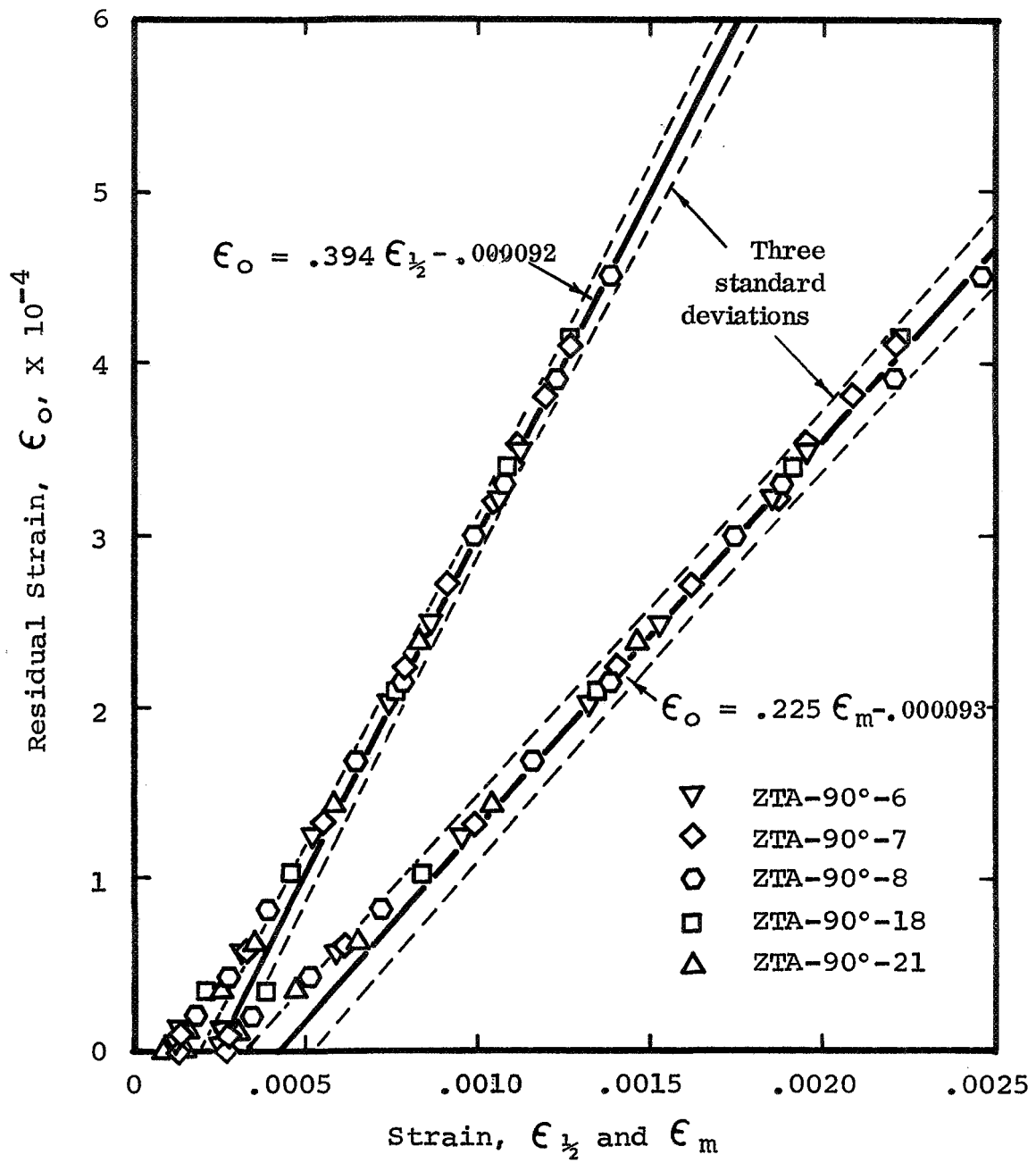


Figure 32. The relationships between the residual strain, ϵ_o , and: (a) the strain at the maximum stress per cycle, ϵ_m ; (b) the strain at half the maximum stress per cycle, $\epsilon_{1/2}$. ZTA graphite with the applied tensile stress perpendicular to the pressing direction.

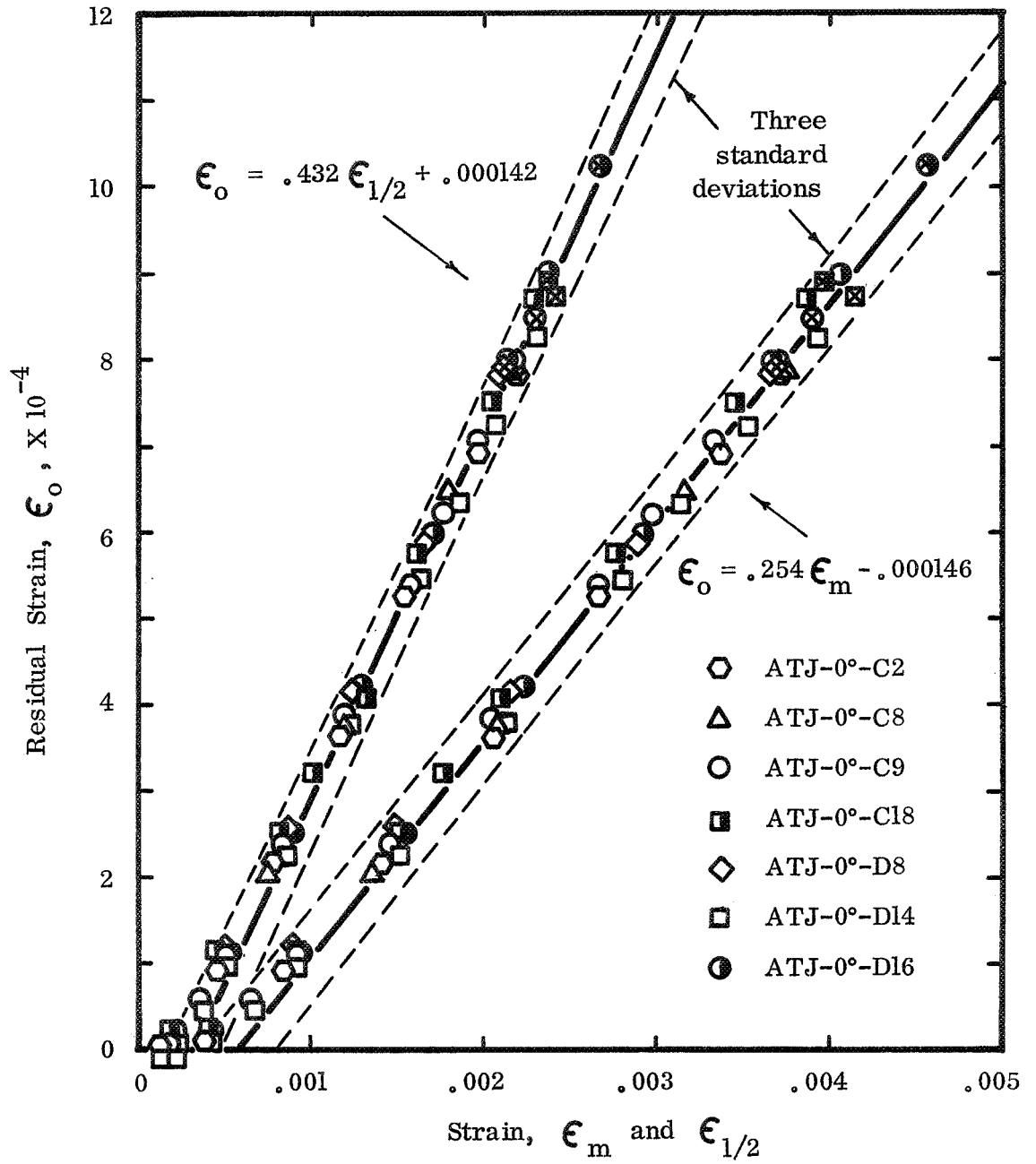


Figure 33. The relationships between the residual strain, ϵ_o , and: (a) the strain at the maximum stress per cycle, ϵ_m ; (b) the strain at half the maximum stress per cycle, $\epsilon_{1/2}$. ATJ graphite with the applied tensile stress parallel to the pressing direction.

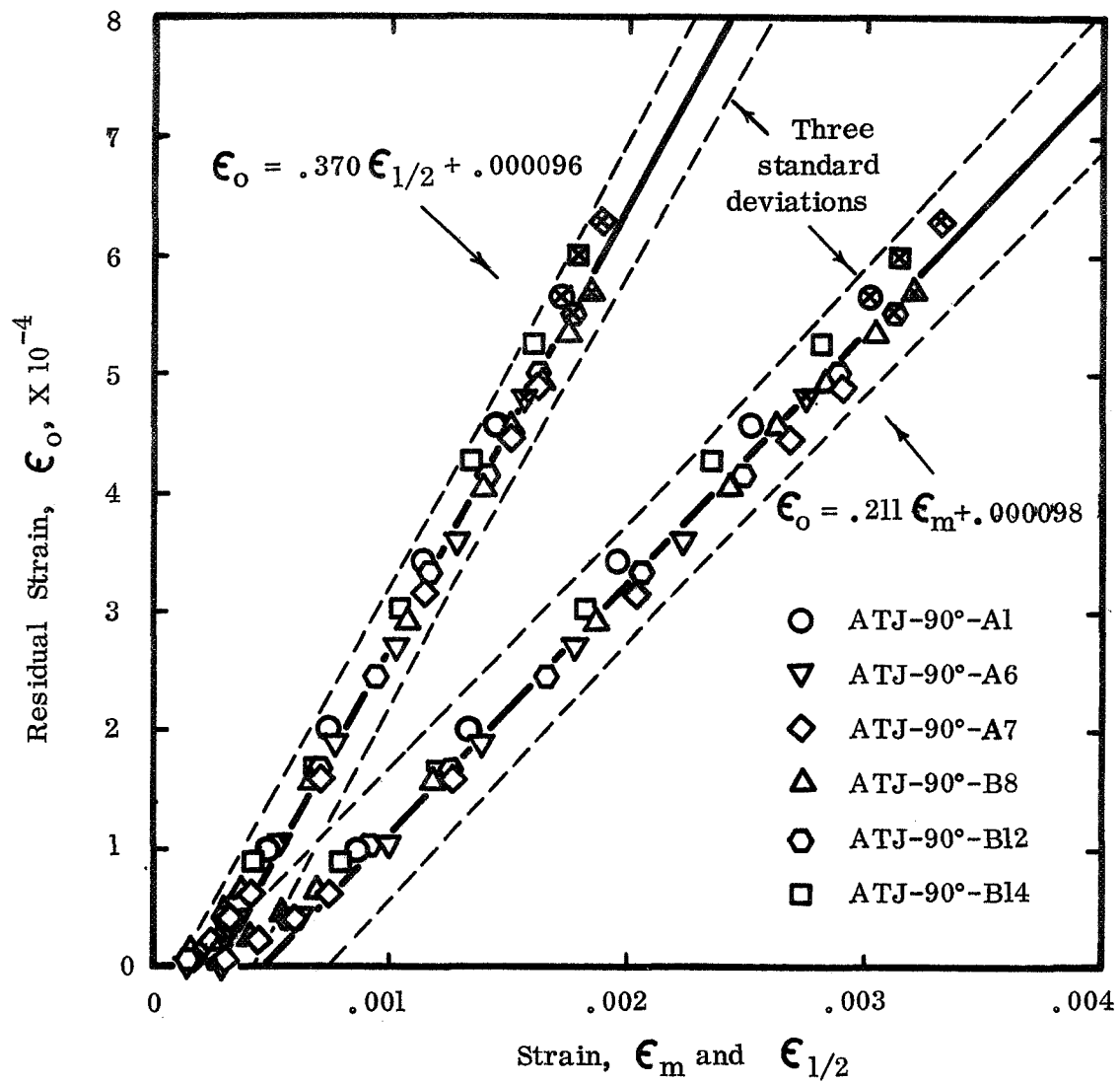


Figure 34. The relationships between the residual strain, ϵ_0 , and: (a) the strain at the maximum stress per cycle, ϵ_m ; (b) the strain at half the maximum stress per cycle, $\epsilon_{1/2}$. ATJ graphite with the applied tensile stress perpendicular to the pressing direction.

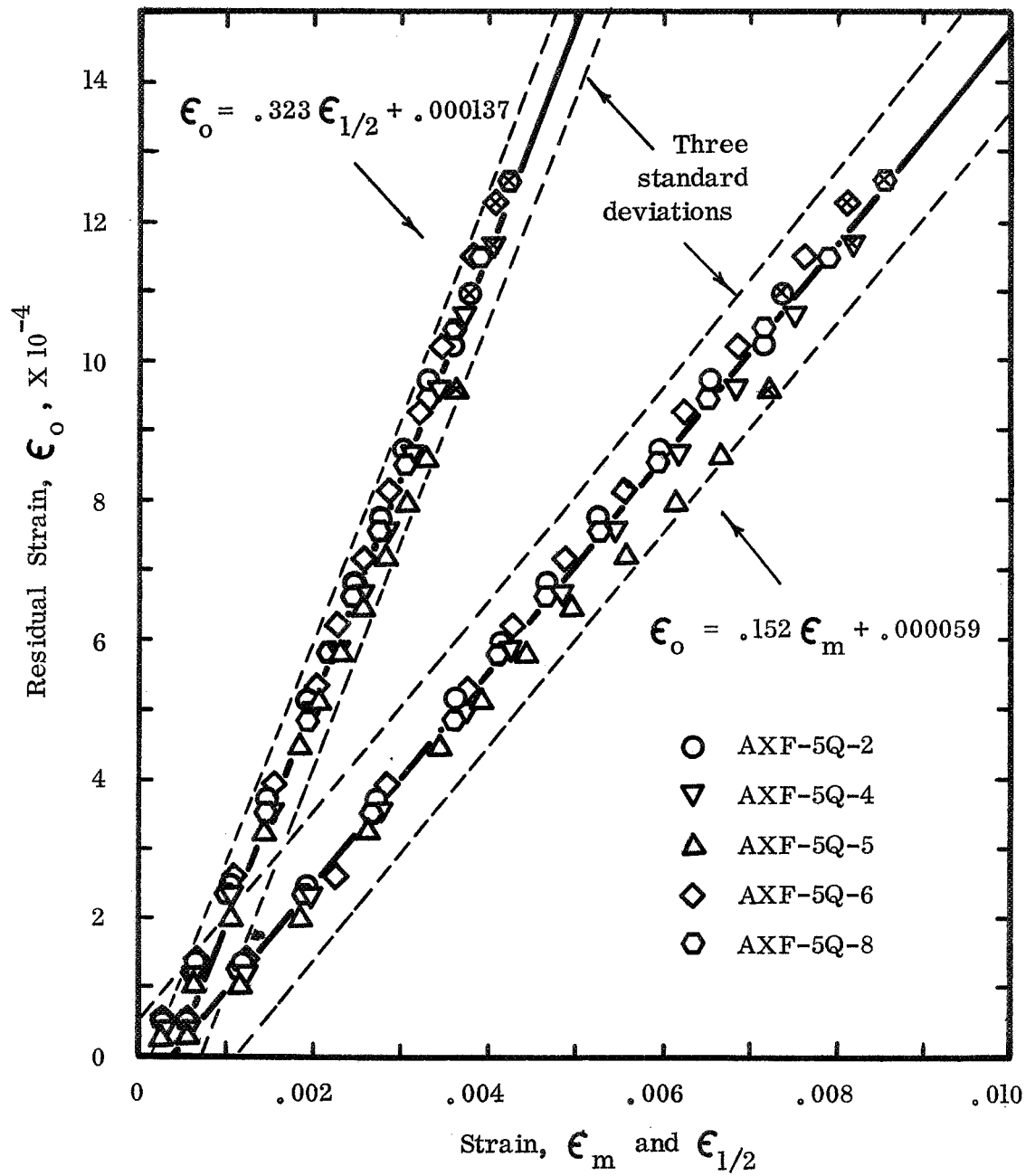


Figure 35. The relationships between the residual strain, ϵ_o , and: (a) the strain at the maximum stress per cycle, ϵ_m ; (b) the strain at half the maximum stress per cycle, $\epsilon_{1/2}$. AXF-5Q graphite.

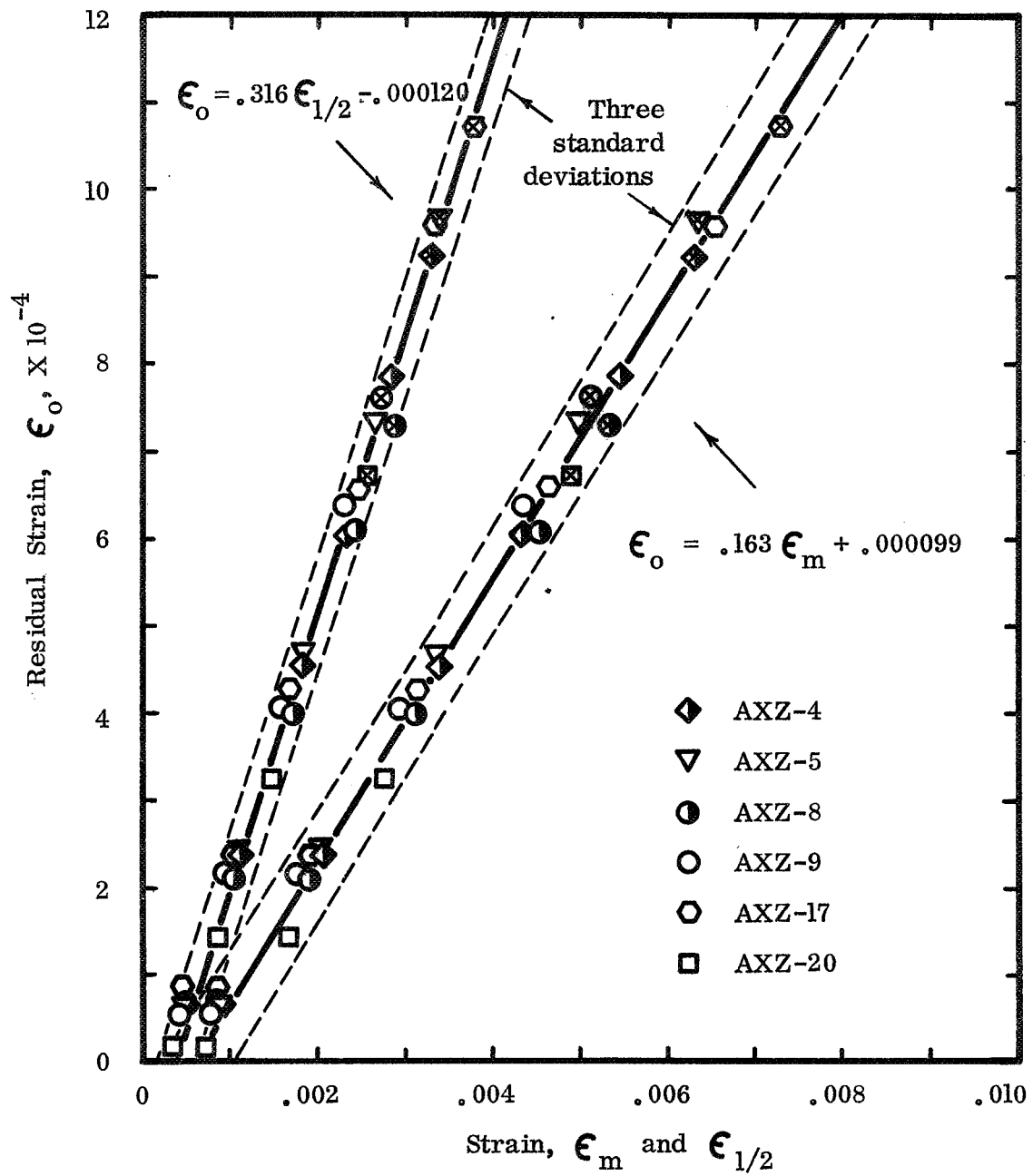


Figure 36. The relationships between the residual strain, ϵ_o , and: (a) the strain at the maximum stress per cycle, ϵ_m ; (b) the strain at half the maximum stress per cycle, $\epsilon_{1/2}$. AXZ graphite.

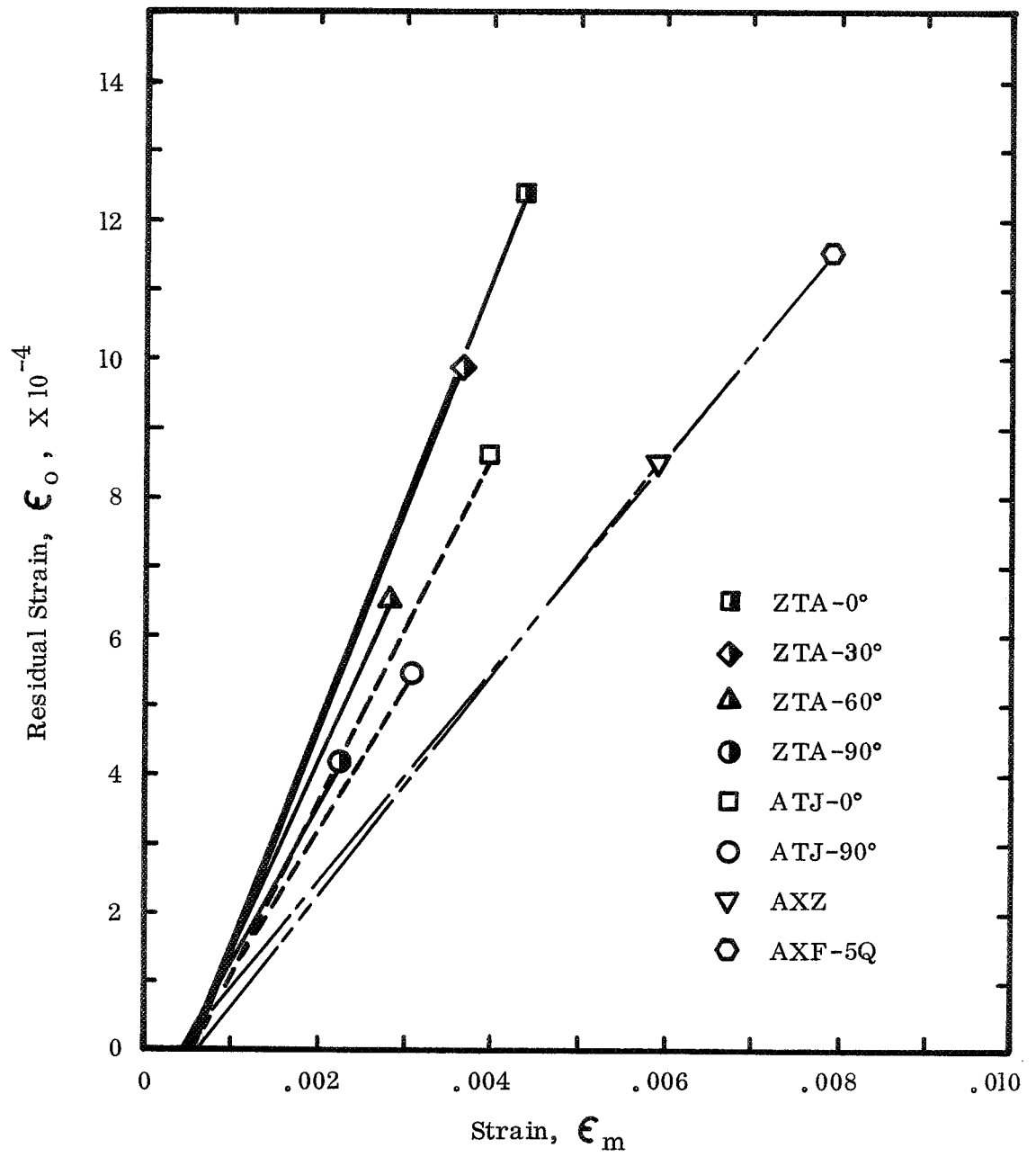


Figure 37. The relationships between the residual strains, ϵ_0 , and the strains at the maximum stresses per cycle, ϵ_m , for several graphite grades and orientations.

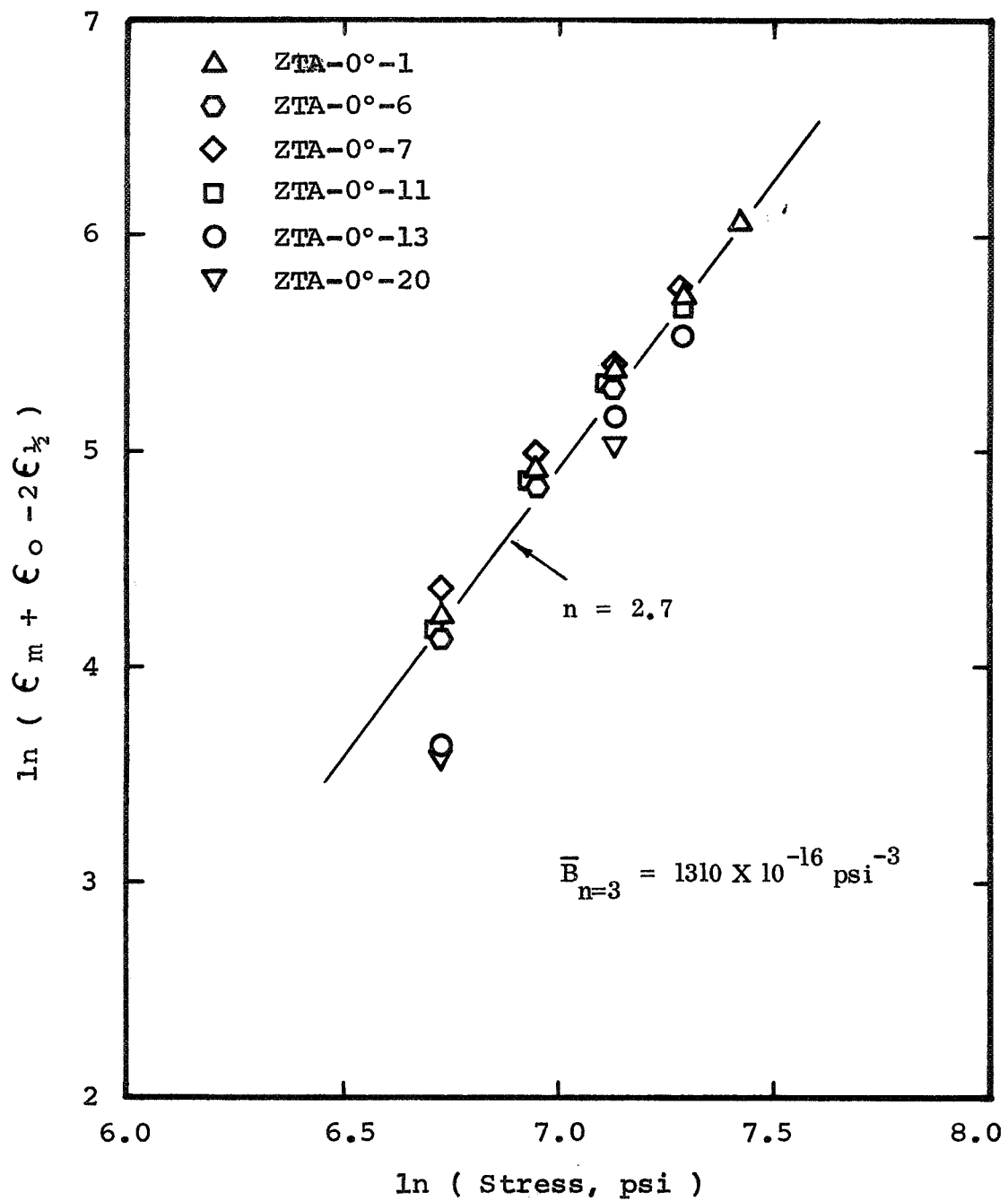


Figure 38. The stress dependence of the nonlinear strain component, ϵ_{pin} , for ZTA graphite stressed parallel to the pressing direction.

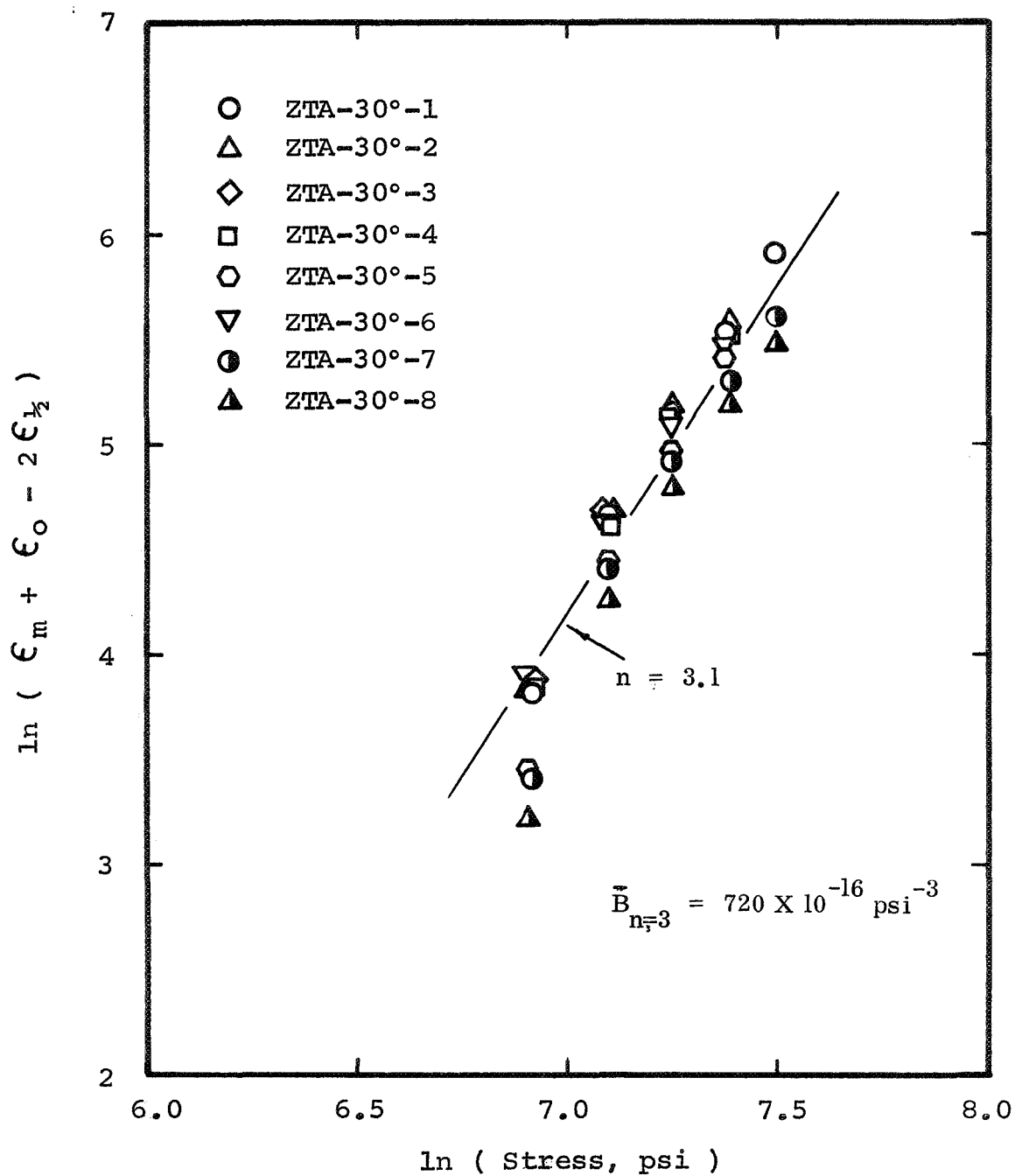


Figure 39. The stress dependence of the nonlinear strain component, ϵ_{pm} , for ZTA graphite stressed 30° to the pressing direction.

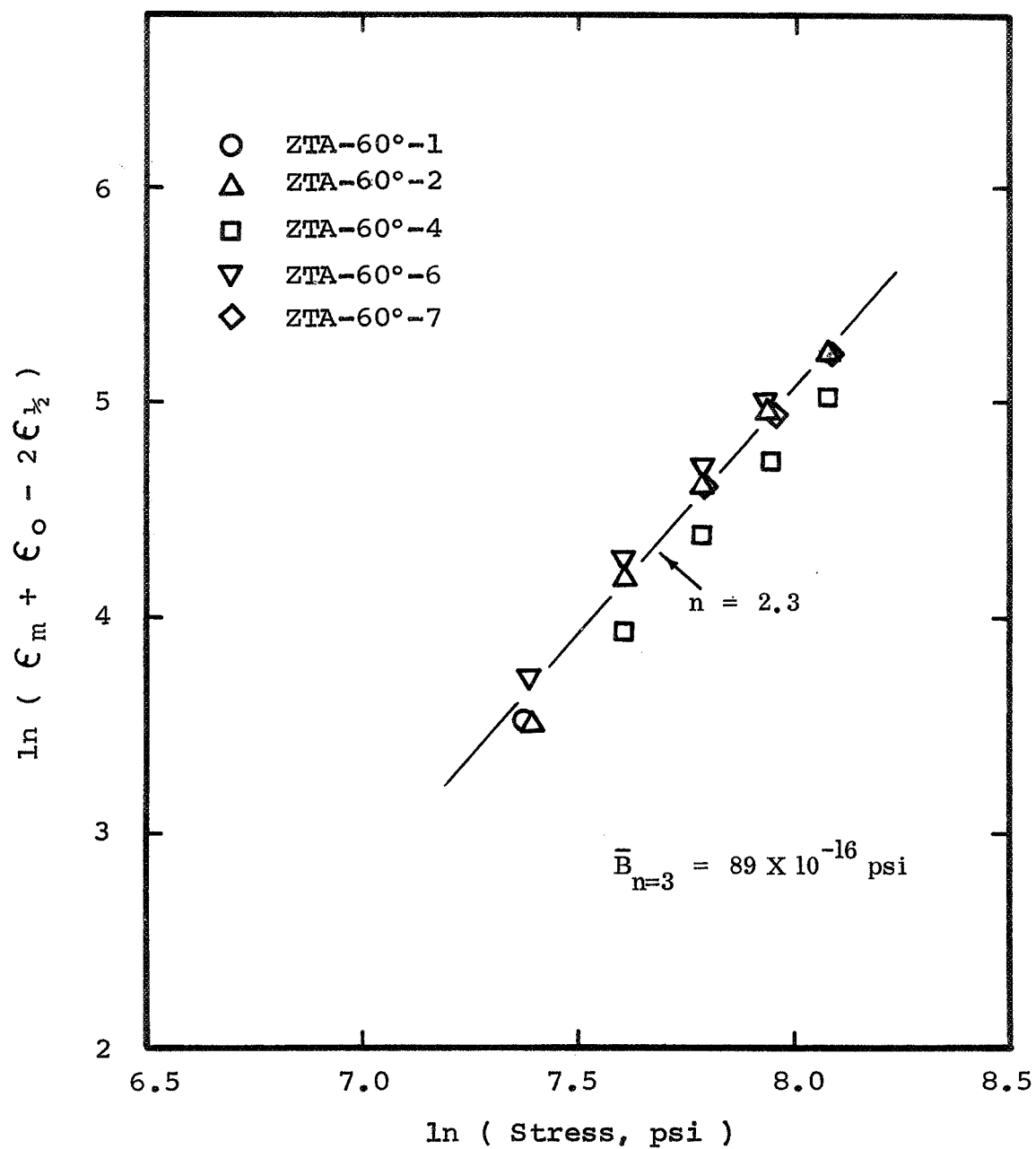


Figure 40. The stress dependence of the nonlinear strain component, ϵ_{pm} , for ZTA graphite stressed 60° to the pressing direction.

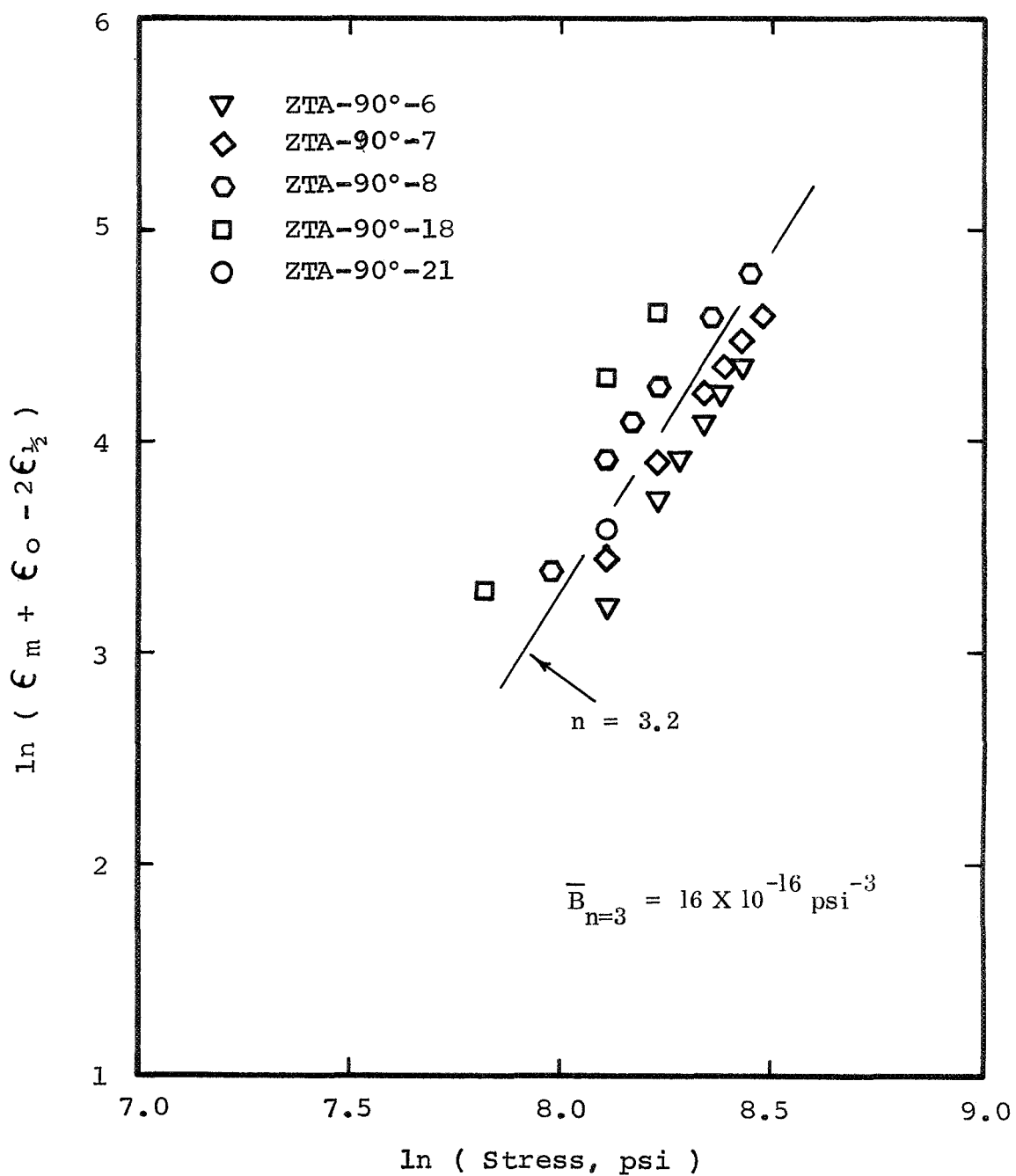


Figure 41. The stress dependence of the nonlinear strain component, ϵ_{pm} , for ZTA graphite stressed perpendicular to the pressing direction.

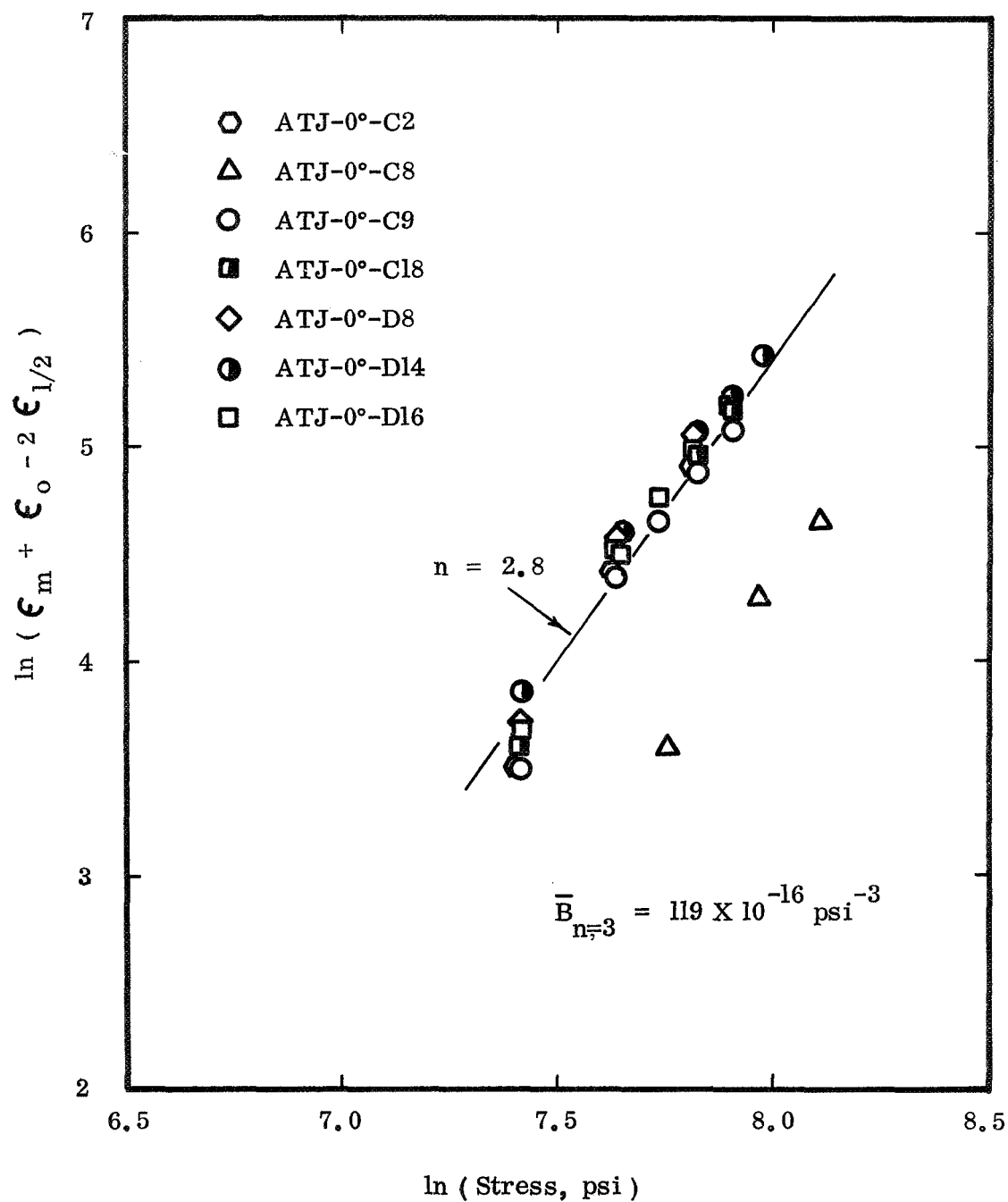


Figure 42. The stress dependence of the nonlinear strain component, ϵ_{pm} , for ATJ graphite stressed parallel to the pressing direction.

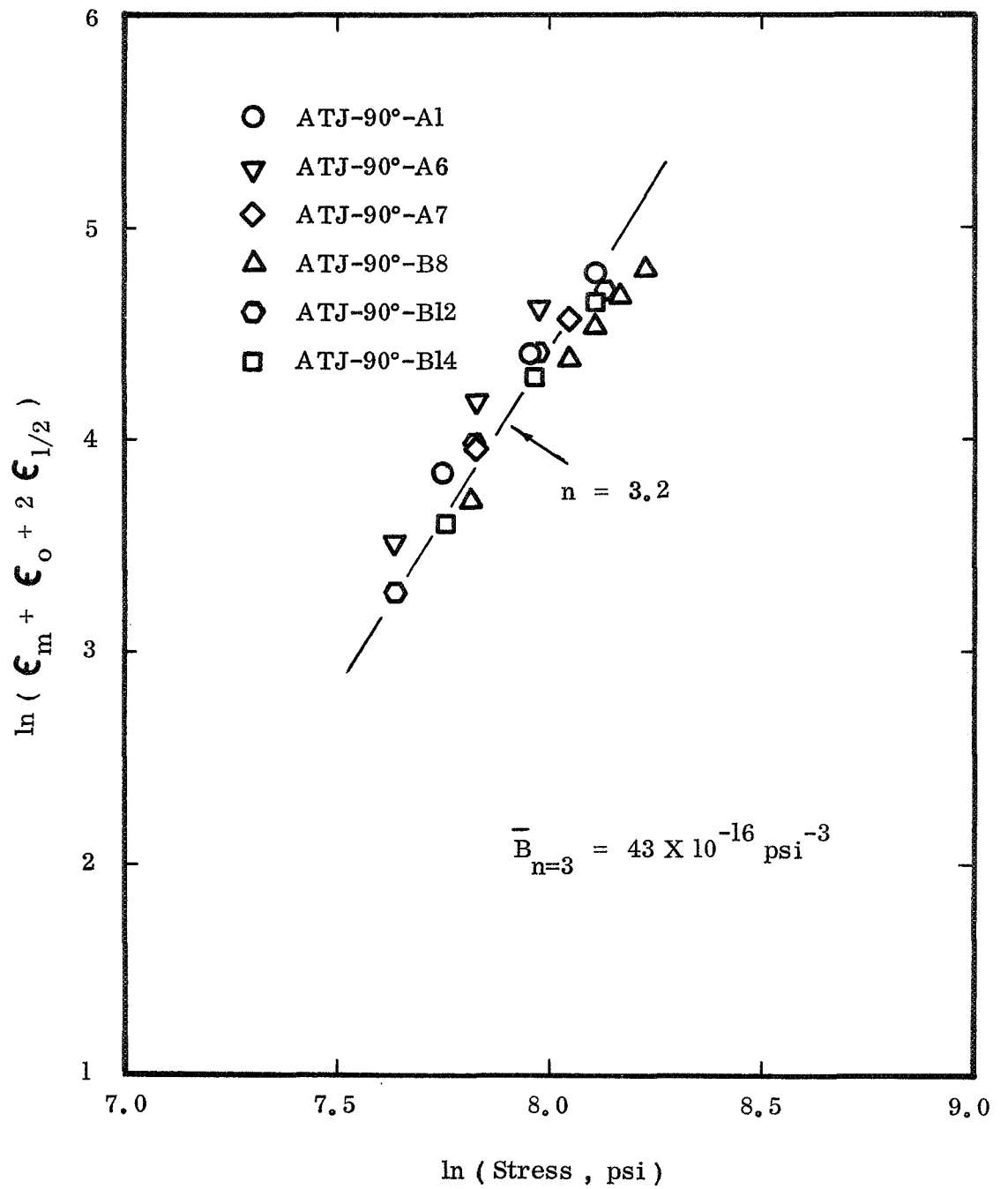


Figure 43. The stress dependence of the nonlinear strain component, ϵ_{pm} , for ATJ graphite stressed perpendicular to the pressing direction.

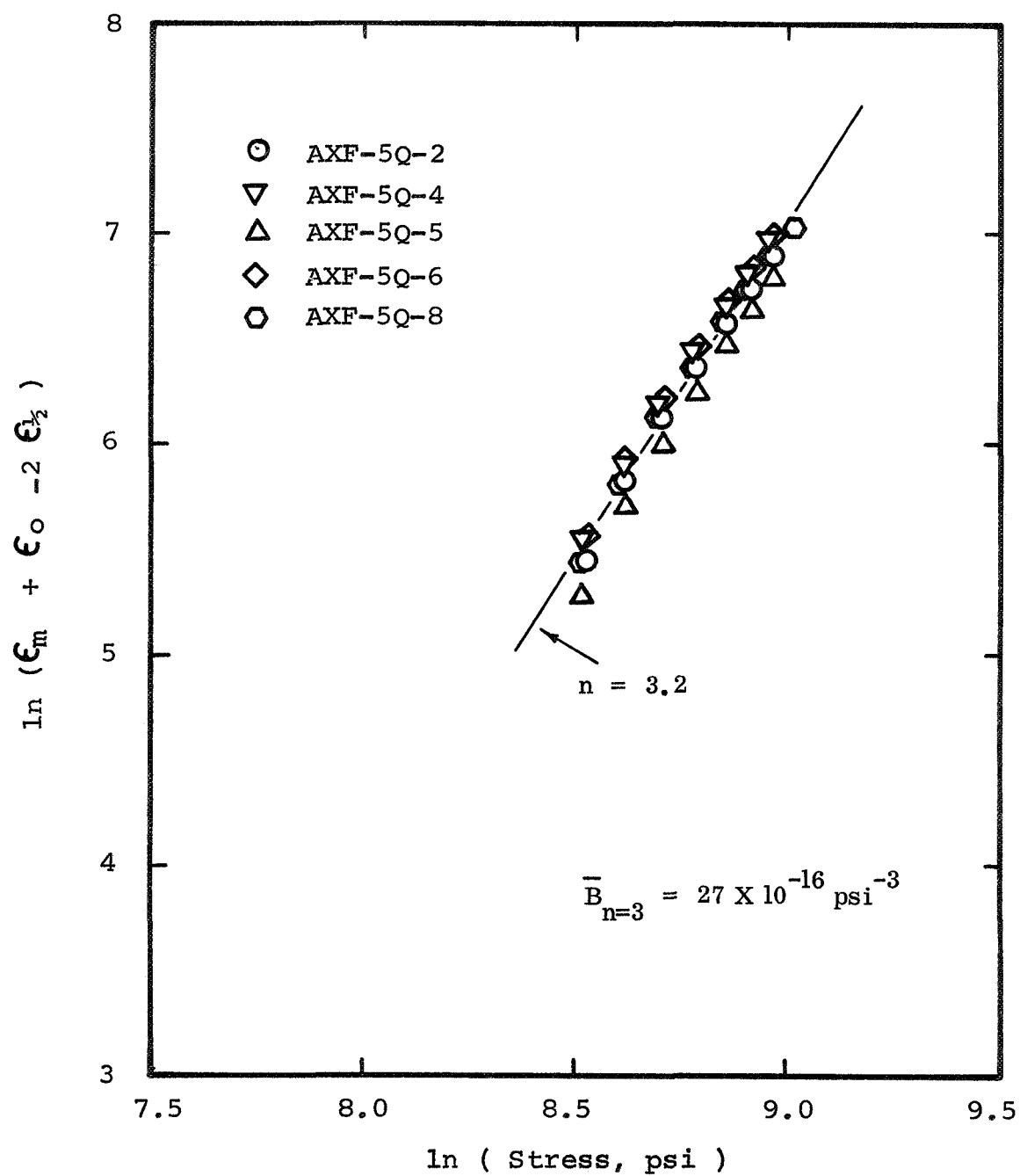


Figure 44. The stress dependence of the nonlinear strain component, $\epsilon_{\text{pnl.}}$, for AXF-5Q graphite.

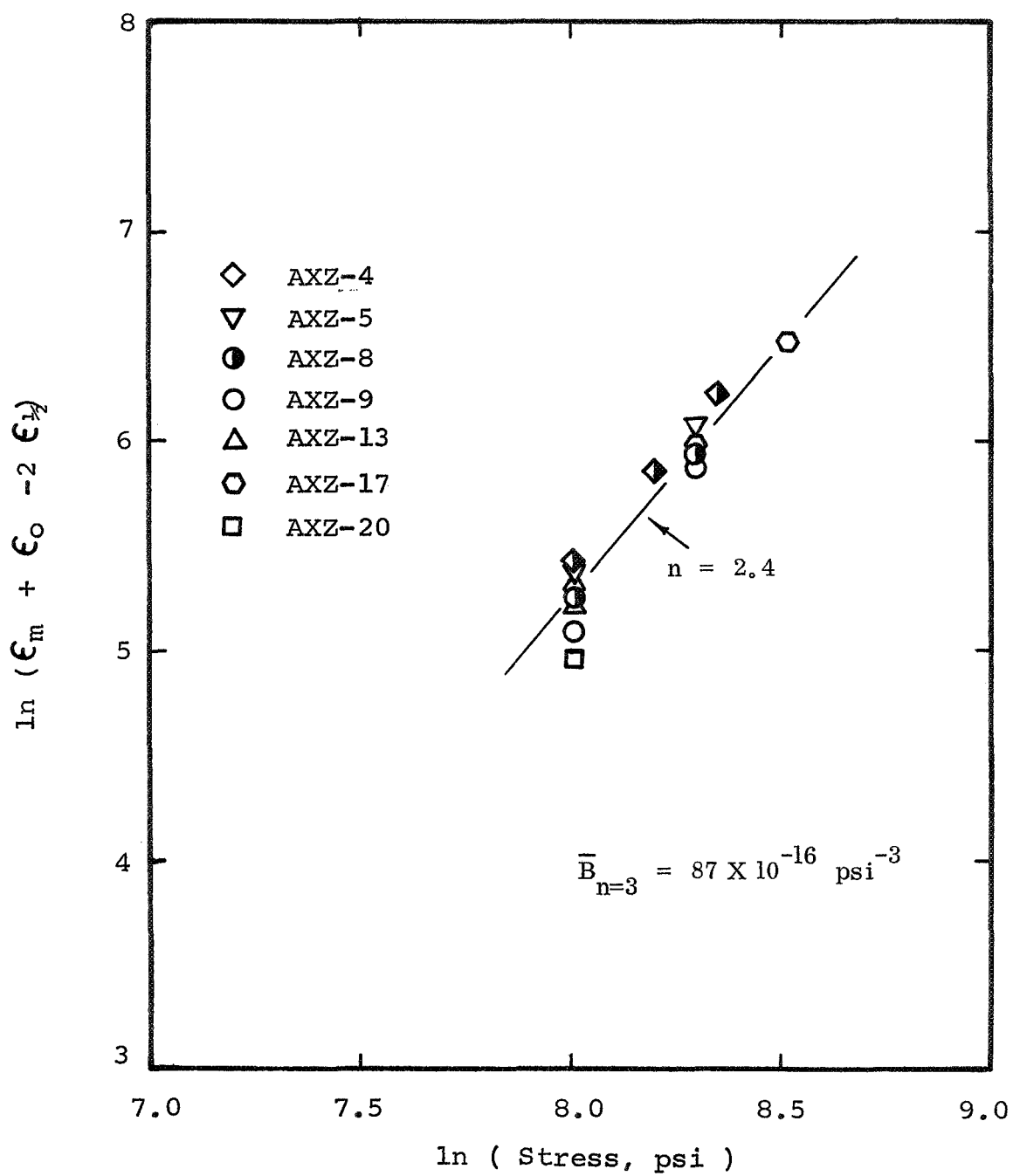


Figure 45. The stress dependence of the nonlinear strain component, ϵ_{pm} , for AXZ graphite.

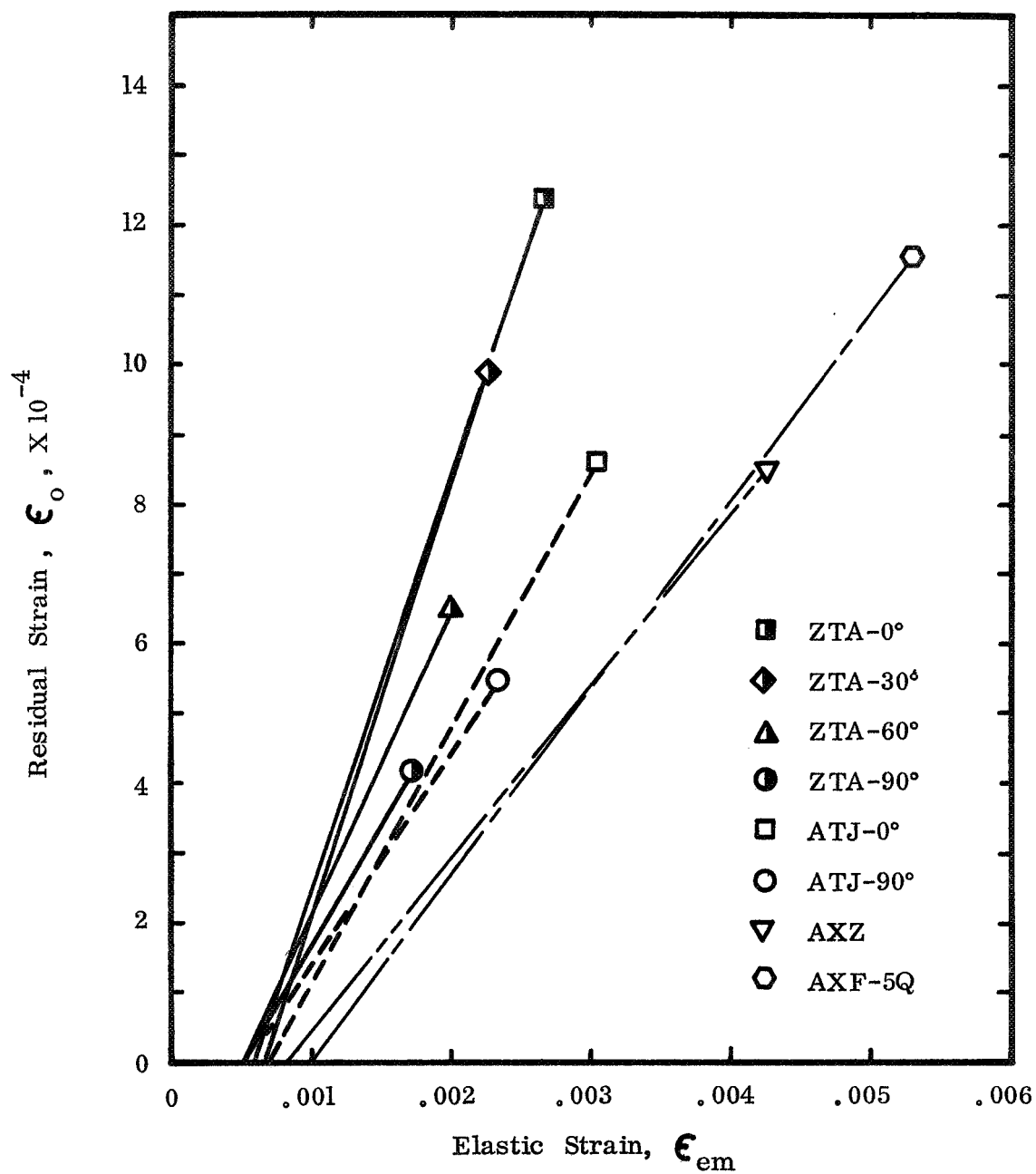


Figure 46. The relationships between the residual strains, ϵ_o , and the elastic strains at the maximum stresses per cycle, ϵ_{em} , for several graphite grades and orientations.

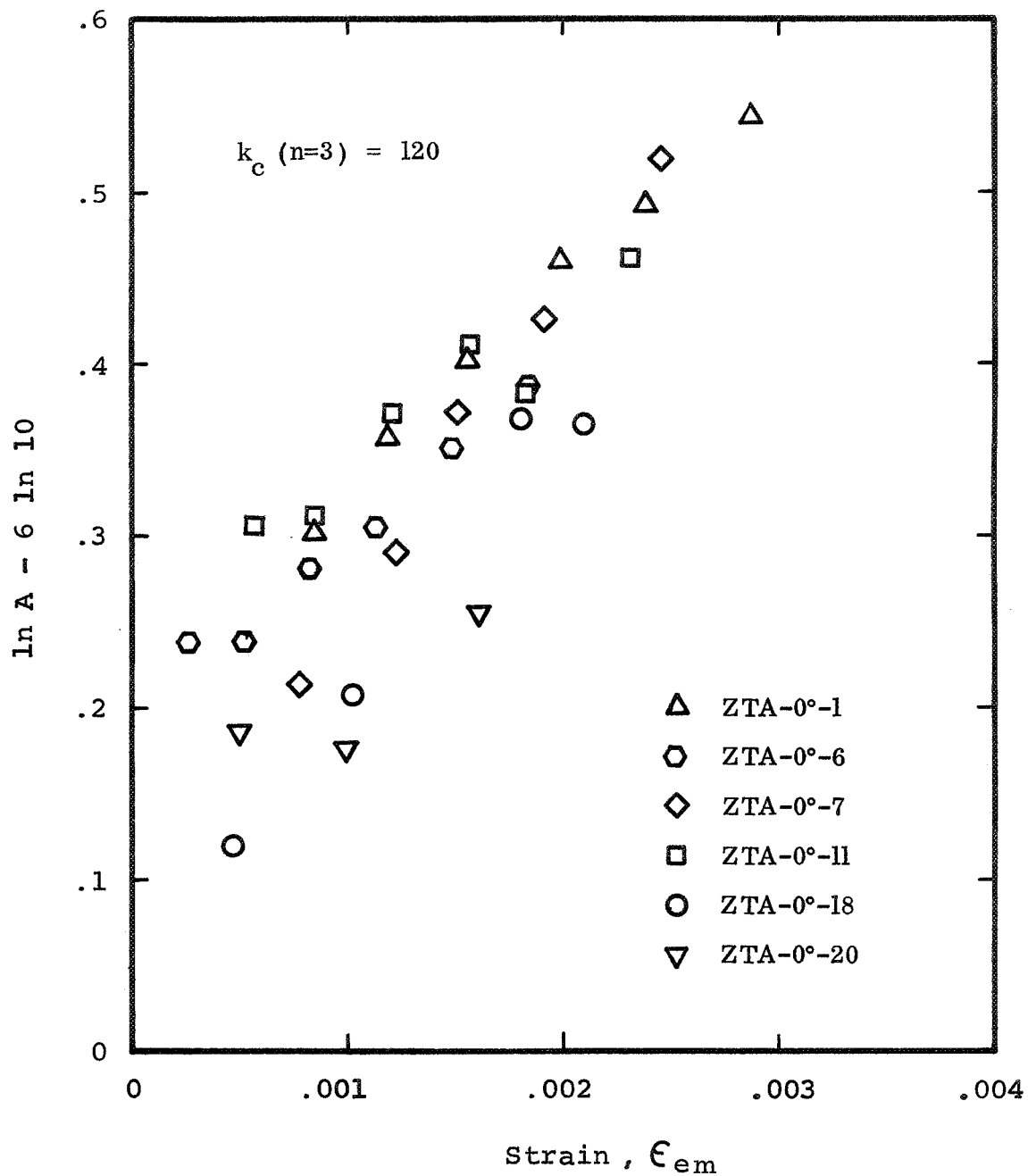


Figure 47. The elastic strain dependence of the elastic compliance, A , for ZTA graphite stressed parallel to the pressing direction.

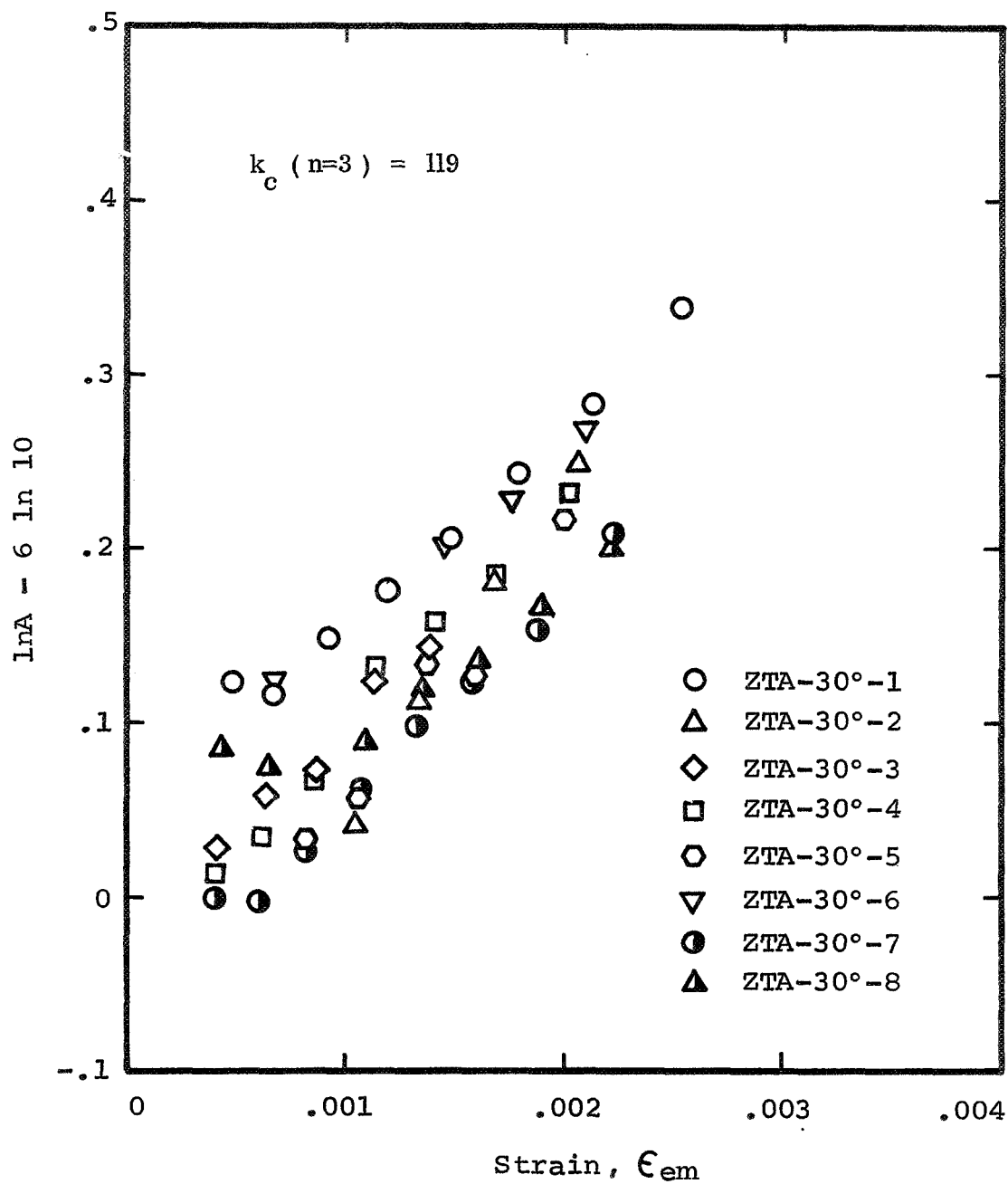


Figure 48. The elastic strain dependence of the elastic compliance, A , for ZTA graphite stressed 30° to the pressing direction.

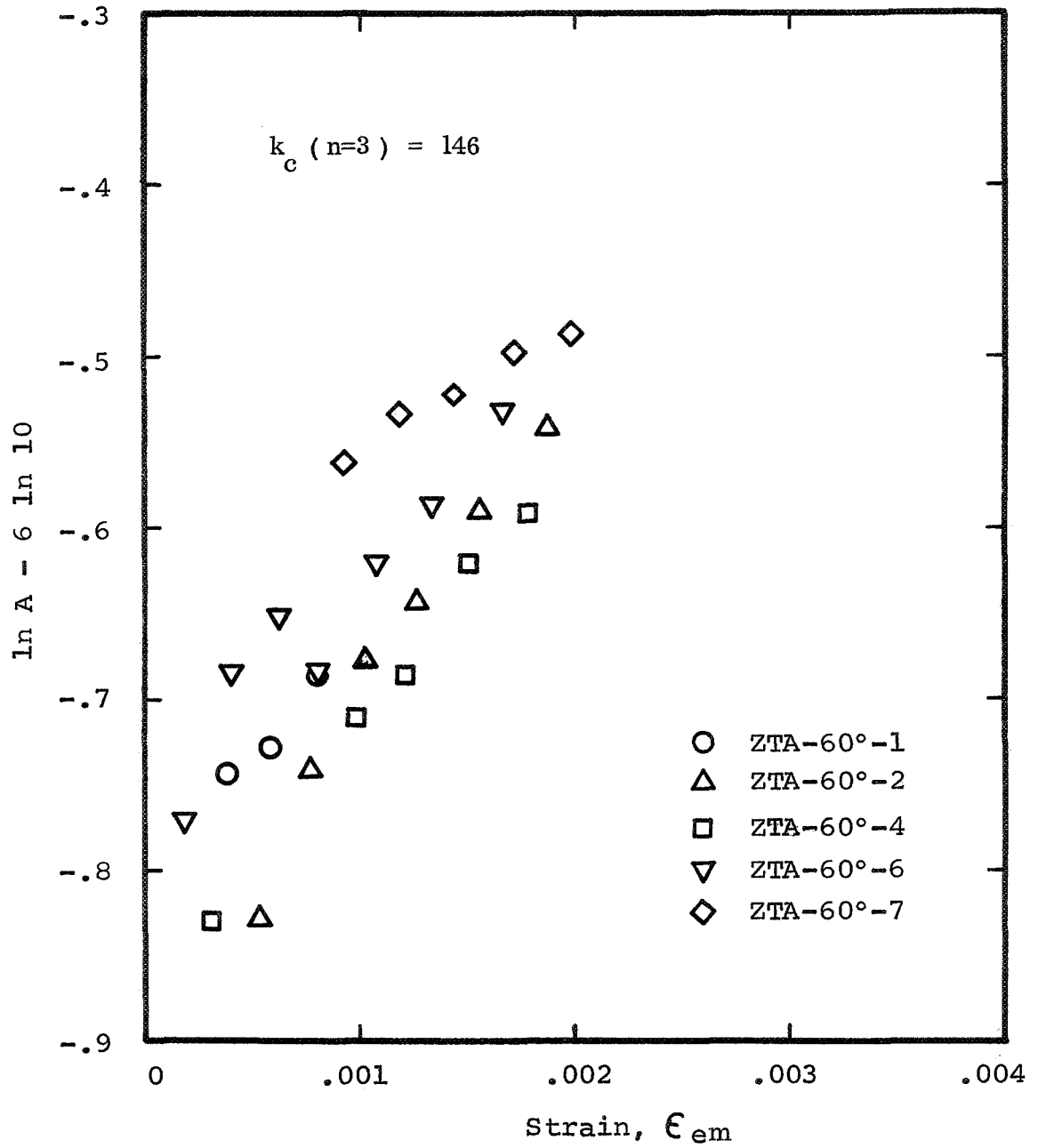


Figure 49. The elastic strain dependence of the elastic compliance, A , for ZTA graphite stressed 60° to the pressing direction.

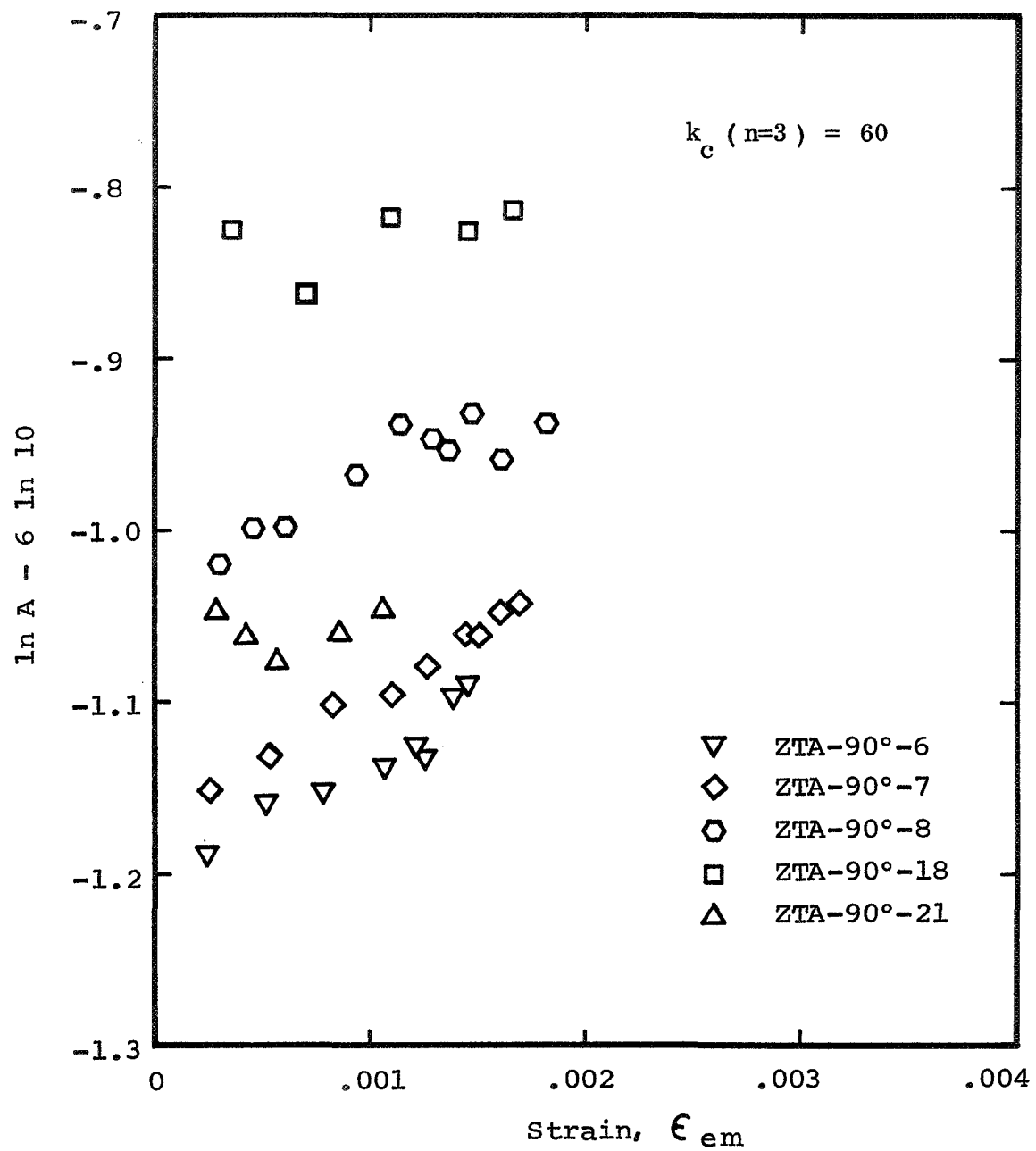


Figure 50. The elastic strain dependence of the elastic compliance, A , for ZTA graphite stressed perpendicular to the pressing direction.

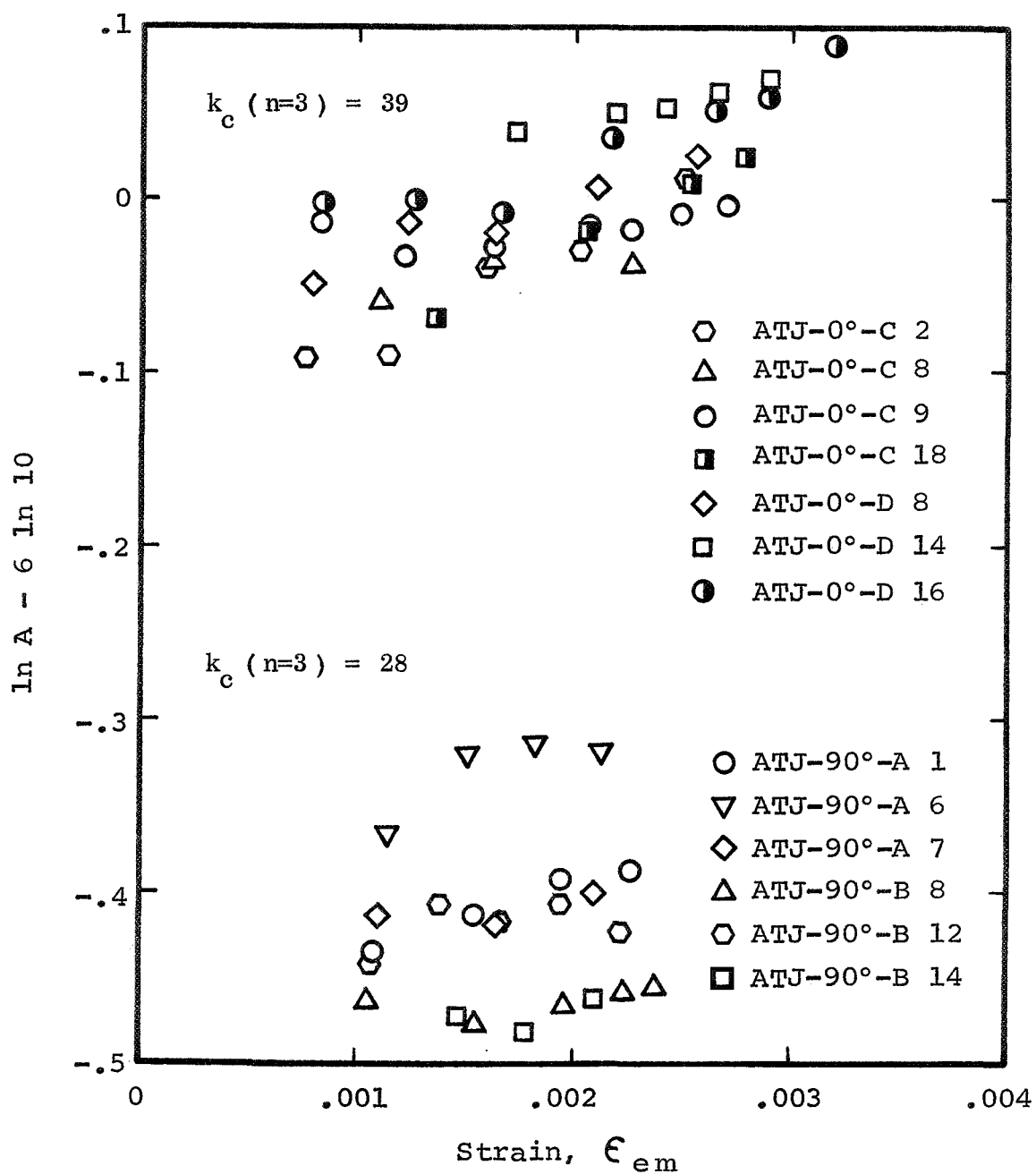


Figure 51. The elastic strain dependence of the elastic compliance, A , for ATJ graphite stressed both parallel to and perpendicular to the pressing direction.

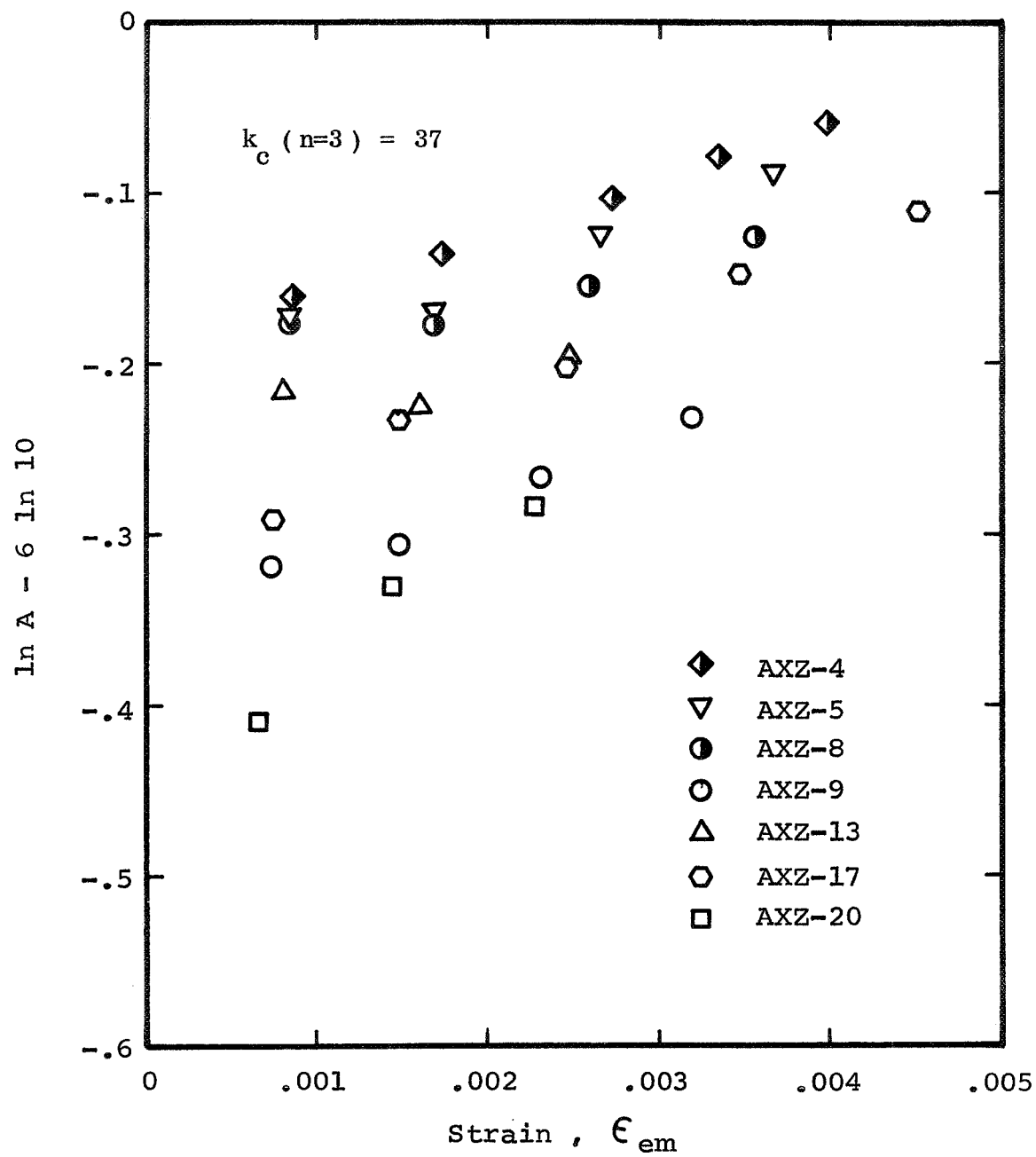


Figure 52. The elastic strain dependence of the elastic compliance, A , for AXZ graphite.

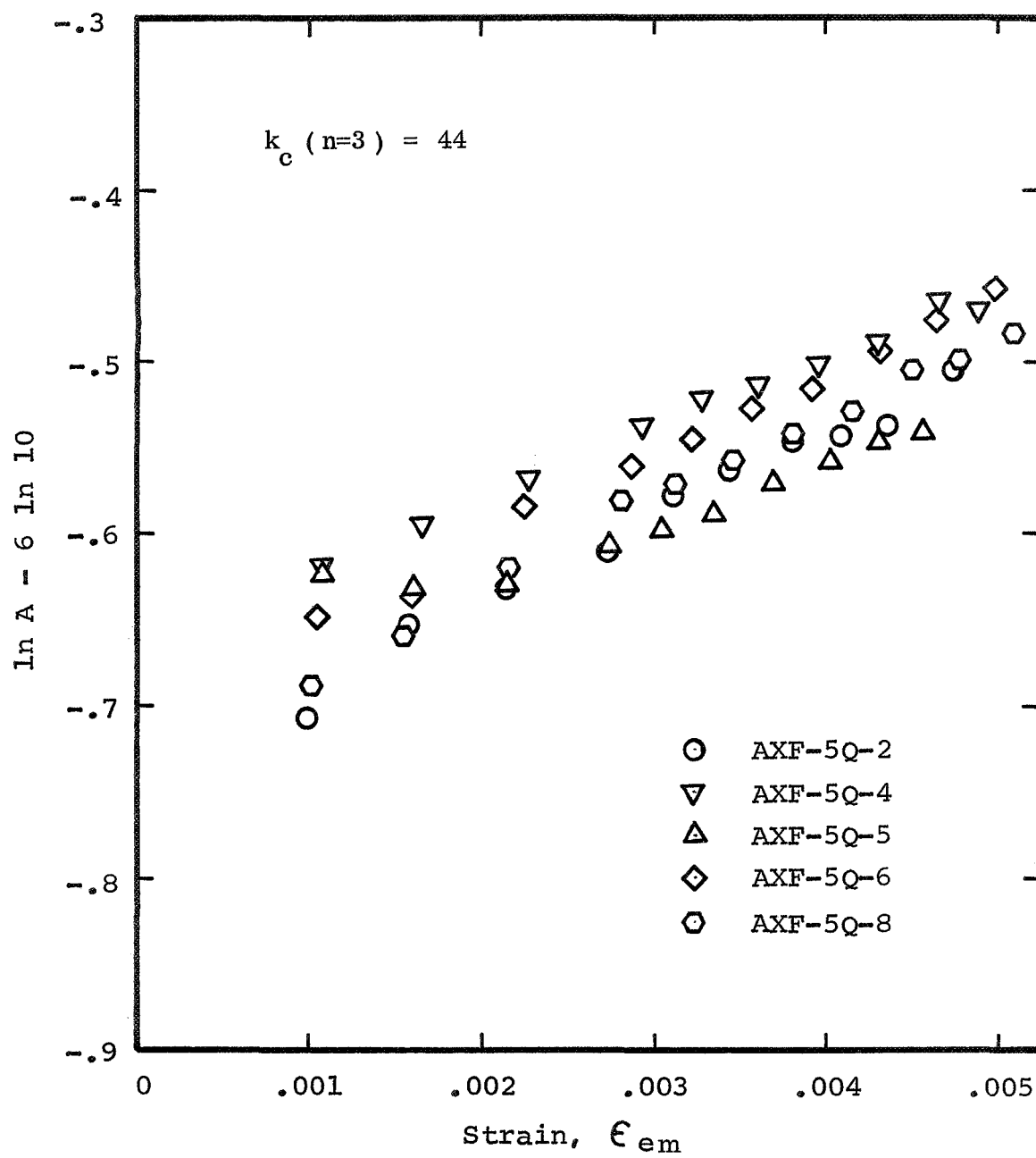


Figure 53. The elastic strain dependence of the elastic compliance, A , for AXF-5Q graphite.

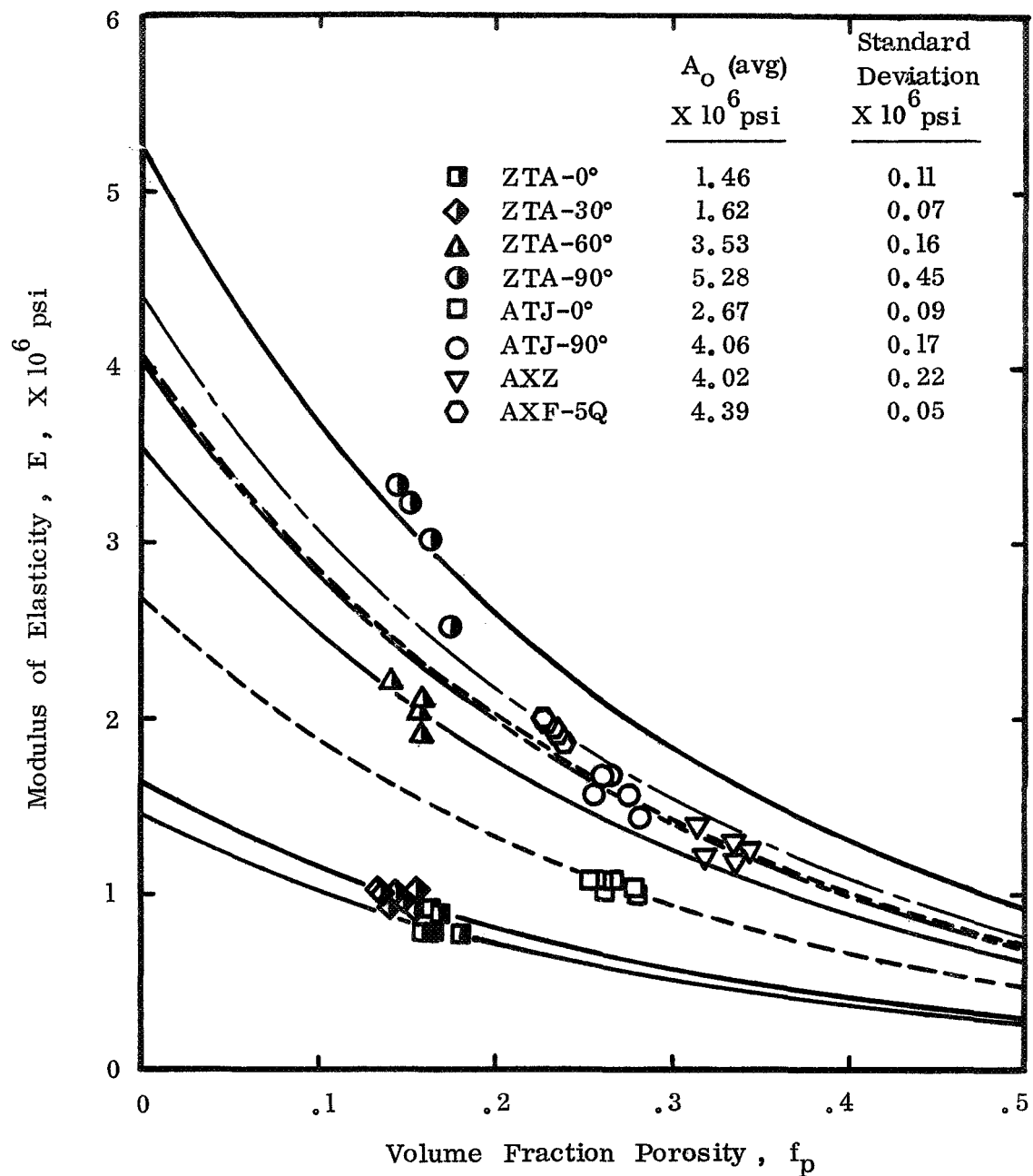


Figure 54. The effect of the volume fraction porosity on the elastic moduli of several graphite grades and orientations.

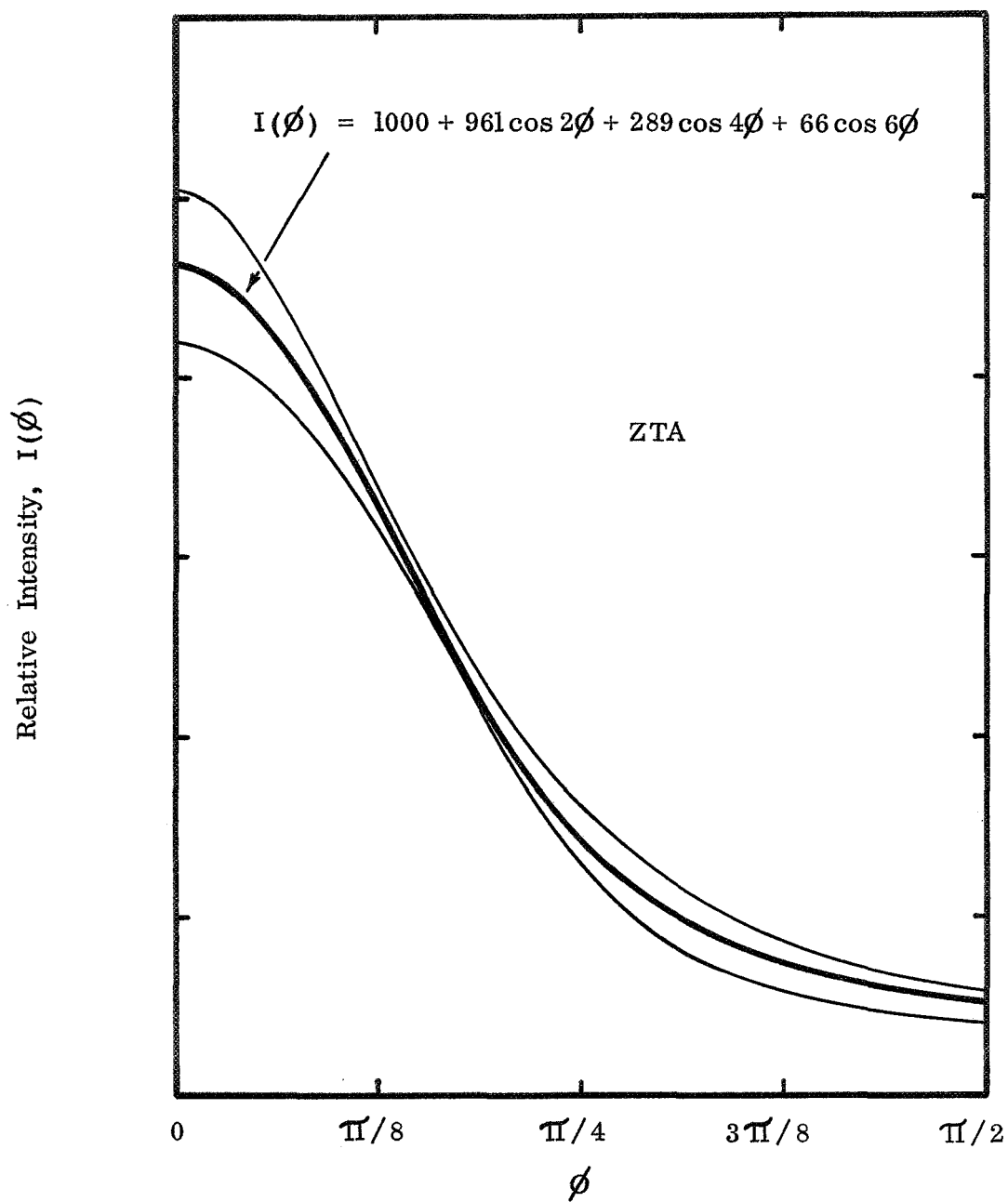


Figure 55. The relative intensity of 0002 plane normals as a function of the angle ϕ from the pressing direction. ZTA graphite.

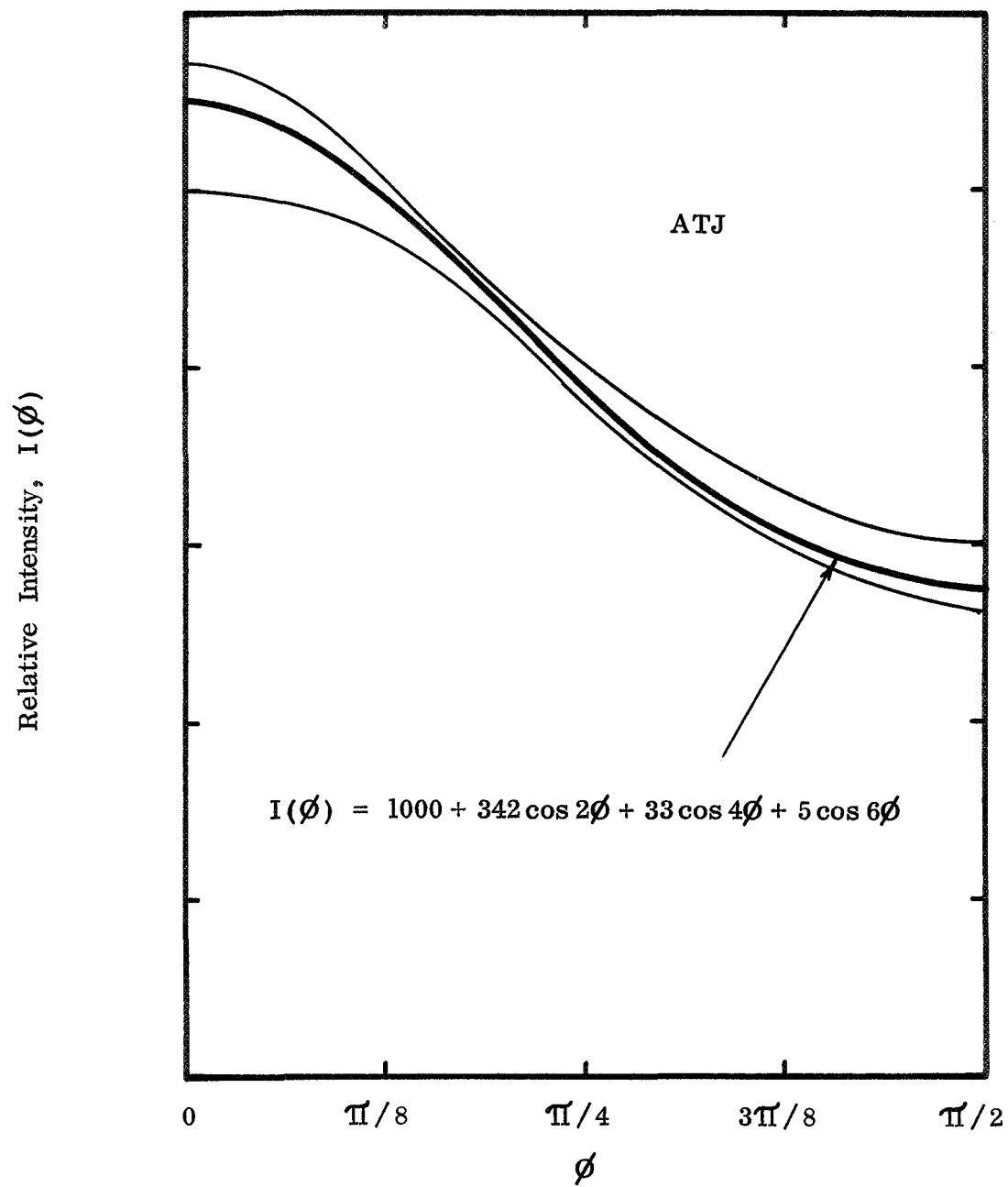


Figure 56. The relative intensity of 0002 plane normals as a function of the angle ϕ from the pressing direction. ATJ graphite.

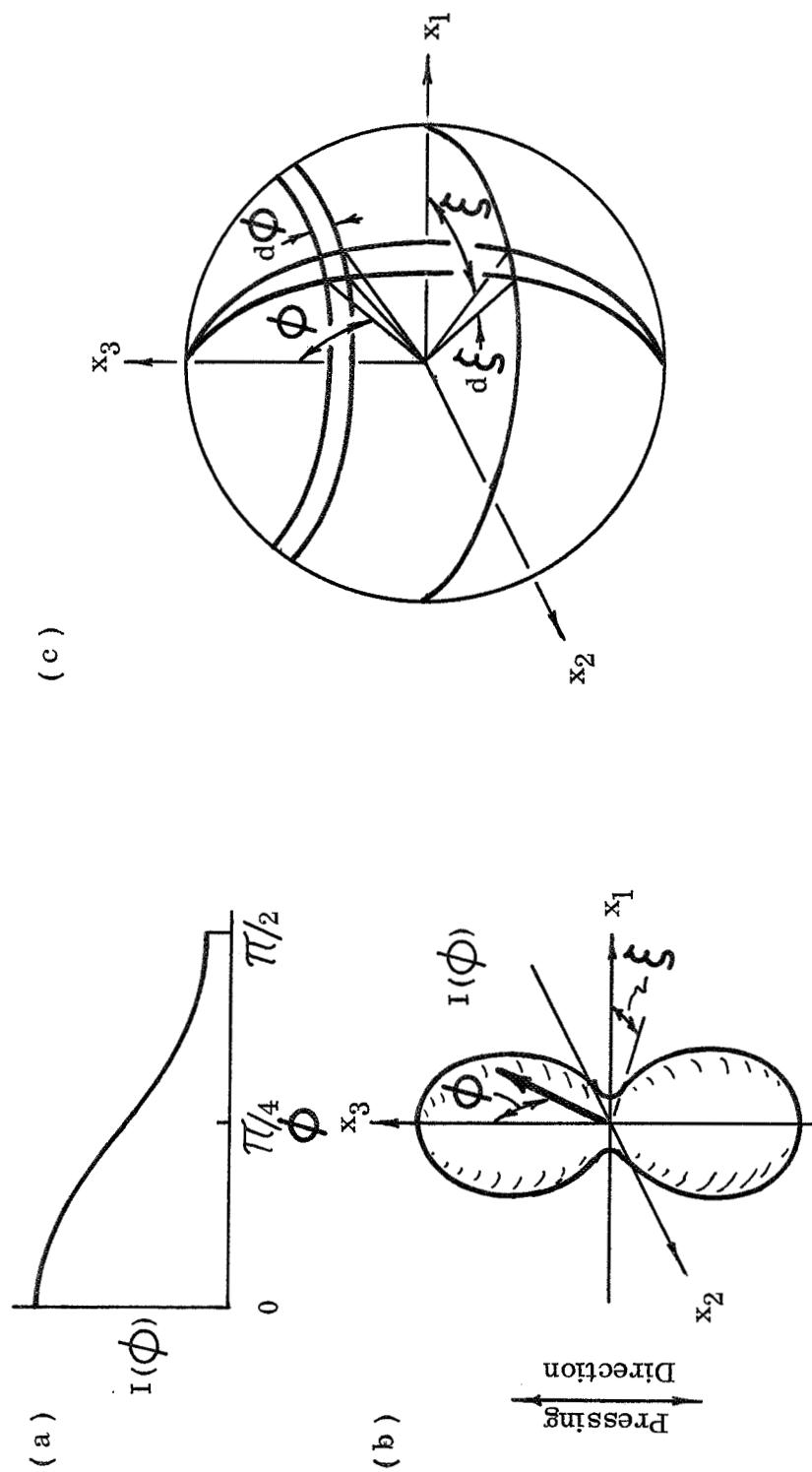


Figure 57. (a) X ray diffraction intensity of (0002) planes measured in the x_1 - x_3 plane; and (b) the equivalent intensity in three dimensions. (c) A volume element of the bulk material showing the relationship between the densities of (0002) planes and the solid angles.

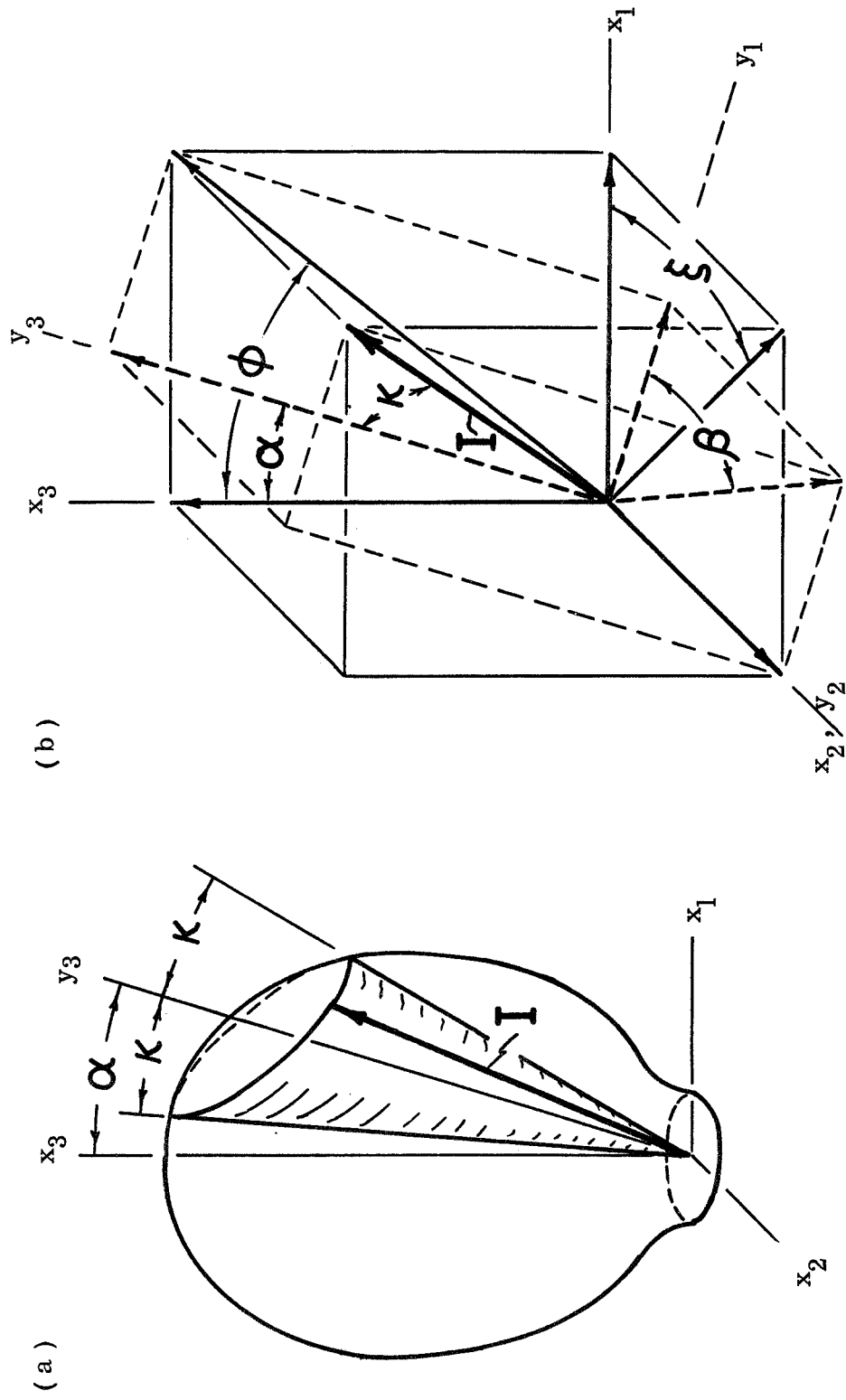


Figure 58. The vector transformation to determine the intensity $I(\kappa, \beta, \alpha)$ from $I(\phi, \xi)$, where α is the angle from the pressing direction, x_3 , of the new axis under consideration, y_3 ; κ is the orientation angle from y_3 ; and β is the rotational angle from y_1 about y_3 .

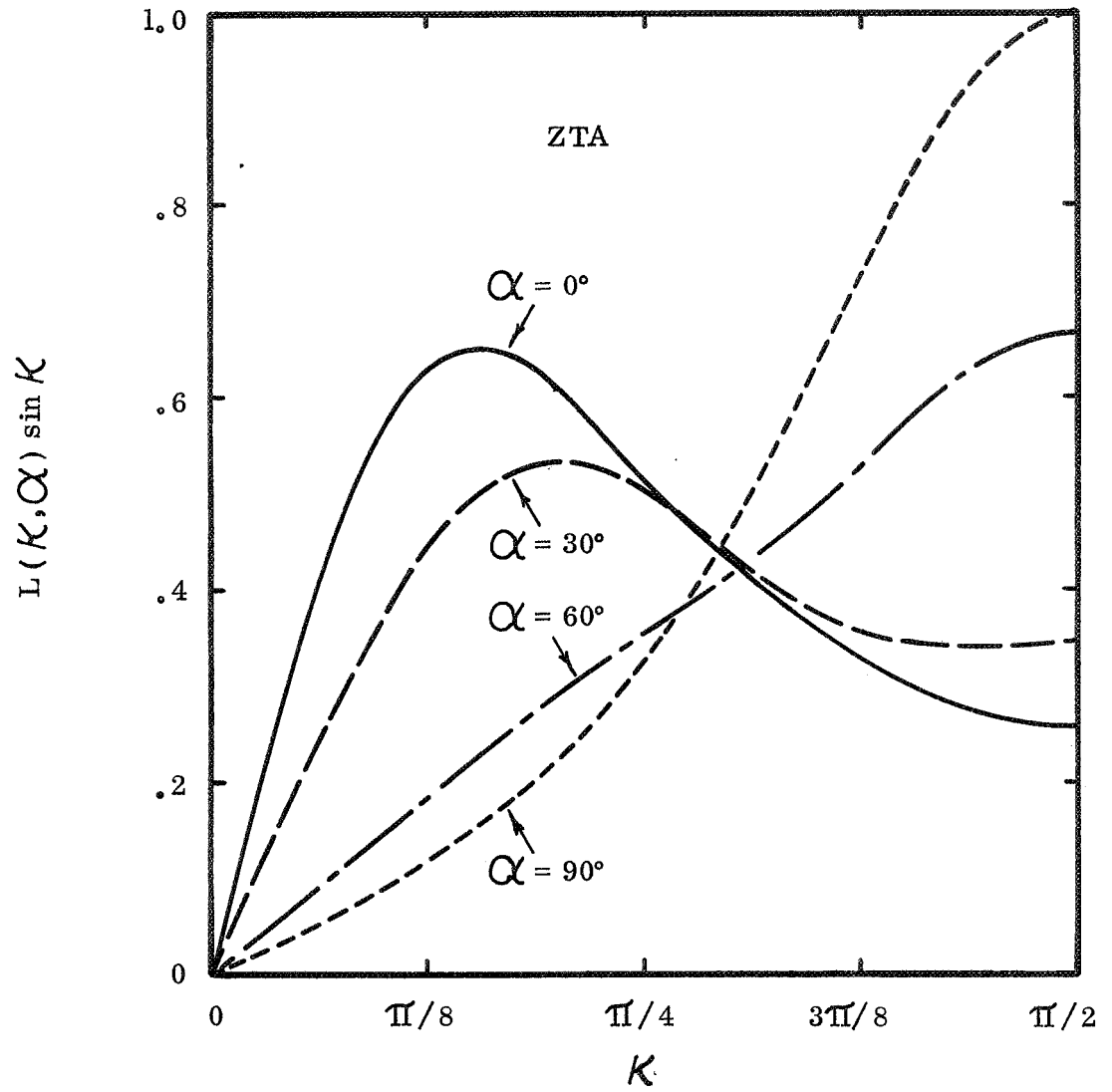


Figure 59. The relative density of 0002 plane normals per unit solid conical angle, K , from an axis that has been rotated by an angle α from the pressing direction. ZTA graphite.

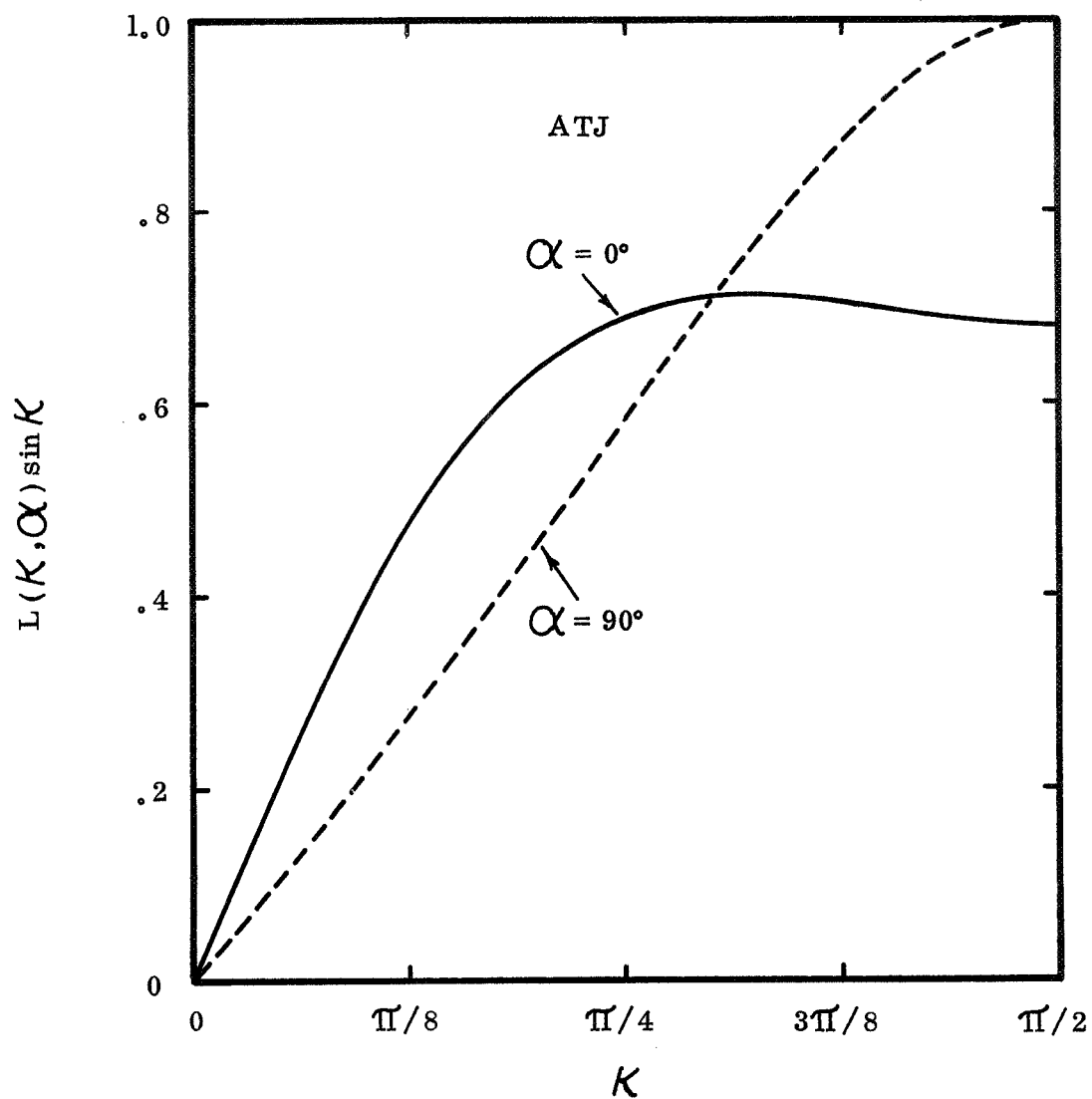


Figure 60. The relative density of 0002 plane normals per unit solid conical angle, K , from an axis that has been rotated by an angle α from the pressing direction. ATJ graphite.

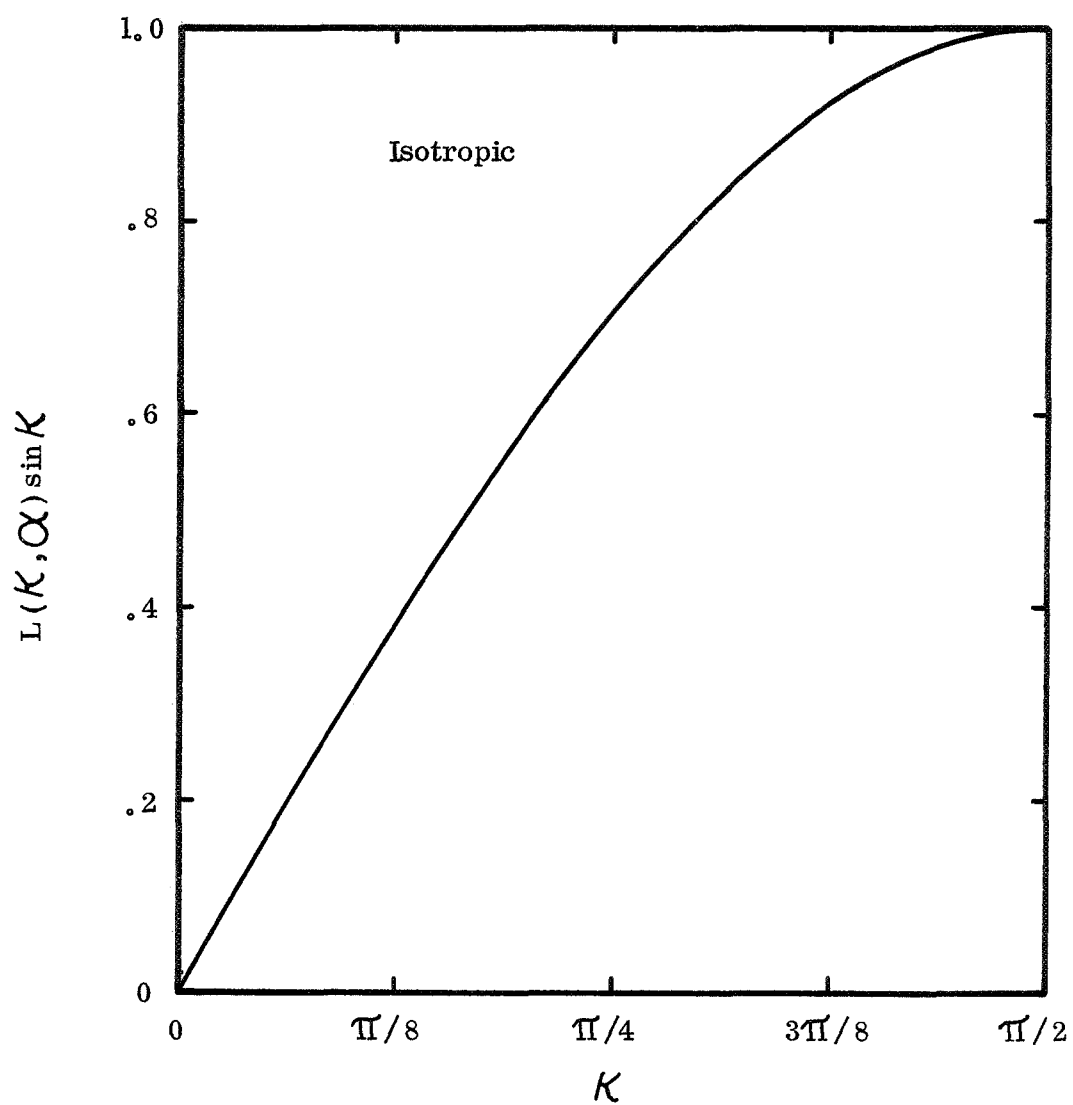


Figure 61. The relative density of 0002 plane normals per unit solid conical angle, K . Isotropic graphite.

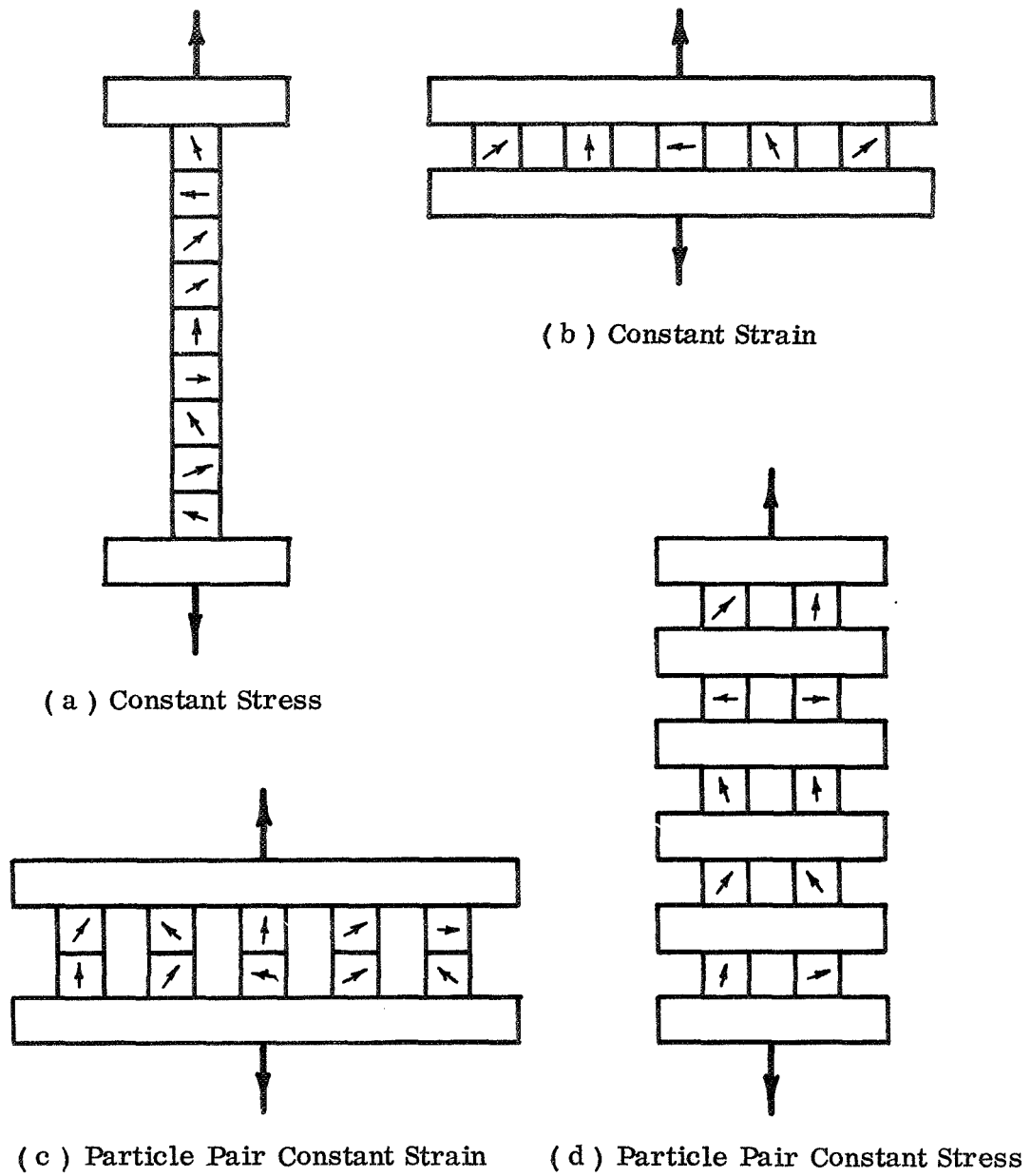


Figure 62. Models used to calculate polycrystalline properties from single crystal properties.

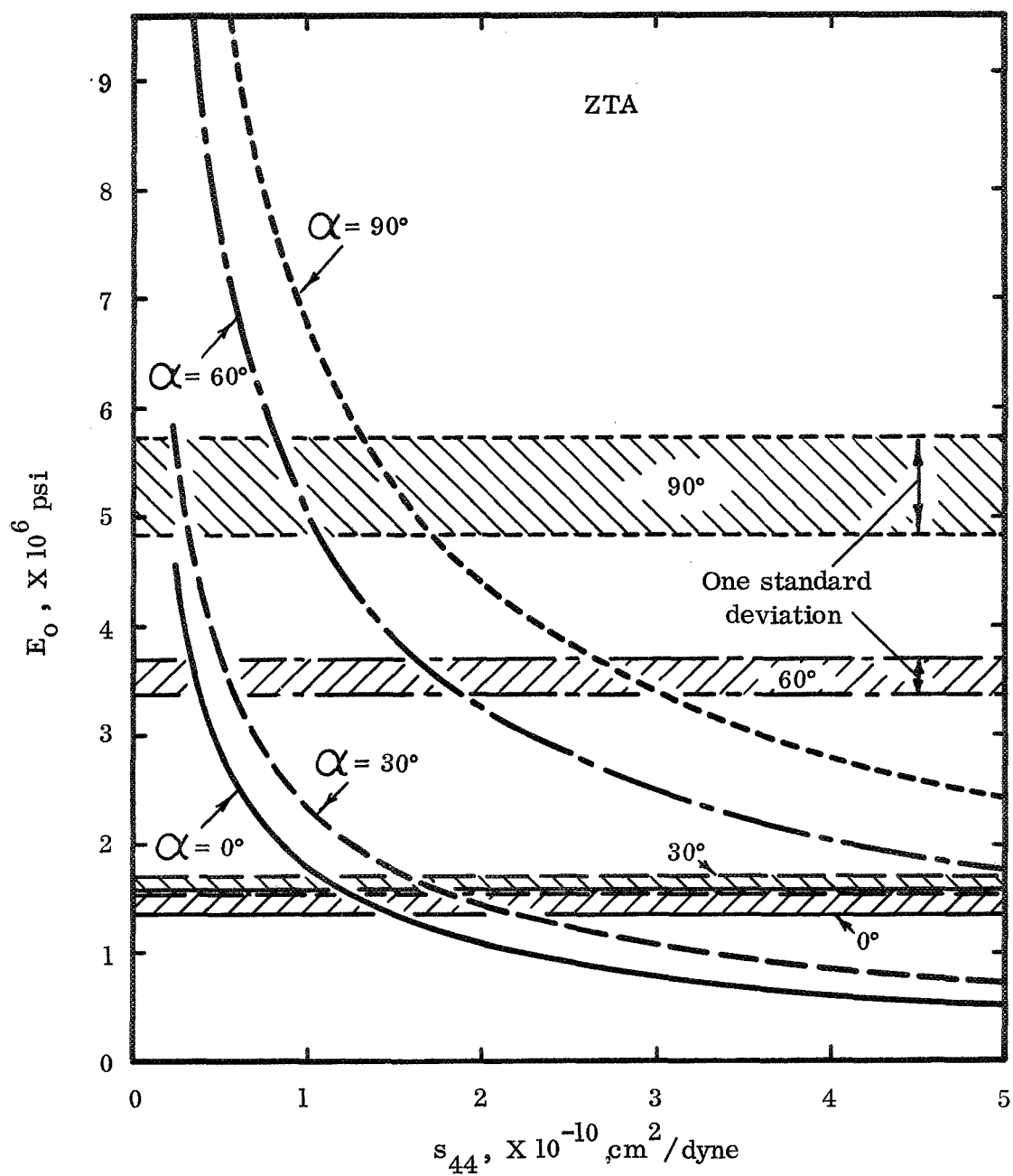


Figure 63. Calculated elastic moduli as a function of the angle, α , from the pressing direction and the basal plane shear compliance, s_{44} . ZTA graphite.

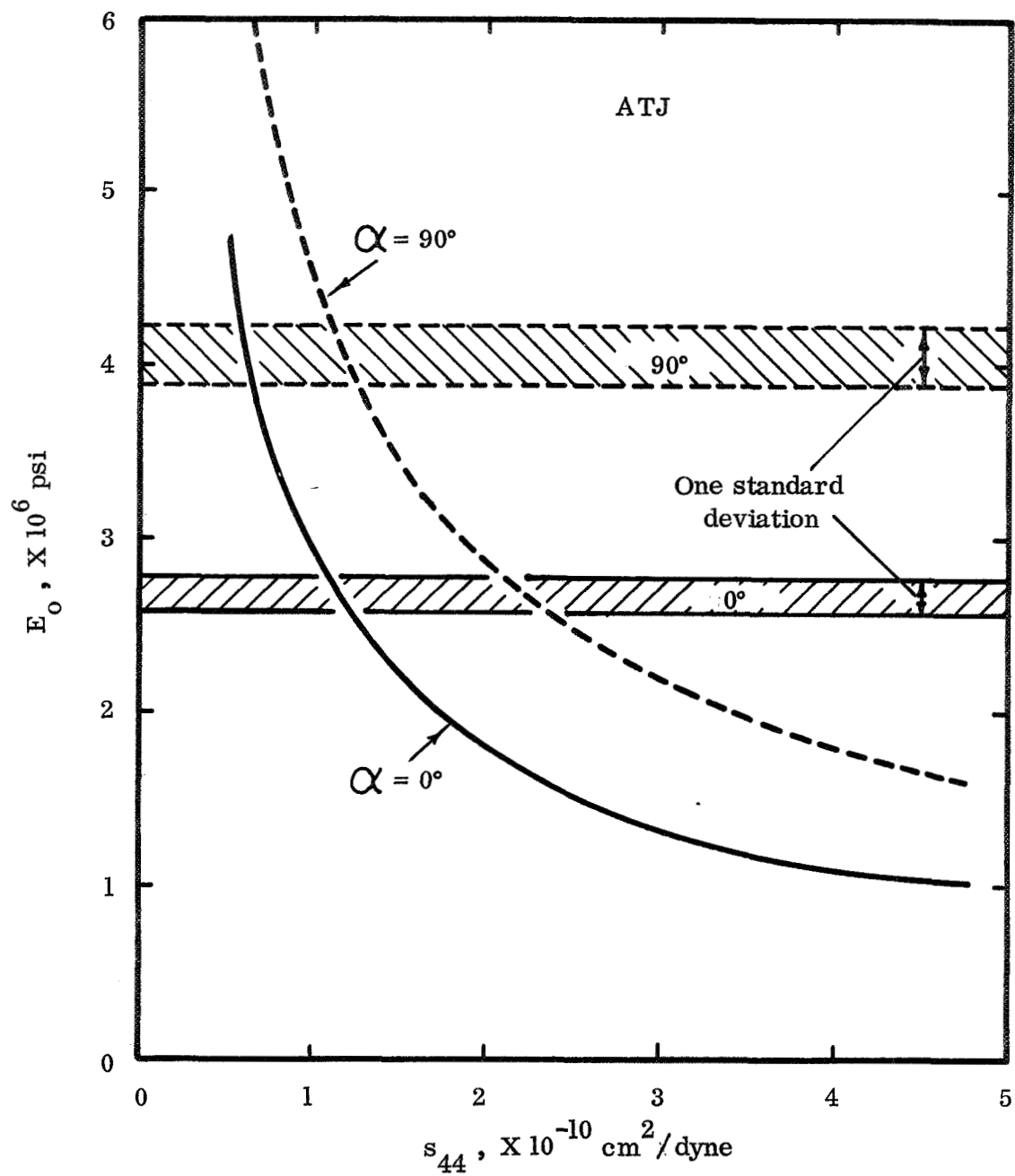


Figure 64. Calculated elastic moduli as a function of the angle, α , from the pressing direction and the basal plane shear compliance, s_{44} . ATJ graphite.

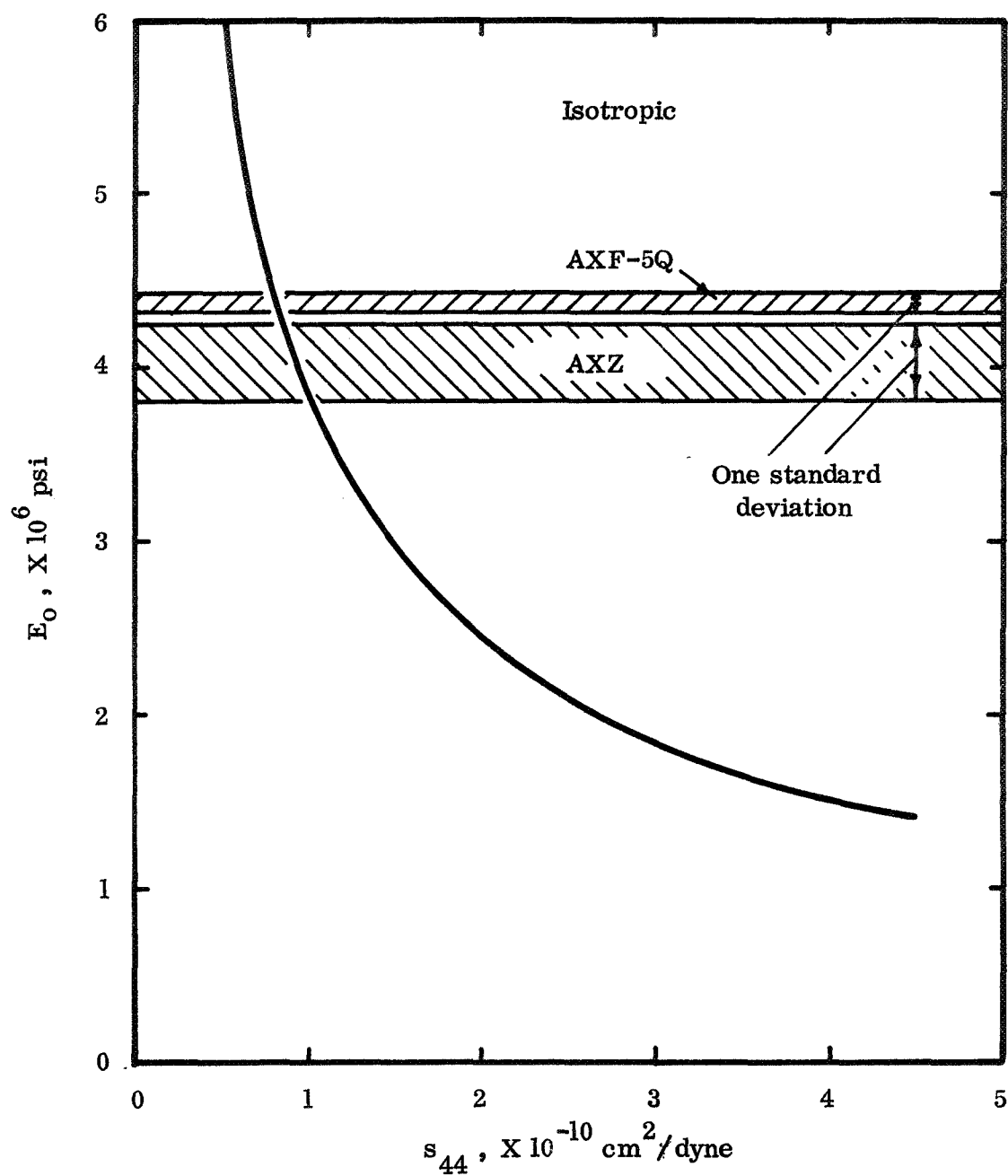


Figure 65. Calculated elastic moduli as a function of the basal plane shear compliance, s_{44} . Isotropic graphite.

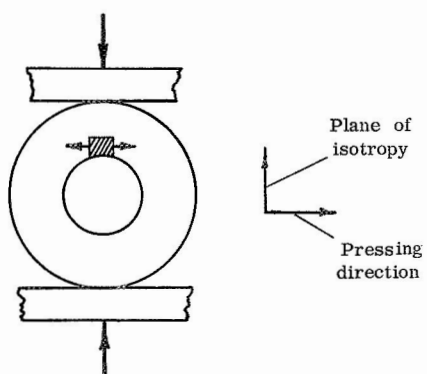
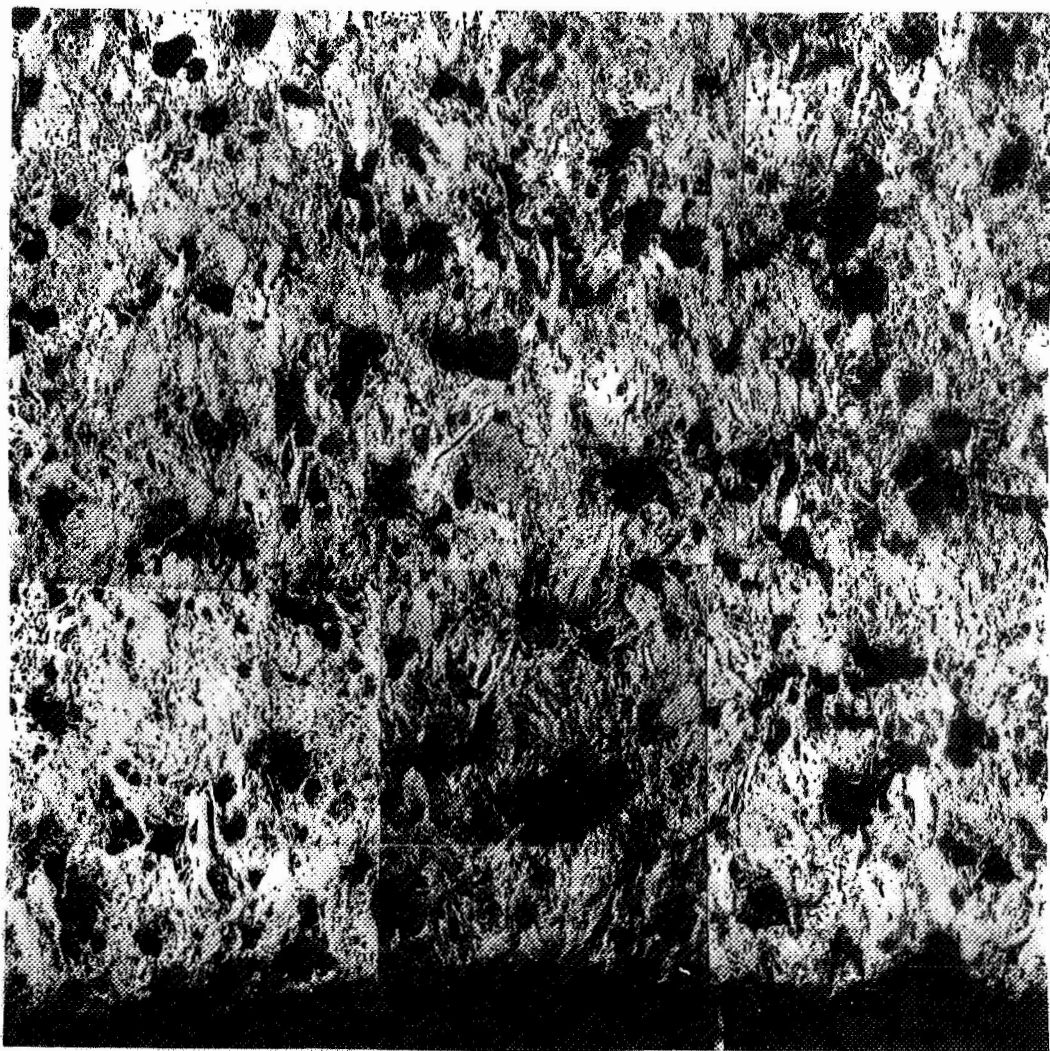


Figure 66. An area of a ZTA graphite ring-shaped specimen prior to loading. Magnification: 200 X.

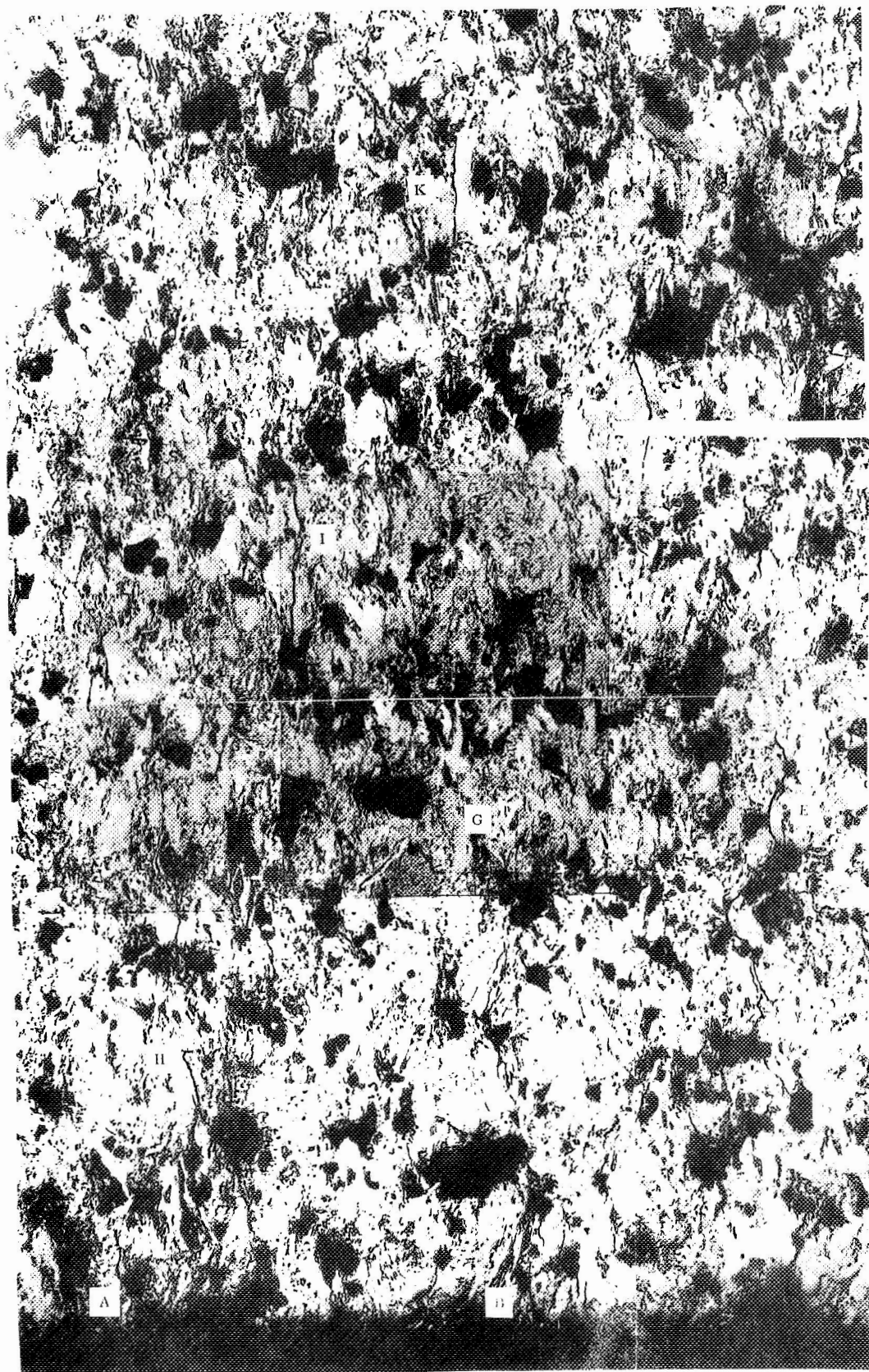


Figure 67. The area of the ZTA graphite ring-shaped specimen (shown in Figure 66) under stress.
Magnification: 200 X.

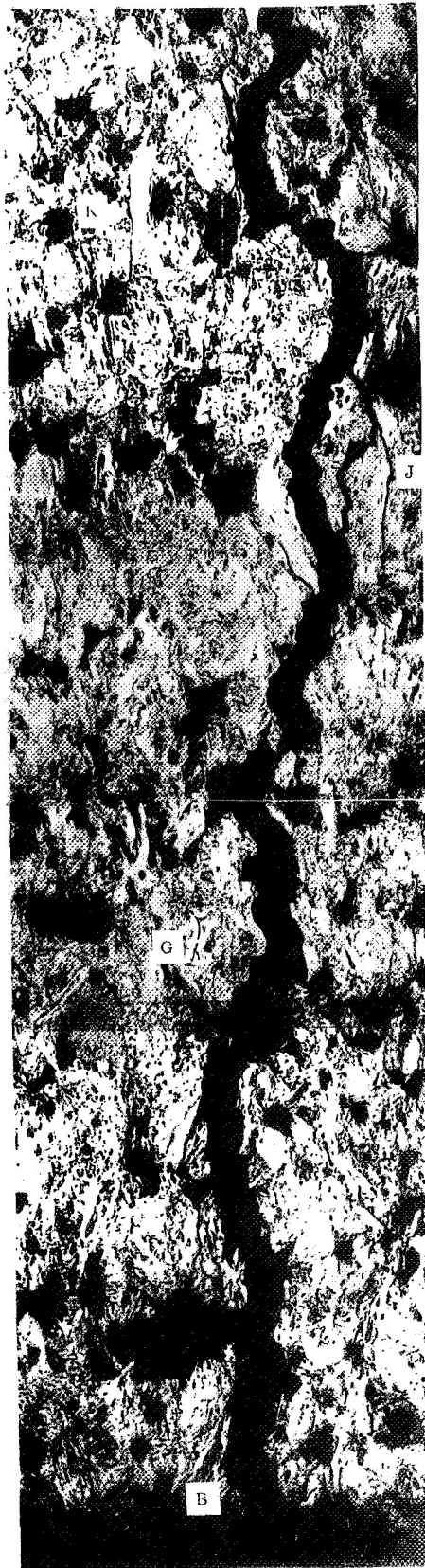


Figure 68. The area of the ZTA graphite ring-shaped specimen (shown in Figures 66 and 67) after failure. Magnification: 200 X.

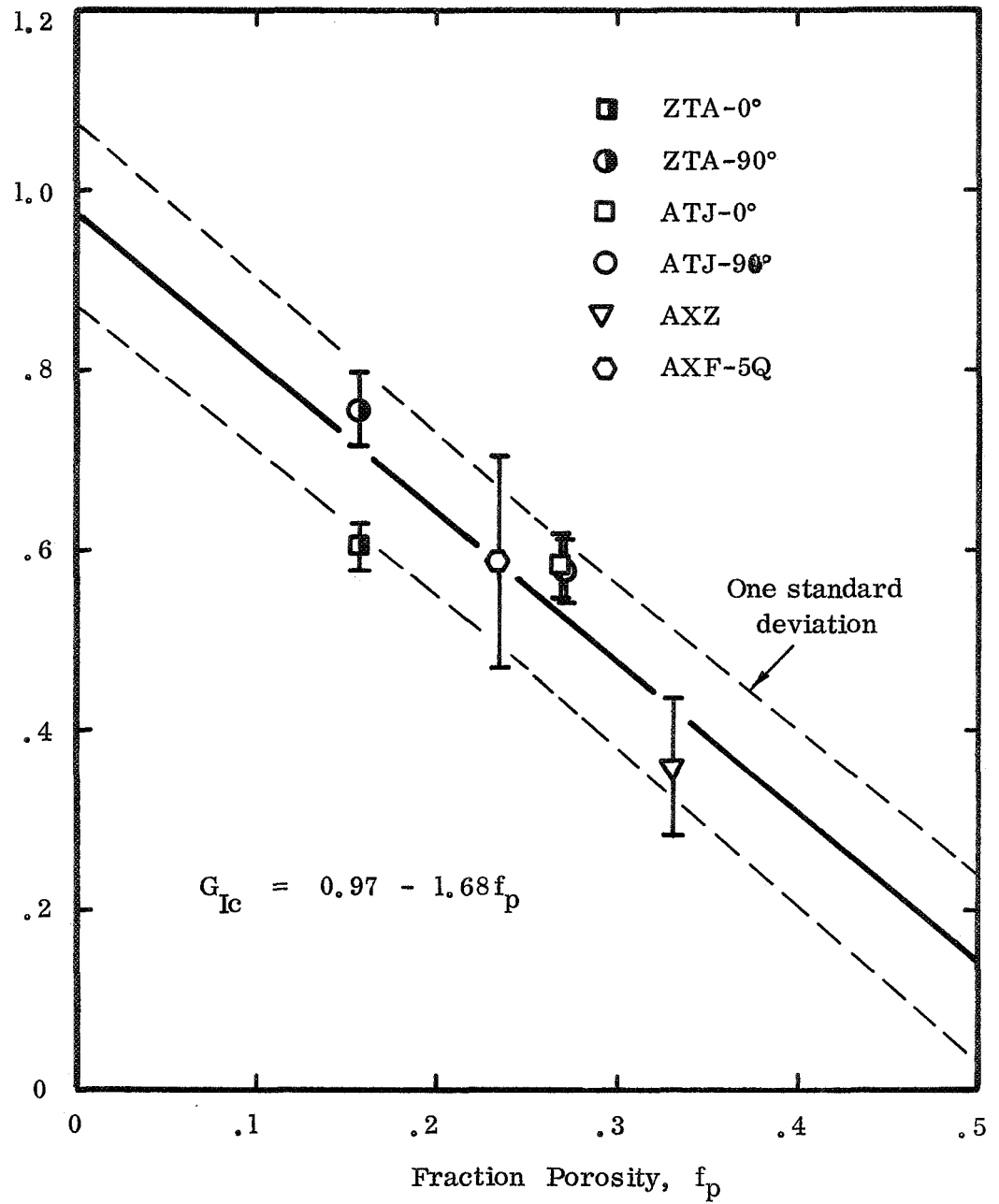


Figure 69. The critical crack extension force (critical energy release rate or fracture surface energy), G_{Ic} , as a function of the fraction porosity, f_p , for several graphite grades.

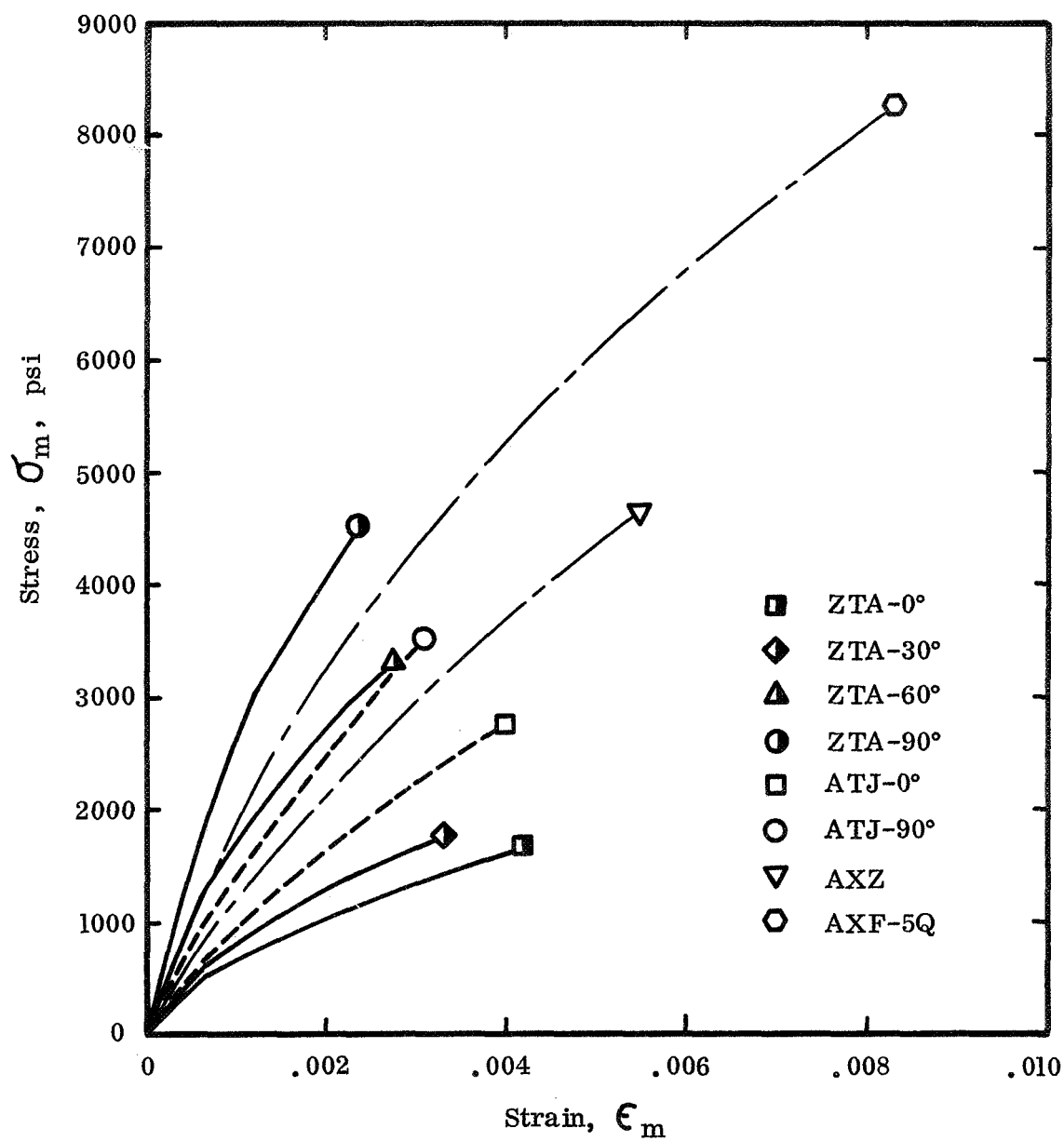
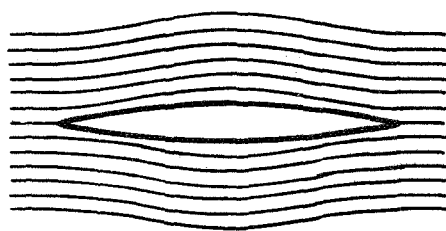
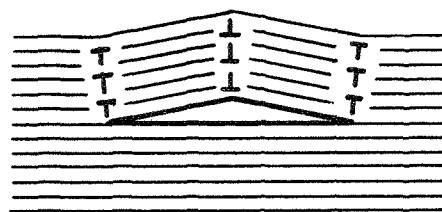


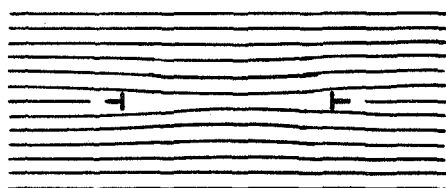
Figure 70. The calculated stress-strain curves of four grades of polycrystalline graphite.



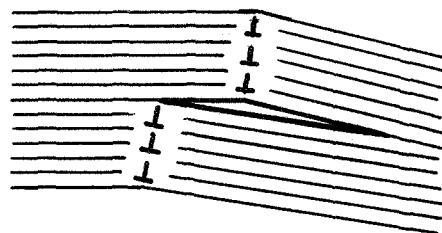
(a) Cleavage Crack



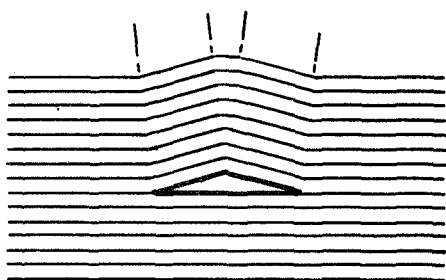
(d) Dislocation Crack



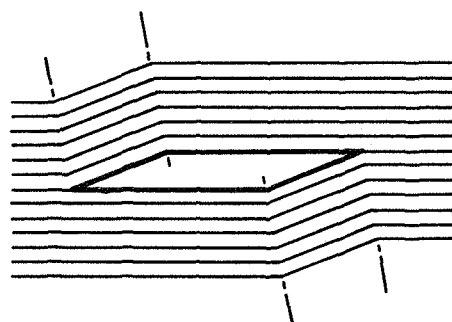
(b) Stacking Fault



(e) Dislocation Crack



(c) Twinning Crack



(f) Twinning Crack

Figure 71. Schematic representations of crack nuclei. ⁽³⁾

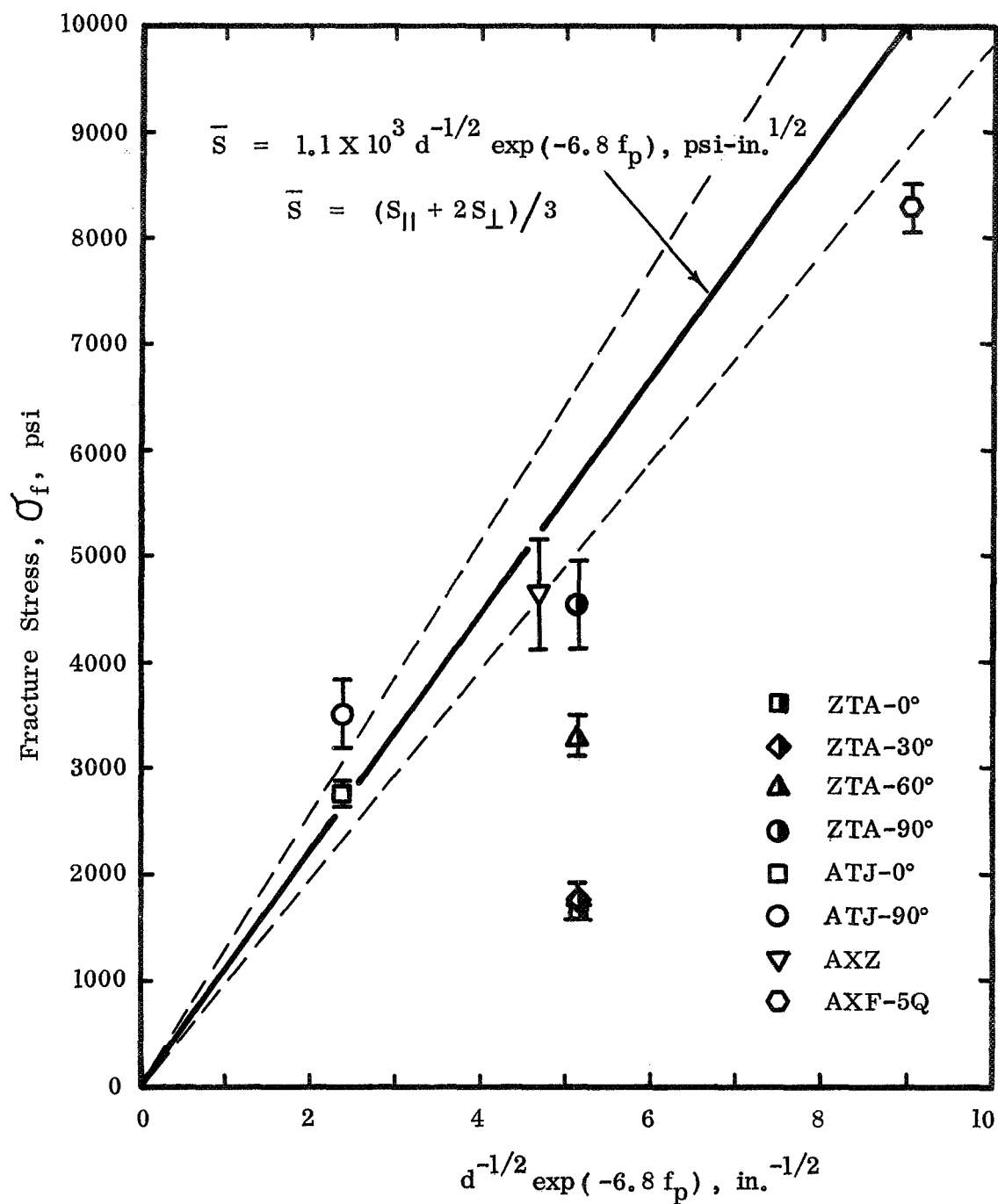


Figure 72. The Knibbs' (Knudsen) criteria for failure of polycrystalline graphite: failure stress, σ_f , as a function of the particle size, d , and the volume fraction porosity, f_p .

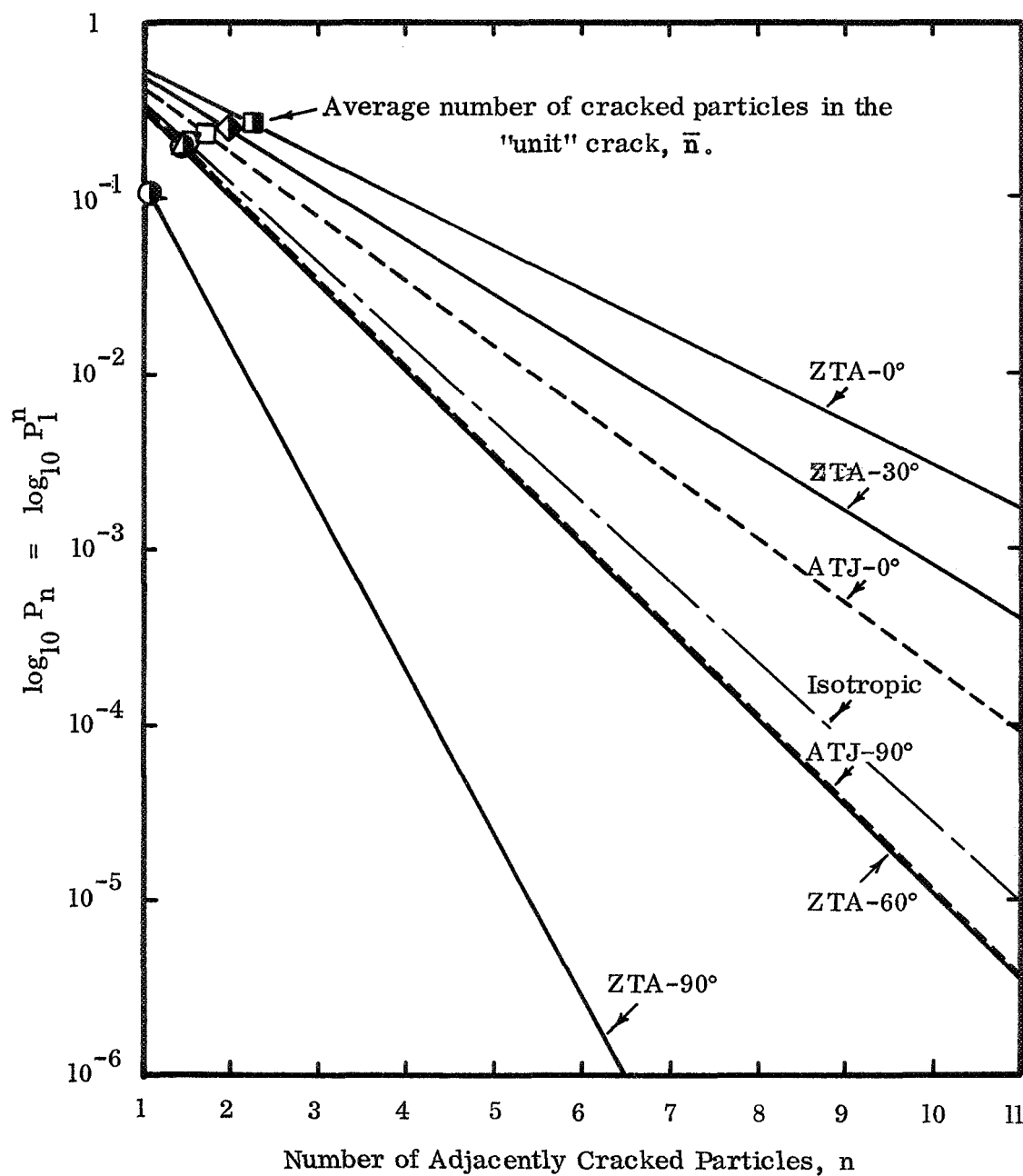


Figure 73. The probability, P_n , that n graphite flour particles in adjacent positions are cracked.

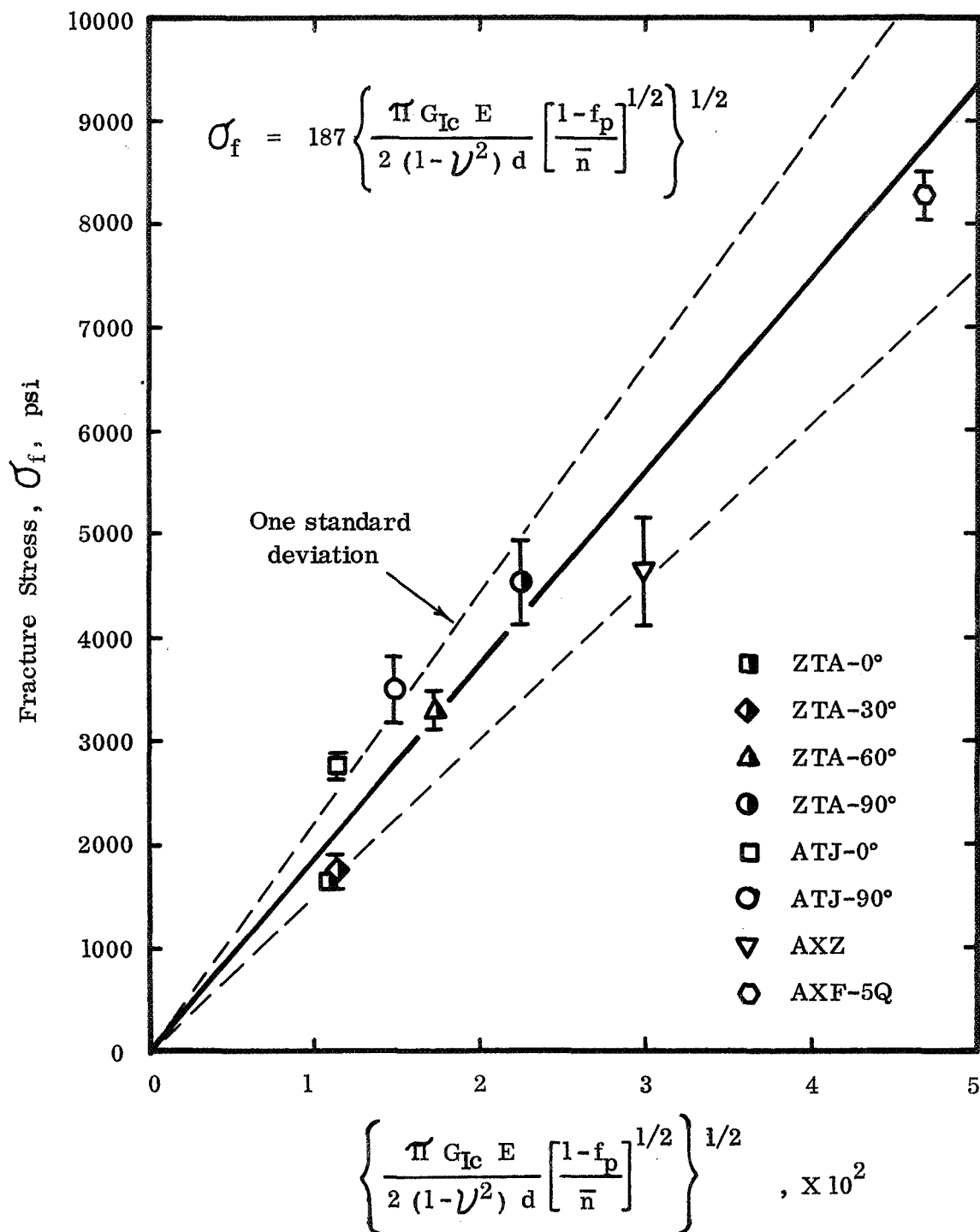
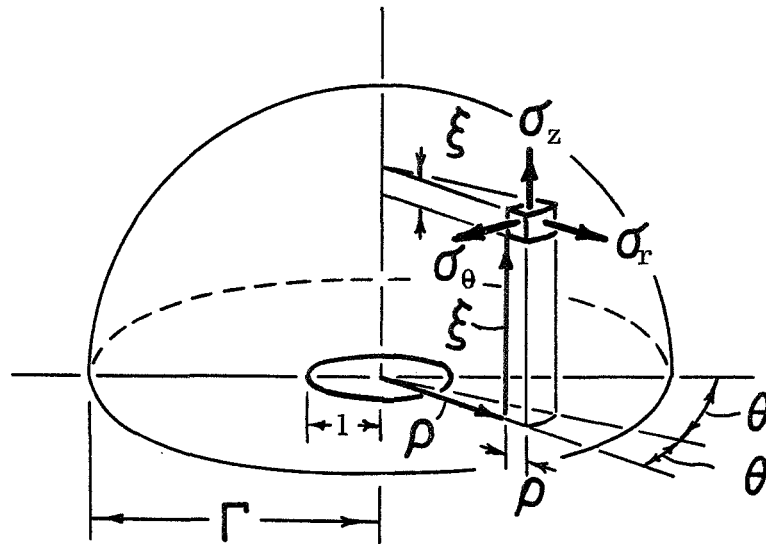


Figure 74. The fracture stresses, σ_f , of several polycrystalline graphites as a function of certain material parameters.

(a)



(b)

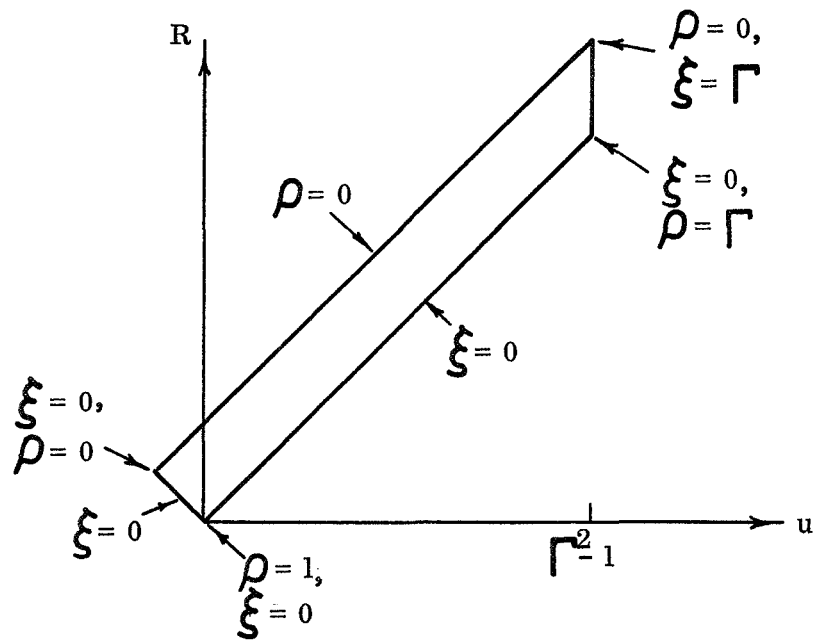


Figure 75. Schematic diagrams used in the calculation of the effect of penny-shaped cracks on the elastic compliance.

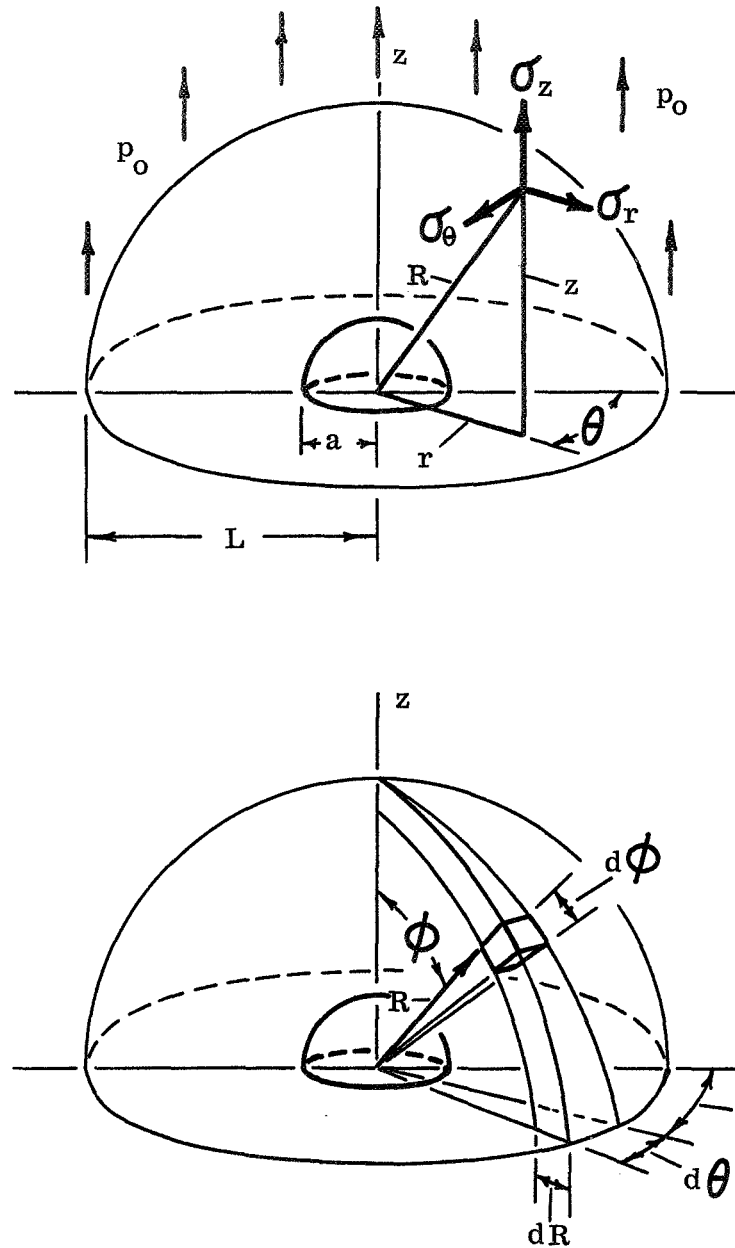
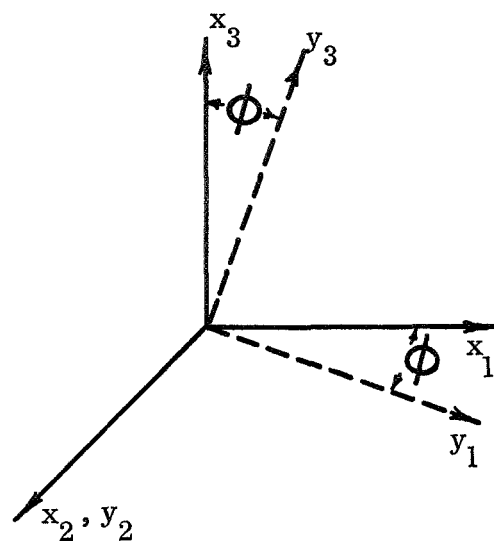


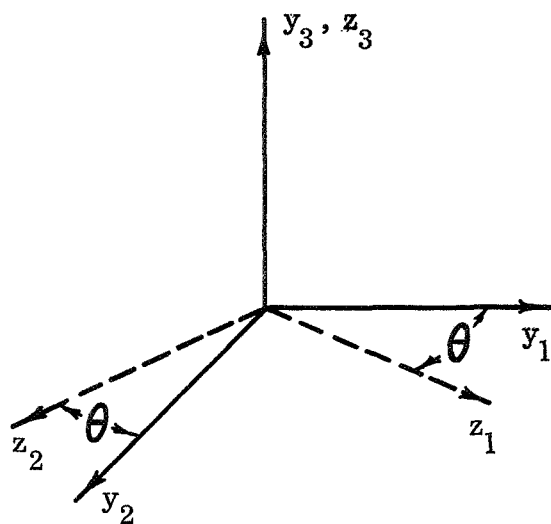
Figure 76. Schematic diagrams used in the calculation of the effect of spherical pores on the elastic compliance.

(a)



Direction Cosines
for Transformation

	x_1	x_2	x_3
y_1	$\cos \phi$	0	$-\sin \phi$
y_2	0	1	0
y_3	$\sin \phi$	0	$\cos \phi$



Direction Cosines
for Transformation

	y_1	y_2	y_3
z_1	$\cos \phi$	$\sin \phi$	0
z_2	$-\sin \phi$	$\cos \phi$	0
z_3	0	0	1

Figure 77. Axes rotations used in averaging model of Appendix D.

Table 1. The elastic constants of single crystal graphite, determined on compression-annealed pyrolytic graphite. (2)

Elastic Compliances $\times 10^{-13} \text{ cm.}^2/\text{dyne}$	Elastic Moduli $\times 10^{-13} \text{ dynes/cm.}^2$
$S_{11} = 0.98 \pm 0.03$	$C_{11} = 1.06 \pm 0.02$
$S_{12} = -0.16 \pm 0.06$	$C_{12} = 0.18 \pm 0.02$
$S_{13} = -0.033 \pm 0.08$	$C_{13} = 0.015 \pm 0.005$
$S_{33} = 27.5 \pm 1.0$	$C_{33} = 0.0365 \pm 0.001$
$*S_{44} = 29. \text{ to } 56.$	$*C_{44} = 0.00018 \text{ to } 0.00035$

* Range given by all authors:

$$S_{44} = 221. \text{ to } 10000.$$

$$C_{44} = 0.0001 \text{ to } 0.00452$$

Table 2. Poisson's ratios for several graphite grades.

Material	$\nu_{13} = \nu_{23} = -\frac{\epsilon_1}{\epsilon_3}^*$	$\nu_{31} = -\frac{\epsilon_3}{\epsilon_1}$	$\nu_{21} = -\frac{\epsilon_2}{\epsilon_1}$
ZTA	.06 (.05)**	.17 (.25)	.08 (.07)
ATJ	.10 (.11)	.14 (.16)	.10 (.10)
	ν		
AXF-5Q	.21		
AXZ	.23		

* Subscripts refer to strain axis orientation relative to the pressing direction :

1 : perpendicular

2 : perpendicular

3 : parallel

** () : Seldin's data. (10)

Table 3. The linear relationships between the various strain components.

Specimen Type	Experimental Constants				Calculated Constants, $n = 3$			
	P	$Q \times 10^{-6}$	R	$S \times 10^{-6}$	T	$U \times 10^{-6}$	V	$W \times 10^{-6}$
ZTA-90°	0.225	- 93	0.394	- 92	0.664	209	0.339	- 164
ZTA-60°	0.269	- 129	0.454	- 112	0.620	197	0.434	- 215
ZTA-30°	0.323	- 183	0.535	- 170	0.523	363	0.617	- 407
ZTA-0°	0.320	- 162	0.527	- 147	0.538	302	0.595	- 342
ATJ-90°	0.211	- 98	0.370	- 96	0.697	216	0.303	- 164
ATJ-0°	0.254	- 146	0.432	- 142	0.643	313	0.395	- 270
AXF-5Q	0.152	- 59	0.323	- 137	0.564	777	0.269	- 268
AXZ	0.163	- 99	0.316	- 120	0.659	405	0.247	- 199

Equations : $\epsilon_o = P \epsilon_m + Q$, $\epsilon_o = R \epsilon_{1/2} + S$, $\epsilon_{em} = T \epsilon_m + U$, $\epsilon_o = V \epsilon_{em} + W$

Table 4. Fracture toughness parameters for several graphite grades.

Specimen Type	Number of Specimens	K_{Ic} psi - in. ^{1/2}	G_{Ic} psi - in.
ZTA-0°	5	660 (20)*	.660 (.030)
ZTA-90°	6	1440 (80)	.760 (.040)
ATJ-0°	6	750 (20)	.580 (.040)
ATJ-90°	6	905 (20)	.580 (.040)
AXF-5Q	3	1120 (130)	.590 (.120)
AXZ	8	720 (100)	.360 (.080)

* () : One standard deviation.

Table 5. The parameters of the deformation equation for several graphite grades.

$$\epsilon = A_0 \sigma^{\exp} [k_p f_p + k_c (\epsilon_{em} - \epsilon_{th})] + C_0 [A_0 \sigma]^n + \epsilon_0$$

Specimen Type	No. of specs.	n	n = 3					ϵ_{th} $\times 10^{-6}$	\bar{B} $\times 10^{-16}$ psi ⁻³	C_o $\times 10^2$
			A_o $\times 10^{-6}$ psi ⁻¹	k_p	f_p	k_c				
ZTA-90°	5	3.2	.191 (.016)*	3.5	.165 (.016)	60 (12)	480	16 (6)	22 (4)	
ZTA-60°	4	2.3	.284 (.013)	3.5	.154 (.008)	146 (55)	490	89 (17)	39 (9)	
ZTA-30°	7	3.1	.618 (.025)	3.5	.145 (.008)	119 (65)	660	720 (40)	31 (6)	
ZTA-0°	6	2.7	.691 (.053)	3.5	.167 (.007)	120 (26)	570	1310 (230)	40 (5)	
ATJ-90°	5	3.2	.247 (.011)	3.5	.269 (.011)	28 (15)	680	43 (7)	28 (2)	
ATJ-0°	7	2.8	.375 (.012)	3.5	.266 (.010)	39 (19)	540	119 (10)	23 (3)	
AXF-5Q	5	3.2	.228 (.003)	3.5	.234 (.006)	44 (5)	1000	27 (2)	23 (2)	
AXZ	5	2.4	.249 (.004)	3.5	.330 (.013)	37 (7)	810	87 (11)	57 (4)	

* () : One standard deviation

Table 6. Fracture toughness data and failure criterion parameters.

Specimen Type	G_{Ic} psi-in.	E $\times 10^6$ psi	\bar{U}	σ_f psi	c in.	d $\times 10^{-3}$ in.	f_p	P_1	$F. C. = \left\{ \frac{\pi G_{Ic} E}{2 (1 - \bar{U}^2) d} \left[\frac{1 - f_p}{\bar{n}} \right]^{1/2} \right\}^{1/2}, \quad \bar{n} = \frac{\sum_{n=1}^{\infty} n P_1^n}{\sum_{n=1}^{\infty} P_1^n}$	
									\bar{n}	F. C.
ZTA-90°	0.760	2.72	.13	4530	.062	4.4	.158	.12	1.14	505
ZTA-60°	0.710 *	1.68	.12	3290	.080	4.4	.158	.32	1.47	298
ZTA-30°	0.650 *	0.781	.07	1740	.143	4.4	.158	.49	1.96	130
ZTA-0°	0.600	0.650	.06	1640	.146	4.4	.158	.56	2.27	108
ATJ-90°	0.580	1.51	.12	3490	.056	4.4	.271	.32	1.47	223
ATJ-0°	0.580	0.961	.10	2570	.059	4.4	.271	.42	1.72	131
AXF-5Q	0.590	1.62	.21	8270	.011	0.5	.235	.35	1.54	2200
AXZ	0.360	1.14	.23	4630	.016	0.5	.332	.35	1.54	892

* interpolation

APPENDIX A

A CALCULATION OF THE EFFECTS OF PENNY-SHAPED CRACKS ON THE ELASTIC COMPLIANCE OF AN ISOTROPIC BODY

The procedure used is to first establish the effect of a single crack on the overall elastic compliance, and then to assess the effect of adding a number of independent cracks into the body. For a polycrystalline body consisting of a collection of spherical particles, the compliance will be shown to be dependent only on the volume fraction of particles that have cracked and not on the crack sizes.

Sneddon⁽³⁴⁾ has determined the stress distributions in the neighborhood of a penny-shaped crack in a homogeneous isotropic material whose outside dimensions are very much greater than the radius of the crack. The calculations were made by first considering the infinite elastic media to be deformed by an internal pressure acting across the surfaces of the crack and then the effect of tensile stresses (equal to the pressure) applied to the body to free the internal crack of axial stresses were deduced. The stress equations are written in dimensionless cylindrical coordinates, and the strain in the axial direction can be determined by the relationship:

$$\epsilon_z = \frac{1}{E_i} [\sigma_z - \nu(\sigma_r + \sigma_\theta) + p_o] \quad (69)$$

where E_i is the elastic modulus of a crack free material, ν is Poisson's ratio, p_o is the internal pressure and σ_r and σ_θ are the

radial and tangential stresses respectively. Referring to Figure 74 (a), the average strain, $\bar{\epsilon}_z$ of the body containing the crack can be determined by integrating the strain over the entire body, adding the volume of the opened crack and dividing by the initial volume:

$$\bar{\epsilon}_z = \frac{2\pi \int_0^\Gamma \int_0^{\sqrt{\Gamma^2 - \rho^2}} \rho \epsilon_z d\xi d\rho + V_{oc}}{2\pi \int_0^\Gamma \int_0^{\sqrt{\Gamma^2 - \rho^2}} \rho d\xi d\rho} \quad (70)$$

where ρ is the radial distance divided by the radius of the crack, c ; ξ is the axial distance divided by the radius of the crack, Γ is the outer dimension of the sphere divided by the crack radius, and V_{oc} is the volume of the crack opened in the axial direction by the applied pressure, p_o . The compliance of the body containing the single crack can be determined by:

$$A = \epsilon_z / p_o \quad (71)$$

For a penny-shaped crack with an internal hydrostatic pressure applied normal to its surface, Snedden gives the following stress distribution equations:

$$\sigma_z = \frac{2p_o}{\pi} (c_1^o - s_o^o + \xi c_2^o - \xi s_1^o) \quad (72)$$

$$\sigma_r + \sigma_\theta + \sigma_z = \frac{4(1+\nu)}{\pi} p_o (c_1^o - s_o^o) \quad (73)$$

where

$$C_1^0 = R^{-1/2} \cos (\phi / 2) \quad (74)$$

$$C_2^0 = r R^{-3/2} \cos [(3\phi / 2) - \theta] \quad (75)$$

$$S_1^0 = R^{-1/2} \sin (\phi / 2) \quad (76)$$

$$S_0^0 = \tan^{-1} \left[\frac{R^{1/2} \sin (\phi / 2) + r \sin \theta}{R^{1/2} \cos (\phi / 2) + r \cos \theta} \right] \quad (77)$$

and

$$r^2 = 1 + \xi^2 \quad (78)$$

$$R^2 = (\rho^2 + \xi^2 - 1)^2 + 4\xi^2 \quad (79)$$

$$\tan \theta = 1 / \xi \quad (80)$$

$$\cot \phi = (\rho^2 + \xi^2 - 1) / 2\xi \quad (81)$$

By substitution into Equation 69, the axial strain is given by:

$$\epsilon_z = \frac{2p_0}{\pi E_i} \left[(1 - \nu - 2\nu^2) (C_1^0 - S_0^0) + (1 - \nu) (\xi C_2^0 - \xi S_1^0) + \frac{\pi}{2} \right] \quad (82)$$

The integration is simplified by the transformation of ρ - ξ coordinates to R-u coordinates which are related by:

$$u = \rho^2 + \xi^2 - 1 \quad (83)$$

$$R = (u^2 + 4\xi^2)^{1/2} \quad (84)$$

The limits of the integration must be suitably changed also to those shown on Figure 71 (b). When the integration of Equation 82 is carried out, the following results:

$$\int \epsilon_z^V = -\frac{4 p_o}{E_i} \left[\frac{2}{9} (1 - \nu - 2\nu^2) + \frac{1}{20} (1 - \nu) - \frac{\pi}{6} \Gamma^3 \right] \quad (85)$$

The displacements, W , of the surface of the crack due to the pressure p_o in the axial direction is derived by Snedden to be:

$$W = \frac{4 p_o (1 - \nu^2)}{\pi E_i} (1 - \rho^2)^{1/2} \quad (86)$$

The volume due to extension in axial direction is determined by integration over the crack surface:

$$V_{oc} = 2\pi \int_0^1 w \rho \, d\rho \quad (87)$$

and is found to be:

$$V_{oc} = 8 (1 - \nu^2) p_o / 3 E_i \quad (88)$$

The total volume of the hemisphere is:

$$2\pi \int \int \rho \, d\rho \, d\xi = \frac{2\pi}{3} \Gamma^3 \quad (89)$$

By substituting equations- 85, 88 and 89 into Equation 70, the average strain due to the introduction of a single small crack into a body under

a uniaxial stress is determined:

$$\bar{\epsilon}_z = \frac{p_o}{E_i} \left\{ 1 + \left[71 + 49\nu - 80\nu^2 \right] / 30\pi r^3 \right\} \quad (90)$$

The average compliance of the body with this crack is found by dividing both sides of the equation by the stress p_o , and

$$A = \frac{\bar{\epsilon}_z}{E_i} = A_i \left\{ 1 + \left[71 + 49\nu - 80\nu^2 \right] \frac{c^3}{30\pi L^3} \right\} \quad (91)$$

where A_i is the compliance of the crack free body, L is the outer dimension of the body where:

$$L = r c \quad (92)$$

Since the effect on the compliance of adding a single crack to a given material is:

$$A_1 = A_i (1 + k_c c^3 / L^3) \quad (93)$$

The effect of adding n independent cracks (spaced at least several crack diameters apart) will be given by:

$$A_n = A_i (1 + k_c c^3 / L^3) \quad (94)$$

where $k_c c^3 / L^3$ is the rate of compliance increase per crack given in Equation 91.

If the body is assumed to consist of a collection of spherical particles or grains and that these particles can crack independent of one another, then the volume fraction, f_c , of cracked particles will

be:

$$f_c = \frac{4 n \pi c^3 / 3}{4 \pi L^3 / 3} = n \frac{c^3}{L^3} \quad (95)$$

On substitution into the previous equation

$$A_n = A_i \left[1 + k_c c^3 / L^3 \right]^{f_c L^3 / c^3} \quad (96)$$

Taking the natural logarithm of this equation:

$$\ln A_n = \ln A_i + f_c \frac{L^3}{c^3} \ln \left[1 + k_c c^3 / L^3 \right] \quad (97)$$

or

$$\ln A_n = \ln A_i + f_c \frac{L^3}{c^3} \left[k_c \frac{c^3}{L^3} \right] \quad (98)$$

since $k_c c^3 / L^3$ is small compared to 1. Then,

$$\ln A_n = \ln A_i + k_c f_c \quad (99)$$

or

$$A_n = A_i \exp (k_c f_c) \quad (100)$$

The equivalent equation for the modulus of elasticity is

$$E_n = E_i \exp (- k_c f_c) \quad (101)$$

The constant, k_c , is related only to the Poisson's ratio of material. It is therefore shown that the elastic constants, A_n and E_n , are exponentially related only to the fraction of particles

APPENDIX B

A CALCULATION OF THE EFFECTS OF SPHERICAL VOIDS ON THE ELASTIC COMPLIANCE OF AN ISOTROPIC BODY

The procedure used is to establish the effect of a single spherical void on the overall elastic compliance, and then to assess the effect of a number of independent voids. The compliance for a given material will be shown to be dependent only on the volume fraction of pores and not on the pore sizes.

Southwell⁽³⁵⁾ has determined the stress distribution in the neighborhood of a small spherical flaw in a homogeneous isotropic body when the stress at points far away from the flaw is uniform uniaxial tension. Referring to Figure 75 (a), in cylindrical coordinates, these are given to be:

$$\sigma_r = \frac{p_0}{14 - 10\nu} \frac{a^3}{R^3} \left[9 - 15\nu - 12 \frac{a^2}{R^2} - \frac{r^2}{R^2} \left(72 - 15\nu - 105 \frac{a^2}{R^2} \right) + 15 \frac{r^4}{R^4} \left(5 - 7 \frac{a^2}{R^2} \right) \right] \quad (102)$$

$$\sigma_\theta = \frac{p_0}{14 - 10\nu} \frac{a^3}{R^3} \left[9 - 15\nu - 12 \frac{a^2}{R^2} - 15 \frac{r^2}{R^2} \left(1 - 2\nu - \frac{a^2}{R^2} \right) \right] \quad (103)$$

$$\sigma_z = p_0 \left\{ 1 - \frac{1}{14 - 10\nu} \frac{a^3}{R^3} \left[38 - 10\nu - 24 \frac{a^2}{R^2} - \frac{r^2}{R^2} \left(117 - 15\nu - 120 \frac{a^2}{R^2} \right) + 15 \frac{r^4}{R^4} \left(5 - 7 \frac{a^2}{R^2} \right) \right] \right\} \quad (104)$$

where σ_r , σ_θ , and σ_z are respectively to the radial, tangential and axial stresses, p_0 is the applied stress in the axial direction z ,

is Poisson's ratio, a is the radius of the spherical pore, r is the radial distance from the origin, and

$$R = (z^2 + r^2)^{1/2} \quad (105)$$

The strain in the axial direction, ϵ_z , can be determined from:

$$\epsilon_z = \frac{1}{E_i} [\sigma_z - \nu(\sigma_r + \sigma_\theta)] \quad (106)$$

where E_i is the modulus of elasticity of the material, free of voids.

Noting that

$$r / R = \sin\phi \quad (107)$$

the axial strain can be written as:

$$\begin{aligned} \epsilon_z = \frac{P_o}{E_i} \left\{ 1 + \frac{1}{14 - 10\nu} \left[(30\nu^2 - 8\nu - 38) \frac{a^3}{R^3} \right. \right. \\ + 24(1 + \nu) \frac{a^5}{R^5} + (117 + 72\nu - 45\nu^2) \frac{a^3}{R^3} \sin^2\phi \\ - 120(1 - \nu) \frac{a^5}{R^5} \sin^2\phi - 75(1 + \nu) \frac{a^3}{R^3} \sin^4\phi \\ \left. \left. + 105(1 + \nu) \frac{a^5}{R^5} \sin^4\phi \right] \right\} \end{aligned} \quad (108)$$

The average strain ϵ_z of the body containing the void can be determined by integrating the above strain over the entire body, adding the integrated displacement of the surface of the void in the axial direction V , and dividing by the initial volume. To simplify the integration, it is done in spherical coordinates, Figure 72 (b), and:

$$\epsilon_z = \frac{2\pi \int_0^{\pi/2} \int_a^L R^2 \epsilon_z \sin\phi \, dR \, d\phi + \Delta V_p}{2\pi \int_0^{\pi/2} \int_a^L R^2 \sin\phi \, dR \, d\phi} \quad (109)$$

The integration of equation 108 results in:

$$\int^V \epsilon_z = L^3 - a^3 - \frac{72(1+\nu)}{14-10\nu} a^5 \left(\frac{1}{L^2} - \frac{1}{a^2} \right) \quad (110)$$

The displacement, W , of the surface of the void in the axial direction can be written as: ⁽³⁴⁾

$$W = \frac{4 p_o (1-\nu^2)}{\pi E_i} (c^2 - r^2)^{1/2} \quad (111)$$

The volume change due to the extension in the axial direction, ΔV_p , is found by integration of this equation:

$$\Delta V_p = 2\pi \left[\frac{4 p_o (1-\nu^2)}{\pi E_i} \right] \int_0^a r (a^2 - r^2)^{1/2} dr \quad (112)$$

which becomes:

$$\Delta V_p = \frac{8 p_o (1-\nu^2)}{3 E_i} a^3 \quad (113)$$

Finally, the initial volume is found to be:

$$V_i = \frac{2\pi}{3} (L^3 - a^3) \quad (114)$$

By substituting equations 110, 113 and 114 into equation 109, the average strain due to the introduction of a single small spherical pore into a body under a uniaxial stress is determined:

$$\bar{\epsilon}_z = \frac{p_o}{E_i} \left[1 + \frac{72(1+\nu)}{14-10\nu} \frac{a^3 (L^2 - a^2)}{L^2 (L^3 - a^3)} + \frac{4(1-\nu^2)}{\pi} \frac{a^3}{(L^3 - a^3)} \right] \quad (115)$$

Since a is very much smaller than L , the compliance may be written as:

$$A = \frac{\bar{\epsilon}_z}{p_o} = A_i \left\{ 1 + \left[\frac{72(1+\nu)}{14-10\nu} + \frac{4(1-\nu^2)}{\pi} \right] \frac{a^3}{L^3} \right\} \quad (116)$$

or for a given material:

$$A = A_i (1 + k_p a^3 / L^3) \quad (117)$$

The effect of adding n independent pores (spaced at least several pore diameters apart) will be given by:

$$A_n = A_i (1 + k_p a^3 / L^3)^n \quad (118)$$

where $k_p a^3 / L^3$ is the rate of compliance increase per pore. The volume fraction of pores is given by:

$$f_p = \frac{4 n \pi a^3 / 3}{4 \pi L^3 / 3} = n \frac{a^3}{L^3} \quad (119)$$

On substitution into the previous equation:

$$A_n = A_i (1 + k_p a^3 / L^3)^{f_p L^3 / a^3} \quad (120)$$

Taking the natural logarithm of this equation:

$$\ln A_n = \ln A_i + f_p \frac{L^3}{a^3} \ln (1 + k_p a^3 / L^3) \quad (121)$$

or

$$\ln A_n = \ln A_i + f_p \frac{L^3}{a^3} (k_p \frac{a^3}{L^3}) \quad (122)$$

since $k_p a^3 / L^3$ is small compared to 1. Then

$$\ln A_n = \ln A_i + k_p f_p \quad (123)$$

and

$$A_n = A_i \exp (k_p f_p) \quad (124)$$

The equivalent equation for the modulus of elasticity is:

$$E_n = E_i \exp (-k_p f_p) \quad (125)$$

The constant, k_p , is related only to the Poisson's ratio of the material.

It is therefore shown that the elastic constants, A_n and E_n , are exponentially related to the fraction of pores only, and not on the pore size.

APPENDIX C

Uniaxial pressing used in the production of certain synthetic graphites causes the layer planes of the crystallites to be preferentially oriented perpendicular to the pressing direction. This produces anisotropic graphite blocks which have an axis of rotational symmetry with isotropic planes normal to this axis. The magnitude of the preferred orientation can be determined by X-ray diffraction methods. This is achieved by: (a) cutting a thin slab whose plane is normal to the plane of isotropy; and (b) determining the relative intensity of the diffraction of (0002) planes as a function of the angle from the pressing direction. This procedure measures the relative density of c-axes in the plane. It is of interest, however, to obtain the relative density of c-axes per unit of solid angle in the volume in order to relate these measurements to the bulk materials properties. The purpose of this section is to establish the transformation equations to accomplish this.

The procedure used is a modification of that given by Bacon.⁽²⁵⁾ Referring to Figure 56, the relative intensities, $I(\phi)$, as a function of angle ϕ from the pressing direction are schematically shown in (a) and (b). To determine volume density distribution, Bacon considered the solid angle element between the angles ϕ and $(\phi + d\phi)$, and ξ and $(\xi + d\xi)$ as shown in Figure 56 (c). The size of this element is:

$$dV = \sin\phi \, d\phi \, d\xi \quad (126)$$

The number of crystallites which have their c-axes within this angle is proportional to:

$$I(\phi) dV = I(\phi) \sin\phi d\phi d\xi \quad (127)$$

Bacon shows that if some property, $M(\phi)$, is known for the crystallite as a function of the orientation angle, ϕ , then the average property, \bar{M}_{x_3} in the direction of the axis of symmetry, x_3 , can be determined by:

$$\bar{M}_{x_3} = \frac{\int_0^{2\pi} \int_0^{\pi/2} M(\phi) I(\phi) \sin\phi d\phi d\xi}{\int_0^{2\pi} \int_0^{\pi/2} I(\phi) \sin\phi d\phi d\xi} \quad (128)$$

He also gives the equation to determine the properties in a direction perpendicular to the axis of symmetry.

The purpose of the following is to extend the treatment to determine the equations which can be used to find the average properties at any angle. This will be done by transforming the intensity vector to a new set of coordinates rotated to the direction of interest. Referring to Figure 57, the pressing direction is taken to be x_3 , and the plane of isotropy is x_1 - x_2 . It is of interest to determine the properties in the y_3 direction, rotated at some angle α from x_3 about x_2 .

For pressed graphites the measured intensity of (0002) planes in the x_1 - x_3 plane as a function of the angle ϕ can be written in terms of a Fourier series:

$$I(\phi) = W + X \cos 2\phi + Y \cos 4\phi + Z \cos 6\phi \quad (129)$$

where W,X,Y and Z are experimentally determined constants for the particular graphite. Using the identity:

$$\cos 2\phi = 2 \cos^2 \phi - 1 \quad (130)$$

the Fourier equation can be rewritten:

$$I(\phi) = 32Z \cos^6 \phi + (8Y - 48Z) \cos^4 \phi + (2X - 8Y + 18Z) \cos^2 \phi + W - X + Y - Z \quad (131)$$

The $\cos \phi$ term can be transformed to the new coordinate system by:

$$\cos \phi = \cos K \cos \alpha - \sin K \cos \beta \sin \alpha \quad (132)$$

On substitution of equation 132 into equation 131, the intensity becomes:

$$\begin{aligned} I(K, \beta, \alpha) = & 32Z [A^6 - 6A^5 C \cos \beta + 15A^4 C^2 \cos^2 \beta - 20A^3 C^3 \cos^3 \beta \\ & + 480A^2 C^4 \cos^4 \beta - 6AC^5 \cos^5 \beta + C^6 \cos^6 \beta] \\ & + (8Y - 48Z) [A^4 - 4A^3 C \cos \beta + 6A^2 C^2 \cos^2 \beta - 4AC^3 \cos^3 \beta \\ & + C^4 \cos^4 \beta] + (2X - 8Y + 18Z) [A^2 - 2AC \cos \beta + C^2 \cos^2 \beta] \\ & + W - X + Y - Z \end{aligned} \quad (133)$$

where

$$A = \cos K \cos \alpha \quad (134)$$

and

$$C = \sin K \sin \alpha \quad (135)$$

To determine the relative intensity of crystallites which have their c-axes within the solid conical angle between K and $K + dK$,

equation 133 must be integrated with respect to β , to produce a new intensity function:

$$L(K, \alpha) \sin K \, dK = \int_0^{2\pi} [I(K, \beta, \alpha) \sin K \, dK] d\beta \quad (136)$$

and

$$\begin{aligned} L(K, \alpha) \sin K \, dK = 2\pi \left\{ 2Z \left[16 \cos^6 K \cos^6 \alpha + 120 \cos^4 K \cos^4 \alpha \sin^2 K \sin^2 \alpha \right. \right. \\ \left. \left. + 90 \cos^2 K \cos^2 \alpha \sin^4 K \sin^4 \alpha + 5 \sin^6 K \sin^6 \alpha \right] \right. \\ \left. + 8(Y - 6Z) \left[\cos^4 K \cos^4 \alpha + 3 \cos^2 K \cos^2 \alpha \sin^2 K \sin^2 \alpha \right. \right. \\ \left. \left. + 0.375 \sin^4 K \sin^4 \alpha \right] + (X - 4Y + 9Z) \left[2 \cos^2 K \cos^2 \alpha \right. \right. \\ \left. \left. + \sin^2 K \sin^2 \alpha \right] + W - X + Y - Z \right\} \sin K \, dK \quad (137) \end{aligned}$$

This equation then gives the relative density of c-axes at any angle K from an axis that has been rotated from the pressing direction by an angle α . Therefore, the average property, \bar{M}_α , at any angle α from the pressing direction may be determined by:

$$\bar{M}_\alpha = \frac{\int_0^{\pi/2} M(K) L(K, \alpha) \sin K \, dK}{\int_0^{\pi/2} L(K, \alpha) \sin K \, dK} \quad (138)$$

where $M(K)$ is equivalent to $M(\phi)$.

APPENDIX D

A DETERMINATION OF THE ELASTIC MODULI OF POLYCRYSTALLINE GRAPHITES
FROM THE ELASTIC CONSTANTS OF SINGLE CRYSTALS - USING A PARTICLE
PAIR CONSTANT STRAIN MODEL

The purpose of this section is to establish an averaging technique whereby the elastic moduli of bulk polycrystalline materials can be determined from knowledge of the elastic properties of the hexagonal crystal and of the orientations of those crystals. The elastic constants of single crystals of graphite have been determined by several investigators and a summary of these results has been given by Blakslee, et.al.⁽²⁾ With the exception of c_{44} there is reasonable agreement between the values. The basal plane shear constant appears to be dependent on the degree of dislocation pinning. The values of the c_{ij} and the s_{ij} including the range of c_{44} and s_{44} reported by the cited authors are given in Table 1. The orientations of the crystallites can be determined from X-ray diffraction techniques by determining the relative intensity of (0002) plane diffractions as a function of the angle from the axis of symmetry of the bulk material. From this planar determination, the relative density of basal plane normals per unit solid conical angle can be calculated using the methods arrived at in Appendix C. These densities when divided by the integrated density over all angles give the measured probability that a crystallite is oriented at a given angle from the applied stress direction.

Averaging techniques are all based on multiplying this probability by the crystal property (e.g., the elastic modulus) at the particular angle and summing the results over all orientations. The techniques developed differ from one another depending on whether the material is considered to be in a state of constant applied stress or constant applied strain, i.e., whether the individual crystallites are considered to be loaded in series or parallel. These models give the extrema of the averaging models, the actual state being intermediate to these. Modified models have also been developed. These consider pairs of particles and from the average crystal properties of the pairs (in parallel or in series) and the probabilities of the single particles forming the given pairs, the bulk polycrystalline properties can be calculated. Therefore, the constant stress model is modified by considering the pairs to be in constant strain with respect to one another, and the constant strain model is modified by having the individual pairs in a constant stress state. The four models are shown in Figure 61. It should be noted that models can also be modified by considering triplets, or larger groups treated analogously.

The following is the procedure used to determine the bulk properties of the polycrystalline materials using the model in which single particles form pairs with other particles in series, and the pairs are in turn parallel to one another, as in Figure 61 (d). There are two possible ways of performing the calculations: (a) the individual particles can be considered to be very much longer in the applied stress direction

than transverse to it, or (b) they can be considered to be relatively short in the applied stress direction. In case (a) the transverse strain interactions between particles can be ignored and the transverse stresses set to zero. This is essentially the procedure suggested by Slagle.⁽³²⁾ In case (b), each particle is considered to be fixed to its pair partner, and transverse strain interactions give rise to transverse stresses. This in turn modifies the axial stress in the pair subjected to a constant axial strain. Both cases will be considered.

D.1 Particle Pairs under Constant Strain with No Transverse Strain Interaction

The elastic constants as a function of the crystal orientation from the principle directions can be determined from transformations given in the theory of elasticity.⁽³⁶⁾ For hexagonal symmetry, the crystal has only five independent elastic compliances, s_{ij} : s_{11} , s_{12} , s_{13} , s_{33} , s_{44} . In the model under consideration, it is of interest to determine only one rotationally transformed compliance, s'_{33} , due to rotation by an angle ϕ about an axis in the plane of isotropy is given by:

$$s'_{33} = s_{11} \sin^4 \phi + s_{33} \cos^4 \phi + (s_{44} + 2s_{13}) \sin^2 \phi \cos^2 \phi \quad (139)$$

There will, of course, be a distribution of rotations about the axis of symmetry, but this is irrelevant in this model. The modulus of elasticity in the rotated orientation is given by the reciprocal of s'_{33} .

The density of basal plane normals per solid conical angle are determined by the methods outlined in Appendix C. To determine the properties of the bulk material in some direction, α , from the pressing

direction, the value of α and the Fourier constants must be first substituted into equation 137 to determine the proper distribution function, $L(K, \alpha) \sin K$. From this function a new distribution function must next be generated, i.e., the one for the particle pairs. It can be shown from probability theory, that for large numbers of particles the probability that two particles of the same orientation, $P(i)$, form a pair, is given by:

$$P_{ii} = P(i) / \left[\sum P(i) \right]^2 \quad (140)$$

where $\sum P(i)$ is the sum of the probabilities over all orientations.

Also, the probability that two particles of different orientations, $P(i)$ and $P(j)$, form a pair is given by:

$$P_{ij} = 2 P(i) P(j) / \left[\sum P(i) \right]^2 \quad (141)$$

The average elastic modulus for a single pair of like orientations in constant strain is:

$$E_{ii} = \frac{P(i)^2}{s'_{33}(i) \left[\sum P(i) \right]^2} \quad (142)$$

For unlike pairs the average modulus is:

$$E_{ij} = \frac{2 P(i) P(j)}{\left[\sum P(i) \right]^2 \left[s'_{33}(i) + s'_{33}(j) \right] / 2} \quad (143)$$

These last two relationships result from the condition that the stresses are equal in each of the particles, and the strains in each must sum to the total applied strain.

The next step in the procedure is to divide the distribution $L(K, \alpha) \sin K$ into m equal parts with respect to the angle K (between

0 and $\pi/2$) and to characterize each interval by a value of $s'_{33}(K)$ at the midpoint. Setting

$$P(i) = L\left(\frac{\pi i}{4m}, \alpha\right) \sin\left(\frac{\pi i}{4m}\right), \quad i = 1, 2, \dots, m \quad (144)$$

then the average modulus for the bulk material for this model is:

$$E = \left[\sum_{i=1}^m \frac{P(i)^2}{s'_{33}(i)} + \sum_{i=1}^{m-1} \sum_{j=i+1}^m \frac{4 P(i) P(j)}{[s'_{33}(i) + s'_{33}(j)]} \right] \left[\sum_{i=1}^m P(i) \right]^2 \quad (145)$$

A computer program written in FORTRAN IV is presented in the back of this appendix.

D.2 Particle Pairs under Constant Strain with Transverse Strain Interaction

The basis for this treatment is that when a pair of differentially oriented particles in series is subjected to a constant strain, the stresses in each adjust so as to minimize the total strain energy. If, as in the previous model, there were no lateral constraints, the particles would extend different amounts in the transverse directions. Fixing two particles to one another causes the transverse strains to be equal in any given lateral direction, creating tensile stresses in one particle and compressive stresses in the other. By Hooke's Law the longitudinal stresses must therefore be effected. To determine the average elastic modulus of each pair, this longitudinal stress must be determined and divided by the applied strain. The procedure used in this averaging model is many times more complex since it involves

rotations about two axes, the need to determine all the transformed elastic compliances, and the solution of six simultaneous equations to determine the average elastic compliances for each particle pair.

As in the previous model, the elastic compliances due to a rotation about an axis in the isotropic plane must be determined. However, all thirteen require evaluation. Since the rotation about the stress axis of one particle relative to the other is pertinent in this model, another transformation must be performed. This is shown in Figure 76(b). The latter transformation generates twenty-one new compliances for each new orientation.

To determine the average modulus of elasticity of a particle pair of given orientations, a set of simultaneous equations are written by adding the Hookean equations for the longitudinal strains in each particle and subtracting the others:

$$\epsilon_a = \epsilon_3^a + \epsilon_3^b = \sum_{i=1}^6 (s_{i3}^a + s_{i3}^b) \sigma_i = 1 \quad (146)$$

$$\epsilon_j^a - \epsilon_j^b = \sum_{i=1}^6 (s_{ij}^a - s_{ij}^b) \sigma_i = 0 \quad , \quad j = 1, 2, 4, 5, 6 \quad (147)$$

where the superscripts refer to one or the other particle in a given pair, ϵ_a is the applied longitudinal strain, ϵ_3 is the longitudinal strain in each particle, the ϵ_j are the transverse and shear strains, and the σ_i are the stress components. The average modulus is determined by setting ϵ_a to unity, solving the equations for σ_3 , and dividing by 2.

The averaging procedure is similar to the one described before,

with the additional complication of the necessity to average the values obtained from the second rotation. The rotation of one particle relative to the other about the applied stress axis was accounted for in the following manner. One of the particles was held fixed and the other rotated at intervals of $\pi/10$ from 0 to π . The average particle pair compliance was determined at each interval, and the values at the 10 intervals were in turn averaged. This latter value provided the input of $s'_{33} \text{ (i)}$ and $[s'_{33} \text{ (i)} + s'_{33} \text{ (j)}]$ in equation 145, from which the grand average bulk modulus was determined.

The computer program used is presented in the back of this appendix. The transformation equations were not previously given since they are contained therein.


```

2  READ (5,2) M2,H2,W,X,Y,Z
   FORMAT (I3,E6.3,4E10.4)
3  READ (5,3) A11,A12,A13,A33,A44
   FORMAT (5E10.3)
   M4=M2-1
   H=1.570796/H2
   A(1)=H/2
   DO 6 I=1,M4
6  A(I+1)=A(I)+H
   COMPLIANCES# Y-AXIS ROTATION
   DO 7 I=1,M2
   P00(I)=P0(A(I))
   P30(I)=P3(A(I))
   P60(I)=P6(A(I))
   P90(I)=P9(A(I))
   S33(I)=R33(A(I))
7  WRITE (6,8)
8  FORMAT (///6H LOOP1)
   DIAGONAL WEIGHTED MODULI
   SUM1=0.
   SUM4=0.
   SUM7=0.
   SUM10=0.
   SUM3=0.
   SUM6=0.
   SUM9=0.
   SUM12=0.
   DO 40 I=1,M2
   SUM3=SUM3+P00(I)
   SUM6=SUM6+P30(I)
   SUM9=SUM9+P60(I)
   SUM12=SUM12+P90(I)
9  SUM1=SUM1+P00(I)**2/S33(I)
   SUM4=SUM4+P30(I)**2/S33(I)
   SUM7=SUM7+P60(I)**2/S33(I)
   SUM10=SUM10+P90(I)**2/S33(I)
40 CONTINUE
   WRITE (6,10)
10 FORMAT (6H LOOP2)
   NON-DIAGONAL WEIGHTED MODULI
   SUM2=0.
   SUM5=0.
   SUM8=0.
   SUM11=0.
   DO 50 I=1,M4
   K=I+1

```



```

DO 51 J=K,M2
SUM2=SUM2+(P00(I)*P00(J))/(S33(I)+S33(J))
SUM5=SUM5+(P30(I)*P30(J))/(S33(I)+S33(J))
SUM8=SUM8+(P60(I)*P60(J))/(S33(I)+S33(J))
SUM11=SUM11+(P90(I)*P90(J))/(S33(I)+S33(J))
51 CONTINUE
50 WRITE (6,13)
13 FORMAT (6H LOOP3)
EOAV=(SUM1+4.*SUM2)/SUM3**2
E30AV=(SUM4+4.*SUM5)/SUM6**2
E60AV=(SUM7+4.*SUM8)/SUM9**2
E90AV=(SUM10+4.*SUM11)/SUM12**2
EE0AV=EOAV/69000.
EE30AV=E30AV/69000.
EE60AV=E60AV/69000.
EE90AV=E90AV/69000.
WRITE (6,14) M2,W,X,Y,Z
140FORMAT (12H INTERVALS=,I3,3H W=,E14.7,3H X=,E14.7,3H Y=,E14.7,
13H Z=,E14.7)
WRITE (6,15) A11,A12,A13,A33,A44
15 FORMAT (5H A11=,E11.4,5H A12=,E11.4,5H A13=,E11.4,5H A33=,E11.4,
15H A44=,E11.4)
WRITE (6,16) SUM1,SUM2,SUM3,SUM4,SUM5,SUM6
16 FORMAT (6E15.8)
WRITE (6,17) SUM7,SUM8,SUM9,SUM10,SUM11,SUM12
17 FORMAT (6E15.8)
WRITE (6,18) EOAV,EE0AV
18 FORMAT (21H AVERAGE MODULUS(00)=,E15.8,6HDSC
,E15.8)
WRITE (6,19) E30AV,EE30AV
19 FORMAT (21H AVERAGE MODULUS(30)=,E15.8,6HDSC
,E15.8)
WRITE (6,20) E60AV,EE60AV
20 FORMAT (21H AVERAGE MODULUS(60)=,E15.8,6HDSC
,E15.8)
WRITE (6,21) E90AV,EE90AV
21 FORMAT (21H AVERAGE MODULUS(90)=,E15.8,6HDSC
,E15.8)
90 CONTINUE
END

```

[illegible]

UU

00

00

30

50

30

U

U

U

00

U

00

UU

0

U

3

```

R13(S)=(A11+A33-A44)*(SIN(S)*COS(S)**2+A13*(SIN(S)**4+COS(S)**4)
R15(S)=(2.*A11-2.*A13-A44)*SIN(S)*COS(S)**3+(2.*A13+A44-2.*A33)*
1COS(S)*SIN(S)**3
R22(S)=A22*(SIN(S)**2+COS(S)**2)
R23(S)=A12*SIN(S)**2+A13*COS(S)**2
R25(S)=2.*(A12-A13)*SIN(S)*COS(S)
R33(S)=A11*SIN(S)**4+A33*COS(S)**4+(A44+2.*A13)*(SIN(S)*COS(S)**2
OR35(S)=(2.*A11-2.*A13-A44)*COS(S)*SIN(S)**3+(2.*A13+A44-2.*A33)*
1SIN(S)*COS(S)**3
R44(S)=2.*(A11-A12)*SIN(S)**2+A44*COS(S)**2
R46(S)=(2.*A11-2.*A12-A44)*SIN(S)*COS(S)
OR55(S)=4.*(A11+A33-2.*A13)*(SIN(S)*COS(S)**2+A44*(COS(S)**2
1-SIN(S)**2)**2
R66(S)=2.*(A11-A12)*COS(S)**2+A44*SIN(S)**2
FUNCTIONS#ROTATION ABOUT Z
T11(S)=B11*COS(S)**4+(B66+2.*B12)*(COS(S)*SIN(S)**2+B22*SIN(S)**4
T12(S)=(B11+B22-B66)*(SIN(S)*COS(S)**2+B12*(COS(S)**4+SIN(S)**4)
T13(S)=B13*COS(S)**2+B23*SIN(S)**2
T14(S)=(B46-B15)*SIN(S)*COS(S)**2-B25*SIN(S)**3
T15(S)=(B25+B46)*COS(S)*SIN(S)**2+B15*COS(S)**3
T16(S)=(2.*B12-2.*B11+B66)*SIN(S)*COS(S)**3+(2.*B22-2.*B12-B66)
1*COS(S)*SIN(S)**3
T22(S)=B11*SIN(S)**4+(B66+2.*B12)*(SIN(S)*COS(S)**2+B22*COS(S)**4
T23(S)=B13*SIN(S)**2+B23*COS(S)**2
T24(S)=-B15*SIN(S)**3+(-B25-B46)*COS(S)**2*SIN(S)
T25(S)=(B15-B46)*COS(S)*SIN(S)**2+B25*COS(S)**3
T26(S)=(2.*B12-2.*B11+B66)*SIN(S)**3*COS(S)+
1(2.*B22-2.*B12-B66)*SIN(S)*COS(S)**3
T33(S)=B33*(SIN(S)**2+COS(S)**2)
T34(S)=-B35*SIN(S)
T35(S)=B35*COS(S)
T36(S)=2.*(B23-B13)*SIN(S)*COS(S)
T44(S)=B44*COS(S)**2+B55*SIN(S)**2
T45(S)=(B44-B55)*SIN(S)*COS(S)
T46(S)=(2.*B15-2.*B25-B46)*COS(S)*SIN(S)**2+B46*COS(S)**3
T55(S)=B44*SIN(S)**2+B55*COS(S)**2
T56(S)=(B46-2.*B15+2.*B25)*SIN(S)*COS(S)**2-B46*SIN(S)**3
T66(S)=4.*(B11+B22-2.*B12)*(SIN(S)*COS(S)**2+
1B66*(COS(S)**2-SIN(S)**2)**2
FUNCTIONS# PROBABILITIES
OP0(S)=(64.*Z*COS(S)**6+(16.*Y-96.*Z)*COS(S)**4+(4.*X-16.*Y+
136.*Z)*COS(S)**2+2.*(W-X+Y-Z))*SIN(S)
OP3(S)=(Z*(27.*COS(S)**6+67.5*COS(S)**4*SIN(S)**2+3125*SIN(S)**6)
1+(9.*Y-54.*Z)*(COS(S)**4+2.*(COS(S)*SIN(S)**2+SIN(S)**4/24)
2+(X-4.*Y+9.*Z)*(3.*COS(S)**2+5*SIN(S)**2)*(W-X+Y-Z))*SIN(S)
OP6(S)=(Z*(COS(S)**6+22.5*(COS(S)**2*SIN(S)**2+8.4375*SIN(S)**6)

```

C

C

```

1+(Y-6.*Z)*(COS(S)**4+9.*(COS(S)*SIN(S))**2+3.375*SIN(S)**4)
2+(X-4.*Y+9.*Z)*(COS(S)**2+1.5*SIN(S)**2)+2.*(W-X+Y-Z)*SIN(S)
OP9(S)=(20.*Z*SIN(S)**6+(6.*Y-36.*Z)*SIN(S)**4+(2.*X-8.*Y+
118.*Z)*SIN(S)**2+2.*(W-X+Y-Z))*SIN(S)
WRITE(6,1)
1 FORMAT(36H1TWO PART MOD COMB STAT CONST STRAIN)
4 READ(5,4) NN
4 FORMAT(I3)
DO 90 N=1,NN
READ(5,2) M2,H2,W,X,Y,Z
2 FORMAT(I3,E6.3,4E10.4)
READ(5,3) A11,A12,A13,A33,A44
3 FORMAT(5E10.3)
M4=M2-1
H=1.570796/H2
A(1)=H/2
DO 6 I=1,M4
6 A(I+1)=A(I)+H
COMPLIANCES# Y-AXIS ROTATION
DO 7 I=1,M2
S11(I,1)=R11(A(I))
S12(I,1)=R12(A(I))
S13(I,1)=R13(A(I))
S14(I,1)=0.
S15(I,1)=R15(A(I))
S16(I,1)=0.
S22(I,1)=R22(A(I))
S23(I,1)=R23(A(I))
S24(I,1)=0.
S25(I,1)=R25(A(I))
S26(I,1)=0.
S33(I,1)=R33(A(I))
S34(I,1)=0.
S35(I,1)=R35(A(I))
S36(I,1)=0.
S44(I,1)=R44(A(I))
S45(I,1)=0.
S46(I,1)=R46(A(I))
S55(I,1)=R55(A(I))
S56(I,1)=0.
S66(I,1)=R66(A(I))
PROBABILITIES
P00(I)=P0(A(I))
P30(I)=P3(A(I))
P60(I)=P6(A(I))
7 P90(I)=P9(A(I))

```

C

```

C COMPLIANCES# Z-AXIS ROTATION
G(1)=0.
DO 30 J=1,10
30 G(J+1)=G(J)+.3141592
DO 31 I=1,M2
B11=S11(I,1)
B12=S12(I,1)
B13=S13(I,1)
B15=S15(I,1)
B22=S22(I,1)
B23=S23(I,1)
B25=S25(I,1)
B33=S33(I,1)
B35=S35(I,1)
B44=S44(I,1)
B46=S46(I,1)
B55=S55(I,1)
B66=S66(I,1)
DO 32 J=2,11
S11(I,J)=T11(G(J))
S12(I,J)=T12(G(J))
S13(I,J)=T13(G(J))
S14(I,J)=T14(G(J))
S15(I,J)=T15(G(J))
S16(I,J)=T16(G(J))
S22(I,J)=T22(G(J))
S23(I,J)=T23(G(J))
S24(I,J)=T24(G(J))
S25(I,J)=T25(G(J))
S26(I,J)=T26(G(J))
S33(I,J)=T33(G(J))
S34(I,J)=T34(G(J))
S35(I,J)=T35(G(J))
S36(I,J)=T36(G(J))
S44(I,J)=T44(G(J))
S45(I,J)=T45(G(J))
S46(I,J)=T46(G(J))
S55(I,J)=T55(G(J))
S56(I,J)=T56(G(J))
S66(I,J)=T66(G(J))
32 CONTINUE
31 WRITE(6,8)
8 FORMAT (///6H LOOP1)
C DIAGONAL WEIGHTED MODULI
SUM1=0.
SUM4=0.

```

```

SUM7=0.
SUM10=0.
SUM3=0.
SUM6=0.
SUM9=0.
SUM12=0.
DO 40 I=1,M2
SUM3=SUM3+P00(I)
SUM6=SUM6+P30(I)
SUM9=SUM9+P60(I)
SUM12=SUM12+P90(I)
DO 41 J=1,11
AA(1)=S33(I,1)+S33(I,J)
AA(2)=S13(I,1)-S13(I,J)
AA(3)=S23(I,1)-S23(I,J)
AA(4)=S34(I,1)-S34(I,J)
AA(5)=S35(I,1)-S35(I,J)
AA(6)=S36(I,1)-S36(I,J)
AA(7)=S13(I,1)-S13(I,J)
AA(8)=S11(I,1)+S11(I,J)
AA(9)=S12(I,1)+S12(I,J)
AA(10)=S14(I,1)+S14(I,J)
AA(11)=S15(I,1)+S15(I,J)
AA(12)=S16(I,1)+S16(I,J)
AA(13)=S23(I,1)-S23(I,J)
AA(14)=S12(I,1)+S12(I,J)
AA(15)=S22(I,1)+S22(I,J)
AA(16)=S24(I,1)+S24(I,J)
AA(17)=S25(I,1)+S25(I,J)
AA(18)=S26(I,1)+S26(I,J)
AA(19)=S34(I,1)-S34(I,J)
AA(20)=S14(I,1)+S14(I,J)
AA(21)=S24(I,1)+S24(I,J)
AA(22)=S44(I,1)+S44(I,J)
AA(23)=S45(I,1)+S45(I,J)
AA(24)=S46(I,1)+S46(I,J)
AA(25)=S35(I,1)-S35(I,J)
AA(26)=S15(I,1)+S15(I,J)
AA(27)=S25(I,1)+S25(I,J)
AA(28)=S45(I,1)+S45(I,J)
AA(29)=S55(I,1)+S55(I,J)
AA(30)=S56(I,1)+S56(I,J)
AA(31)=S36(I,1)-S36(I,J)
AA(32)=S16(I,1)+S16(I,J)
AA(33)=S26(I,1)+S26(I,J)
AA(34)=S46(I,1)+S46(I,J)

```

9

```

AA(35)=S56(I,1)+S56(I,J)
AA(36)=S66(I,1)+S66(I,J)
BB(1)=1.
BB(2)=0.
BB(3)=0.
BB(4)=0.
BB(5)=0.
BB(6)=0.
KS=0
CALL SIMQ(AA,BB,6,KS)
IF (KS) 41,41,53
41 RE(J)=1/BB(1)
   ODD=0.
   EVEN=0.
   DO 45 J=2,8,2
   EVEN=EVEN+RE(J)
   ODD=ODD+RE(J+1)
45 REAVG=(RE(1)+RE(11)+4.*(EVEN+RE(10))+2.*ODD)/30.
   SUM1=SUM1+P00(I)**2/REAVG
   SUM4=SUM4+P30(I)**2/REAVG
   SUM7=SUM7+P60(I)**2/REAVG
   SUM10=SUM10+P90(I)**2/REAVG
40 CONTINUE
WRITE (6,10)
10 FORMAT (6H LOOP2)
C NON-DIAGONAL WEIGHTED MODULI
SUM2=0.
SUM5=0.
SUM8=0.
SUM11=0.
DO 50 I=1,M4
K=I+1
DO 51 J=K,M2
DO 52 L=1,11
AA(1)=S33(I,1)+S33(J,L)
AA(2)=S13(I,1)-S13(J,L)
AA(3)=S23(I,1)-S23(J,L)
AA(4)=S34(I,1)-S34(J,L)
AA(5)=S35(I,1)-S35(J,L)
AA(6)=S36(I,1)-S36(J,L)
AA(7)=S13(I,1)-S13(J,L)
AA(8)=S11(I,1)+S11(J,L)
AA(9)=S12(I,1)+S12(J,L)
AA(10)=S14(I,1)+S14(J,L)
AA(11)=S15(I,1)+S15(J,L)
AA(12)=S16(I,1)+S16(J,L)

```

```

AA(13)=S23(I,1)-S23(J,L)
AA(14)=S12(I,1)+S12(J,L)
AA(15)=S22(I,1)+S22(J,L)
AA(16)=S24(I,1)+S24(J,L)
AA(17)=S25(I,1)+S25(J,L)
AA(18)=S26(I,1)+S26(J,L)
AA(19)=S34(I,1)-S34(J,L)
AA(20)=S14(I,1)+S14(J,L)
AA(21)=S24(I,1)+S24(J,L)
AA(22)=S44(I,1)+S44(J,L)
AA(23)=S45(I,1)+S45(J,L)
AA(24)=S46(I,1)+S46(J,L)
AA(25)=S35(I,1)-S35(J,L)
AA(26)=S15(I,1)+S15(J,L)
AA(27)=S25(I,1)+S25(J,L)
AA(28)=S45(I,1)+S45(J,L)
AA(29)=S55(I,1)+S55(J,L)
AA(30)=S56(I,1)+S56(J,L)
AA(31)=S36(I,1)-S36(J,L)
AA(32)=S16(I,1)+S16(J,L)
AA(33)=S26(I,1)+S26(J,L)
AA(34)=S46(I,1)+S46(J,L)
AA(35)=S56(I,1)+S56(J,L)
AA(36)=S66(I,1)+S66(J,L)
BB(1)=1.
BB(2)=0.
BB(3)=0.
BB(4)=0.
BB(5)=0.
BB(6)=0.
KS=0.
CALL SIMQ(AA,BB,6,KS)
IF (KS) 52,52,53
53 WRITE (6,54)
54 FORMAT (16H SINGULAR MATRIX)
GO TO 90
52 RE(L)=1/BB(1)
ODD=0.
EVEN=0.
DO 55 L=2,8,2
EVEN=EVEN+RE(L)
ODD=ODD+RE(L+1)
55 REAVG=(RE(1)+RE(11)+4.*(EVEN+RE(10))+2.*ODD)/30.
SUM2=SUM2+(P00(I)*P00(J))/REAVG

```



```

SUM5=SUM5+(P30(I)*P30(J))/REAVG
SUM8=SUM8+(P60(I)*P60(J))/REAVG
51 SUM11=SUM11+(P90(I)*P90(J))/REAVG
50 CONTINUE
WRITE (6,13)
13 FORMAT (6H LOOP3)
E0AV=(SUM1+4.*SUM2)/SUM3**2
E30AV=(SUM4+4.*SUM5)/SUM6**2
E60AV=(SUM7+4.*SUM8)/SUM9**2
E90AV=(SUM10+4.*SUM11)/SUM12**2
EE0AV=E0AV/69000.
EE30AV=E30AV/69000.
EE60AV=E60AV/69000.
EE90AV=E90AV/69000.
WRITE (6,14) M2,W,X,Y,Z
140FORMAT (12H INTERVALS=,I3,3H W=,E14.7,3H X=,E14.7,3H Y=,E14.7,
13H Z=,E14.7)
WRITE (6,15) A11,A12,A13,A33,A44
15 FORMAT (5H A11=,E11.4,5H A12=,E11.4,5H A13=,E11.4,5H A33=,E11.4,
15H A44=,E11.4)
WRITE (6,16) SUM1,SUM2,SUM3,SUM4,SUM5,SUM6
16 FORMAT (6E15.8)
WRITE (6,17) SUM7,SUM8,SUM9,SUM10,SUM11,SUM12
17 FORMAT (6E15.8)
WRITE (6,18) E0AV,EE0AV
18 FORMAT (21H AVERAGE MODULUS(00)=,E15.8,6HDSC
,E15.8)
WRITE (6,19) E30AV,EE30AV
19 FORMAT (21H AVERAGE MODULUS(30)=,E15.8,6HDSC
,E15.8)
WRITE (6,20) E60AV,EE60AV
20 FORMAT (21H AVERAGE MODULUS(60)=,E15.8,6HDSC
,E15.8)
WRITE (6,21) E90AV,EE90AV
21 FORMAT (21H AVERAGE MODULUS(90)=,E15.8,6HDSC
,E15.8)
90 CONTINUE
END

```

BIBLIOGRAPHY

1. Erle I. Shobert II, Carbon and Graphite (New York: Academic Press, 1964) pp. 1-15.
2. O. L. Blakslee, D. G. Proctor, E. J. Seldin, G. B. Spence and T. Weng, Elastic Constants of Compression-Annealed Pyrolytic Graphite, Report No. PP-69-6 (Parma: Union Carbide Corporation, Carbon Products Division, Parma Technical Center, August 1, 1969).
3. D. E. Soule and C. W. Nezbeda, "Direct Basal-Plane Shear in Single-Crystal Graphite," Journal of Applied Physics, Vol. 8 (1952), pp. 5122-5139.
4. E. J. Seldin and C. W. Nezbeda, Elastic Constants and Electron Microscope Observations of Neutron Irradiated Compression-Annealed Pyrolytic and Single Crystal Graphite, Report No. PP-69-8 (Parma: Union Carbide Corporation, Carbon Products Division, Parma Technical Center, August 1, 1969).
5. G. M. Jenkins, "Analysis of the Stress-strain Relationships in Reactor Grade Graphite," British Journal of Applied Physics, Vol. 13 (1962), pp.30-32.
6. G. M. Jenkins, "Fracture in Reactor Graphite", Journal of Nuclear Materials, Vol. 5 (1962), pp. 280-286.
7. O. D. Slagle, "Deformation Mechanisms in Polycrystalline Graphite," Journal of The American Ceramic Society, Vol. 50 (1967), pp. 495-500.
8. G. M. Jenkins, "Effect of Microporosity on the Elastic Modulus and Yield Curve of Polycrystalline Graphite," Journal of Nuclear Materials, Vol. 29 (1969), pp. 322-328.
9. Morton C. Smith, "Longitudinal Tensile Behavior of H⁴LM Graphite in Nitrogen to 2750°C," Journal of Nuclear Materials, Vol. 13, No. 1 (1964), pp. 57-62.
10. E. J. Seldin, "Stress-Strain Properties of Polycrystalline Graphites in Tension and Compression at Room Temperature", Carbon, Vol. 4 (1966), pp. 177-191.
11. B. A. Bilby, A. H. Cottrell and K. H. Swinden, "The Spread of Plastic Yield from a Notch", Proceedings of the Royal Society of London, Vol. 272 (1963), pp. 304-314.

12. Tewksbury Symposium on Fracture.1st, Melbourne, 1963, Fracture, "Mechanisms of Fracture, by A. H. Cottrell," (Melbourne: University of Melbourne, 1965), pp. 1-27.
13. Conference on Carbon.5th, University Park, 1961, Proceedings of the Fifth Conference on Carbon, Vol. 2, "The Strength of Graphite, by H. H. W. Losty and J. S. Orchard", (New York: The Macmillan Company, 1963), pp. 519-532.
14. E. G. Zukas and W. V. Green, "The High-Temperature Creep Behavior of a Highly-Oriented Polycrystalline Graphite", Carbon Vol. 6 (1968), pp. 101-110.
15. Conference on Carbon.3rd, Buffalo, 1957, Proceedings of the Third Conference on Carbon, "High-Temperature Tensile-Properties of Graphites, by H. E. Martens, L. D. Jaffe and J. E. Jepsang", (New York: Pergamon Press, 1959), pp. 529-542.
16. Conference on Carbon. 5th, University Park, 1961, Proceedings of the Fifth Conference on Carbon, Vol. 2, "The Strength of Commercial Graphite, by I. B. Mason, (New York: The Macmillan Company, 1963), pp. 597-610.
17. Conference on Carbon. 4th, Buffalo, 1959, Proceedings of the Fourth Conference on Carbon, "The Dependence of the Properties of Graphite on Porosity, by J. M. Hutcheon and M.S.T. Price", (New York: Pergamon Press, 1960), pp. 645-656.
18. R. H. Knibbs, "Fracture in Polycrystalline Graphite", Journal of Nuclear Materials, Vol. 24 (1967), pp. 174-187.
19. W. L. Greenstreet, J. E. Smith, and G. T. Jahr, "Mechanical Properties of EGCR-Type AGOT Graphite", Carbon, Vol. 7 (1969), pp. 15-45.
20. F. P. Knudsen, "Dependence of Mechanical Strength of Brittle Polycrystalline Specimens on Porosity and Grain Size", Journal of The American Ceramic Society, Vol. 42 (1959), pp. 376-387.
21. H. G. Tattersall and G. Tappin, "The Work of Fracture and Its Measurement in Metals, Ceramics and Other Materials", Journal of Materials Science, Vol. 1 (1966), pp. 296-301.
22. A Seminar on the Fracturing of Metals. Chicago, 1947, Fracturing of Metals, "Fracture Dynamics, by George Irwin" (Cleveland: American Society for Metals, 1948), pp. 147-166.

23. G. R. Irwin, "Analysis of Stresses and Strains near the End of a Crack Traversing a Plate", Transactions of the American Society of Mechanical Engineers, Journal of Applied Mechanics, Vol. 79, (1957), pp. 361-364.
24. E. T. Wessel, W. G. Clark and W. K. Wilson, Engineering Methods for the Design and Selection of Materials against Fracture, Final Technical Report (Pittsburgh: Westinghouse Research Laboratories, June 24, 1966), pp. 11-141.
25. Symposium on Fracture Toughness Testing and Its Applications, Chicago, 1964, Fracture Toughness Testing and Its Applications, (Philadelphia: American Society for Testing and Materials, 1965).
26. J. M. Corum, "A Determination of the Fracture Toughness of EGCR-type AGOT Graphite", Journal of Nuclear Materials, Vol. 22 (1967), pp. 41-54.
27. G. E. Bacon, "A Method for Determining the Degree of Orientation of Graphite", Journal of Applied Chemistry, Vol. 6 (1956), pp. 477-481.
28. A. M. Barrachin, G. Jouquet, G. Micaud and F. Patton, "Effet de la Porosite et de L'Orientation Cristalline sur le Module D'Young du Graphite Artificiel", Journal of Nuclear Materials, Vol. 20 (1966), pp. 294-302.
29. J. R. Cost, K. R. Janowski and R. C. Rossi, "Elastic Properties of Isotropic Graphite", The Philosophical Magazine, Vol. 17 (1968), pp. 851-854.
30. R. M. Spriggs, "Expression for Effect of Porosity on Elastic Modulus of Polycrystalline Refractory Materials, Particularly Aluminum Oxide", Journal of the American Ceramic Society, Vol. 44 (1961), pp. 628-629.
31. D. K. Bazaj and E. E. Cox, "Stress-Concentration Factors and Notch-Sensitivity of Graphite", Carbon, Vol. 7 (1969), pp. 689-697.
32. R. J. Price, "Young's Modulus of Pyrolytic Carbon in Relation to Preferred Orientation", The Philosophical Magazine, Vol. 12 (1966), pp. 561-571.
33. O. D. Slagle, "Averaging Techniques in Polycrystalline Graphites", Carbon, Vol. 6 (1968), pp. 111-121.
34. D. B. Fischbach, "Isotropic. High-Temperature Plasticity of Graphite," The Philosophical Magazine, Vol. 21 (1970), pp. 1-6.

35. I. N. Sneddon, "The Distribution of Stress in the Neighbourhood of a Crack in an Elastic Field", *Proceedings of the Royal Society of London*, Vol. 187 (1946), pp. 229-260.
36. R. V. Southwell and H. J. Gough, "On the Stress Concentration of a Small Spherical Flaw; and on the Propagation of Fatigue Fractures in 'Statistically Isotropic' Materials", *The Philosophical Magazine*, Vol. 1 (1926), pp. 71-85.
37. S. G. Lekhnitskii, *Theory of Elasticity of an Anisotropic Elastic Body* (San Francisco, Holden-Day, Incorporated, 1963), pp. 1-68.
38. E. A. Bush and F. A. Hummel, "High-Temperature Mechanical Properties of Ceramic Materials: I, Magnesium Dinitate", *Journal of The American Ceramic Society*, Vol. 41 (1958), pp. 189-195.
39. E. A. Bush and F. A. Hummel, "High-Temperature Mechanical Properties of Ceramic Materials: II, Beta-Eucryptite", *Journal of The American Ceramic Society*, Vol. 42 (1959), pp. 388-391.
40. R. M. Spriggs and T. Vasilos, "Effect of Grain Size on Transverse Bend Strength of Alumina and Magnesia," *Journal of The American Ceramic Society*, Vol. 46 (1963), pp. 224-228.
41. R. E. Fryxel and B. A. Chandler, "Creep, Strength, Expansion and Elastic Moduli of Sintered BeO as a Function of Grain Size," *Journal of The American Ceramic Society*, Vol. 47 (1964), pp. 283-291.
42. J. S. O'Neil, "Strength and Elastic Modulus Relationships in BeO-SiC Bodies," *Transactions of the British Ceramic Society*, Vol. 69 (1970), pp. 81-85.
43. E. M. Passmore, R. M. Spriggs and T. Vasilos, "Strength-Grain Size - Porosity Relationships in Alumina," *Journal of The American Ceramic Society*, Vol. 48 (1965), pp. 1-7.
44. D. M. Choy, H. Palmour III, and W. W. Kriegel, "Microstructure and Room-Temperature Mechanical Properties of Hot Pressed Magnesium Aluminate as Described by Quadratic Multivariable Analysis," *Journal of The American Ceramic Society*, Vol. 51 (1968), pp. 10-16.
45. D. P. H. Hasselman, "Griffith Flaws and the Effect of Porosity on Tensile Strength of Brittle Ceramics," *Journal of The American Ceramic Society*, Vol. 52 (1969), p. 457.
47. H. P. Kirchner and R. M. Gruver, "Strength-Anisotropy-Grain Size Relations in Ceramic Oxides," *Journal of The American Ceramic Society*, Vol. 53 (1970), pp. 232-236.

48. W. R. Manning, O. Hunter, Jr. and B. R. Powell, Jr., "Elastic Properties of Polycrystalline Yttrium Oxide, Dysprosium Oxide, Holmium Oxide and Erbium Oxide: Room Temperature Measurements," Journal of The American Ceramic Society, Vol. 52 (1968), pp. 436-442.
49. R. D. Carnahan, "Elastic Properties of Silicon Carbide," Journal of The American Ceramic Society, Vol. 51 (1968), pp. 223-224.
50. P. L. Gutshall and G. E. Gross, "Fracture Energy of Polycrystalline Beryllium Oxide," Journal of The American Ceramic Society, Vol. 51 (1968), p. 602.
51. S. C. Carniglia, "Petch Relation in Single-Phase Oxide Ceramics," Journal of The American Ceramic Society, Vol. 48 (1965), pp. 580-583.
52. D. Kalish, E. V. Clougherty and K. Kreder, "Strength, Fracture Mode and Thermal Stress Resistance of HfB_2 and ZrB_2 ," Journal of The American Ceramic Society, Vol. 52 (1969), p. 30-36.